TIN CATALYST PREPARATION FOR SILICON NANOWIRE SYNTHESIS

By

FORTUNATE MOFAO MODIBA

Submitted in fulfilment of the requirements of the degree of

Magister Scientiae in the Department of Physics and Astronomy,

University of the Western Cape

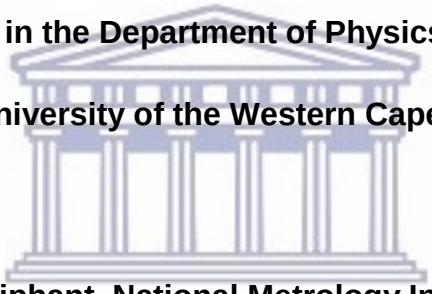

Supervisor: Prof C.J Oliphant, National Metrology Institute of South Africa

Co-supervisors: Prof C.J. Arendse, University of the Western Cape

Dr Theophillus Miller, University of the Western Cape

March 2018

I dedicate this thesis to my loving family:

My sons Joshua & Letlhogonolo, My husband Donald,

My parents Phineas & Ruth

&

My siblings Sholly |Phenyo, Mosima, Maite, Mack & Phatudi

ACKNOWLEDGEMENTS

I thank God of Major 1 for His Grace!

I am very grateful to the following people and organisations without whose assistance, advice and guidance this thesis would not have been possible.

- Prof Christopher Arendse (UWC) for the exceptional supervision, guidance, friendship and the sustained support throughout the duration of this thesis.
- Prof Clive Oliphant (NMISA) for the excellent supervision of this thesis, his guidance, encouragement, friendship and for the many stimulating discussions.
- Dr Franscious Cummings (UWC) for an amazing assistance with the HRTEM technique.
- Material characterisation team (NMISA) for all your support and assistance in this study
- Department of Physics (UWC) team for the love and support through this study.
- NMISA and NRF for their great financial support.

Thank You!

DECLARATION

I declare that

"TIN CATALYST PREPARATION FOR SILICON NANOWIRE SYNTHESIS"

is my own work, it has not been submitted for any degree or examination in any other university, and that all sources I have used or quoted have been indicated and acknowledged by means of complete references

FORTUNATE MOFAO MODIBA **MARCH 2018**

SIGNED: 

KEYWORDS

TIN CATALYST PREPARATION FOR SILICON NANOWIRE SYNTHESIS

FORTUNATE MOFAO MODIBA

Photovoltaic solar cells

Silicon nanowires

Metal catalyst

Phase diagram

Tin

Deposition

Annealing

X-ray photoelectron spectroscopy

ABSTRACT

TIN CATALYST PREPARATION FOR SILICON NANOWIRE SYNTHESIS

FORTUNATE MOFAO MODIBA

M.Sc. Thesis, Department of Physics and Astronomy, University of the Western Cape

Solar cells offer SA an additional energy source. While Si cells are abundantly available they are not at an optimal efficiency and the cost is still high. One technology that can enhance their performance is SiNW. However, material properties such as the diameter, porosity and length determine their effectiveness during application to solar cell technology. One method of growing SiNW uses Sn catalysts on a Si substrate. As the properties of the Sn nanoparticle govern the properties of the SiNW, this thesis investigates their formation and properties by depositing a Sn layer on a Si wafer and then subjecting it to different temperatures, during process the layer forms into nanoparticles. At each temperature the morphology, composition and crystallinity will be determined using XPS, SEM, TEM and EDS. Thus, in Chapter 1 there is an overview, Chapter 2 deals with techniques used in this study, Chapter 3 will give the quantitative and qualitative results on the XPS analysis and Chapter 4 will illustrate the structural behaviour of the annealed Sn film samples.

The dimensional properties of silicon nanowires (SiNWs), i.e. the diameter and length, influences the emission and absorption properties of SiNW based optoelectronic devices such as solar cells. The SiNW dimensional properties in turn are influenced by the size and composition of the metal catalyst used to grow the SiNWs. The relationship between the catalyst and the SiNW emanating from it, is a consequence of the vapour solid liquid mechanism (VLS), which is a metal catalyst assisted method.

Tin as a metal catalyst has a low eutectic temperature allowing less power consumption, for SiNW synthesis found to be favourable as compared to other metal catalyst such as gold (Au) for low cost deposition of SiNWs. This study will focus on investigating the 3 nm thin film of tin (Sn) catalyst exposed to different temperatures under x-ray photoelectron spectroscopy system.

A 3 nm Sn thin film was thermally evaporated on a Si (100) wafer, after which the wafer was cut into 1x1 cm pieces to be annealed at different temperatures within an x-ray photoelectron spectroscopy system to ascertain the evolution of the Sn film chemical composition at different temperatures. At room temperature, the XPS results detected the presence of metallic Sn and its oxides. The adventitious carbon (C) was also observed indicating surface contamination. The decrease in the C content leads to an increase in Sn at temperatures >232 °C. The Sn content decreased at temperatures ≥ 350 °C, which can be due to the formation of bigger Sn nanoparticles (i.e. more Si surface exposed), Sn evaporation from the surface or in-diffusion of Sn into Si. SEM and low electron beam energy EDS analysis revealed that the surface morphology of the as-deposited Sn film consisted of Sn clusters. Increasing the temperature to 350 °C resulted in the coalescence of nanoparticles. Further increasing the temperature led to well separated nanoparticles at 450 °C.

The internal structure of the Sn nanoparticles was probed using transmission electron microscopy. The aSTEM HAADF mode images of the Sn film annealed at 350°C. The Sn nanoparticles are brighter due to high atomic number. The interface between the Sn/Si substrate possessed a darker contrast due to the high oxygen content. The STEM-EDS elemental mapping of the as-deposited sample confirms the presence of Sn. Oxygen is observed to be extending from the Pt/Sn interface to the Sn/Si interface. The crystallinity of the Sn film was measured by high resolution transmission electron microscopy. HRTEM images of a Sn nanoparticle reveals the diffraction planes with interplanar space of corresponding to pure Sn (200) planes. The amorphous region on the film surface, the Sn oxides are formed as SnO and SnO_2 as deduced from the d-spacings corresponding to the (101) and (200) planes. The high-resolution XPS sputter profiles acquired on during heating, revealed the presence of Sn-oxides at the surface with a pure Sn metallic core towards the substrate. The results have illustrated the possibility of growing Sn catalysed SiNWs since there is a crystalline Sn core present on the Si substrate.

CONTENTS

CHAPTER 1

Abstract

Solar cells offer SA an additional energy source. While Si cells are abundantly available they are not at an optimal efficiency and the cost is still high. One technology that can enhance their performance is SiNW. However, the structural properties such as the diameter, length, porosity determines the effectiveness of SiNW applied to solar cells. One method of growing SiNW uses Sn catalysts on a Si substrate. As the properties of the Sn nanoparticle determine the properties of the SiNW, this thesis investigates their formation and properties by depositing a Sn layer on a Si wafer and then subjecting it to different temperatures, in which process the layer forms into nanoparticles. At each temperature the morphology, composition and crystallinity will be determined using XPS, SEM, TEM and EDS. Thus, in Chapter 1 there is an overview of the study, Chapter 2 deals with techniques used in this study, chapter 3 will give the quantitative and qualitative results on the XPS analysis and chapter 4 will illustrate the structural behaviour of the annealed Sn film samples.

INTRODUCTION

1.1 Energy crisis in South Africa

South Africa is one of the countries around the world that is currently experiencing dwindling energy resources. The country's concern is the accessibility to safe and sustainable energy supply at low costs [1.1]. South Africa has been using fossil fuel in the form of coal as its major energy supply for decades [1.2]. However, coal is not only a non-renewable resource but one of the most polluting energy sources on the planet as it plays a major role in the climate change due to the emissions of carbon dioxide (CO_2) which causes global warming. In addition, coal production was reduced because it is expensive to implement techniques to reduce the health risks of coal [1.3].

The negative side effects of coal on the environment and its dwindling supply have led to wide scale research to find a renewable energy resource at low cost for the country and globally. Examples of renewable energy sources include wind power, hydroelectric power, ocean/tidal energy, geothermal energy, biomass and solar energy [1.4]. South Africa experience sunlight radiation of about 4.5 to 6.5 kWh/m^2 in one day which makes it higher in sunlight efficient as compared to other countries [1.5]. As a result, South Africa has identified solar energy as one of the renewable sources for its energy supply.

1.2 Solar cells

Harnessing solar energy is done using the solar cells which converts solar energy into electricity. The working principle of solar cells is based on the photovoltaic effect, i.e. the generation of a potential difference at the junction of the acceptor (p-type) and donor (n-type) semiconductor materials in response to electromagnetic radiation.

Silicon is the material that is mostly used to build a solar cell and it is the second most abundant (after oxygen) on earth [1.6, 1.7]. Silicon is not the only material however that can be used to fabricate solar cells, other examples include gallium arsenic (GaAs) germanium, zinc oxide, zinc sulphide, cadmium telluride, cadmium selenide, copper oxide, titanium oxide, gallium nitride, indium gallium nitride, gallium arsenide, indium arsenide, and polymer/nanowire combinations [1.8-1.23]. Silicon can be toxic in some forms. Efficiencies are higher than 6%. [1.24].

However, silicon possesses an indirect band gap of 1.12 eV at ambient temperatures which leads to poor light absorption in solar cells; it only requires a small amount of energy to excite electrons from the valence band to the conduction band.

The band-gap is an important property as it determines the functionality of a solar cell. Semiconductors materials are found to have an advantage over the conductors or meter and insulator (and glasses) [1.25 - 1.27]. Semiconductor materials differ from conductors and insulators by their band-gap ranging from 0.5 to 3 eV, while the conductors have overlapping band-gaps and insulators have a wide gap, which is roughly more than two electron volts (2 eV). Figure 1.1 shows the basic operation of the solar cell, where there is a generation of the electron-hole pair from incident photon in a semiconductor.

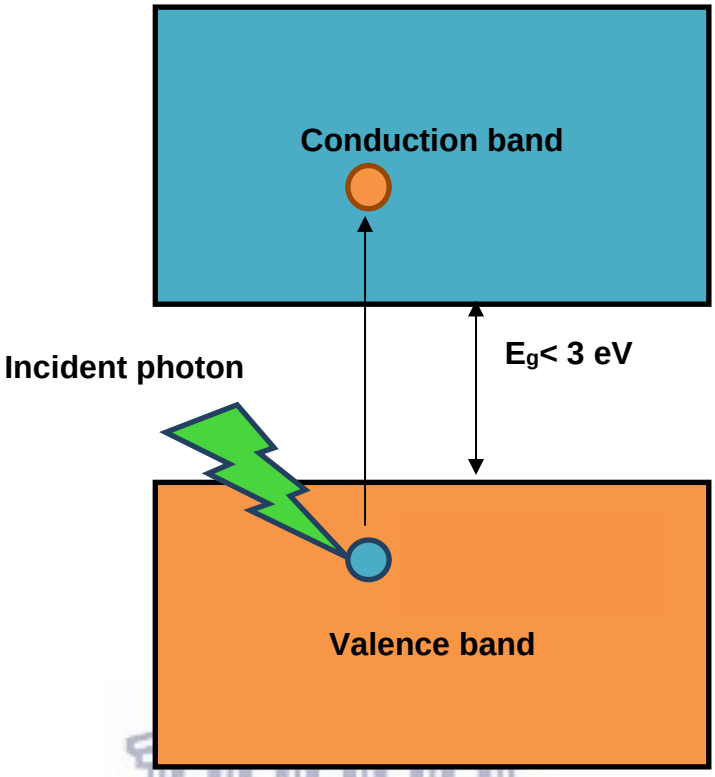

Figure 1.1: Generation of electron -hole pair from incident photon in a semiconductor [1.27-1.28].

The basic principle of the solar cell is the excitation of the electron from the valence band by the incident photon which has higher energy as compared to the band gap of the Silicon (Si) semiconductor material. The process will lead to the formation of the electron-hole pair which means there will a hole (positively charged) in the valence band and the electron (negatively charged) in the conduction band which moves freely. The transfer of electron and hole will lead to the generation of electricity (figure.1.1). However, the recombination of the electron-hole pair can occur after a short time which will stop the charge mobility leading to no electricity generation. Recombination processes can be prevented through the creation of an electrical field by the charge transfer to separate the electron-hole pair resulting in a potential different. [1.27–1.28].

1.3 Doping

Silicon (Si) as an intrinsic semiconductor, it has few electron-hole pairs to be generated at room temperature, leading to low conductivity which has a limitation in solar cell application. The pentavalent (donor) and trivalent (acceptor) impurity materials can be added in the semiconductor to improve the conductivity of the material creating the n-type and p-type semiconductor using a doping process as indicated in figure 1.2.

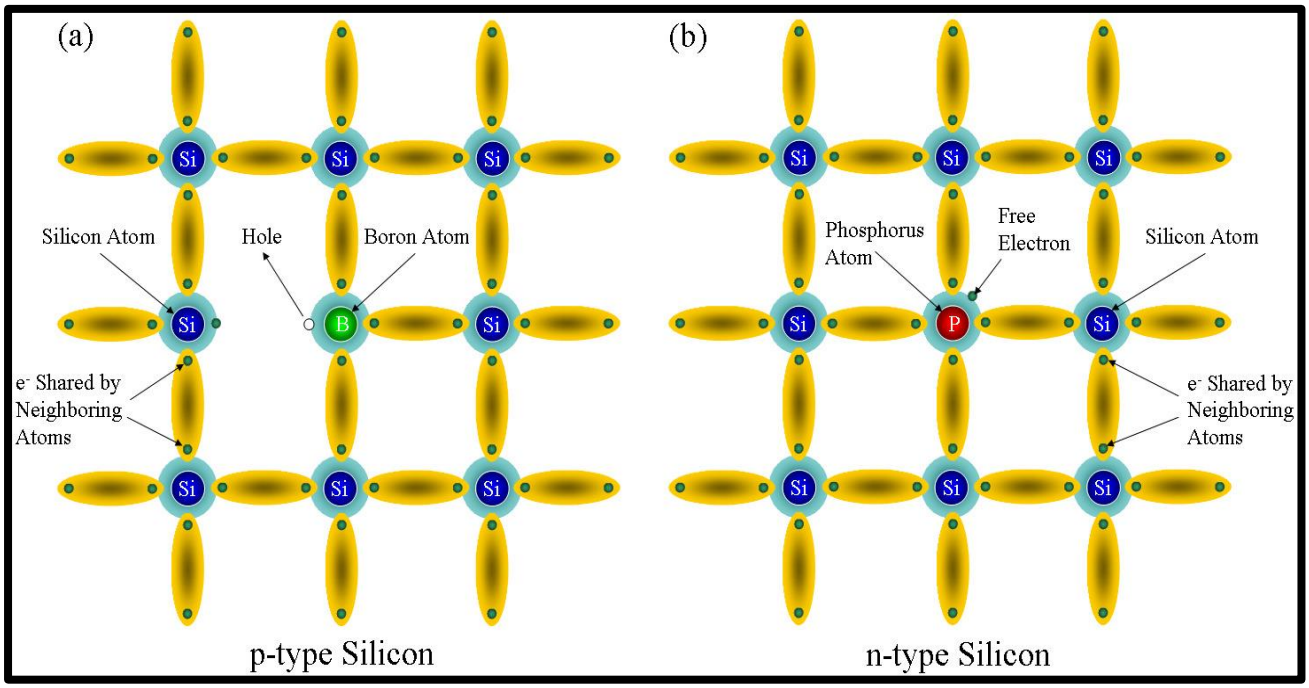

Figure 1. 2: Schematic presentation of the cross-section of doped silicon lattice : (a) boron (B) doped p-type silicon with an extra hole (b) phosphorous (P) n-type silicon with an extra electron [1.29].

Doping is the process of introducing foreign atoms in semiconductors. The process improves the electronic properties of the semiconductor by substituting its lattice sites. There are two types of dopants depending on their valence electrons which take part in the bonding with other neighbouring atoms. The dopant atom known as acceptor or p-type accepts an extra electron, each from a single host atom while the

n-type dopant, donate an extra electron each to a single host atom. The crystalline Silicon (c-Si) as a semiconductor, it has four valence electrons, each electron is equally shared with the nearest neighbour atom forming a covalent bond between Si atoms and therefore there are no free electrons in the lattice. At temperatures, higher than 0°C bonds start to break due to thermal absorption which leads to formation of mobile electron and holes. When a bond is broken, a hole is created due to the removal of the electron which can be replaced by an electron from the neighbouring atom, leaving a hole at the original bond [1.28] (see Figure 1.2)

The group III elements including Boron (B), Gallium (Ga) and Aluminium (Al) are common dopant impurities for producing n-type doping in the group IV semiconductors such as Silicon (Si) and Germanium (Ge).

The p-type are usually in the group IV element of the periodic table such as boron (B) and gallium, while for the n-type dopants are (Ga) phosphorous (P), Arsenic (As) and Antimony (Sb). The concentration of electrons and holes in crystalline-Silicon (c-Si) can be controlled by doping. The p-type in a Si lattice accepts an electron from a Si atom, which leads to the reduction of electron or increase of the number of 'holes' that act as majority carrier charge [1.29]. Donor impurities donates negatively charged electrons to the Si lattice, which leads to free electron outnumbering the holes in compound, so the electrons are the majority carries and holes are the minority carriers.

The importance of doping on the properties of pure c-Si in terms of energy band diagram of Si for the n-type dopant shift the Fermi level (EF) upward moving it closer to the conduction band (E_c), thus lowering the barrier of between the conduction and valence band. The p-type dopant lowers the E_i of Si moving it close to the valence

band (E_v) and reducing the energy barrier for the holes to contribute to electrical conductivity [1.29]. The increase in conductivity of the semiconductors through doping can be observed when creating a pn junction.

1.4 P-N junction

The p-n junction comprises of the n- and p-type semiconductors which are chemical combined to form a diode shown by the schematic in figure 1.3. The p-n junction contributes to the basic building block for most of the microelectronic devices formed when p-type Si (p-Si) is joined to n-type (n-Si). The majority charge carriers diffuse across the junction where the electrons move to the p-doped and holes moves to the n-doped. The presence of a space charge region induces an internal electric field. The electric field created by the two regions, thus drifting all incoming electrons resulting in an electric current across the devices [1.30]. The p-n junction gives an understanding of the number of electronic circuits, applications and devices.

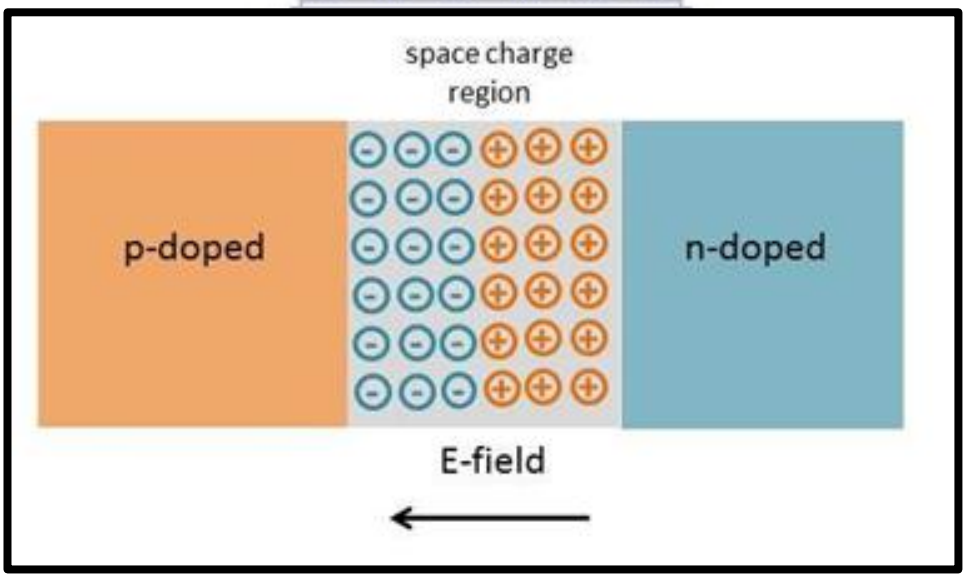

Figure 1.3: Schematic diagram of the p-n junction [1.31]

1.5 Generation of solar cells

The first solar cell was discovered in 1839, which has led to the beginning of solar cell technology research and development [1.32]. There are three generations of solar cells of which were developed in finding the ideal solar cell.

1.5.1 First generation (mono-crystalline silicon wafer)

The first solar cell which was called the crystalline solar cell - wafer based which was made in 1946 [1.33]. The mono-crystalline had higher efficiency of 17- 18% [1.31, 1.34] as compared to the poly crystalline approximately 12-14 % [1.35] (around 10% [1.36]). The mono-crystalline had limitations in high cost. From the observed limitations, the second generation was developed.

1.5.2 Second generation (thin film)

The use of thin film was found to be at low cost since it reduces the amount of material used to fabricate the solar cell. The second generation was classified as;

a) Amorphous Silicon Thin Film (a-Si)

The amorphous silicon thin film solar cell has higher absorbing rate of light as compared to the crystalline cells. Furthermore, it is abundant and easy to fabricate. However, the amorphous silicon thin film solar cell has high inherent disorder and dangling bonds making it poor and less efficient [1.36, 1.37].

b) Cadmium Telluride (CdTe)

Cadmium Telluride (CdTe) is found to be the first photovoltaic device developed at low cost. CdTe is found to be good in light absorption and have an improved efficiency (9 - 11%), since it's an excellent direct band gap crystalline semiconductor compound [1.34, 1.38]. However, cadmium is regarded as a heavy metal and a potential toxic agent that can affect all living things. And the re-cycling can be highly expensive and not environmentally friendly [1.39, 1.40].

c) Copper Indium Gallium di-Selenide (CIGS)

The copper indium gallium di-selenide (CIGS) solar cells are the quaternary direct band gap type semiconductor compound. The CIGS are a flexible choice of the substrate for fabrication but at high cost. CIGS have a higher efficiency (~10 - 12%) as compared to the CIS solar cells [1.37, 1.41]

1.5.3 Third generation (thin film)

The 3rd generation was introduced to improve the second generation's poor electricity performance at low cost with the modern technology at small scale.

a) Polymer Solar Cell (PSC)

Polymer solar cells (PSC) are known to be flexible solar cells. More research work was done and in the year 2000, where conducting polymers were discovered [1.42, 1.43]. According to [1.45] there is a great improvement in the efficiency by preparing a chlorinated polymer donor, where it was reported to be more than 14%.

b) Dye-Sensitized Solar Cells (DSSC)

Dye-Sensitized Solar Cells (DSSC) was developed to improve the efficiency by molecular manipulation using nanotechnology [1.46, 1.47]. The DSSC had attracted great attention due to their flexibility which leads to easy fabrication at low cost. However, the dye molecules tend to degrade, which brought a great concern in its stability. Moreover, it has poor optical absorption which leads to poor conversion efficiency [1.34,1.48 - 1.51].

c) Concentrated Solar Cells (CSC)

The concentrated solar cells (CSC) principle is based on optics by using large mirrors and lens arrangement to focus sunlight into a small region on the solar cell which tends to produce a large amount of heat energy [1.34]. The CSC had limited thermal mass and can be controlled to a wide range of sizes with the efficiency of more than 40 %. However, the installation can be expensive [1.37].

d) Perovskite Base Solar Cells (PBSC)

Perovskite based solar cells (PBSC) are composed of halogens and cations of different sizes [1.37]. PBSC had the efficiency of up to 31% [1.52]. However, the material used tends to degrade over a period which affects the PBSC's efficiency, which limits the stability and durability of the PBSC [1.37].

e) Nanocrystal Based Solar Cells

The nano-crystal solar cells which are generally known as the Quantum dots solar cell since they are made up of semiconductor and transition metal group [1.37]. Tandem cell can be created combining nano-crystal silicon (nc-Si) in thin layers [1.36]. However, there is a low carrier transport mainly because of the defects which leads to low efficiency. The lead sulphite (PbS) quantum dots have reached the efficiency of 8.55 % which was the best efficiency for the quantum dots [1.53]. The challenges involved in integrating these nanostructures in devices include precise dot size/band gap control, optimizing electrical conductivity and improving optical response, while considering the limitations of large-scale fabrication [1.53].

The growth of technology has brought wide range of new techniques to improve on the solar cell. Thin film technologies have gained much interest because of their potential for low cost, large area fabrication. Amorphous silicon is a widely used thin film material in solar cells because it has a high absorption coefficient. However, the lack of long-range atomic order also results in high defect densities, limiting the film thickness to values ~ 300-500 nm for efficient charge collection. Optical absorption in thin layers is generally weak at infrared wavelengths and therefore requires a light trapping mechanism to increase the path of light travel within the film [1.5]. The patterning of thin film solar cell with nanostructure materials is a promising attempt, where the properties of the bulk material (thin film) can be changed at low cost.

1.6 Light trapping in solar cell

The solar cell should allow complete light absorption and photo carrier current collection. To obtain enhanced efficiencies, the solar cells require thicknesses that are several times smaller than the minority carrier diffusion lengths [1.5].

Several methods were developed to enhance the optical properties of the thin film such as surface texturing to improve light absorption in crystalline and amorphous silicon. In crystalline silicon, solar cells surface texturing by anisotropically-etching pyramids was conducted improving device performance by lowering optical reflectance [1.54]. The most common light trapping mechanism in thin film silicon solar cells is texturizing of the transparent conductive oxide layer such as SnO_2: F [1.55] and ZnO: Al [1.56]. The anti-reflective coating (ARC) thin film with a specific refractive index at the surface of the active-layer of the semiconducting material it can prevent the incident radiation to be reflected [1.57]. Other methods are plasmonic back-reflectors, [1.58], photonic crystals [1.59], periodic nano - dome back-reflectors [1.60] and silicon nanowires [1.61].

1.6.1 Silicon thin film nanostructure patterning.

The nanostructure used to enhance the thin film surface were nano rods, nanotube, nanoparticles and nanowires [1.62]. The prefix nano means 10^{-9} hence nanostructures have a size range of about a few to several nanometres (10^{-9} - 10^{-7}m). The nanowires which are hair/whisker-like one dimensional (1D) [1.63] nonmaterial has been given more attention as compared to other nanostructures due to their unique properties, easy to fabricate and wide range of applications [1.64].

1.7 Properties of Silicon nanowires (SiNWs)

Treuting and Arnold have reported the artificial silicon fibre in 1957 [1.65] leading to the discovery of the SiNWs by Wagner and Ellis in 1964 [1.66] and since then continual investigations were conducted till present. The main objective of the investigations is mostly on the synthesis, physical properties, device fabrication and their applications. Silicon nanowires (SiNWs) are attractive nanomaterial due to their principal role of the semiconductor industry [1.67-1.71]. SiNWs have their potential applications such as lithium-ion battery anode [1.72, 1.73] and various nanowire-based photovoltaic (PV) solar cells due to their high surface - volume ratio [1.74-1.76]. The technological potential for SiNWs observed in field - effect [1.77 - 1.79] and single - electron [1.8] transistor geometries, as well as in configurations of sensing of biomolecules [1.81, 1.82].

Silicon nanowires can be defined as nanostructures having a very high length-diameter aspect ratio with diameters on the order of ranging from 10 – 100 nm their quantum physical effect such as quantum confinement become more dominant [1.83]. Larger diameter silicon nanowires with diameters on the order of tens to hundreds of nanowires have been shown to exhibit strong anti-reflective properties and can enhance optical absorption as compared to bulk silicon. This is due to the changes in the atomic structure because of direct influence of ultra-small length scale on the energy band structure [1.84].

1.7.1 Optical Properties

Quantum confined silicon nanowires show improved emission and absorption, along with a tuneable band gap as compared to bulk crystalline silicon. The optical absorption properties can be enhanced by nanostructures within the visible and infrared regions ranging 400 to 800 nm [1.85]. The tuning of the emission

wavelength in arrays of SiNWs opens the opportunity to develop light-emitting diodes in the visible and ultraviolet regime [1.86, 1.88].

1.7.2 Mechanical Properties

SiNWs have been used in a broad range of applications including nano-electronics [1.79,1.89-1.90] nano-resonators [1.86] light-emitting diodes [1.87] and thermo electric energy scavengers [1.88, 1.91]. The operation and reliability of these nano devices depend on the mechanical properties of SiNWs, which are expected to be different from their bulk counterparts [1.92]. The mechanical properties of the silicon nanowire were found to be made as a building block of the devices of the future electronics since they possess superior elastic modulus to those of bulk silicon [1.88]. The silicon nanowires as a nano-mechanical resonator were employed by Roukes *et.al.* [1.86] using the piezoresistive properties for actuation. According to Young –Soo Sohn *et al.* [1.193], the size of the silicon nanowires does not contribute on the mechanical properties of silicon nanowires when its diameter is larger than 100nm. The decreases in thickness [1.94] and change in crystallinity of the silicon nanowire increases their flexibility [1.93].

1.7.3 Electrical Properties

The effect of electrical conductivity of nanostructures and nano-materials is usually due to reduced impurity, structural defects and dislocation [1.95]. According to Schottky Walter the energy barrier that arises when bringing a metal and a semiconductor in contact cause space charge layer near the interface [1.96]. Cui *et.al* [1.77] reported that the decrease in resistance was due to better metal-to-nanowire contacts and passivation of defects in the nanowires.

The choice of the metal catalyst can affect the electrical properties of the nanowire [1.97].

1.8 Silicon nanowires (SiNWs) synthesis

1.8.1 Top-Down Approach

Top-down nano-patterning techniques provide a different path for fabricating high-density, high-quality nanoscale sensors that can be integrated with Si-based signal processing and communication circuits. The top-down SiNW nanofabrication includes well established techniques for nano-patterning, semiconductor doping, electrical contact formation, and high-quality silicon-on-insulator (SOI) substrates. [1.98 - 1.117]. The top-down approach involves the synthesis of SiNWs starting from the bulk material and scaled down by etching into distinct SiNWs. The etching process can be wet or dry. The techniques such as plasma etching, electron beam lithography (EBL), nano-print lithography and reactive ion bombardment are classified as the dry etching process through template assisted method.

The synthesis via top - down technique has been reported by Park and co-workers [1.118], by using electron beam lithography and reactive ion etching on silicon-on-insulator (SOI) wafer. The approached has led to the production of high-pitched control of the geometry and alignment of SiNWs with efficient electrical properties. However, these techniques are extremely expensive and demand a high-volume application to be cost-effective. The bulk material is etched to nanowires which lead to wasting a material.

The metal assisted etching process is where a Si substrate is introduced into a liquid solution that contained metal catalyst salts. The chemical deposition of metals onto the Si substrate is followed by the etchant chemical, often hydrofluoric acid (HF), selectively etching the areas not covered by the metal particle deposition [1.118]. The reported metal assisted chemical etching (MACE) experiment were a thin

Aluminium (Al) film was deposited on a Si wafer prior to stain etching in a solution containing HF, HNO_3 and H_2O [1.119].

The top-down approach has less attention as compared to the bottom-up method because it is a well understood and widely used method.

1.8.2 Bottom-Up Approach

The bottom-up method is generally the self-assembly of atoms or molecules to form bigger structure. The growth approaches focus more on the control of composition, size and crystallinity of the nanowire synthesised. The methods developed have their unique strategy and different mechanisms. The synthesis of nanowires is the control of composition, size and crystallinity. Among the methods employed, some are based on vapour phase techniques, while others are solution techniques [1.120].

1.8.2.1 Vapour phase growth

The first SiNWs were proposed by Wagner and Ellis in 1964 via the Vapour liquid solid (VLS) mechanism and as the name explains that it is the vapour phase growth method. The first dominant part of the synthesis was the metal catalyst which was used as assistance in the nanowire growth. The metal catalyst used was gold (Au) because it meets most of the criteria for the ideal metal catalyst which will be explained in the next section [1.64-1.66].

a) Vapour liquid solid mechanism (VLS)

The VLS has become widely used because it was simple and versatile in semiconductor applications. The Au catalyst became a desirable choice for growing most diverse types of semiconductor, nanowires (e.g. Si [1.121, 1.66], Ge [1.122] and III–V [1.123]). The schematic overview of the VLS is indicated in figure 1.4.

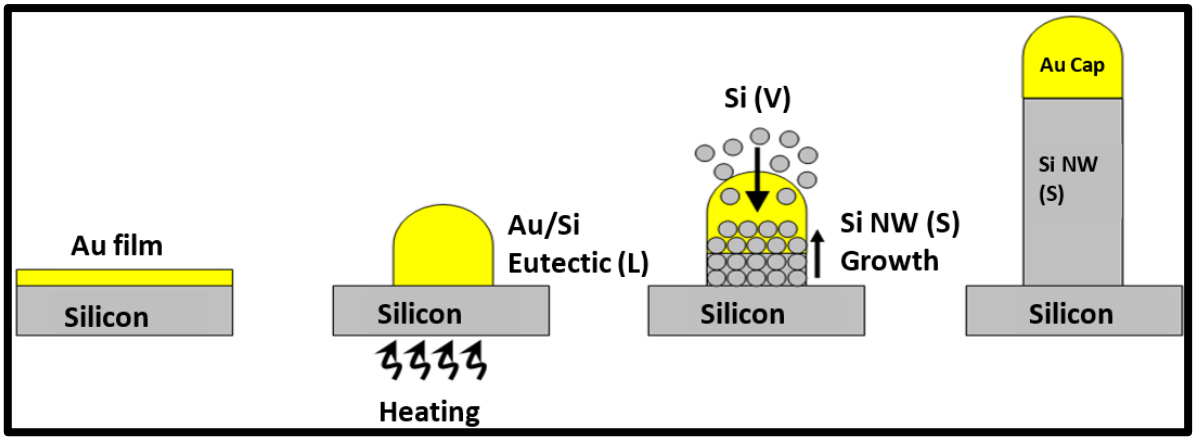

Figure.1.4: Schematic of the metal assisted vapour liquid solid growth mechanism of the SiNWs [1.66].

According to the report by Wegner *et.al* [1.66], the Au catalyst thin film was deposited on the substrate (silicon (Si)) under vacuum, which was then heated above its melting point (about 363 ˚C). The liquid metal catalyst form small nanoparticles or islands on the substrate. The Si containing gaseous species such as SiH_4 is introduced on the surface of the molten Au catalyst nanoparticles which acts as a sink causing the continued incorporation into the lattice which leads to a diffusion of Si through the nanoparticles. The nucleation and crystallization of Si at the gold catalyst (liquid)/Si substrate (solid) interface, forming lateral growth of silicon nanowires. The metal catalysts remain on the tip of the nanowire which is evident that the growth mechanism conducted is the VLS [1.66]. Figure 1.5 shows the interaction of the Si gas at the metal catalyst interface, metal catalyst and Si substrate interface for SiNW growth.

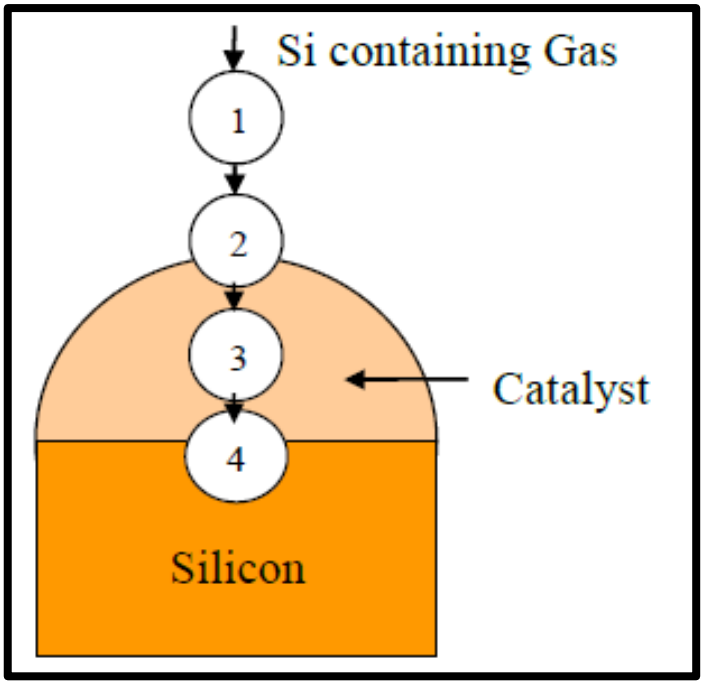

Figure 1.5: An illustration of the VLS growth process [1.124].

The name of the mechanism (VLS) does give the behaviour of the synthesis growth steps with three phases (gas, liquid, and solid) and two interfaces (gas/solid and liquid/solid). The VLS mechanism consists of four steps: (1) mass (Si precursor) transport in the gas phase; (2) chemical reaction at the vapour–liquid interface (gold catalyst acting as a sink); (3) rapid diffusion in the liquid phase (gold catalyst); and (4) incorporation of atoms in a crystal lattice where diffused Si attaches at the liquid-solid interface leading to the one-dimensional growth of a silicon nanowire with the Au droplet located at the tip [1.66, 1.125-1.126]

There are other mechanisms which were developed in reference to the VLS method to grow SiNWs.

b) Vapour-Solid-Solid (VSS) Mechanism

The VLS growth mechanism implies a growth temperature above the eutectic point of the catalysts but if the growth temperature is less than the eutectic point of the catalysts, the metal droplet becomes a solid, and the growth mechanism is called the vapour-solid-solid (VSS) mechanism. Recent studies have reported the formation of

III-V and II-VI NWs based on the VSS growth mechanism. The vapor-solid-solid mechanism was proposed recently to explain the growth temperature of Sn-catalysed Si nanowires under the eutectic point of the catalyst and the nanowire component alloy [1.12, 1.129].

c) Vapour-Solid (VS) Mechanism

The vapour-solid (VS) mechanism is a process where the morphology of the deposited product controls the substrate temperature and the supersaturation ratio for the nanowire growth. The self-catalyst nanowires such as InAs do not have the metal particles at the top. The VS growth process is done by gaseous surface of a solid substrate which is a low controlled temperature than the surface material. The low superstation ratio is preferred for nucleation and growth of nanowires [1.130]

d) Oxide assisted growth (OAG)

The Oxide assisted growth (OAG) mechanism was conducted by growing Ge [1.130] and III - V [1.132 - 1.135] semiconductor nanowire growth. The OAG method is widely since it can produce SiNWs of 1nm in diameter which are metal contaminated free [1.136]. Compared to VLS growth mechanism, OAG uses oxides to induce the nucleation and growth of nanowires and other nanostructures such as rods, chains, ribbons. Lee and co-workers synthesized bulk-quantity SiNWs by thermal evaporation of a powder mixture of silicon and SiO_2 [1.135, 1.136.]. Furthermore, the fabrication of ultra-small diameter (e.g. 1 nm) SiNWs via the optimized OAG approach, whose surfaces were terminated with hydrogen by a hydrofluoric acid dip was also conducted [1.137, 1.138].

The approach of the bottom up SiNW synthesis was also conducted using the liquid phase methods.

e) Solution based growth

In this method crystals are prepared from a solution at a temperature well below its melting point. The constituents of the material to be crystallized are dissolved in a suitable solvent and crystallization occurs as the solution becomes critically supersaturated. This may be achieved by lowering the temperature of the solution by slow evaporation or by continuous supply of the material to compensate for that which is precipitated out. The solution growth methods are classified according to the temperature range and to the nature of the solvents used [1.139].

1.8.2.2 Solid liquid solid (SLS)

The solution-liquid-solid (SLS) is a solution-based method used on the crystalline nanowires of III - V semiconductors. The mechanism is conducted by thermally heating a low melting point metal catalyst on the substrate such as silicon (Si) up to around the eutectic point to form metal-Si alloy, it is then followed by a rapid cooling to synthesize dense SiNWs. However, large diameter, amorphous nanowires are formed with a non-straight stems and rough surface [1.140- 1.141].

a) Template assisted growth

The template serves as a scaffold to control the length and diameter of the nanowire. The template could have nanoscale channels within meso - porous material, porous alumina with hexagonal packed 2D array cylindrical and polycarbonate membrane. The solution, the sol-gel [1.142.] or the electro-chemical [1.143] method is used to fill the nanoscale channels pores with a uniform size. However, it is difficult to obtain materials that are single crystalline.

b) Solvothermal and hydrothermal growth

Solvothermal synthesis is a soft chemical synthesis which involves the use of organic solvents to form crystals with few lattice defects. The method can control the

morphology of the material produced under the temperature range of 100 - 400˚C, the size, shape distribution and the crystallinity of the nanoparticles synthesized. [1.144].

The hydrothermal is almost similar to solvothermal but it only uses water as the solvent. The principle of hydrothermal method is that an insoluble material at ambient temperatures could be made soluble using high temperatures and pressures. The method allows to grow crystals of compounds with high melting points at lower temperatures, and to obtain the crystals which cannot be grown by any other method. The unstable materials at elevated temperatures, solution growth offers slow cooling and slow evaporation methods to grow the desired crystals [1.145].

From the mechanisms developed the VLS is found to have reliable results of nanowires since they are of high quality single crystalline at large quantities. it is mostly used since it is simple, versatile and a well understood method [1.66].

1.9 Growth Techniques

In the past years, techniques and mechanisms have been developed with new improving technology to control SiNW growth, diameter, and morphology which in turn affect the electrical and optical response of the SiNWs [1.66,1.64]. There is a SiNW growing technique which involves the VLS mechanism steps to have fabrication choice of the material depending on the nanowire applications.

1.9.1 Chemical Vapour Deposition (CVD)

Figure 1.6 illustrates the chemical vapour deposition mechanism for growing the SiNWs. Chemical vapour deposition (CVD) is a versatile process suitable for the manufacturing of coatings, powders, fibres, and monolithic components. Chemical vapour deposition may be defined as the deposition of a solid on a heated surface

from a chemical reaction in the vapour phase. It belongs to the class of vapour-transfer processes which is atomistic in nature that is the deposition species are atoms or molecules or a combination of atoms and molecules.

Depending on temperature and type of Si precursor used, CVD allows epitaxial growth of silicon wires with the growth velocity varying from about 10^{-2} to 10^{-3} nm min^{-1} [1.85]. The CVD process is where a substrate is exposed to one or more volatile precursors silicon gaseous precursor such as silane, SiH_4 or silicon tetrachloride, $SiCl_4$ which react and/or decompose on the substrate surface to produce the desired deposit (e.g. Si). The volatile by-products produced are removed by gas flow through the reaction chamber [1.148.]. CVD has proven to be useful in the fabrication of solid state electronic devices as it can provide excellent coverage of substrate features and can deposit high quality thin films of various materials over a large area.

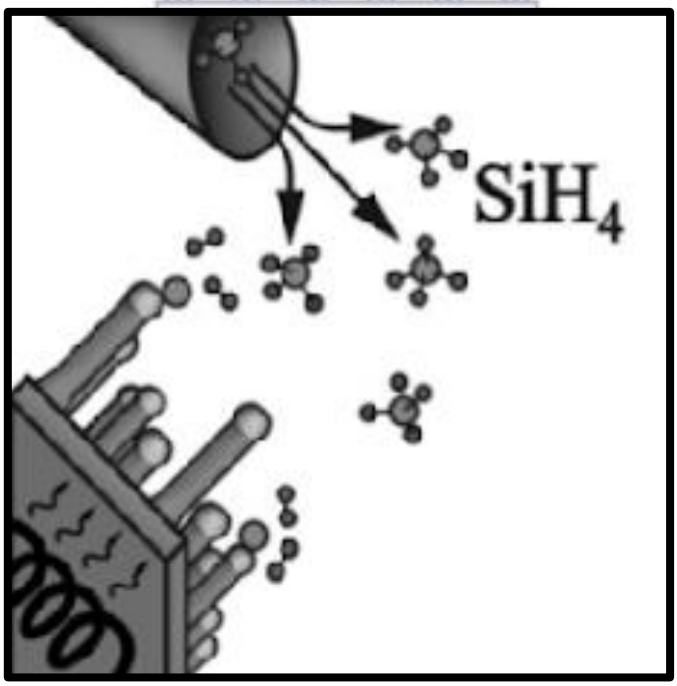

Figure 1.6: Schematic of experimental setup for silicon nanowires growth using CVD [1.125].

The ability to easily control doping levels in thin film growth is advantageous for studying the solubility levels of impurity atoms in materials. There are also a variety of enhanced CVD processes, which involve the use of plasmas, ions, photons, lasers, hot filaments, or combustion reactions to increase deposition rates and/or lower deposition temperatures.

There are also many derivatives of the CVD terminology, such as metal-organic chemical vapour deposition (MOCVD) or, organo-metallic chemical vapour deposition (OMCVD), which are used to identify the class of molecules used in the deposition process. Besides CVD, they include various physical-vapour deposition processes (PVD) such as evaporation, sputtering, molecular beam epitaxy, and ion plating. In many respects, CVD competes directly with the PVD processes, but it is also used in conjunction with them and many of the newer processes are combinations of the two systems such as plasma enhanced CVD or activated sputtering [1.149].

1.9.2 Molecular Beam Epitaxy (MBE)

Molecular beam epitaxy is a technique for epitaxial growth via the interaction of one or several molecular or atomic beams that occurs on a surface of a heated crystalline substrate. The solid sources materials are placed in evaporation cells to provide an angular distribution of atoms or molecules in a beam. The substrate is heated to the necessary temperature and, when needed, continuously rotated to improve the growth homogeneity [1.150]. Figure 1.7 shows a schematic of the MBE process for SiNW synthesis.

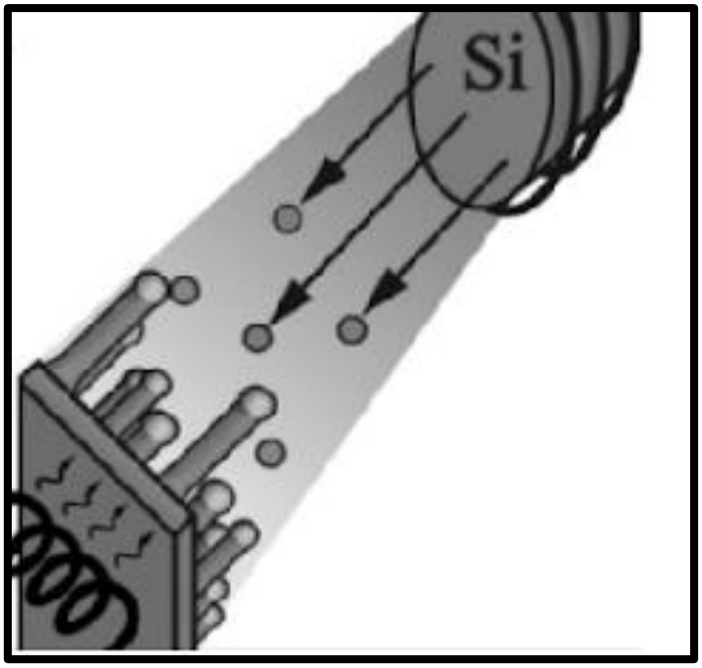

Figure 1.7: Schematic of experimental setup for silicon nanowire growth using MBE [1.125]

MBE was initially speculated to be impossible since the material should be in the form of atom, since no catalytic activity of Au to decompose the precursors to atoms is required as in MOCVD. However, in the year 2000 it was proven to possess great advantages on the growth mechanism investigations of nanowires [1.150].

1.9.3 Thermal Evaporation

The thermal evaporation system employs elevated temperature and relatively low-pressure system to synthesize SiNWs. It is conducted by using the furnace to fabricate nano-materials including carbon nanotubes, either on the substrate on in bulk. The thermal evaporation is a method where by the Si source is placed in a quarts or alumina tube under elevated temperatures at specific pressure.

The method does follow the VLS mechanism with metal catalyst assistance, whereby Hutgalung *et al.* [1.151] as well as Shao et.al. [1.152] reported on using Nickel (Ni) as the metal catalyst. Furthermore, it can still be conducted as free metal catalyst method as it was reported that the SiO is used as the Si source which is

conducted under elevated temperatures of about 850 to 1300 °C which liquefies to SiO nanoparticles which lead to the SiNWs growth. The use of various sources such as a Si powder mixed with Iron (Fe) powder and hot pressed at around 1200 °C was reported. Thermal evaporation can yield nanowires randomly grown on a substrate, the same as in the VLS and laser ablation method [1.151, 1.152].

1.9.4 Laser Ablation

The method was proposed by Wang *et al.* 1998 to growth SiNWs on the metal catalyst free growth. Similar to the thermal evaporation as a solid phase of Si and a source of energy to evaporate or ablate the (metal+ Si or SiO_2 + Si) for the synthesis of high purity, high yield and large quantity of nanowires [1.154].

A high-power pulsed laser ablates material from a mixed Si-metal catalyst target, purged, placed in a tube furnace held at elevated temperature and purged with an inert product downstream where they are deposited as nanowire. The different ambient gases such as He, $Ar+H_2$ and N_2. The Si material ablated from the target tools by colliding with inert gas molecules and the atoms condenses to form liquid nano-droplets with the same composition as the target. The nanoparticles contain both Si and the catalyst material. Following the VLS mechanism where there is a Si vapour source transfer making the metal catalyst supersaturated then forming the SiNWs. The method requires metal catalyst with high eutectic temperature such as Fe since it operates at elevated temperatures [1.154].

1.10 Metal catalyst

The VLS is a unique method as it is the only mechanism wherein the tip of SiNW has a metal catalyst droplet/nanoparticle at the tip [1.66, 1.64]. The metal catalyst is found to be one of the most principal factors for the synthesis of the SiNW growth via the VLS mechanism. According to Ekstrøm [1.154], metal catalyst influences the

diameter and distribution of the nanowires. For the ideal nanowires size, growth direction, growth stability and rate the metal catalyst used should be investigated first to check if it does fit the criteria for the nanowire synthesis using the VLS mechanism because not all the metal can be used to grow the nanowires. The choice of the Wagner and Ellis on gold as a metal catalyst can give a clear understanding on the ideal metal catalyst [1.66].

1.10.1 Gold (Au) as metal catalyst

Figure 1.8 illustrates the metal catalyst assistance in the growth of the SiNW via VLS mechanism. The application of Au as a catalyst for SINW growth via VLS comes as no surprise considering its chemical stability. The property allows Au to have limited technical requirements such as minimum tolerable oxygen background pressure for the nanowire growth. Au is non-toxic which makes it easy to use with low safety measures.

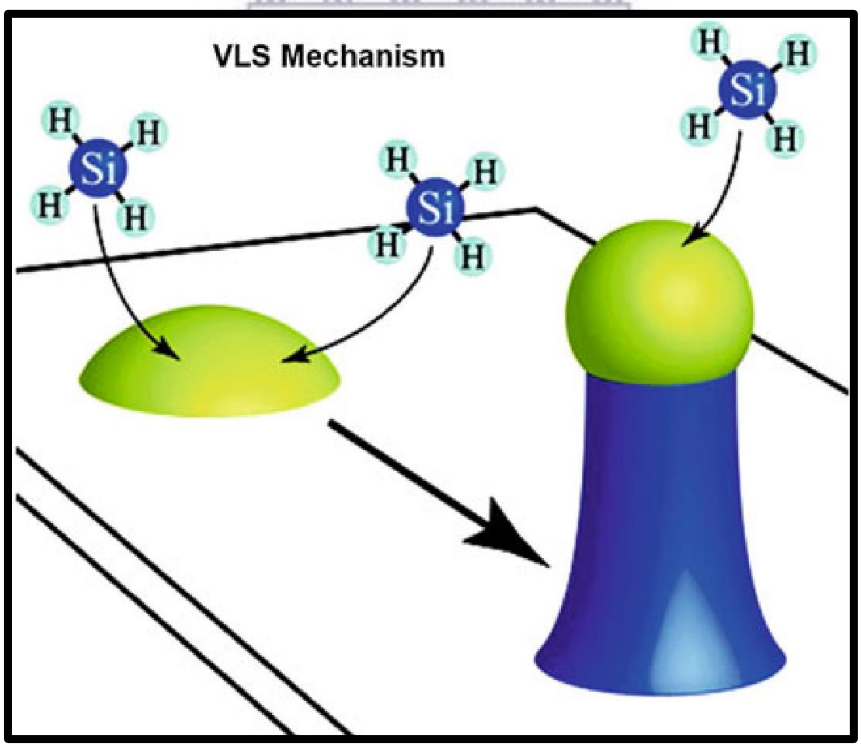

Figure 1. 8: Schematic illustration of the VLS growth mechanism [1.156].

Figure 1. 9: The role of Si chemical potential in the Si VLS growth process, where Si-Si is the bond between the Si atoms, Si-Cat refers to dissolved Si and metal catalyst and Si-Hx bonds between the atoms in the gas phase [1.156]. After the deposition of Au on Si substrate, the Si atoms will diffuse in the Au thin film and vice versa until their concentration reaches the Si equilibrium solubility in the thin film still having most of the Au film on the surface because the solubility of Au in Si is low [1.156]. The Au-Si alloy is formed upon heating the Au coated Si substrate above the eutectic temperature (363 °C). The low solubility of Au in Si results in dewetting where the distribution of Au-Si droplets will be formed instead of homogeneous layer.

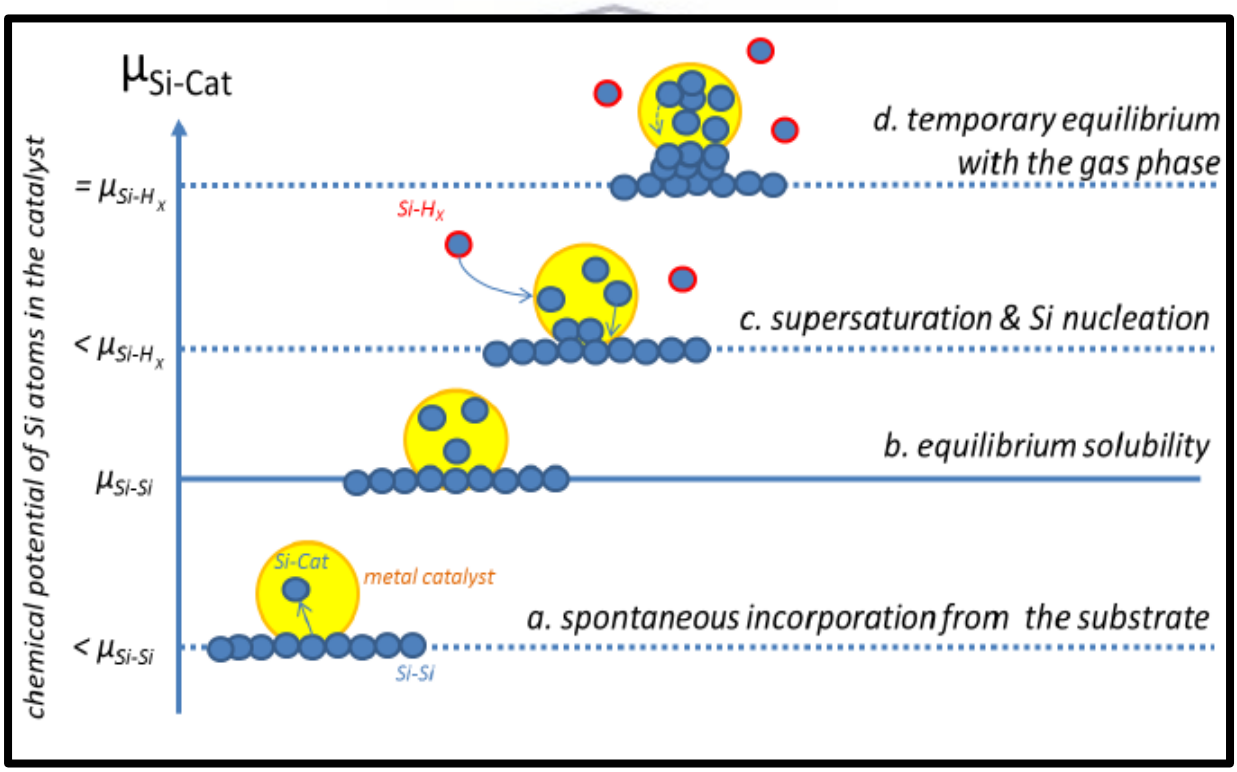

Figure 1. 9: The role of Si chemical potential in the Si VLS growth process.

Figure 1.10 illustrates the phase diagram of Au-Si alloy. According to the Au - Si phase diagram, Au does not form a silicide which can deprive its catalytic functions. It has a low eutectic temperature of about 363 °C (636 K) with 19 at% of Si which allows the low temperature and Si-precursor pressure for SiNW synthesis. The compositions of the Au - Si alloy above the eutectic point, follow the liquidus line (solid line), that denotes equilibrium between the solid and liquid phase. The synthesis of nanowires is also established by the liquid Au catalyst, for the Si precursor gas to be incorporated which mean the solubility limit of Au in liquid phase is higher than the solid Si substrate (figure 1.10). The silicon precursor gas (SiH_4, $SiCl_4$, etc.) will then integrate the drop (incubation time), increasing the chemical potential of the silicon atoms which lead to supersaturation of the Au droplet. The concentration of Si builds up inside the catalyst drop until it reaches the equilibrium solubility [1.64-1.66, 1.156, 1.154].

Silicon will then move from an adsorbed gaseous state to an incorporated liquid continuous flow of the Si atoms. The Au droplet disturbs the equilibrium as leading to the composition of the alloy goes beyond the equilibrium composition, moving to the right side of the liquidus line. The supersaturation state is thermodynamically a non-equilibrium and unstable state.

The composition will then move back to the left and reach the liquidus line leading to the precipitated solid phase corresponding to that of the phase boundary and the pure Si. Si atoms precipitate and nucleate at the interface with the substrate because of the chemical potential of Si atoms in a solid crystal is lower than that of the silicon atoms in the drop. The crystallisation of Si from its liquid state to solid state is a continuous process in which Si atoms from the gas phase continually replace the Si atoms from within the drop which is incorporated in the wire form [1.154].

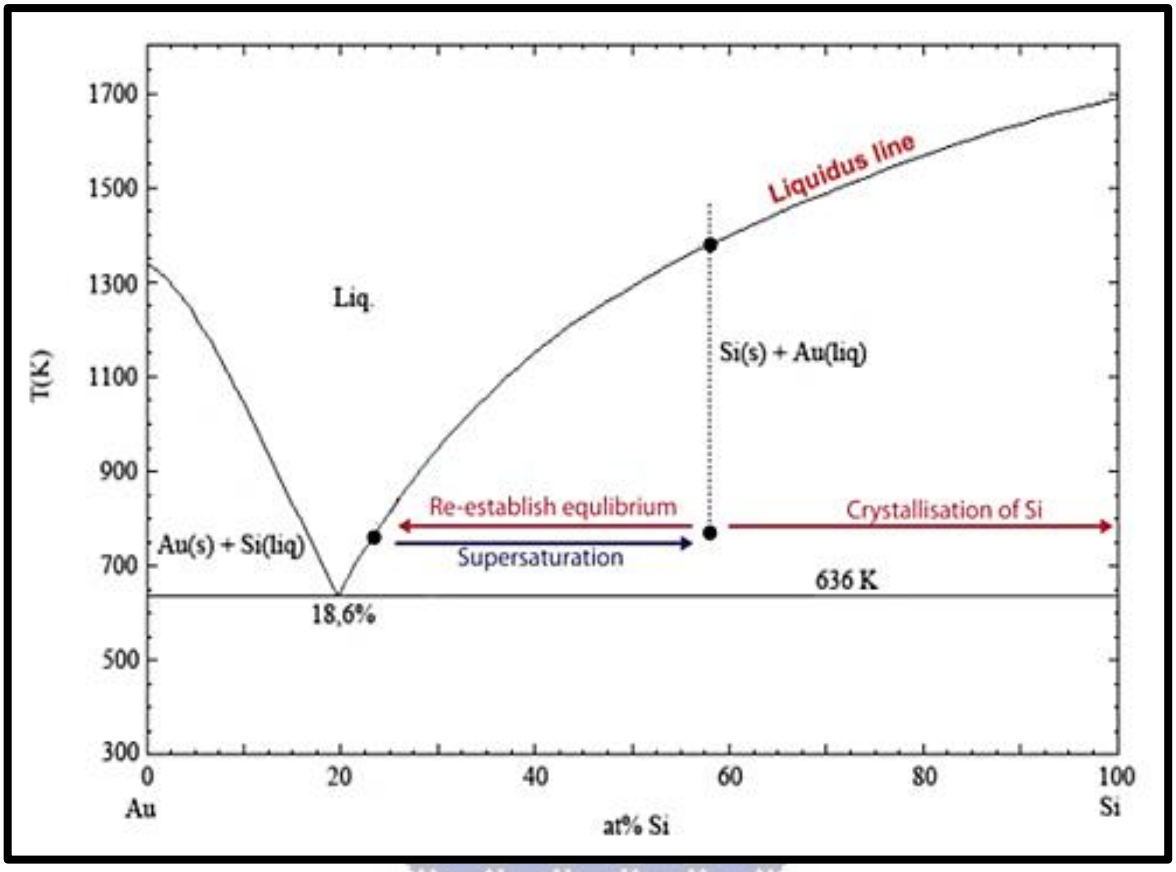

Figure 1. 10: Phase diagram of Au-Si alloy [1.156].

1.10.2 Au contamination

The search of the Au alternative was conducted in recent years as the Au has its limitations in the Si semiconductor applications. It was discovered that Au create deep level defects in Si which can affect the charge-carrier lifetime by acting as centres for charge-carrier recombination [1.154]. There is metal that were found to be successful to grow the SiNW as reported by different authors.

Research work was conducted to investigate the impurity level of Au. Davis *et al.* [1.155] incorporated metal atoms in crystalline silicon wafers which were assembled into solar cells. According to O'Donnell [1.156], the concentration at which the metal was observed to substantially degrade the performance of cells was recorded as its degradation threshold. Some metals with comparatively low solubility in Si (e.g. Au)

can prove more damaging to the electronic properties of solar cells than other metals with higher solubility (e.g. Cu). The reason they differ from predictions based on solubility values is that the efficiency with which each contaminant atom causes charges to recombine varies from metal to metal. Figure 1.11 indicates the case of an impurity possesses two or more levels, these are shown connected by a line.

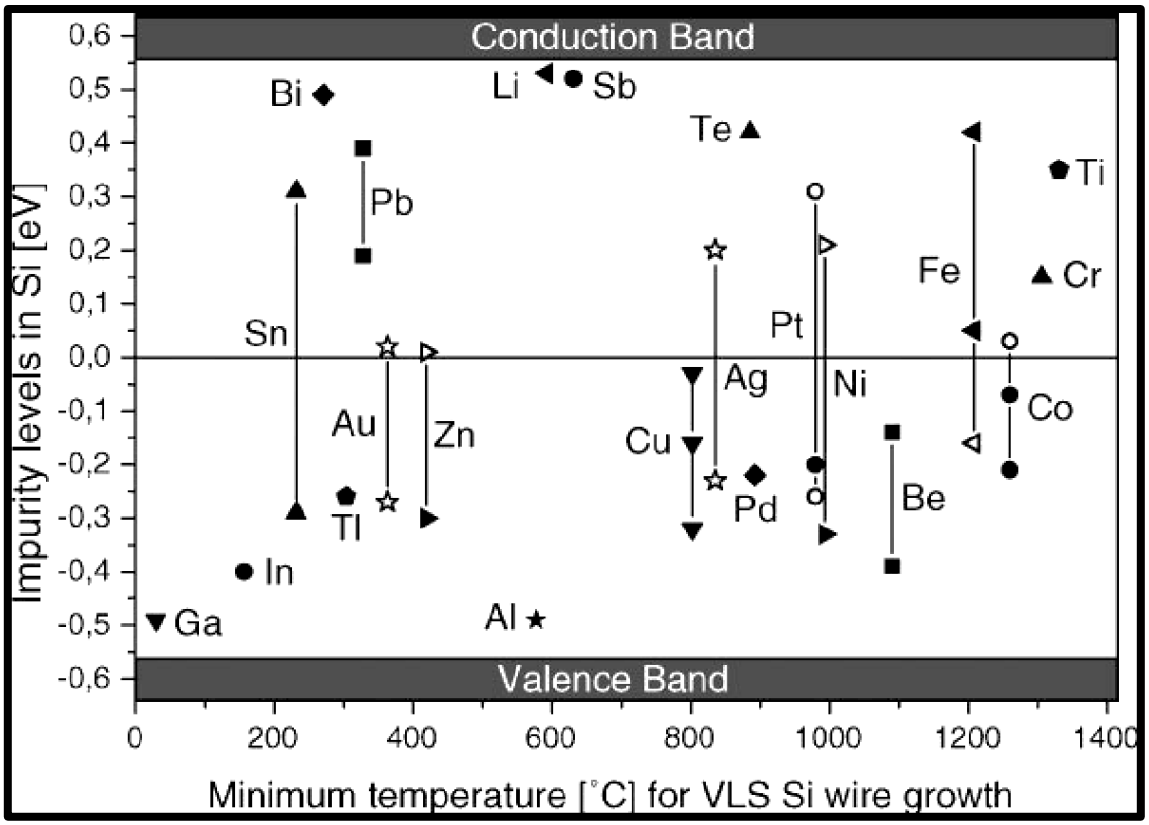

Figure 1 11: Ionisation energies of various impurities in Si (after size [1.157]), given with respect to the middle of the band gap (assuming a band gap of Si is of 1.12 eV) as a function of the minimum temperature necessary for VLS growth.

According to Shockley-Read-Hall [1.158] recombination statistics, the rate of carrier capture scales exponentially with the energy separating the Fermi level of a Si crystal from the energy level introduced in its band gap by an impurity. The closer

this energy level is to the middle of the band gap, the higher the recombination rate and the lower the carrier lifetime in the material (Figure 1.11). Levels above the band gap middle that are marked with solid symbols are donor levels, whereas open symbols indicate acceptor levels. The band gap middle are acceptor levels, whereas open symbols are donor levels [1.174, 1.154].

Au provides particularly efficient centres for recombination in the silicon matrix which is why it becomes a deep level impurity in the Si band gap.

Other metals, including Sn, Ag, Pt and Ni introduce energy levels within 0.2 and 0.3 eV from the centre of the band gap which can be less damaging to charge conduction in the material.

1.10.3 Au alternatives

Figure 1.12 displays the periodic table with potential metal catalyst classified according to their phase diagrams.

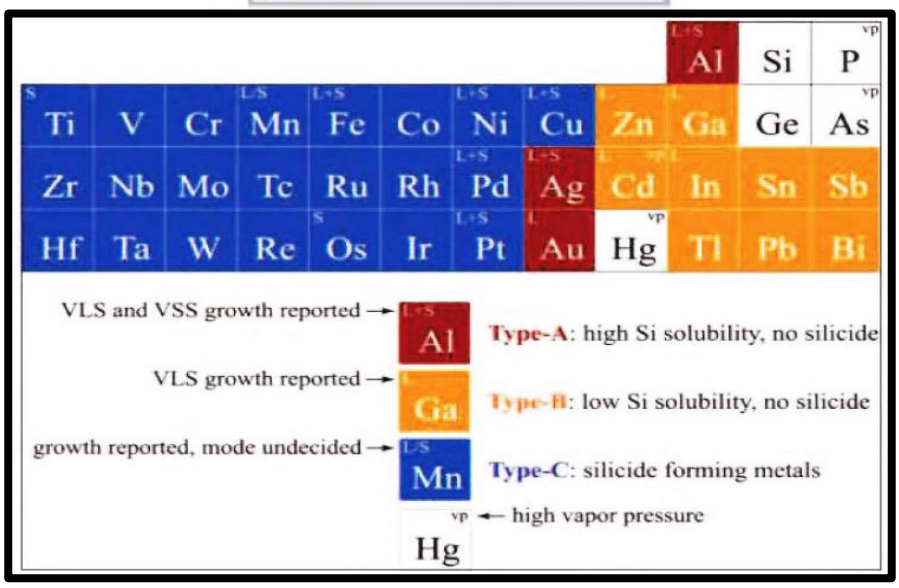

Figure 1. 12: Periodic table with potential metal catalyst classified according to their phase diagrams [1.157].

Figure 1.13 illustrates the various catalysts with respect to their corresponding metal - Si binary PD.

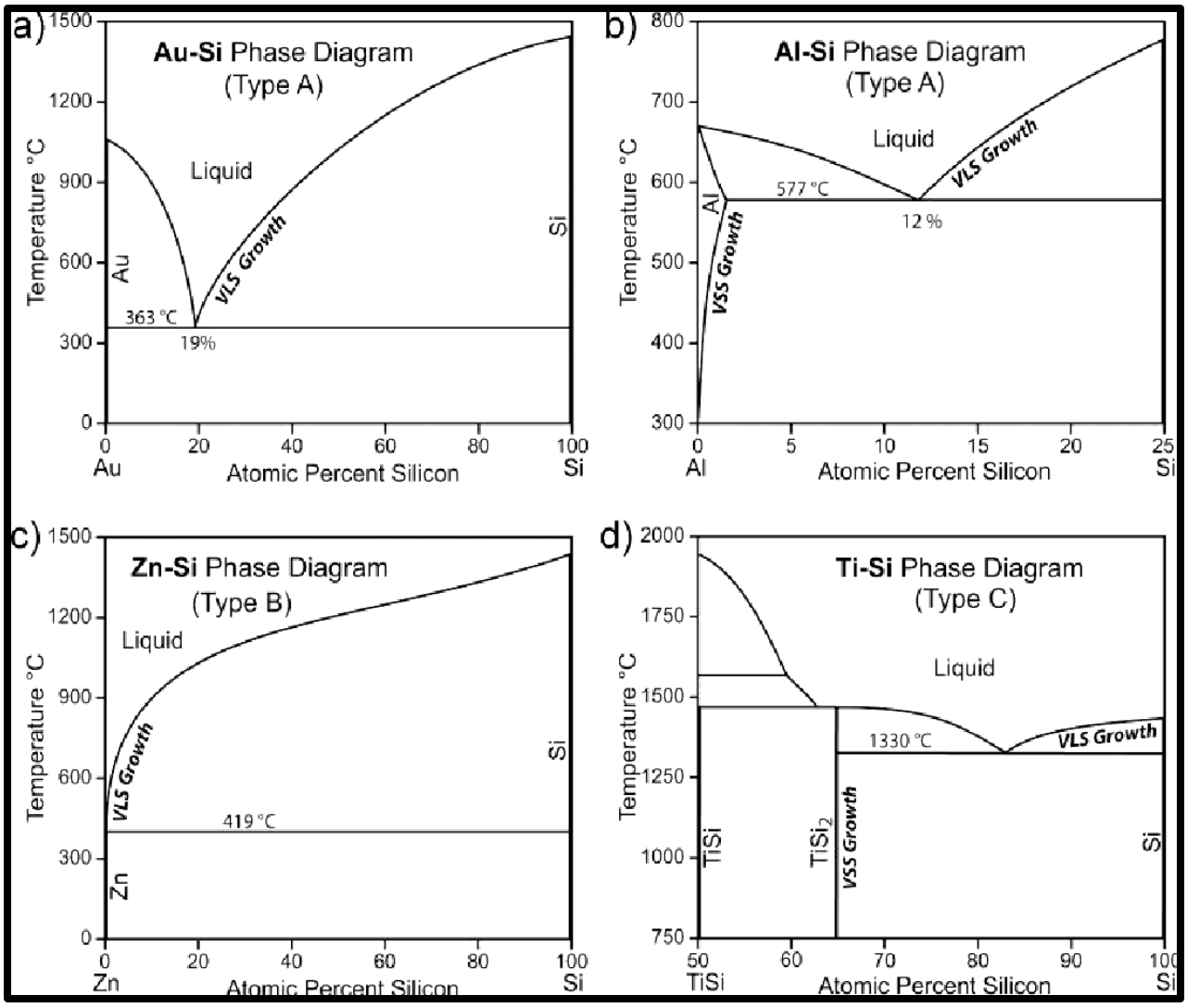

Figure 1. 13: Schematic of various metal-Si PDs or parts of the metal -Si PDs: (a) Au-Si, (b) Al-Si, (c) Zn-Si, (d) Ti-Si [1.125].

1.10.3.1 Type A

a) Aluminium (Al).

Aluminium (Al) is a metal catalyst having the higher eutectic temperature of about 577 °C with a lower Si concentration of 12 as compared to Au. The growth of SiNWs using the physical vapour deposition was found to have a drawback on Al as it oxidises. The use of ultra-high vacuum was required, but another approach is the ion implant technique which controls the exposure of the Al catalyst on the substrate surface.

There are reports on the Al catalyst SiNW synthesis which are successful. The report on CVD process using silane at temperatures between 580 and 700 °C was published. Furthermore, Wang *et al.* [1.271] claimed to have grown the SiNWs in a CVD using silane at the temperature below the Al - Si eutectic, 540 °C [1.127]. The Al catalyst was also reported on the VSS mechanism through CVD method by Wang *et al.* [1.271].

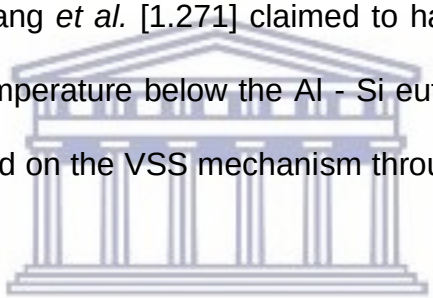

The VSS growth is at the pocket on the right-hand side (figure 1.13) where the solubility of Si in Al is reduced from 12 % (VLS) to 2 % compared to VLS, below solubility in VSS can assist producing sharp interphases in Si-Ge heterostructures. Wang *et al.* [1.271], reported on the single crystalline Si nanowires grown epitaxially on the Si (111) substrate at a growth temperature between 430 and 490 °C. The low temperature can reduce tapering during the SiNW growth.

b) Silver (Ag)

The other non-gold type A catalyst is silver. The Ag-Si system possesses a single eutectic point at 835 °C with 11 at. % Si. The high temperature does not give a good impression on the Ag but Wagner and Ellis [1.66] reported on VLS-grown single-crystalline Si wires using Ag as catalyst, synthesized in a CVD process with $SiCl_4$ as

precursor at 950 - 1050 °C. Nebol'sin *et al.* [1.146] also reported on the Si wires synthesis at a growth rate of about 1.5 mm in a CVD process at 1197 °C, also using $SiCl_4$ as precursor.

The Ag catalyst Si nanowire using VSS mechanism was reported by Tatsumi *et al.* [1.159], giving the amorphous Si wires in a silane CVD process at a temperature of 650 °C, which is below the eutectic temperature. VSS growth via solid Ag particle seems to be promising, as the impurity levels of Ag (see figure 1.13) are neither very close to the band-gap centre nor to the band-gap edges. In reference to the PD [1.159,1.160], which revealed that the solid solubility of Si in Ag is about 0.9 at. % at the eutectic temperature, and 0.2 at. % at 650 °C does not indicate any Si solubility in solid Ag.

1.10.3.2 Type B.

a) Zinc (Zn)

The transition metals such as Zn and Cd have a characteristic feature of type B catalysts with eutectic point at very low Si concentrations. The Zn–Si binary PD, (in Figure 4c), is dominated by a eutectic point at 420 °C at 0.02 at. % Si. Even though Zn has a vapour pressure of about 0.2 at 420.8 °C, Chung *et al.* [1.161] and Yu *et al.* [1.162] demonstrated VLS Si-nanowire growth by means of a CVD process using silane at a partial pressure of 6.7 mbar and a temperature between 440 and 500 °C. The Si nanowires obtained were found to have diameters between 15 and 35 nm and observed both <111> and <211> oriented nanowires with the <211> being nearly defect - free [1.156]. However, the impurity level of Zn is the same as the Au, but it can be removed by annealing as compared to Au.

b) Cadmium (Cd)

The use of Cd as catalyst with the eutectic point at 321 °C and 0.14 at. % Si. The PD of Cd and that of Zn are almost the same but with high vapour pressure of more than 1 mbar at 321 °C which limits it usability and it is impossible to grow the SiNW via VLS as it is easily evaporated during growth. It was reported that ‘‘cadmium promoted whisker growth when the source material was arsenic-doped silicon’’ [1.163, 1.156].

c) Gallium (Ga) and Indium (In)

Gallium (Ga) and Indium (In) as catalyst, have attracted great attention in the electronics field because they cause a strong p-type doping of the wires (see Fig. 5), with the eutectic temperatures of Ga (30 °C) and In (156 °C) at a Si concentration of < 0.01 at.%. The vapour pressure of In is below 107 mbar at 500 °C and Ga below 1010 mbar which makes them more favourable as compared to Zn or Cd. Givargizov and Sheftal [1.163], synthesised conical Si wires using In and Ga in a high-temperature (900–1050 °C) CVD process using $SiCl_4$.The conical shape was reported to be the incorporation and/or evaporation of the catalyst material [1.163]. Furthermore, Lacopi *et al.* [1.164, 1.165] using In, and Sharma and Sunkara [1.166] using Ga, demonstrated the synthesis of SiNWs of good crystallinity. Both used PECVD with silane at temperatures between 500 and 600 °C for growth.

d) Tin (Sn)

Sn is one of the alternative metal catalysts that was favoured over Au because of the low eutectic temperature of 232 °C and a Si concentration of <0.01 at% Si. The growth of SiNWs with uniform diameters between 80 - 200 nm at the orientation of <220> and <200> was a combination of VLS/oxide assisted growth mechanism and thermal evaporation from SiO: Sn (99:1) powder with the growth temperature of 1350 °C by Z. H. Chen *et al.* [1.167]. However, the SiNWs were covered by an oxide

sheath (demonstrated an *n*-type conductivity), which was then removed by a hydrofluoric acid treatment. The conductivity was reduced after those SiNWs were treated with palladium chloride solution to obtain palladium-coated SiNWs, which are used as hydrogen sensors application. The conductivity was seen to improve by a factor of 20 by using a mixture of argon and hydrogen during the growth process. The growth of Sn catalyst SiNWs was further conducted using plasma-assisted CVD at temperatures of 300-400 °C [1.168]

According to Nebol'sin *et al.* [1.146] the surface tensions of liquid Sn or In are in a range that does not allow stable wire growth because Nebol'sin *et al.* [1.146] tried tin catalysed nanowire growth but was unsuccessful. The same assumption on low surface tension was also presented for indium. The tin catalysed SiNWs are assumed to contain a large degree of instabilities such as bending and kinking as presented for indium because of the low droplet stability when using normal CVD growth at higher SiH_4 partial pressure.

For the electronic properties of Si, with two impurity levels in the Si band, they won't act as active recombination centres or induce p-type doping as with indium (In). This is because it may be removed much easier since has a very small negative standard electrode potential of ~ -0.14 V which indicates a reduced chemical stability compared to silver and gold. The negative standard electrode potential indicates that tin is exposed to spontaneous oxidation under normal conditions, but since there are found no reports on oxidations problems it is assumed that oxidation of tin is not a major problem, as for indium.

1.10.3.3 Type C.

Type C catalysts forms silicides and have rather complex phase diagrams with several silicide phases and eutectic points. This group contains a large aspect of

different catalysts with a wide range of properties. It appears to be a trend that nanowires grown via silicide phases have a higher probability of crystallographic defects (3). Schmidt *et al.* [1.125] concludes that type - C catalysts work well for VLS growth at elevated temperatures (higher than 800 °C) and not so well for growth at lower temperature via silicide phases. The presence of the silicide phases, the type C catalyst offer, in addition to growth via the VLS mechanism. The opportunity of VSS wire growth via the solid silicide particle [1.169], which was observed on the Titanium (Ti) catalysed SiNWs.

a) Titanium (Ti)

Ti–Si possesses a eutectic point at 1330 °C next to the pure Si side of the PD, which allows the corresponding liquidus line be used for Si wire growth via VLS mechanism.

Kamins *et al.* [1.129] synthesized Si nanowires at 640 - 670 °C by means of CVD process. This process was successful as Kamins *et al.* [1.129] has observed that the growth at 1000 °C starting from a Ti particle, the Ti particle will transform into a Ti_5Si_3particle, due to the Si-rich conditions, which transforms into Ti_5Si_4, which transforms into TiSi, which finally transforms into $TiSi_2$ ($Ti(\beta/\alpha) \xrightarrow{\triangle} Ti_5Si_3$ + Si-rich $\rightarrow TiSi_4 \xrightarrow{\triangle} TiSi \rightarrow TiSi_2$). Si-nanowire growth via the VSS mechanism catalysed by a $TiSi_2$ particle can begin after the completion of this process.

Ti or $TiSi_2$ is deemed compatible with complementary metal-oxide-semiconductor (CMOS) technology as it lies in the favourable positioning of its impurity level. However, the crystallographic quality of Si nanowires grown via $TiSi_2$ catalyst particles seems to be poor compared to what can be obtained by using Au as catalyst.

b) Palladium (Pd) and Platinum (Pt)

The noble metals Pd and Pt are known to have similar physical and chemical properties which require elevated temperatures for VLS growth of 892 °C for Pd, 979 °C for Pt according to their PDs with Si. Wagner *et al.* [1.66] who both used $SiCl_4$ CVD processes to synthesize Pt-catalysed Si wires via the VLS mechanism at temperatures around 1000 °C have found similar results as with Au. Both obtained <111> oriented wires with hexagonal cross-sections and <211> side faces. The Filamentary growth was also obtained with Ag, Cu, Ni, and Pd at substrate temperatures of about 800 °C, which is the eutectic temperature (Pd the reported growth temperature is almost 100 K below the minimum temperature required for VLS growth) Bootsma *et al.* [1.170]. This can be due to the VSS growth mechanism, employing a solid silicide particle because according to the Pd–Si PD, one can expect that VSS growth at 824 - 892 °C is mediated by a PdSi silicide particle, whereas at temperatures below 824 °C VSS growth should be catalysed by a Pd_2Si particle. Hofmann *et al.* [1.169.] also reported the VSS Si nanowire growth via a Pd_2Si, by using in-situ transmission electron microscopy (TEM) to study the growth of SiNWs at temperatures around 892 °C and found that Si-nanowire growth works via lateral ledge flow at the silicide - silicon interface. Similarly, Baron *et al.* [1.171.] demonstrated VSS SiNW growth using PtSi catalyst particles at temperatures as low as 500 °C.

1.11 Metal catalyst thin film growth

Thin films of metal deposited over foreign substrates naturally tend to reconfigure into drops. This occurs because atoms at the surface of a solid or liquid, being bound by fewer neighbouring atoms than they would be in the bulk of the material, are in

unstable states. The physical characteristics of a thin film can be determined by surface diffusion and nucleation during a deposition.

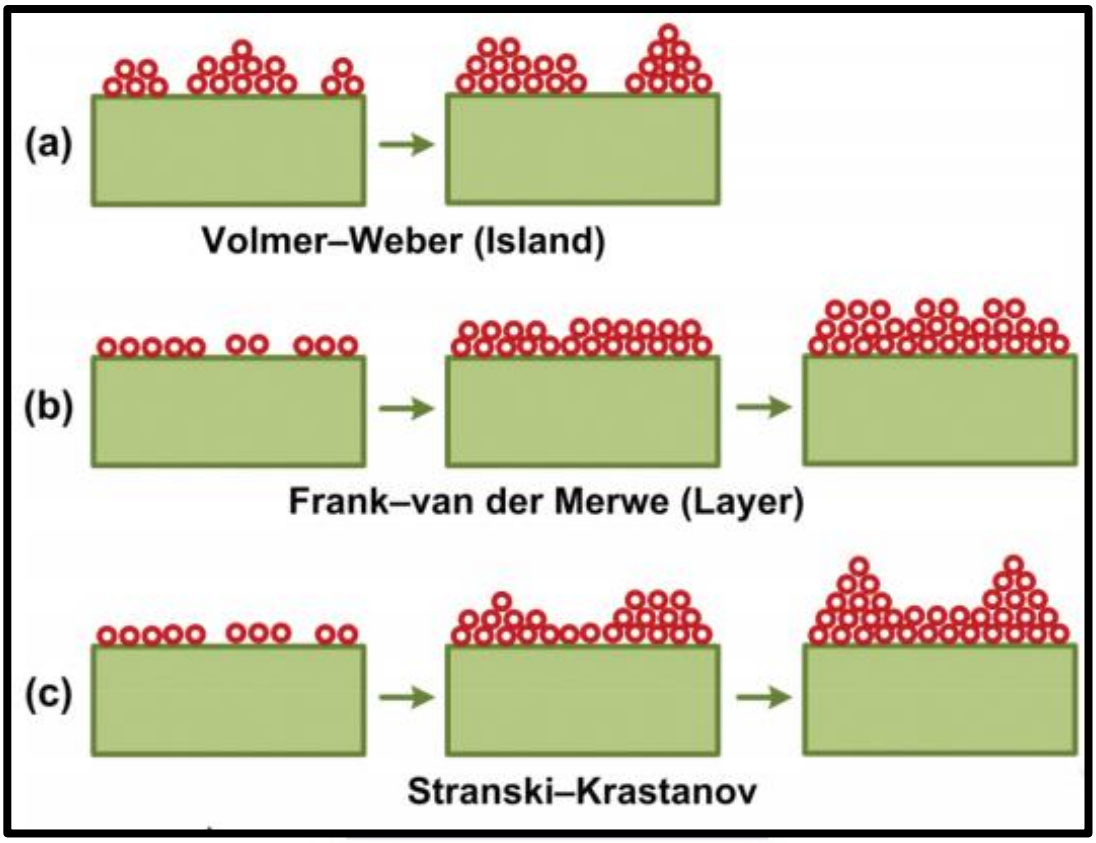

Figure 1. 14: Basic modes of thin film growth: (a) island in the Volmer-Weber mode, (b) layer by layer in the two -dimensional Frank van der Merwe mode, and (c) layer plus island in the Stranski-Krastanov mode [1.172].

The layer morphology (thin film growth) is affected by substrate temperatures, partial pressures of gaseous species and total pressure of the system [1.173] which give different modes. There are three modes of film growth related to the ad-atom and surface interaction. as shown in Figure 1.1 [1.174]

a) **Volmer-Weber (VW) growth** for metal films deposited on insulators or contaminated single crystal surfaces it exhibits three-dimensional island growth.

The direct nucleation of small clusters to the substrate surface, resulting in coalescence into a continuous film [1.175]. Film growth can start both by randomly oriented or epitaxially grown nuclei depending on the kind of substrate and deposition temperature (Figure 1.14a).

b) Frank-Vander growth the interaction between ad-atoms and substrate surface is stronger than the ad-atom interaction consequently the nuclei are growing in monolayer islands [1.176] (Figure1.14b). The growth of many amorphous layers can be considered as such growth modes.

c) Stranski–Krastanov (SK) growth is where the initial growth forms one or possibly multiple monolayers until this two-dimensional growth becomes unfavourable, where by three-dimensional island growth resumes to an intermediary process characterised by both 2D layer and 3D island growth.

The island-based growth occurs at a critical layer thickness which is highly dependent on the chemical and physical properties, such as surface energies and lattice parameters, of the substrate and film (Figure 1.14c) [1.177].

1.12 Surface tension of the metal catalyst

When a metal is in contact with the substrate (Si), it tends to respond to the surface energy of the film, the substrate as well as the film/substrate interface. To minimise the sum of all three components the film will adopt a shape.

According to Young's equation the three quantities can be used to define the contact – angle configuration of the metal droplet. The surface tension of the liquid droplet (δ_l), surface of the substrate (δ_s) and surface tension of the liquid – substrate interface is indicated in Figure 1.15

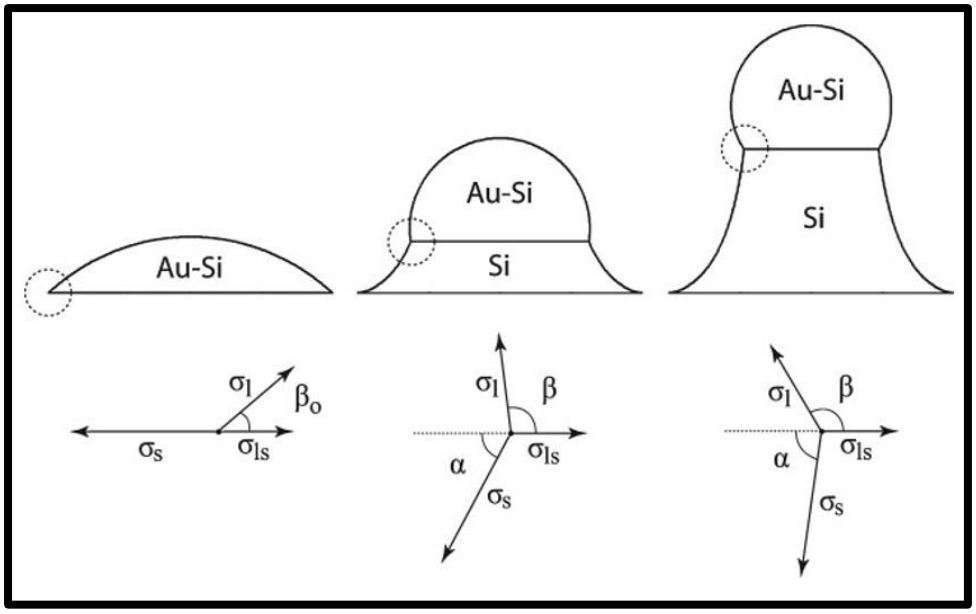

Figure 1. 15: Schematic development of the droplet and wire shape in the initial phase of VLS wire growth [1.146]

Assuming, the wire growth velocity is insignificant compared to the reaction velocity of the droplet, the droplet-wire system formed can be described in a quasi-static growth model. The shape of the droplet may undergo a transition, but the development corresponds to a sequence of equilibrium states. The contact angle β of the droplet is related to the inclination angle α and the surface tension values δ_s, δ_l and δ_{ls} by the Neumann triangle relation.

$$\delta_l \cos(\beta) = \delta_s \cos(\alpha) - \delta_{ls} \qquad (1.1)$$

When α = 0,

$$\delta_l \cos(\beta) = \delta_s - \delta_{ls} \qquad (1.2)$$

This is the Young equation, stating that in equilibrium, the horizontal components of the surface force must cancel each other such that there is no net force action on the perimeter of the droplet as shown in figure above.

It was also reported that the angle of the metal catalyst against the substrate surface can control the base of the SiNW grow which makes it stable as it grows.

By taking the shape of the metal droplet as the segment of a sphere, the radius of the liquid - solid interface can be expressed as a function of the contact angle β and the volume V which is measured on the metal droplet.

$$r = (\frac{3V}{\pi})^{1/3} \frac{(1+\cos(\beta))^{1/2}}{(1-\cos(\beta))^{1/6}(2+\cos(\beta))^{1/3}} \quad (1.3)$$

The volume of the metal droplet is given by the initial radius metal droplet – solid substrate of the interface r_o and the initial contact angle β_o, at α = 0.

$$V = \frac{\pi}{3}(\frac{r_o}{\sin(\beta_o)})^3(1-\cos(\beta_o))^2(2+\cos(\beta_o)) \quad (1.4)$$

The inclination angle of the wire flanks the angle α, which is trivially related to the slope of the wire via

$$\frac{dh(r)}{dr} = -\tan(\alpha) \quad (1.5)$$

Where h is the height of the wire. By using cos (α), the shape of the wire expansion for a certain configuration of the surface tension can be obtained.

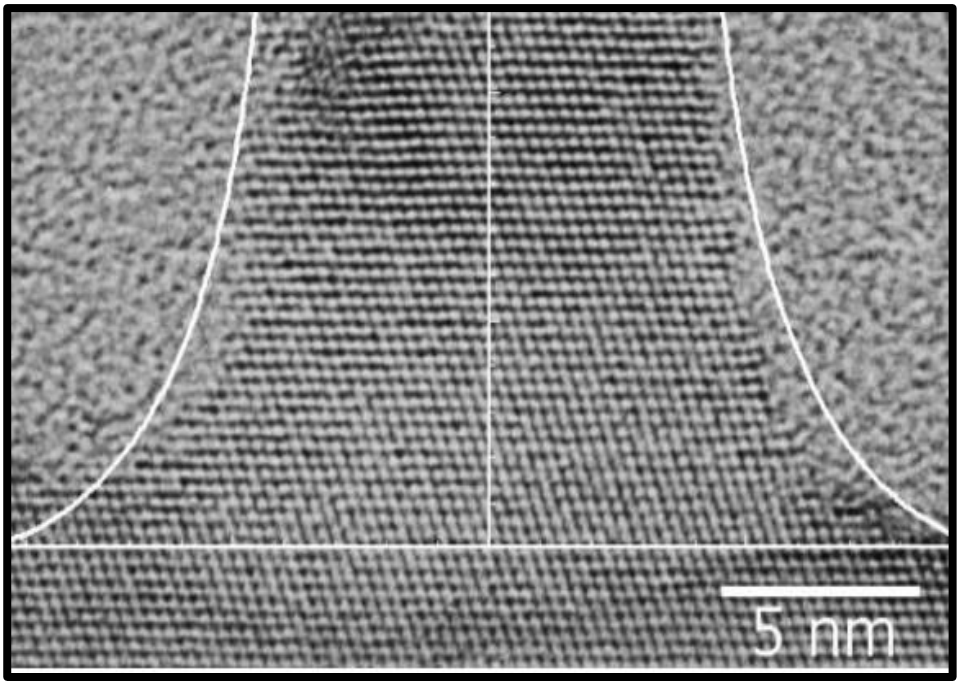

Figure 1. 16: TEM image of an epitaxially grown Si nanowire. the white line corresponds to the calculated shape assuming δ_s= 1.24 J/m^2, δ_l = 0.85 J/m^2 and δ_{ls} = 0.62J/m^2

The surface tension of solid Si is in the range of 0.94 - 1.2 N/m and the minimum surface tension required for a liquid metal catalyst to promote straight SiNW growth would need to be 0.67 - 0.85 N/m. This has led to predictions that In, Ga, Al and Zn are likely to catalyse only short and unstable growth, while and Sn and Bi should be incapable of catalysing SiNW growth altogether (see table 1.1).

1.13 Post transition metals

The type B catalyst was found to have limitation in growing the SiNWs via VLS mechanism. The report was done by Wagner *et al.* [1.66] where they grew Au, Mg, Cu, Ni, Gd and Pd catalyst nanowires but with Sn and Zn were unsuccessful. The same observations were reported by Bootsma *et al.* [1.170] who grew Au, Ag, Cu, Ni and Pd catalyst nanowires and no growth with the In, Sn and Bi.

The unsuccessful growths of nanowires by type B catalyst which are post transition metals was investigated and from Nebol'sin *et al.* [1.146], who also reported on the growth and concluded that the catalysts are not stable for the SiNWs growth, Nebol'sin *et al.* [1.147] also did the theoretical calculation were done to prove the observations. This was explained that a certain minimum value of, the surface tension (δ_l) of the droplet, is required to allow a stable wire growth via VLS. There are three quantities used to describe the contact-angle configuration of the droplet are δ_l, the surface tension of the liquid (the catalyst droplet), δ_s, the surface of the solid (the Si wire), and δ_{ls}, the surface tension of the liquid–solid interface.

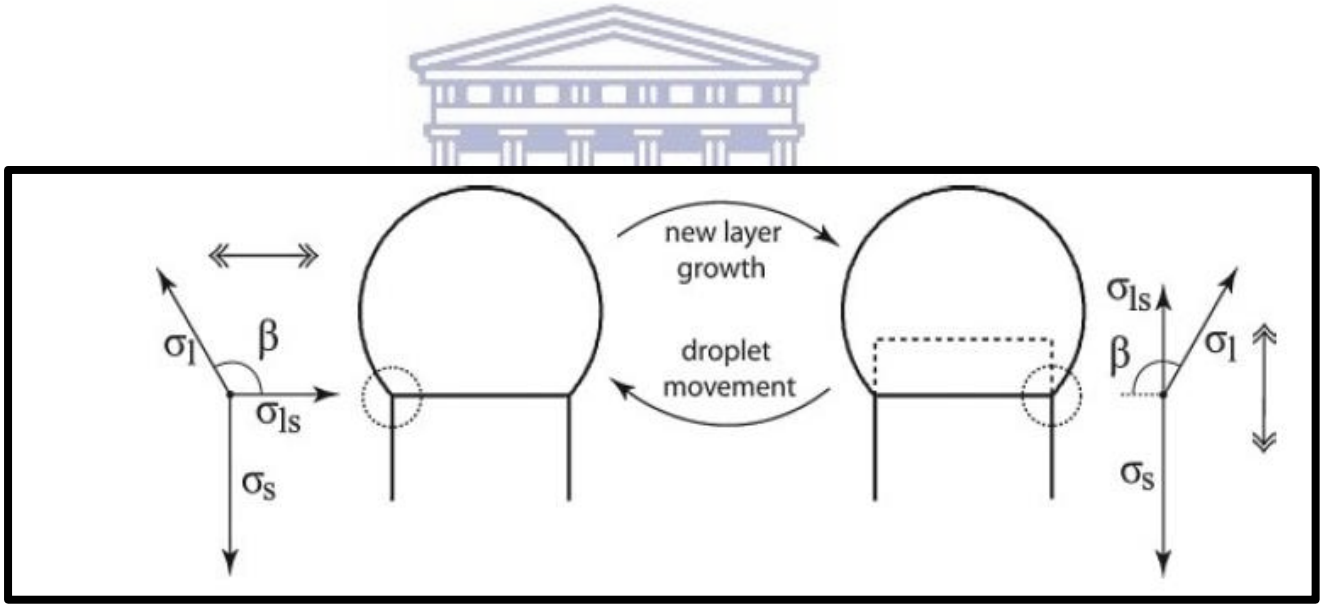

Figure 1. 17: Si wire growth as a repetition of two consecutive growth steps shown on the left-had side (lhs) and right-hand side (rhs). On the lhs the force balance in horizontal direction must be considered. On the lhs the force balance in horizontal direction must be considered, on the rhs, the force balance of the vertical force components needs to be considered [1.146]

It was assumed that the Si-wire growth proceeds by the continuous repetition of two alternating growth steps which are the nucleation and growth of a new layer of Si at the droplet Si interface, and step two, the upward movement of the droplet to the edge of the newly grown layer (figure 1.16).

After the first step, that is, the growth of the new layer (dashed line). The growth of the new layer causes the droplet to wet the side surface of the wire. The droplet has only one degree of freedom, namely the vertical position of its triple phase line. For the droplet to recover its starting position it is necessary for the droplet to move its triple phase line upward by an amount equal to the thickness of the newly grown layer, that is, the droplet should dewett the side-surface portion of the new layer. This is only possible if there exist a net force component pointing upwards, which according to the force balance will give

$$\sin(\beta) - \cos(\beta) > \frac{\delta_s}{\delta_l}$$

Since sin (β) – cos (β) can maximally reach a value of $\sqrt{2}$, at β= 135°, condition (7) can only be fulfilled if

$$\delta_l > \frac{\delta_s}{\sqrt{2}} \qquad (1.7)$$

Adopting the value also used by Nebol'sin *et al.* [1.146] of δ_s=1.2 Jm^{-2} for Si, we obtain a lower threshold for δ_l of about 0.85 Jm^{-2}. If the surface tension δ_l of the liquid droplet is smaller than 0.85 J m^{-2}, the droplet is not capable of dewetting the side surfaces of the wire.

Table 1.1: Surface tension of liquid metals- δ_{ls} (N/m).

Transition Metals		Post-Transition Metals	
Fe	1.8	0.9 – 1.1	**Al**
Ni	1.8	0.79	**Zn**
Pt	1.7	0.70	**Ga**
Pd	1.5	0.55	**Sn**
Cu	1.4	0.55	**In**
Au	1.1	0.40	**Pd**
Ag	0.9	0.35	**Bi**

Droplets with too-small surface tensions do not sit on top of cylindrical Si wires studied the possible implications of surface tensions on the suitability of different metals to catalyse the VLS growth of SiNWs by assessing the

Nebol'sin *et al.* [1.146] report high surface-tension values of >1.3 Jm^{-2} for the type B metals Cu, Pt, and Ni, and, as expected, the reported growth stability is correspondingly high. The surface-tension values of the three type A metals Ag, Au, and Al, are already considerably lower, having values of about 0.9 J m^{-2} (Au and Ag), and 0.8 J m^{-2} Al [1.146]. Since this is at the limit of δ_l=0.85 J m^{-2}, we expect a change of the growth characteristics; and indeed, according to Nebol'sin *et al.* [1.146] the growth stability changes, being high for Au but low for Al. The type C metals, Bi, Sb, Pb, Sn, Zn, In, and Ga, do have even lower surface tension values, ranging from 0.6 to 0.8 J m^{-2} for Sn, Ga, and Zn, [1.146, 1.17-8-1.180] to values of around 0.4 J m^{-2} for Bi, Sb, Pb. [1.1471.146,1.180]. The overall tendency that wire growth becomes more and more difficult with smaller surface-tension values of the liquid still holds. According to Nebol'sin *et al.* [1.146] only a low growth stability can be achieved with Zn (0.8 J m^{-2} [1.180]), and no wires at all can be grown with Bi, Sb, and Pb (0.4 J m^{-2}). An exception to the rule seems to be In, for which wire growth has been reported

by several authors, [1.146, 1.182-1.184] despite its low surface tension of about 0.5 J m^{-2} [1.154, 1.185]. Nebol'sin *et al.* [1.146], concluded that for the catalyst to promote stable (rectilinear) growth, the horizontal component of the resultant force on the Triple Phase Line (at the rim of the catalyst drop where liquid, solid and vapour phases meet) must be zero and the vertical component must be directed upwards for the replacement of liquid-vapour interfaces with solid-vapour interfaces to be energetically favourable.

The straight and epitaxial SiNWs were synthesised with Al catalyst [1.186], In [1.184] and Bi catalysts [1.187]. Parlevliet and Cornish, [1.189] and Yu *et al.* [1.190] showed results with Sn [1.191, 1.192].

1.14 Controlling the diameter of the metal catalyst

The ideal SiNW should be <10 nm in diameter to trap light in solar cell applications [1.96]. This can improve the efficiency and cost of solar cell, by using low cost materials such as metal catalyst and fabrication methods.

The type B metal catalyst which are found to be the post transition metal, they were reported to have limitations in growing the SiNWs which were also proved theoretically [1.146] however there were studies which proved to can grow the SiNWs by influencing the metal catalyst 's reaction. Tin (Sn) which is one of the type B catalyst was also used as an alternative of Au to grow SiNWs which will be used in the electronic applications. The Au-Si eutectic temperature is 363 °C and according to Wagner and Ellis 1964 [1.166] the formation of the metal catalyst nanoparticles is when heating the Au coated Si substrate above its eutectic. There are reports that by

controlling the heating temperature, the diameter of the metal catalyst can be controlled.

1.14.1 Annealing the metal catalyst thin film

The control of the thin film to nano-droplets /particles is due to the surface tension of the substrate (Si) [1.125, 1.154] reported theoretically that it is difficult to reduce the metal catalyst size, where thermodynamically, the minimum radius of liquid metal droplets is given by

$$\mathrm{R_m} = \frac{2V_1}{RT\ln(\mathrm{s})}\delta_{\mathrm{lv}} \qquad (1.8)$$

where V_l is the molar volume of the droplet, δ_{lv} is the liquid–vapour surface energy, and s is the degree of supersaturation of the vapour. This equation is suggesting that when using a smaller catalyst, higher degree of saturation is required. However, Gibbs –Thompson effect, explains that the chemical potential of the component in the metal – alloy nanoparticle becomes high as the size of the catalyst is reduced to the equation,

$$\Delta\mu = \frac{2\gamma}{\mathrm{r}} \qquad (1.9)$$

were, Δμ is the chemical potential difference of the component species in the liquid droplet, γ is the surface energy, and r is the radius of curvature of the droplet. It does show from the equation that by dissolving a vapour component into a liquid alloy becomes difficult as the size decreases. Furthermore, the formation of the nanoparticles cannot be changed which mean that to manipulate the nanoparticles size while they are already formed is thermodynamically difficult challenge. This observation was done by studying the formation of the nanoparticles. The increase in the heating temperature can lead to Ostwald ripening where the small particles

agglomerate to form bigger particles due to strong van der Wall attractive forces between the nanoparticles. The larger particles are formed as they are energetically favourable side because of the surface tension and as explained, these bigger particles can lead to wider Si wires [1.132].

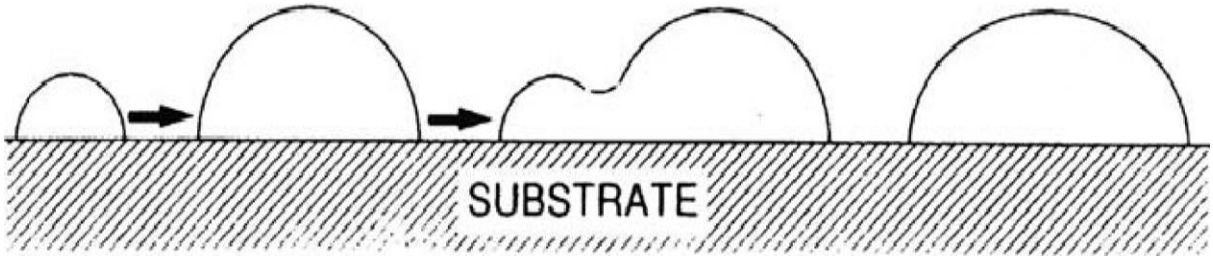

Figure 1. 18: Coalescence of nanoparticle "islands", due to Ostwald ripening [1.213]

Liquid Sn, In, Ga and Bi also have unusually low Si solubility which can grow sharp hetero-structures according to Hugh *et al.* [1.193] and low surface tensions.

Finding the optimum temperature to form the ideal size of the metal catalyst was widely investigated [1.194, 1.195]. The control of the size of the nanoparticles can be done by using high temperatures, which can lead to smaller particle diameter because of the evaporation, depending on the thickness of the film.

1.14.1 Thickness of the film

The thickness of the metal catalyst was also found to contribute on the diameter of the metal catalyst. The variation was observed and reported by HF Al-Taay *et al.* [1.196], where Sn thin film thickness was varied from 10 to 100 nm, and annealing the film coated substrate to 400 °C and droplets size were of 60 to 110 nm with a catalyst thickness of 10 nm, increased to a range of 80 - 130 nm with use of 20 nm Sn thin film catalyst and 100 nm was 160 - 220 nm.

1.14.2 Synthesis ambient

The metal catalysts are active when immersed in a reactive environment, such as plasma [1.154]. The use of atomic hydrogen gas (H_2) is to remove the oxides on the Sn film. The oxides can cause a hard cover shell over the Sn nanoparticles and it limits the growth of the SiNWs. There still more observations when using a different substrate other than Si. Meshram *et al.* [1.197]; reported the 300 nm Sn thin film was thermally evaporated on the glass substrate and the atomic hydrogen treatment was done to form the Sn nanoparticles. The surface structures comprising of 200 - 500 nm wide grains 250 °C in the presence of molecular hydrogen for 10 min, it is observed that molten Sn forms some irregularly shaped structures distributed over the substrate. Atomic hydrogen was generated over a 250 nm thick Sn film and it was reported that the spherical tin balls of a size ranging from 10-20 nm were formed.

1.14.3 Different substrates

To investigate substrate impact, substrates of glass/SnO_2 (80 nm) and glass/ITO (20 nm) were exposed to standard H_2 plasmas at temperatures of 200, 250 and 500 °C. SnO_2 substrates, the diameter of Sn drops formed at 200 °C was 10 to 30 nm and increased by a factor of 20 as the temperature was increased to 500 °C. The ITO substrates showed that the drops with diameters larger than a micron formed at temperatures as low as 200 °C. The average diameter reduced to 700 nm at 250 °C and to 50 nm at 500 °C.

Characterization of tin-catalysed silicon nanowires synthesized by the hydrogen radical-assisted deposition method was also reported [1.198]. A 100 nm Sn film was deposited on the glass substrate and it was heated at the temperature of 400 °C for 10 min. The diameters of SiNWs on the bottom side were gradually increased

ranging from approximately 50 to 200 nm with increasing H_2 gas flow rates. The length of the wires extended up to ~2 μm.

The ultra-thin film was also reported to avoid Ostwald ripening process which leads to a larger diameter. The Sn thin film thickness of 7 nm [1.71] and 1 [1.198] nm was reported, where both used the H_2 gas and same temperature of 400 C (for 1 hour (7 nm) and 2 hours (1 nm)). For the 7 nm, the diameters of SiNWs on the bottom and top were approximately 60 nm and thinner than 10 nm, respectively. Their lengths extended up to ~1.5 μm. While for 1 nm, The SiNW has a crystalline core of~10 nm diameter and polycrystalline shell that is ~ 60 nm thick.

1.14.4 Evolution of Crystallinity of SiNW growth

Mullane *et al*. [1.192] reported on the crystallinity of the Sn catalyst SiNW using the HRTEM. The 20 nm Sn thin was thermally evaporated on the stainless steel (SS). The SiNWs had the growth direction of <111> and the Sn particles at the tip did not show any diffraction lines because the areas close to the particle are amorphous. There is no band gap between the Sn particle and the wire.

The study on the tin-catalysed plasma-assisted growth of silicon nanowires was report on a 1 nm Sn thin film was thermally evaporated on Si (111) n-type wafers at room temperature. High-resolution TEM images showed the wire having a crystalline core with a polycrystalline shell. The ratio of core diameter to shell thickness varies with growth condition and increases toward the seed end of the wire. The SiNW has a crystalline core of~10 nm diameter and polycrystalline shell that is ~60 nm thick [1.199].

Most recently, Tang *et al.* [1.200.] reported on the plasma-assisted growth of silicon nanowires by Sn catalyst: step-by-step observation, where a Sn layer with a nominal

thickness of 1 nm was deposited on a ~1.4 μm thick ZnO: Al corning glass by thermal evaporation. The TEM analysis was conducted on the SiNW which were grown for 2, 30 and 90 minutes duration. The conclusion was that the increase in the growth duration leads to crystallinity evolution where in the beginning the crystalline structure of NWS becomes mono-crystalline.

1.15 Aim and Objectives

The efficiency improvement of a solar cell is one of the most important aspects in most research studies. As already highlighted the approach of the SiNW based solar cell, attention is mostly on the control of the growth steps via VLS mechanism. The objectives of the study are: 1) to investigate the composition of the Sn ultra-thin film as the substrate temperature increases under the XPS vacuum and depth profiling using XPS after heating, 2) to investigate the surface morphology and elemental composition of the Sn film by FIBSEM, after in-situ heating the substrate and 3) to investigate the crystallinity of the Sn thin film after subjected to high temperatures, using HRTEM.

The outline of the thesis is as follows:

- Chapter 1 highlights the importance of solar cell, operation, history, current developments in the field of SiNW research and synthesis at micro to nano scale.
- Chapter 2 give brief descriptions of the XPS system and the characterisation techniques used in this study.
- Chapter 3 reports on the study of the chemical bonding states of the Sn thin film at various temperatures within an XPS.
- Chapter 4 focuses on the investigation of the surface and internal microstructure of the Sn thin films.

References

1.1 Hilton Trollip, Anthony Butler, Jesse Caetano, Catrina Godinho. “Energy security in South Africa”. Research paper. Issue 17, Mitigation Action plans & Scenarios. South Africa (2014).

1.2 O’Connor, Peter A. "Energy transitions." Boston University, Boston (2010).

1.3 Greenpeace international .2008. The true cost of coal: how people and the planet are paying the price for the world’s dirtiest fuel. Available: http://www.greenpeace.org/raw/content/international/press/reports/true-cost-coal.pdf.

1.4 Johansson, Thomas B. Renewable energy: sources for fuels and electricity. Island press, 1993.

1.5 Popoola, Olawale M., and Clément Burnier. "Solar water heater contribution to energy savings in higher education institutions: Impact analysis." Journal of Energy in Southern Africa 25, no. 1 (2014): 51-58.

1.6 Sharma, Shruti, Kamlesh Kumar Jain, and Ashutosh Sharma. "Solar cells: in research and applications—a review." Materials Sciences and Applications 6, no. 12 (2015): 1145.

1.7 Quaschning, Volker. Understanding renewable energy systems. Routledge, 2016.

1.8 Surana, Kavita. "Towards silicon quantum dot solar cells: comparing morphological properties and conduction phenomena in Si quantum dot single layers and multilayers." PhD diss., Université de Grenoble, 2011

1.9 Cao L, Park J, Fan P, Clemens B, Brongersma ML. 2010. Resonant germanium nano antenna photo detectors. Nano Lett. 10(4):1229–33

1.10 Garnett E, Yang P. 2010. Light trapping in silicon nanowire solar cells. Nano Lett. 10(3):1082–87

1.11 Law M, Greene LE, Johnson JC, Saykally R, Yang P. 2005. Nanowire dye-sensitized solar cells. Nat. Mater. 4(6):455–59

1.12 Wang K, Chen JJ, Zeng ZM, Tarr J, ZhouWL, *et al.* 2010. Synthesis and photovoltaic effect of vertically aligned ZnO/ZnS core/shell nanowire arrays. Appl. Phys. Lett. 96(12):123105

1.13 Fan Z, Razavi H, Do J, Moriwaki A, Ergen O, *et al.* 2009. Three-dimensional nanopillar-array photovoltaics on low-cost and flexible substrates. Nature Mater. 8(8):648–53

1.14 L´evy-Cl´ement C, Tena-Zaera R, Ryan MA, Katty A, Hodes G. 2005. CdSe-sensitized p-CuSCN/nanowire n-ZnO heterojunctions. Adv. Mater. 17(12):1512–15

1.15 Yuhas BD, Yang P. 2009. Nanowire-based all-oxide solar cells. J. Am. Chem. Soc. 131(10):3756–61

1.16 Varghese OK, Paulose M, Grimes CA. 2009. Long vertically aligned titania nanotubes on transparent conducting oxide for highly efficient solar cells. Nature Nanotechnol. 4(9):592–97

1.17 Dong Y, Tian B, Kempa TJ, Lieber CM. 2009. Coaxial group III-nitride nanowire photovoltaics. Nano Lett. 9(5):2183–87

1.18 Colombo C,HeiβM, Gr¨atzelM, Fontcubertal,Morral A. 2009. Gallium arsenide p-i-n radial structures for photovoltaic applications. Appl. Phys. Lett. 94(17):173108

1.19 Briseno AL, Holcombe TW, Boukai AI, Garnett EC, Shelton SW, *et al..* 2010. Oligo- and polythiophene/ hybrid nanowire solar cells. Nano Lett. 10(1):334–40

1.20 Greene L, Law M, Yuhas B, Yang P. 2007. ZnO-TiO2 core-shell nanorod/P3HT solar cells. J. Phys. Chem. C 111(50):18451–56

1.21 Takanezawa K, Tajima K,Hashimoto K. 2008. Efficiency enhancement of polymer photovoltaic devices hybridized with ZnO nanorod arrays by the introduction of a vanadium oxide buffer layer. Appl. Phys. Lett. 93(6):063308

1.22 WeiW, Bao X, Soci C, Ding Y, Wang Z, Wang D. 2009. Direct heteroepitaxy of vertical InAs nanowires on Si substrates for broad band photovoltaics and photodetection. Nano Lett. 9(8):2926–34

1.23 Williams SS, Hampton MJ, Gowrishankar V, Ding I, Templeton JL, *et al..* 2008. Nanostructured titania–polymer photovoltaic devices made using PFPE-based nanomolding techniques. Chem. Mater. 20(16):5229–34

1.24 Kalogirou, Soteris A. Solar energy engineering: processes and systems. Academic Press, 2013.

1.25 M. Kaltschmitt, W. Streicher, A. Wiese, "*Renewable Energy – Technology, Economics and Environment"*, Springer Berlin, Heidelberg and New York (2007).

1.26 Nelson. J, "The Physics of Solar Cells", London: Imperial College Press, (2003)

1.27 Mishra. K, and Singh. J, "Semiconductor Device Physics and Design", Netherlands: Springer, p 60-64 (2008)

1.28 Zeman, Miro. "Introduction to photovoltaic solar energy." Delft University of Technology 2, no. 6 (2003).).

1.29 Das Kanungo, Pratyush. "On the doping of Silicon nanowires grown by molecular beam epitaxy." PhD diss., Halle (Saale), Martin-Luther-Universität Halle-Wittenberg, Diss., 2010, 2010).

1.30 Shah. A, “Thin-Film Silicon Solar Cells”, EPFL Press, (2010)

1.31 A.D. Upadhyaya; Yelundur, Vijay ;Rohatgi, Ajeet, “High Efficiency Mono-Crystalline Solar Cells with Simple Manufacturable Technology”, Georgia Tech, SmartTech Search, 2006

1.32 Goetzberger, Adolf, Joachim Knobloch, and Bernhard Voss. "Crystalline silicon solar cells." editorial John Wiley & Sons Ltd 1 (1998).

1.33 Yadav, A. and Kumar, P. (2015) Enhancement in Efficiency of PV Cell through P&O Algorithm. International Journal for Technological Research in Engineering, 2, 2642-2644

1.34 Bertolli, M. Solar Cell Materials. Course: Solid State II. Department of Physics, University of Tennessee, Knoxville (2008)

1.35 Jayakumar, P. Solar Energy Resource Assessment Handbook. Renewable Energy Corporation Network for the Asia Pacific(2009)

1.36 Swami, Rashmi. "Solar cell." International Journal of Scientific and Research Publications 2, no. 7 (2012): 1-5

1.37 Sharma, Shruti, Kamlesh Kumar Jain, and Ashutosh Sharma. "Solar Cells: In Research and Applications—A Review." Materials Sciences and Applications 6, no. 12 (2015): 1145

1.38 Badawy, W.A. (2015) A Review on Solar Cells from Si-Single Crystals to Porous Materials and Quantum Dots. Journal of Advanced Research, 6, 123-132. http://dx.doi.org/10.1016/j.jare.2013.10.001

1.39 Yogi Goswami, D. and Kreith, F. Handbook of Energy Efficiency and Renewable Energy. CRC Press, Boca Raton. (2007)

1.40 Luque, A. and Hegedus, S. Handbook of Photovoltaic Science and Engineering. 2nd Edition, John Wiley & Sons, Ltd., Hoboken. http://dx.doi.org/10.1002/0470014008. (2003)

1.41 Andorka, F. (2014) CIGS Solar Cells Simplified. Solar Power World.http://www.solarpowerworldonline.com/2014/01/cigs-solar-cells-simplified

1.42 Jassen, R. Introduction to Polymer Solar Cells. http://www.eet.bme.hu/~plesz/Gyarmati%20Adam/2.pdf

1.43 Leroy, F. A Century of Nobel Prize Recipients: Chemistry, Physics, and Medicine. CRC Press, Hoboken. http://dx.doi.org/10.1201/9780203014189 (2003)

1.44 Alex, C., Mayer, Shawn, R., Scully, Brian, E., Hardin, Michael, W., Rowell and Michael, D. McGehee (2007) Polymer-BasedSolar Cells: A Review. Materials Today, 10, 28-33. http://dx.doi.org/10.1016/S1369-7021(07)70276-6

1.45 Zhang,Shaoqing,Yunpeng Qin, Jie Zhu, and Jianhui Hou. “Over 14% efficiency in polymer solar cells enabled by a chlorinated polymer donor. Advanced Materials 30,no.20 (2018):1800868.

1.46 Li, B., Wang, L., Kang, B., Wang, P. and Qiu, Y. (2006) Review of Recent Progress in Solid-State Dye-Sensitized Solar Cells. Solar Energy Materials and Solar Cells, 90, 549-573. http://dx.doi.org/10.1016/j.solmat.2005.04.039

1.47 Zhan, J., Sun, P., Jiang, S., Sun, X. and Lund, T. (2006) An Investigation of the Performance of Dye-Sensitized Nanocrystalline Solar Cell with Anthocyanin Dye and Ruthenium Dye as the Sensitizers. Roskilde University, Roskilde

1.48 D.G. McGehee, M.A. Topinka , Nature Mater. 5, 675-676(2006)

1.49 J. Nelson , Current Opinion in Solid State and Materials Science 6, 87-95 (2002)

1.50 J.J.M. Halls, R.H. Friend, M.D. Archer , R.D. Hill , editors, Clean electricity from photovoltaics, London: Imperial College Press, 377-445 (2001)

1.51 H. Hoppe and N. S. Sariciftci, J. Mater. Res. 19, 1924-1945(2004)

1.52 Shi, D., Zeng, Y. and Shen, W. Perovskite/c-Si Tandem Solar Cell with Inverted Nanopyramids: Realizing High Efficiency by Controllable Light Trapping. Scientific Reports, 5, Article No. 16504 (2015)

1.53 Chuang, Chia-Hao M., Patrick R. Brown, Vladimir Bulović, and Moungi G. Bawendi. "Improved performance and stability in quantum dot solar cells through band alignment engineering." Nature materials 13, no. 8 (2014): 796

1.54 Haynos, J., Allison, J., Arndt, R., Meulenberg, A., The COMSAT Nonreflective Silicon Solar Cell: A Second-Generation Improved Cell, Int. Conf. Photovoltaic Power Generation 1974, 487.

1.55 Sato, K., Gotoh, Y., Wakayama, Y., Hayashi, Y., Adachi, K., Nishimura, N., Rep. Res. Lab.: Asahi Glass Co. Ltd. 1992, 42 129.

1.56 Kluth, O., Rech, B., Houben, L., Wieder, S., Schope, G., Beneking, C., Wagner, H., Loffl, A., Schock, H.W., Texture etched ZnO:Al coated glass substrates for silicon based thin Film solar cells, Thin Solid Films 1999, 351, 247-253.

1.57 Mishra. K, and Singh. J, “Semiconductor Device Physics and Design”, Netherlands: Springer, p 60-64 (2008). Photonic crystals for light trapping in solar cells by Jo Gessing.

1.58 Ferry, V.E., Verschuuren, M.A., Li, H.B.T., Verhagen, E., Walters, R.J., Schropp, R.E.I., Atwater, H.A., Polman, A., Light trapping in ultrathin plasmonic solar cells, Optics Express 2010, 18 (102), A237-245

1.59 Bermel, P., Luo, C., Zeng, L., Kimerling, L.C., Joannopoulos, J.D., Improving thin-film crystalline silicon solar cell efficiencies with photonic crystals, Optics Express 2007, 15 (25), 16986-17000

1.60 Zhu, J, Hsu, C.-M., Yu, Z., Fan, S., Cui, Y., Nanodome Solar Cells with Efficient Light Management and Self-Cleaning, Nano Lett. 2010, 10, 1979-1984.

1.61 Tsakalakos, L., Balch, J., Fronheiser, J., Korevaar, B.A., Sulima, O., Rand, J., Silicon Nanowire Solar Cells, Appl. Phys. Lett., 2007, 91, 233117-1-3.

1.62 Ekstrøm, Kai Erik. "Growth and Characterization of Silicon Nanowires for Solar Cell Applications." (2011).

1.63 Stelzner T, Pietsch M, Andra G, Falk F, Ose E, Christiansen S. Silicon nanowire based solar cells. Nanotechnology. 2008 Jul 23;19 (29).

1.64 Bandaru, P. R., and P. Pichanusakorn. "An outline of the synthesis and properties of silicon nanowires." Semiconductor science and technology 25, no. 2 (2010): 024003.

1.65 Treuting, R.G and S.M Arnold. Torsional strain and the screw dislocation in whisker crystal. Acta Met.5,173-175 (1957)

1.66 Wagner, R. S., and W. C. Ellis. "Vapuor-liquid-solid mechanism of single crystal growth." Applied Physics Letters 4, no. 5 (1964): 89-90.

1.67 Liu, Jian, Shi-Hua Huang, Li-Ping Chen, and Lv He. "Tin catalysed silicon nanowires prepared by magnetron sputtering." Materials Letters 151 (2015): 122-125.

1.68 Adachi MM, Anantram MP, Karim KS. Optical properties of crystalline–amorphous core–shell silicon nanowires. Nano Lett 2010; 10:4093–8.

1.69 Vo TTM, Williamson AJ, Lordi V, Galli G. Atomistic design of thermoelectric properties of silicon nanowires. Nano Lett 2008; 8:1111–4.

1.70 Hangarter CM, Myung NV. Magnetic alignment of nanowires. Chem Mater 2005; 17:1320–4.

1.71 Jeon, Minsung, and Koichi Kamisako. "Synthesis of tin-catalysed silicon nanowires using the hydrogen radical-assisted deposition method and its application for solar cells." Current Applied Physics 10, no. 2 (2010): S191-S195.

1.72 Jeon, Minsung, Hisashi Uchiyama, and Koichi Kamisako. "Characterization of Tin-catalysed silicon nanowires synthesized by the hydrogen radical-assisted deposition method." Materials Letters 63, no. 2 (2009): 246-248.

1.73 Peng K, Jie J, Zhang W, Lee ST. Silicon nanowires for rechargeable lithium-ion battery anodes. Appl Phys Lett 2008; 93:033105.

1.74 Tsakalakos L, Balch J, Fronheiser J, Korevaar BA, Sulima O, Rand J. Silicon nanowire solar cells. Appl Phys Lett 2007; 91:233117.

1.75 Yu LW, O'Donnell B, Alet PJ, iCabarrocas PR. All-in-situ fabrication and characterization of silicon nanowires on TCO/glass substrates for photovoltaic application. Sol Energy Mater Sol Cells 2010; 94:1855–9.

1.76 O'Donnell B, Yu LW, Foldyna M, iCabarrocas PR. Silicon nanowire solar cells grown by PECVD. J Non-Cryst Solids 2012; 358:2299–302.

1.77 Y. Cui and Z. Zhong and D. Wang and W. U. Wang and C. M. Lieber, Nano Lett., 2003, 3, 14

1.78 S. -M. Koo and Q. Li and M. D. Edelstein and C. A. Richter and E. M. Vogel, Nano Lett., 2005, 5,2519

1.79 Goldberger, Josh, Allon I. Hochbaum, Rong Fan, and Peidong Yang. "Silicon vertically integrated nanowire field effect transistors. *"Nano letters* 6, no. 5 (2006): 973-977.

1.80 Zhong, Zhaohui, Ying Fang, Wei Lu, and Charles M. Lieber. "Coherent single charge transport in molecular-scale silicon nanowires." *Nano letters* 5, no. 6 (2005): 1143-1146.

1.81 Hahm, Jong-in, and Charles M. Lieber. "Direct ultrasensitive electrical detection of DNA and DNA sequence variations using nanowire nanosensors. *"Nano letters* 4, no. 1 (2004): 51-54.

1.82 Li, Z., Y. Chen, X. Li, T. I. Kamins, K. Nauka, and R. Stanley Williams. "Sequence-specific label-free DNA sensors based on silicon nanowires. "Nano Letters 4, no. 2 (2004): 245-247.

1.83 G. C. Yi, in 'Semiconductor Nanostructures for Optoelectronic Devices', Springer- Verlag publishers, Berlin Heidelberg (2012)

1.84 Takagahara, Toshihide, and Kyozaburo Takeda. "Theory of the quantum confinement effect on excitons in quantum dots of indirect-gap materials." Physical Review B 46, no. 23 (1992): 15578.

1.85 Hasan, Mehedhi, MdFazlulHuq, and Zahid Hasan Mahmood. "A review on electronic and optical properties of silicon nanowire and its different growth techniques." SpringerPlus 2, no. 1 (2013): 1.

1.86 Feng, X. L., Rongrui He, Peidong Yang, and M. L. Roukes. "Very high frequency silicon nanowire electromechanical resonators. *"Nano Letters* 7, no. 7 (2007): 1953-1959.

1.87 Huang, Yu, Xiangfeng Duan, and Charles M. Lieber. "Nanowires for integrated multicolour nanophotonics." Small 1, no. 1 (2005): 142-147.

1.88 Hochbaum, A. I.; Chen, R.; Delgado, R. D.; Liang, W.; Garnett, E. C.; Najarian, M.; Majumdar, A.; Yang, P. Nature 2008, 451, 163.

1.89 Goldberger, Josh, Allon I. Hochbaum, Rong Fan, and Peidong Yang. "Silicon vertically integrated nanowire field effect transistors. *"Nano letters* 6, no. 5 (2006): 973-977.

1.90 Xiang, Jie, Wei Lu, Yongjie Hu, Yue Wu, Hao Yan, and Charles M. Lieber. "Ge/Si nanowire heterostructures as high-performance field-effect transistors. *"Nature* 441, no. 7092 (2006): 489.nanosensors

1.91 Boukai, A. I.; Bunimovich, Y.; Tahir-Kheli, J.; Yu, J.-K., III; W. A. G.; Heath, J. R. Nature 2008, 451, 168

1.92 Zhu, Yong, Feng Xu, Qingquan Qin, Wayne Y. Fung, and Wei Lu. "Mechanical properties of vapor− liquid− solid synthesized silicon nanowires." Nano letters 9, no. 11 (2009): 3934-3939.

1.93 Sohn, Young-Soo, Jinsung Park, Gwonchan Yoon, Jiseok Song, Sang-Won Jee, Jung-Ho Lee, Sungsoo Na, Taeyun Kwon, and Kilho Eom. "Mechanical properties of silicon nanowires." Nanoscale research letters 5, no. 1 (2009): 211.

1.94 S. Hoffmann, I. Utke, B. Moser, J. Michler, S. H. Christiansen, V. Schmidt, S. Senz, P. Werner, U. Go¨ sele, C. Ballif, Nano Lett. 2006, 6, 622.

1.95 Iñiguez, T. A. Fjeldly, A. Lázaro, F. Danneville, and M. J. Deen, “Compact-Modeling Solutions for Nanoscale Double-Gate and Gate-All-Around MOSFETs,”IEEE Transactions on electron devices, Vol. 53, No. 9, pp. 2128 2142,September 2006

1.96 Schottky, Walter. "Halbleitertheorie der sperrschicht." Naturwissenschaften 26, no. 52 (1938): 843-843.

1.97 Peng, Kui-Qing, and Shuit-Tong Lee. "Silicon nanowires for photovoltaic solar energy conversion." Advanced Materials 23, no. 2 (2011): 198-215.

1.98 Z. Gao *et al..*, “Silicon nanowire arrays for label-free detection of DNA.,” Analytical chemistry,vol. 79, no. 9, pp. 3291-7, May. 2007.

1.99 A. Kim *et al..*, “Ultrasensitive, label-free, and real-time immune detection using silicon field-effect transistors,” Applied Physics Letters, vol. 91, no. 10, p. 103901, Sep. 2007.

1.100 E. Stern *et al..*, “Label-free immunodetection with CMOS-compatible semiconducting nanowires,” Nature, vol. 445, no. 7127, pp. 519-22, Feb. 2007.

1.101 [40] Y. Chen, X. Wang, S. Erramilli, P. Mohanty, and A. Kalinowski, “Silicon-based nanoelectronic field-effect pH sensor with local gate control,” Applied Physics Letters, vol. 89, no. 22, p. 223512, Nov. 2006.

1.102 Z. Li, Y. Chen, X. Li, T. I. Kamins, K. Nauka, and R. S. Williams, “Sequence-Specific LabelFree DNA Sensors Based on Silicon Nanowires,” Nano Letters, vol. 4, no. 2, pp. 245-247, Feb.2004.

1.103 N. Elfström, R. Juhasz, I. Sychugov, T. Engfeldt, A. E. Karlström, and J. Linnros, “Surface charge sensitivity of silicon nanowires: size dependence.,”

Nano letters, vol. 7, no. 9, pp. 2608-12, Sep. 2007. NANOFUNCTION D1.1 Date of submission: 01/09/2011 16

1.104 I. Park, Z. Li, A. P. Pisano, and R. S. Williams, “Selective surface functionalization of silicon nanowires via nanoscale joule heating.,” Nano Letters, vol. 7, no. 10, pp. 3106-3111, 2007.

1.105 G.-J. Zhang *et al.*., “DNA sensing by silicon nanowire: charge layer distance dependence.,” Nano letters, vol. 8, no. 4, pp. 1066-70, Apr. 2008.

1.106 J. Wan *et al.*., “Silicon nanowire sensor for gas detection fabricated by nanoimprint on SU8/SiO2/PMMA trilayer,” Microelectronic Engineering, vol. 86, no. 4-6, pp. 1238-1242, Apr. 2009.

1.107 Z. Li, B. Rajendran, T. I. Kamins, X. Li, Y. Chen, and R. S. Williams, “Silicon nanowires for sequence-specific DNA sensing: device fabrication and simulation,” Applied Physics A, vol. 80, no. 6, pp. 1257-1263, Mar. 2005.

1.108 A. I. Hochbaum *et al.*., “Enhanced thermoelectric performance of rough silicon nanowires.,” Nature, vol. 451, no. 7175, pp. 163-7, Jan. 2008.

1.109 N. Elfstrom and J. Linnros, “Avalanche breakdown in surface modified silicon nanowires,” Applied Physics Letters, vol. 91, no. 10, p. 103502, Sep. 2007.

1.110 K. Peng, X. Wang, and S.-T. Lee, “Silicon nanowire array photoelectrochemical solar cells,” Applied Physics Letters, vol. 92, no. 16, p. 163103, Apr. 2008.

1.111 R. Juhasz, N. Elfström, and J. Linnros, “Controlled fabrication of silicon nanowires by electron beam lithography and electrochemical size reduction,” Nano letters, vol. 5, no. 2, pp. 275-80, Feb. 2005.

1.112 N. Elfström, A. E. Karlström, and J. Linnros, “Silicon nanoribbons for electrical detection of biomolecules.,” Nano letters, vol. 8, no. 3, pp. 945-9, Mar. 2008.

1.113 A. Agarwal, K. Buddharaju, I. Lao, N. Singh, N. Balasubramanian, and D. Kwong, “Silicon nanowire sensor array using top–down CMOS technology,” Sensors and Actuators A: Physical, vol. 145-146, pp. 207-213, Jul. 2008.

1.114 I. Park, Z. Li, X. Li, A. P. Pisano, and R. S. Williams, “Towards the silicon nanowire-based sensor for intracellular biochemical detection.,” Biosensors & bioelectronics, vol. 22, no. 9-10, pp. 2065-70, Apr. 2007.

1.115 A. Zhang, S. You, C. Soci, Y. Liu, D. Wang, and Y.-H. Lo, “Silicon nanowire detectors showing photo-transistive gain,” Applied Physics Letters, vol. 93, no. 12, p. 121110, Sep. 2008.

1.116 J. H. Chua, R.-E. Chee, A. Agarwal, S. M. Wong, and G.-J. Zhang, “Label-free electrical detection of cardiac biomarker with complementary metal-oxide semiconductor-compatible silicon nanowire sensor arrays.,” Analytical chemistry, vol. 81, no. 15, pp. 6266-71, Aug. 2009.

1.117 E. Stern, R. Wagner, F. J. Sigworth, R. Breaker, T. M. Fahmy, and M. A. Reed, “Importance of the Debye screening length on nanowire field effect transistor sensors.,” Nano letters, vol. 7, no. 11, pp. 3405-9, Nov. 2007.

1.118 Park, Inkyu, Zhiyong Li, Albert P. Pisano, and R. Stanley Williams. "Top-down fabricated silicon nanowire sensors for real-time chemical detection."*Nanotechnology* 21, no. 1 (2009): 015501.

1.119 Huang, Zhipeng, Nadine Geyer, Peter Werner, Johannes De Boor, and Ulrich Gösele. "Metal-assisted chemical etching of silicon: a review. "*Advanced materials* 23, no. 2 (2011): 285-308.

1.120 Lipinski, M., J. Cichoszewski, R. P. Socha, and T. Piotrowski. "Porous silicon formation by metal-assisted chemical etching."*Acta Phys. Pol. A* 116 (2009): S117-S119.

1.121 Qi, Cheng, Gary Goncher, Raj Solanki, and Jay Jordan. "SiGe nanowire growth and characterization." Nanotechnology 18, no. 7 (2007): 075302.

1.122 Sun, X. H., C. Didychuk, T. K. Sham, and N. B. Wong. "Germanium nanowires: synthesis, morphology and local structure studies." Nanotechnology 17, no. 12 (2006): 2925.

1.123 Johansson, Jonas, Lisa S. Karlsson, C. Patrik T. Svensson, Thomas Mårtensson, Brent A. Wacaser, Knut Deppert, Lars Samuelson, and Werner Seifert. "Structural properties of⟨ 111⟩ B-oriented III–V nanowires." Nature materials 5, no. 7 (2006): 574-580.

1.124 Givargizov, E. I. "Fundamental aspects of VLS growth." Journal of Crystal Growth 31 (1975): 20-30

1.125 Schmidt, Volker, Joerg V. Wittemann, Stephan Senz, and Ulrich Gösele. "Silicon nanowires: a review on aspects of their growth and their electrical properties." *Advanced Materials* 21, no. 25-26 (2009): 2681-2702

1.126 Choi, Heon-Jin. "Vapor–liquid–solid growth of semiconductor nanowires." In *Semiconductor Nanostructures for Optoelectronic Devices,* pp. 1-36. Springer Berlin Heidelberg, 2012.

1.127 Kuo, Hsun Chih. "Vertically Aligned (In) GaN Nanowires Grown by MOCVD." (2014).

1.128 Wang, Yewu, Volker Schmidt, Stephan Senz, and Ulrich Gösele. "Epitaxial growth of silicon nanowires using an aluminium catalyst."*Nature nanotechnology* 1, no. 3 (2006): 186-189.

1.129 Kamins, T. I., R. Stanley Williams, D. P. Basile, T. Hesjedal, and J. S. Harris. "Ti-catalysed Si nanowires by chemical vapour deposition: Microscopy and growth mechanisms". *Journal of Applied Physics* 89, no. 2 (2001): 1008-1016.

1.130 Yang, Rusen. *Oxide nanomaterials: Synthesis, structure, properties and novel devices*. Georgia Institute of Technology, 2007.

1.131 Zhang, Y. F., Y. H. Tang, Ning Wang, Chun Sing Lee, Igor Bello, and S. T. Lee. "Germanium nanowires sheathed with an oxide layer."*Physical Review B* 61, no. 7 (2000): 4518.

1.132 Shi, W. S., Y. F. Zheng, Ning Wang, Chun-Sing Lee, and Shuit-Tong Lee. "A general synthetic route to III–V compound semiconductor nanowires."*Advanced materials* 13, no. 8 (2001): 591-594.

1.133 Lyu, S. C., Y. Zhang, H. Ruh, H. J. Lee, and C. J. Lee. "Synthesis of high-purity GaP nanowires using a vapor deposition method. "*Chemical physics letters* 367, no. 5 (2003): 717-722.

1.134 Peng, H. Y., X. T. Zhou, N. Wang, Y. F. Zheng, L. S. Liao, W. S. Shi, C. S. Lee, and S. T. Lee. "Bulk-quantity GaN nanowires synthesized from hot filament chemical vapor deposition." *Chemical Physics Letters* 327, no. 5 (2000): 263-270.

1.135 Wang N, Tang YH, Zhang YF, Lee CS, Bello I, Lee S-T (1999) Si nanowires grown from silicon oxide. Chem Phys Lett 299 (2):237 - 242

1.136 Al-Ruqieshi, Majid Salim Mohammed. "Synthesis and characterization of silicon oxide and silicon carbide nanostructures/Majid bin Salim bin Mohammed Al-Ruqieshi." PhD diss., University of Malaya, 2010.

1.137 Zhang, Rui-Qin. "Growth Mechanism of Silicon Nanowires." In Growth Mechanisms and Novel Properties of Silicon Nanostructures from Quantum-Mechanical Calculations, pp. 7-12. Springer Berlin Heidelberg, 2014.

1.138 Caroline, M. Lydia. "Growth and characterization of some organic and semiorganic amino acid based nonlinear optical single crystals." (2009).

1.139 Y. Y. Wong, M. Yahaya, M. M. Salleh, B. Y. Majlis, “Controlled growth of silicon nanowires synthesized via solid-liquid-solid mechanism,” Sci. Technol. Adv. Mater., vol. 6, pp.330-334, 2005.

1.140 D. P. Yu, Y. J. Xing, Q. L. Hang, H. F. Yan, J. Xu, Z. H. Xi, and S. Q. Feng, “Controlled growth of oriented amorphous silicon nanowires via a solid-liquid-solid (SLS) mechanism,” Physica E, vol. 9, pp. 305-309, 2001.

1.141 H. F. Yan, Y. J. Xing, Q. L. Hang, D. P. Yu, Y. P. Wang, J. Xu, Z. H. Xi, and S. Q. Feng, “Growth of amorphous silicon nanowires via a solid-liquid-solid mechanism,” Chem. Phys. Lett., vol. 323, pp. 224-228, 2000.

1.142 Miao, Zheng, Dongsheng Xu, Jianhua Ouyang, Guolin Guo, Xinsheng Zhao, and Youqi Tang. "Electrochemically induced sol− gel preparation of single-crystalline TiO_2 nanowires."*Nano Letters* 2, no. 7 (2002): 717-720

1.143 Liu, Yu-Biao, and Shao-Min Zhou. "Thermoelectric and Magnetic Nanowires." In *Nanowires-Fundamental Research*. InTech, 2011

1.144 Zhang, Chao, Zhenhui Kang, Enhong Shen, Enbo Wang, Lei Gao, Fang Luo, Chungui Tian "Synthesis and evolution of PbS nanocrystals through a surfactant-assisted solvothermal route."*The Journal of Physical Chemistry B*110, no. 1 (2006): 184-189.

1.145 Kodambaka, S., J. Tersoff, M. C. Reuter, and F. M. Ross. "Diameter-independent kinetics in the vapor-liquid-solid growth of Si nanowires."*Physical review letters* 96, no. 9 (2006): 096105

1.146 Nebol'sin, V. A., A. A. Shchetinin, A. A. Dolgachev, and V. V. Korneeva. "Effect of the nature of the metal solvent on the vapor-liquid-solid growth rate of silicon whiskers." *Inorganic materials* 41, no. 12 (2005): 1256-1259

1.147 Rinaldi, Fernando. "Basics of molecular beam epitaxy (MBE)."*NIVERSITÄT ULM* (2002): 31.

1.148 Kodas, Toivo. "Handbook of chemical vapor deposition (CVD), principles, technology, and applications. By Hugh O. Pierson, Noyes, Park Ridge, NJ, 1992. 436 pp., hardback, $68, ISBN 0-8155-1300-3." Advanced Materials 5, no. 5 (1993): 401-402.

1.149 Creighton, J. R., and P. Ho. "Introduction to chemical vapor deposition (CVD)." *Chemical vapor deposition* 2 (2001): 1-22.

1.150 Zhang, Zhi. "Investigation of structural characteristics of III-V semiconductor nanowires grown by molecular beam epitaxy." (2015).

1.151 Hutagalung, Sabar D., Aspaniza Ahmad, and Khatijah A. Yaacob. "Growth of silicon nanostructures by thermal evaporation using nickel catalyst."*Solid State Science and Technology* 16, no. 1 (2008): 100-106.

1.152 Tong, Yanhua, Mingwang Shao, Guixiang Qian, and Youbao Ni. "Large-scale fabrication of high-purity and uniform Zn nanowires by thermal evaporation." *Nanotechnology* 16, no. 11 (2005): 2512.Y

1.153 Wang, N., Y. H. Tang, Y. F. Zhang, D. P. Yu, C. S. Lee, I. Bello, and S. T. Lee. "Transmission electron microscopy evidence of the defect structure in Si nanowires synthesized by laser ablation. "*Chemical physics letters* 283, no. 5 (1998): 368-372.

1.154 Ekstrøm, Kai Erik. "Growth and Characterization of Silicon Nanowires for Solar Cell Applications." (2011).

1.155 Davis, J. R., Ajeet Rohatgi, Richard H. Hopkins, Philip D. Blais, P. Rai-Choudhury, James R. Mccormick, and H. C. Mollenkopf. "Impurities in silicon solar cells. "*IEEE Transactions on electron devices* 27, no. 4 (1980): 677-687.

1.156 O'Donnell, Benedict. "plasma grown silicon nanowires catalysed by post-transition metals."

1.157 Schmidt V, Wittemann J, Gosele U (2010) Growth, thermodynamics, and electrical properties of silicon nanowires. Chem Rev 110(1):361–388

1.158 W. Shockley, W.T. Read, Jr., Statistics of the Recombinations of Holes and Electrons, Physical Review, 87 (1952) 835-842.wang

1.159 Tatsumi, Yukichi, Mikio Shigi, and Mitsuji Hirata. "Visual observation of whisker growth in amorphous Silicon." *Journal of the Physical Society of Japan* 45, no. 2 (1978): 703-704.

1.160 Massalski, Thaddeus B., Hiroaki Okamoto, P. R. Subramanian, Linda Kacprzak, and William W. Scott, eds. *Binary alloy phase diagrams*. Vol. 1, no. 2. Metals Park, OH: American society for metals, 1986.

1.161 Chung, Sung-Wook, Jae-Young Yu, and James R. Heath. "Silicon nanowire devices."*Applied Physics Letters* 76, no. 15 (2000): 2068-2070.

1.162 Yu, Jae-Young, Sung-Wook Chung, and James R. Heath. "Silicon nanowires: preparation, device fabrication, and transport properties. "*The Journal of Physical Chemistry B* 104, no. 50 (2000): 11864-11870.

1.163 Wagner, R. S., W. C. Ellis, K. A. Jackson, and S. M. Arnold. "Study of the filamentary growth of silicon crystals from the vapor." *Journal of Applied Physics* 35, no. 10 (1964): 2993-3000.

1.164 Iacopi, F., P. M. Vereecken, M. Schaekers, M. Caymax, Nele Moelans, Bart Blanpain, O. Richard, Christophe Detavernier, and H. Griffiths. "Plasma-enhanced chemical vapour deposition growth of Si nanowires with low melting point metal catalysts: an effective alternative to Au-mediated growth."*Nanotechnology* 18, no. 50 (2007): 505307.

1.165 Iacopi, F., O. Richard, Y. Eichhammer, H. Bender, P. M. Vereecken, Stefan De Gendt, and M. Heyns. "Size-dependent characteristics of indium-seeded Si nanowire growth. *“Electrochemical and Solid-State Letters* 11, no. 9 (2008): K98-K100.

1.166 Sharma, S., and M. K. Sunkara. "Direct synthesis of single-crystalline silicon nanowires using molten gallium and silane plasma." *Nanotechnology* 15, no. 1 (2003): 130.

1.167 Z. H. Chen, J. S. Jie, L. B. Luo, H. Wang, C. S. Lee, and S. T.Lee, Nanotechnol. 18, 345502 (2007).

1.168 Rathi, Somilkumar J., Bhavin N. Jariwala, Joseph D. Beach, Paul Stradins, P. Craig Taylor, Xiaojun Weng, Yue Ke, Joan M. Redwing, Sumit Agarwal, and Reuben T. Collins. "Tin-catalysed plasma-assisted growth of silicon nanowires." *The Journal of Physical Chemistry C* 115, no. 10 (2011): 3833-3839.

1.169 Hofmann, Stephan, Renu Sharma, Christoph T. Wirth, Felipe Cervantes-Sodi, Caterina Ducati, Takeshi Kasama, Rafal E. Dunin-Borkowski, Jeff Drucker, Peter Bennett, and John Robertson. "Ledge-flow-controlled catalyst interface dynamics during Si nanowire growth." *Nature materials* 7, no. 5 (2008): 372-375

1.170 Bootsma, G. A., and H. J. Gassen. "A quantitative study on the growth of silicon whiskers from silane and germanium whiskers from germane."*Journal of Crystal Growth* 10, no. 3 (1971): 223-234.

1.171 Baron, T., M. Gordon, F. Dhalluin, C. Ternon, P. Ferret, and P. Gentile. "Solid catalysed PtSi growth of Si nanowires and electrical characterization."*Appl. Phys. Lett* 89 (2006): 233111.

1.172 Venables, J. A., G. D. T. Spiller, and M. Hanbucken. "Nucleation and growth of thin films."Reports on Progress in Physics 47, no. 4 (1984): 399

1.173 Bhachu, D. "The synthesis and characterisation of metal oxide thin films." PhD diss., UCL (University College London), 2013.

1.174 Mishra, D., D. Greving, GA Badini Confalonieri, J. Perlich, B. P. Toperverg, H. Zabel, and O. Petracic. "Growth modes of nanoparticle superlattice thin films." Nanotechnology 25, no. 20 (2014): 205602.

1.175 Antad, Vivek. "Monitoring the growth and reactivity of metal nanoclusters by in situ optical spectroscopy." PhD diss., Université de Poitiers, 2011.

1.176 Brune, Harald. “Epitaxial Growth of Thin Films in Solid-Solid Interfaces and Thin Films”. No. EPFL-BOOK-209107. Wiley-VCH Verlag GmbH & Co. KGaA, 2014.

1.177 Borghi, F. "Engineering the structural and functional properties of transition metal oxide interfaces by cluster assembling." (2015).

1.178 Hardy, S. C. "The surface tension of liquid gallium." *Journal of crystal growth*71, no. 3 (1985): 602-606.

1.179 Demeri, M., M. Farag, and J. Heasley. "Surface tension of liquid Pb-Sn alloys."*Journal of Materials Science* 9, no. 4 (1974): 683-685.

1.180 Falke, W. L., A. E. Schwaneke, and R. W. Nash. "Surface tension of zinc: The positive temperature coefficient." *Metallurgical and Materials Transactions B* 8, no. 1 (1977): 301-303.

1.181 Giuranno, D., F. Gnecco, E. Ricci, and R. Novakovic. "Surface tension and wetting behaviour of molten Bi–Pb alloys."*Intermetallice* 11, no. 11 (2003): 1313-1317.

1.182 Gasior, W., Z. Moser, and J. Pstruś. "Surface tension, density, and molar volume of liquid Sb-Sn alloys: Experiment versus modeling."*Journal of phase equilibria* 24, no. 6 (2003): 504-510.

1.183 Iacopi, F., P. M. Vereecken, M. Schaekers, M. Caymax, Nele Moelans, Bart Blanpain, O. Richard, Christophe Detavernier, and H. Griffiths. "Plasma-enhanced chemical vapour deposition growth of Si nanowires with low melting point metal catalysts: an effective alternative to Au-mediated growth." *Nanotechnology* 18, no. 50 (2007): 505307.

1.184 McClelland, Matthew A., and John S. Sze. "Surface tension and density measurements for indium and uranium using a sessile-drop apparatus with glow discharge cleaning." Surface science 330, no. 3 (1995): 313-322.

1.185 M.H. Huang, Y.Wu, H. Feick, N. Tran, E. Weber, P. Yang, Adv. Mat. 13, 113 (2001)

1.186 Y. Wang, V. Schmidt, S. Senz, U. Gosele, “Epitaxial growth of silicon nanowires using an aluminium catalyst”, Nat Nano, 1 (2006) 186-189, doi:10.1038/nnano.2006.133

1.187 L. Yu, F. Fortuna, B. O’Donnell, T. Jeon, M. Foldyna, G. Picardi, P. Roca i Cabarrocas, Bismuth Catalysed and Doped Silicon Nanowires for One-Pump-Down Fabrication of Radial Junction Solar Cells, Nano Letters, 12 (2012) 4153-4158, doi:10.1021/nl3017187

1.188 L. Yu, B. O'Donnell, P.J. Alet, S. Conesa-Boj, F. Peiro, J. Arbiol, P. Roca i Cabarrocas, Plasmaenhanced low temperature growth of silicon nanowires and hierarchical structures by using tin and indium catalysts, Nanotechnology, 20 (2009) 225604, doi:10.1088/0957-4484/20/22/225604

1.189 D. Parlevliet, J.C.L. Cornish, Silicon Nanowires: Growth Studies Using Pulsed PECVD, MRS Online Proceedings Library, 989 (2007), doi:10.1557/PROC-0989-A23-03

1.190 L. Yu, P.-J. Alet, G. Picardi, I. Maurin, P.R.i. Cabarrocas, Synthesis, morphology and compositional evolution of silicon nanowires directly grown on SnO2 substrates, Nanotechnology, 19 (2008) 485605, doi:10.1088/0957-4484/19/48/485605

1.191 M. Jeon, K. Kamisako, Synthesis and characterization of silicon nanowires using tin catalyst for solar cells application, Materials Letters, 63 (2009) 777-779, doi:10.1016/j.matlet.2009.01.001.

1.192 Mullane, Emma, Tadhg Kennedy, Hugh Geaney, Calum Dickinson, and Kevin M. Ryan. "Synthesis of tin catalysed silicon and germanium nanowires in a solvent–vapor system and optimization of the seed/nanowire interface for dual lithium cycling." Chemistry of Materials 25, no. 9 (2013): 1816-1822.

1.193 Pierson, Hugh O.*Handbook of chemical vapor deposition: principles, technology and applications*. William Andrew, 1999.

1.194 Kumar, R. Rakesh, K. Narasimha Rao, K. Rajanna, and A. R. Phani. "Growth of tin catalysed silicon nanowires by electron beam evaporation."*Adv. Mater. Lett* 4, no. 11 (2013): 836-840.

1.195 Liu, Jian, Shi-Hua Huang, Li-Ping Chen, and Lv He. "Tin catalysed silicon nanowires prepared by magnetron sputtering." *Materials Letters* 151 (2015): 122-125.

1.196 Al-Taay, H. F., M. A. Mahdi, D. Parlevliet, and P. Jennings. "Controlling the diameter of silicon nanowires grown using a tin catalyst." *Materials Science in Semiconductor Processing* 16, no. 1 (2013): 15-22.

1.197 Meshram, Nagsen, Alka Kumbhar, and R. O. Dusane. "Synthesis of silicon nanowires using tin catalyst by hot wire chemical vapor processing."*Materials Research Bulletin* 48, no. 6 (2013): 2254-2258.

1.198 Jeon, Minsung, Hisashi Uchiyama, and Koichi Kamisako. "Characterization of Tin-catalysed silicon nanowires synthesized by the hydrogen radical-assisted deposition method."*Materials Letters* 63, no. 2 (2009): 246-248.

1.199 Rathi, Somilkumar J., Bhavin N. Jariwala, Joseph D. Beach, Paul Stradins, P. Craig Taylor, Xiaojun Weng, Yue Ke, Joan M. Redwing, Sumit Agarwal, and Reuben T. Collins. "Tin-catalysed plasma-assisted growth of silicon nanowires." The Journal of Physical Chemistry C 115, no. 10 (2011): 3833-3839.

1.200 Tang, Jian, Jean-Luc Maurice, Wanghua Chen, Soumyadeep Misra, Martin Foldyna, Erik V. Johnson, and Pere Roca i Cabarrocas. "Plasma-assisted growth of silicon nanowires by Sn catalyst: step-by-step observation." Nanoscale research letters 11, no. 1 (2016): 455

CHAPTER 2

EXPERIMENTAL TECHNIQUES

Introduction

The diameter and length of the silicon nanowires can be controlled by the size of the metal catalyst nanoparticles. The thickness of the film and annealing temperatures in turn influences the size of the nanoparticles. Characterisation the metal catalyst is required to develop the understanding of the relationship between the catalyst and the SiNW emanating from it. The synthesis and characterisation techniques employed to investigate the tin (Sn) nanoparticle's chemical bonding, surface morphology, elemental composition as well as the crystallinity will be discussed in this chapter.

2.1 Sample preparation

2.1.1 Substrate preparation

The importance of the Si wafer cleaning is to remove the contaminations such as oxides and organic materials such as hydrocarbons which can be on the wafer when the surface is exposed to air [2.1]. The thickness of such contaminates can be of 1 to 2 nanometres and the thickness can increase with exposure time. The deposition of the metal thin film on the Si wafer without cleaning can cause poor adhesion of deposited layer, and lead to harmful by-products when the coated wafer is subjected to elevated temperatures [2.2].

The substrates used in this work were prepared by cutting a (100) Si wafer into several 1 cm x 1 cm samples which are easy to handle and characterize. These samples were then carefully marked on the backside using a diamond - tip pen for them to be distinguishable from each other. To clean the samples, a simple procedure was followed which began by, ultrasonic cleaning of the samples in acetone for 5 minutes followed by another 5 minutes of ultrasonic cleaning in ethanol. Furthermore, these samples were dipped in Isopropanol for another 5 minutes after which were air dried before the final cleaning step. The final cleaning step involved dipping the samples in 5% Hydrofluoric acid (HF) solution for 1 minute and then allowed to air dry (nitrogen gas).

2.1.2 Sn thermal evaporation

Figure 2.19 displays a schematic representation of the thermal evaporator. According to the VLS mechanism, a metal catalyst as a nano-droplet is used to assist in the growth of the nanowire since it forms a “sink” for the Si precursor gases. The Sn film as an alternative metal catalyst is deposited on the Si substrate prior the SiNW deposition.

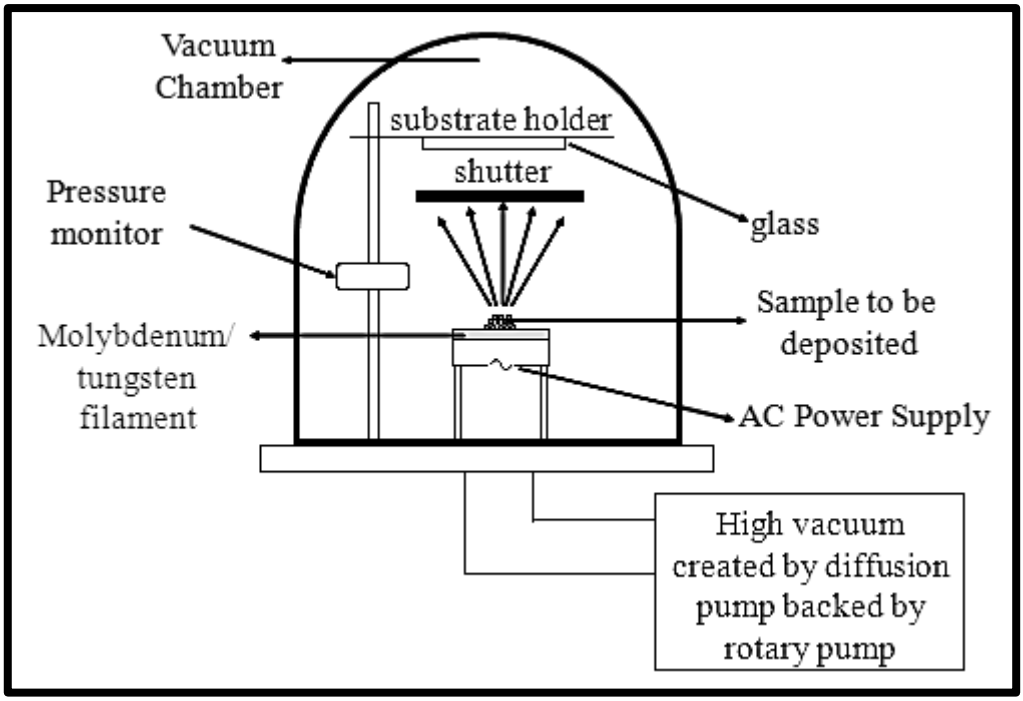

Figure 2.19: Schematic representation of the thermal evaporator.

The Sn thin film was deposited on the cleaned Si (100) substrate (refer 2.1: substrate cleaning step) using the Edwards 306 Thermal Evaporator. The 3 nm Sn thin film was deposited on Si by heating a pure (99%) Sn powder with a current of about 4 A at a pressure of about 10^{-6} mbar. The small current will lead to slow deposition rate which will allow the metal atoms to be well distributed on the Si wafer/substrate. The thickness of the film on the substrate was measured by the crystal monitor. The Sn atoms will simultaneously attach on the substrate and the crystal monitor. The monitor will detect the thickness of the deposited and when the thickness selected is reached, the shutters will cover the substrate then the deposition will be complete.

2.2 Characterisation techniques

The characterisation techniques can give a better understanding on the morphology, size and dimension of the materials. The characterisation techniques can be on the catalyst‘s parameter such as texture, internal structure and chemical surface. The

characterisation techniques such as Focused ion beam scanning electron microscopy (FIBSEM), X-ray photoelectron spectroscopy (XPS), and High-resolution transmission electron microscopy (HRTEM) can be used to understand the chemical bonding, surface morphology, internal structure and crystallinity of the metal catalyst.

2.2.1 Scanning electron microscope system

Scanning Electron Microscopy (SEM) is one of the most versatile technique available for the examination and analysis of the microstructure surface morphology (imaging) and topography down to the nano-meter scale [2.3]. SEM is used in a diverse field of study, stretching from biomedical science to the semiconductor industry. This technique will give an understanding on the morphology, structural properties, topography and chemical/ elemental composition characterisations in thin films and nanostructures such as nanowires and nano-cones. The SEM‘s main component is the column which is used to define the electron beam. Figure 2.20 show the schematic representation of the components comprising the SEM column [2.4]

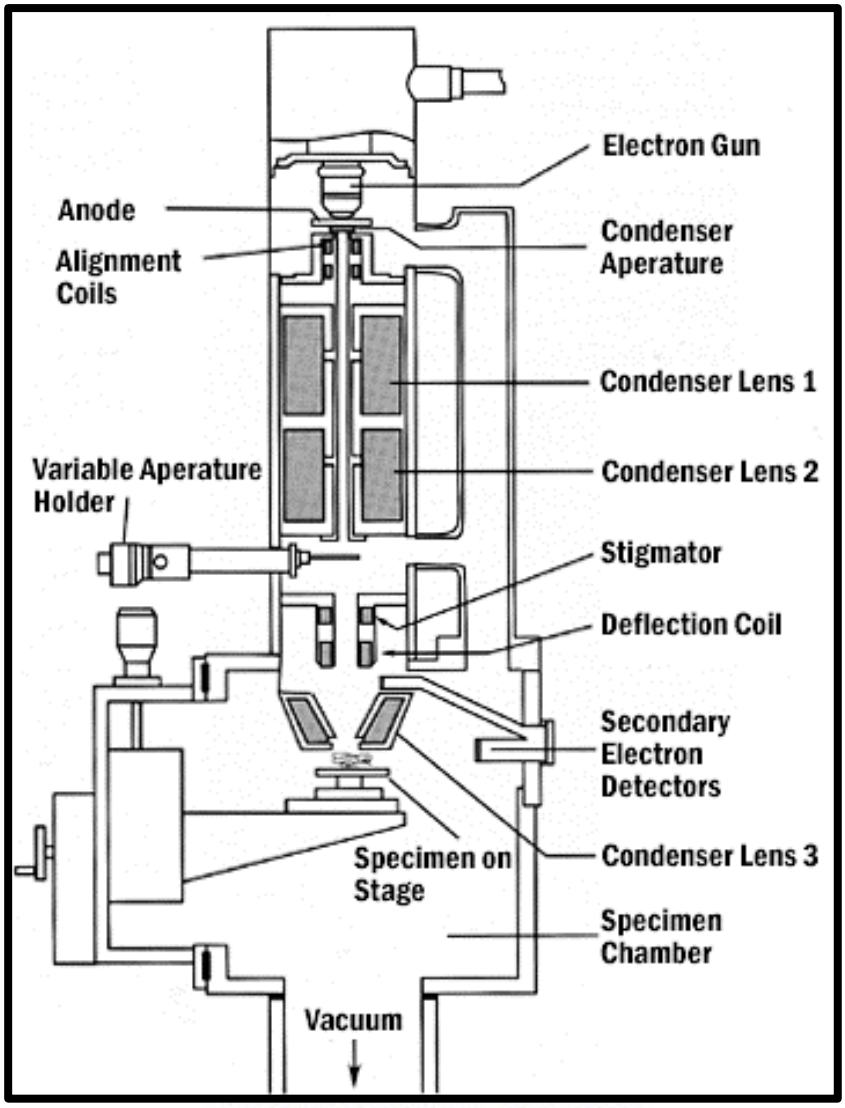

Figure 2.20: Schematic representation of the component comprising the SEM column [2.4].

The first scanning electron microscope (SEM) developed due to the electronic involved in "scanning" the beam of electrons across the material. Electrons emitted via field emission may also be used, with the advantage that the cathode produces a much brighter beam due to the extremely high flux of electrons from an extremely small apparent source. The electrons are accelerated toward a sample-containing anode by an applied voltage. Particles such as electrons possess a wavelike character, with de Broglie's wavelength given by:

$$\lambda = \frac{h}{mv} \qquad (2.1)$$

where h is the Planck constant; *m* and *v* represent the mass and the speed of the electron respectively.

Resolution

Resolution makes the smallest distance at which two objects can be resolve to two entities or spots separately through a microscope [2.5, 2.6]

The image resolution offered by SEM depends not only on the property of the electron probe, but also on the interaction of the electron probe with the specimen [2.7]. The interaction of an incident electron beam with the specimen produces secondary electrons, with energies typically smaller than 50 eV, the emission efficiency of which sensitively depends on surface geometry, surface chemical characteristics and bulk chemical composition. The high-resolution capability afforded by SEM makes it convenient for probing nanomaterial of which the structural features on the nanoscale are critical to their properties and functionalities [2.8-2.9].

The resolution of a SEM, d_r, is mathematically express through Abbe's equation (2.2) [2.10]

$$d_r = \frac{0.612\lambda}{\mu \sin \alpha} \qquad (2.2)$$

where λ is the wavelength of the electron beam, μ is the index of refraction (usually = 1 for vacuum) and α is the semi-angle that the microscope aperture subtends at the

specimen. The product $\mu \sin \alpha$ is known as the numerical aperture. The formula can be used to work out the theoretical limit of any microscope where λ can be reduced and μ increased (usually 1 in a vacuum) or α increased to achieve better resolutions.

The ideal high-resolution can be achieved by allowing more focused electron beam through smaller aperture size and following the de Broglie relation (refer to equation 2.1). The factors cannot be changed above different boundaries like a different medium with high refractive index would be required such as oil, aperture angle has an upper limit of 90° and there would be a limit for electron beam wavelength.

Depth of field and working distance

Figure 2.21 illustrates the Influence of the working distance on the depth of field observed for the specimen. The depth of field as it refers to the range of positions in which the specimen appears to be in focus. The depth profile which is the function of the aperture angle, allows the specimen in SEM to be in focus by controlling the working distance. The aperture angle is the angle formed between a line from the sample through the centre of the lens (or opening) and a line from the sample through the edge of the lens (or opening). The working distance is defined as the distance between the final condenser lens pole piece and the uppermost part of the specimen. The increase in the working distance leads to a low resolution because the apertures size is smaller (large depth of filed) [2.3, 2.4].

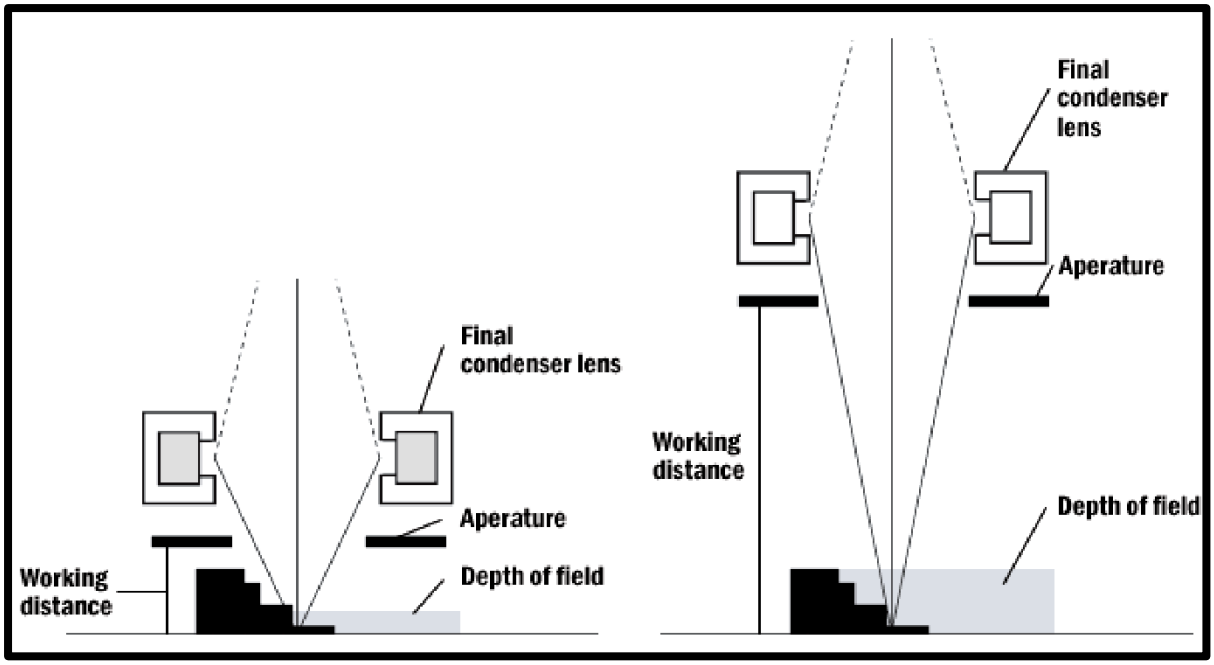

Figure 2.21: Influence of the working distance on the depth of field observed for the specimen.

Electron beam - specimen interaction: signal production

Figure 2.22 displays the schematic diagram of the signals from the incident electron beam – specimen interaction. The accelerating voltage is the voltage that is applied to the filament. Accelerating voltages often used in SEM work varies between 5 kV and 20 kV. Thermo-electrons are emitted from a filament (cathode) made of a thin tungsten wire (of about 0.1 mm) by heating the filament at high temperatures of around 2800K. When accelerated electrons enter a solid they are scattered both elastically (by electrostatic interaction with nuclei) and in-elastically (by interaction with atomic electrons). Most of this interaction between the solid and electrons is forward scattering, which implies deflection angles less than 90°, as shown in figure 2.22.

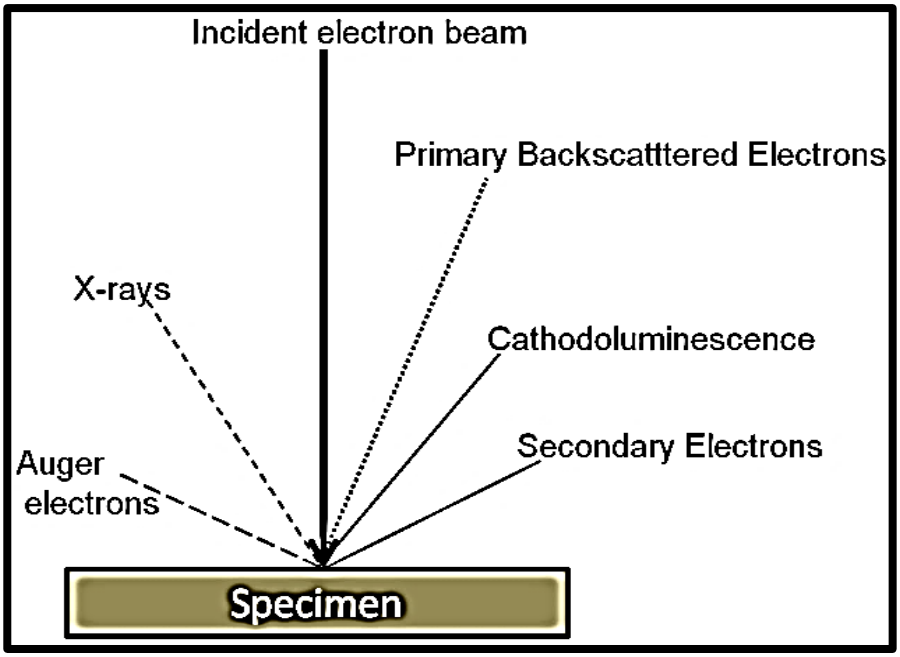

Figure 2.22: Electron beam-specimen interaction signals

Figure 2.23 illustrate the schematic presentation of the escape depth of the electron beam sample interaction signals [2.4]. The depth (below the surface) at which this occurs is called the penetration depth or electron range. The volume of the sample containing most of the scattered electrons is called the interaction volume and it is represented as pear-shaped volume in cross section, because scattering causes the beam to spread laterally as the electrons penetrate the specimen and gradually lose energy [2.9].

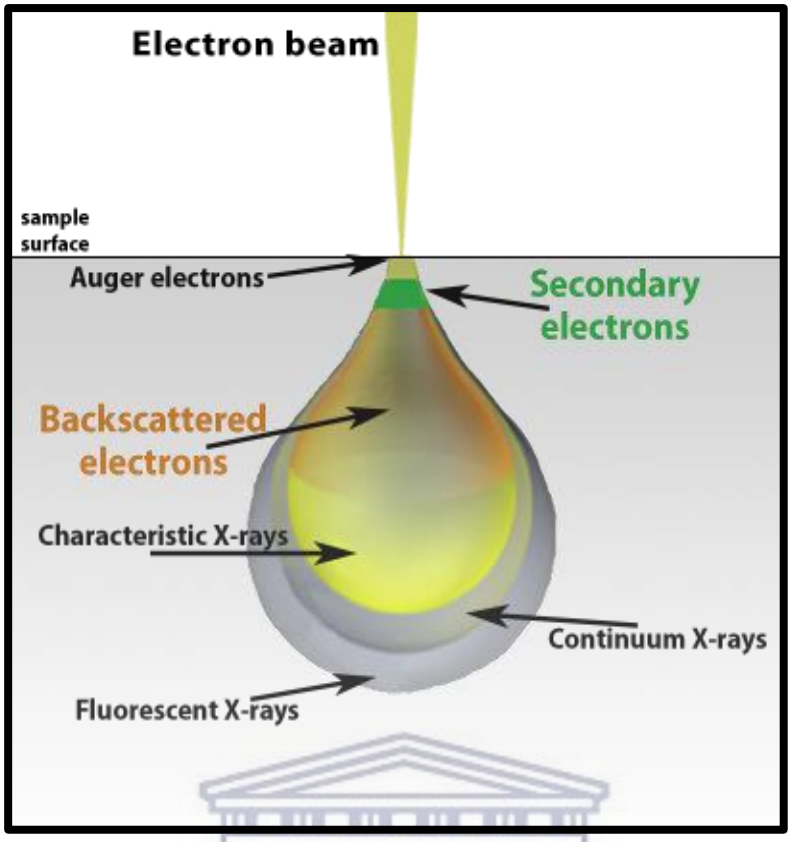

Figure 2.23: The escape depth of the electron beam-sample interaction signals [2.13]

The electron range R for electrons of incident energy E_0 is given by the following formula:

$$\rho R \approx a E_o^r \tag{2.3}$$

where a and r are constants and ρ is the density of the specimen. Expressing the range as a mass-thickness ρR makes the coefficient a roughly independent of atomic number Z. This implies that the distance R itself decreases with Z as the density of the specimen tend to increase with atomic number. The strong Z-dependence arises mainly because backscattering depletes the number of electrons moving forward into the specimen. The interaction volume is therefore smaller for materials of higher atomic number [2.9]. Figure 2.24 illustrates the dependence of

the interaction volume and penetration depth (signals which are observed) as a function of incident energy Eo and atomic number (Z) of the incident electrons.

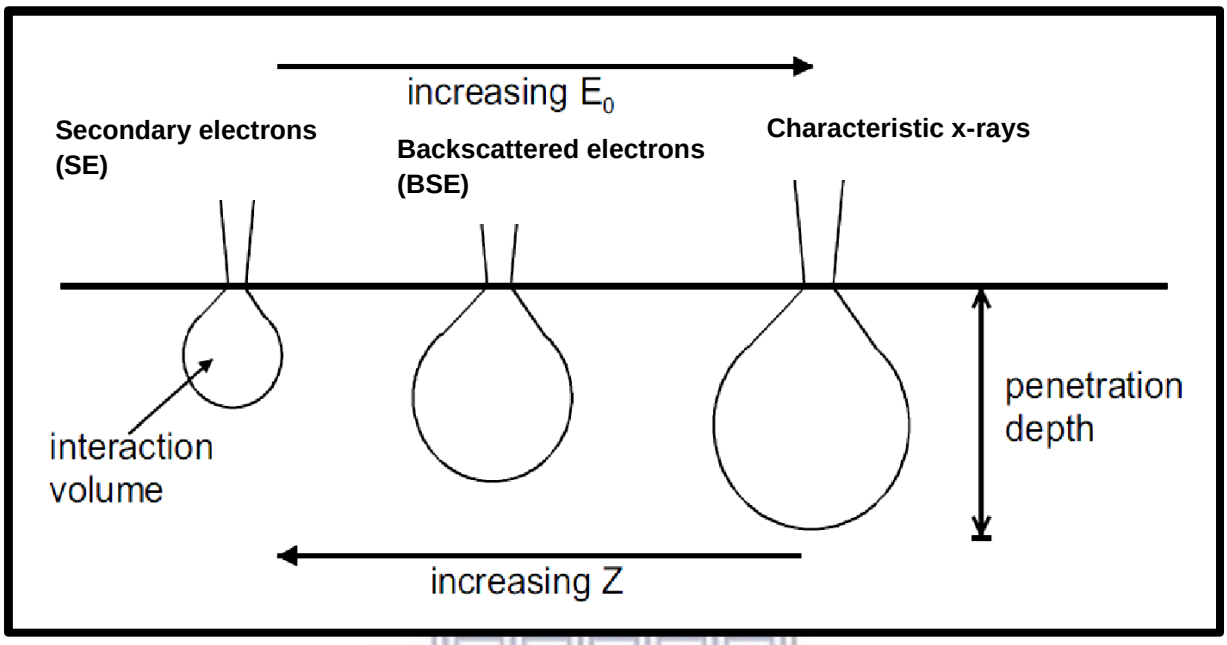

Figure 2.24: Dependence of the interaction volume and penetration depth (signals which are observed) as a function of incident energy Eo and atomic number (Z) of the incident electrons [2.11]

Interaction signals

Secondary electrons

Figure 2.25 displays the secondary electron image of the Si/Ti sample. The beam penetrates with the low accelerating voltage of about 0.1-1 kV (if the material is non-conductive) the sample, electrons are generated which are detected by specialised electronics within the vacuum chamber and from which digital images are formed. The secondary electrons are produced because of collisions between incident electrons and atoms within the specimen. The low energy electrons are detected by

being mounted on the Everhard-Thornley detector which shows the topographic imaging or to an In-lense detector which gives the optimum resolution.

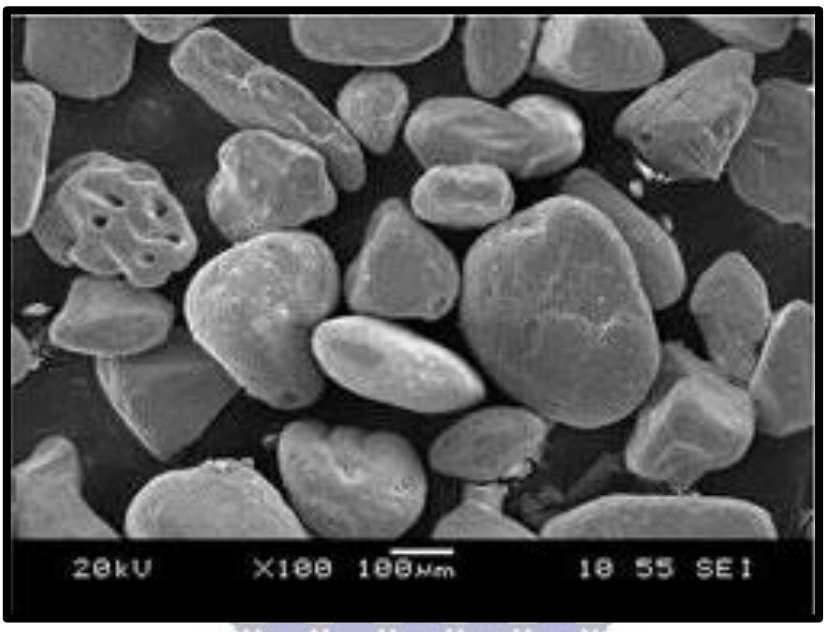

Figure 2.25: Secondary electron image of the Si/Ti sample [2.12]

Backscatter electron

Figure 2.26 is the backscattered electrons of the Si/Ti sample. The incident electrons are elastically backscattered (< 90°) with a small fractional loss of energy. Due to their high kinetic energy, these back-scattered electrons have a high probability of leaving the specimen and re-entering the surrounding vacuum, in which they can be collected as a backscattered-electron (BSE) signal [2.19]. Inelastic scattering involves relatively small scattering angles and so contributes little to the backscattered signal. However, it reduces the kinetic energy of the primary electrons until they are eventually brought to rest and absorbed into the specimen.

The BSE are detected using either a scintillator type detector or a solid-state diode type, either of which is placed directly above the specimen surface. The contrast in

the BSE image shows variations in average atomic number and can distinguish difference as small as 0.1 at Z=29 (copper).

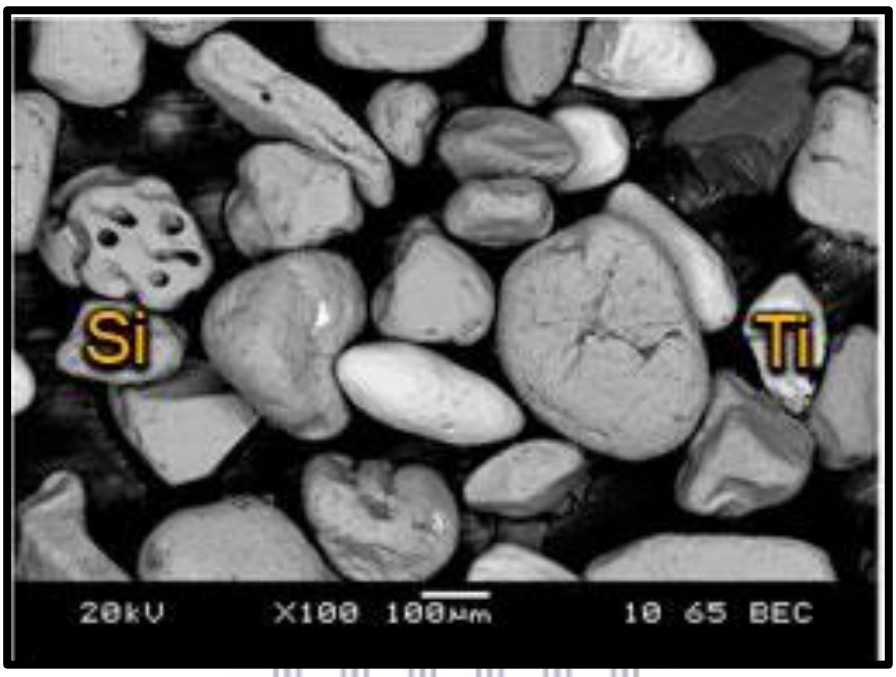

Figure 2.26: Backscattered electron image of Si/Ti sample [2.12]

Characteristic X-ray and Energy Dispersive Spectroscopy

Figure 2.27 presents the schematic representation of the Bohr ‘s atomic model and electronic transitions generating the x-ray radiation. Figure 2.27 illustrate the schematic representation of the Bohr ‘s atomic model and electronic transitions generating the x-ray radiation. X-ray generated within the sample travel in all directions through it and may be absorbed within it. X-ray are either absorbed within the sample or they pass through it they do not gradually lose energy as electron do. Absorption is due to the photo-electric effect. The energy levels (shells) surrounding the nucleus of the atom are labelled K, L, M,… corresponding to the principle quantum number, n = 1, 2, 3. The ionisation energy of an electron characteristics x-

ray is equal to the ionisation energy of an electron shell of an atom in the sample there is a strong probability that the x-ray photon will be absorbed and a photo-electron will be generated. The electron beam interaction with this atom leads to dislodge one of the inner electrons, e.g. the atom in shell K which is in an excited state (figure 2.8) The outer shells (e.g. L or M) electrons will fill the vacancy in the K shell to return to its ground, normal state. Depending on the other elements in the sample and their ionization energy. The principle does also depend on the distance that it travels through the sample before it escapes and enters the x-ray detector [2.4, 2.5]

The production of characteristic x-rays can be detected and analysed is through energy dispersion x-ray spectroscopy (EDS). The technique employs energy dispersion, which is the separation of x-rays according to their energy. This separation of energy is accomplished with the help of a semiconductor detector. When an x-ray strikes a semiconductor crystal, electrons in the crystal absorb a given amount of energy and are thus excited. The greater the x-ray energy, the greater the number of electrons excited. The absorbed energy is then converted to an electronic signal, which is emitted and amplified. The strength of the current from the crystal is proportional to the x-ray energy.

Qualitative analysis can be obtained from this signal where characteristic x-ray wavelength emitted by a specimen gives information about several types of elements present in the specimen. Quantitative analysis is also possible where several different x-ray types emitted per second provide information about the quantity of elements present in the specimen. The elements present in the specimen can be detected and quantified at a level of 1.0 wt%.

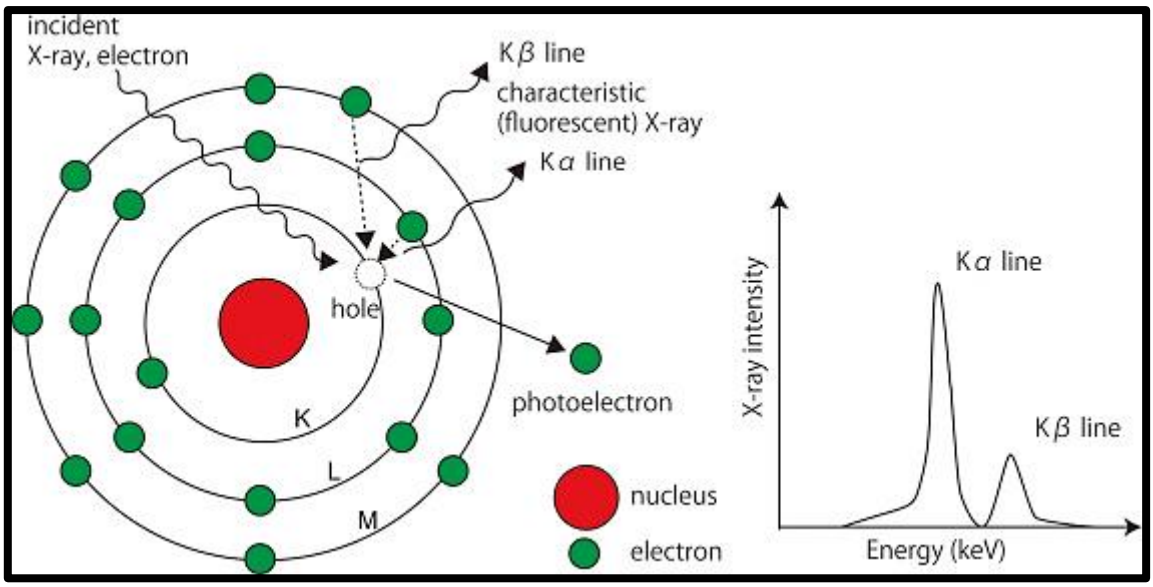

Figure 2.27: Schematic representation of the Bohr's atomic model and electronic transitions generating the x-ray radiation.

2.2.2 Focused ion beam scanning electron microscopy (FIBSEM) system

Figure 2.10 shows the cross-sectional view of the FIBSEM column in crossbeam 540 system with inclination of 54°.

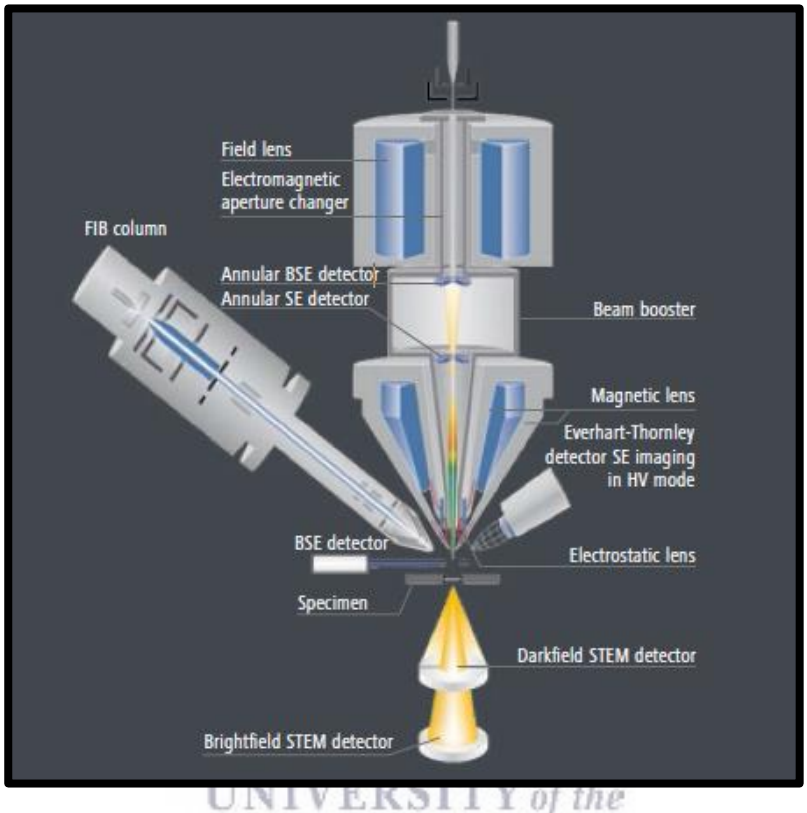

Figure 2.28: Cross-sectional view of the FIBSEM column in crossbeam 540 system with inclination of 54°

Focused ion beam scanning electron microscopy (FIBSEM) is an analytical technique which is composed of the Focused ion beam (FIB) coupled with scanning electron microscope (SEM) and uses focused beam of ions instead of electrons. Figure 2.29 demonstrate the FIBSEM detection for both SEM and FIB.

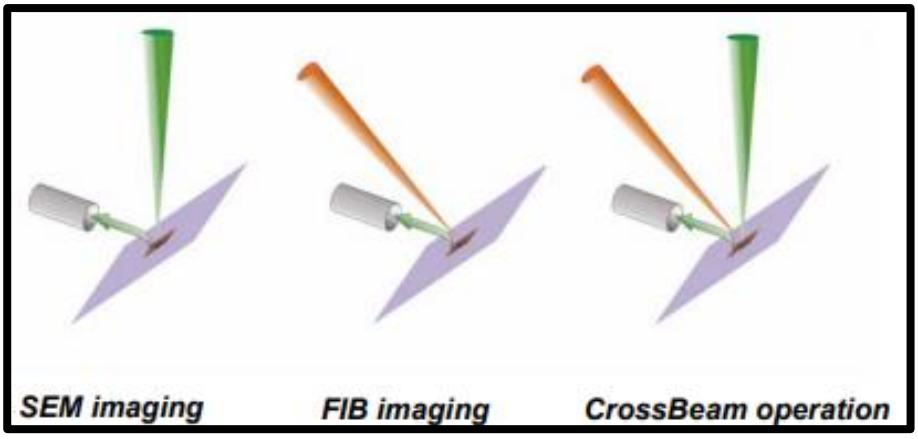

Figure 2.29: FIBSEM detection for both FIB and SEM.

2.2.3 Scanning electron microscope (SEM) system

Figure 2.30 illustrate the Gemini II column of crossbeam 540. The scanning electron microscope (SEM) is one of the well-known instruments used in wide range of fields such as semiconductors and biological industry. The Gemini II Crossbeam 540 was used for the sample characterisation. Compared to the normal SEM column, the Gemini II column has a double condenser system, the beam booster, magnetic lenses, scan coil and combined electrostatic/electromagnetic lenses doublet.

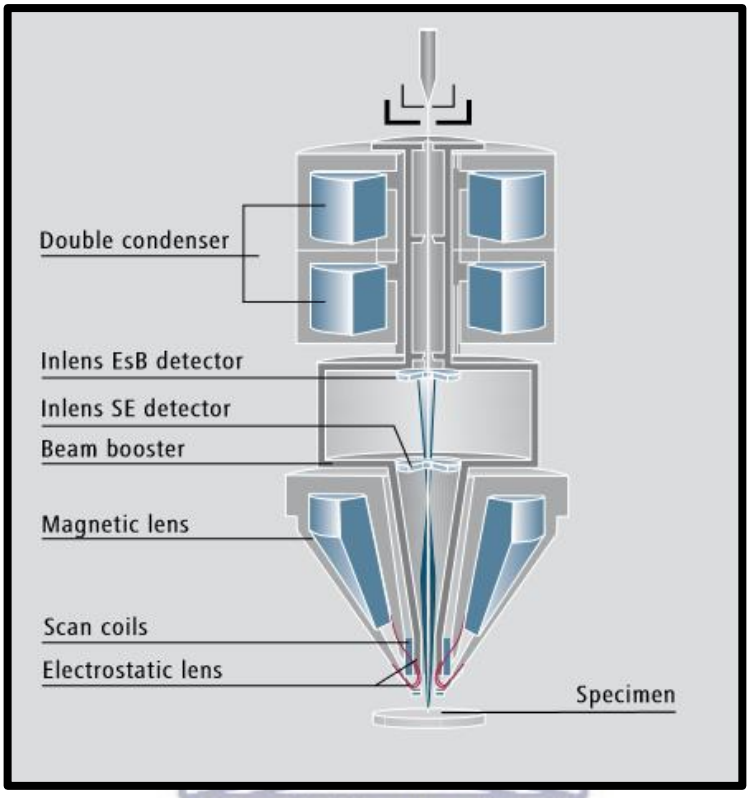

Figure 2.30: Gemini II column of crossbeam 540.

2.2.3.1 Scanning electron microscope principle

The GEMINI II column is the area of the Field Emission SEM (FESEM), where electrons are emitted, accelerated, bundled, focused and deflected. The filament is heated resistively by a current to achieve a temperature between 2000 - 2700 K. The electron gun generates electrons and accelerates electrons to energy in the range 0.1 - 30 keV towards the sample [2.13].

Within the column, the electrons pass through the double condenser system which enables high resolution at low voltage and high current. The incident beam is focussed by a combination of a magnetic lens with an axial gap that avoids field leakage to the specimen. An electrostatic retarding lens formed by the beam booster, focus the beam to small probe sizes with a high signal-to-noise ratio. The Gemini objective lens design combines electrostatic and magnetic fields to maximize

optical performance while reducing field influences at the sample to a minimum. The charged electron beam is accelerated towards the anode and further de-magnified by two or more electromagnetic condenser lenses to reach a specific diameter as it hits the specimen (sample). The beam sample interaction will produce different signals depending on the escape depth of the emitted sample electrons as indicted in figure 2.29.

2.2.3.2 Signal detection

Figure 2.31 displays the Gemini detectors. GEMINI FESEMs microscope comprised of diverse types of detectors. The detectors will have assisted in analysing all scattering products emerging from the sample.

Secondary electrons (SEs) used mostly to resolve topographic and charging information. The SEs emerging from the sample surface are attracted and accelerated by the positively biased electrode of the beam booster and are collected with the SE In-lens detector. The Everhart-Thornley chamber detector (ETD) collects remaining SEs that are not captured by the beam booster (especially at large working distances) or second generation secondary electrons, SE3 type, which are produced by backscatter electrons (BSEs) interaction with the objective lens. Backscattered electrons (BSEs) is used to enhance compositional contrast and crystal orientation, as well as photons to visualise lattice structures or to show luminescence effects. Hence, the ETD typically depicts compositionally enhanced contrast combined with some surface information.

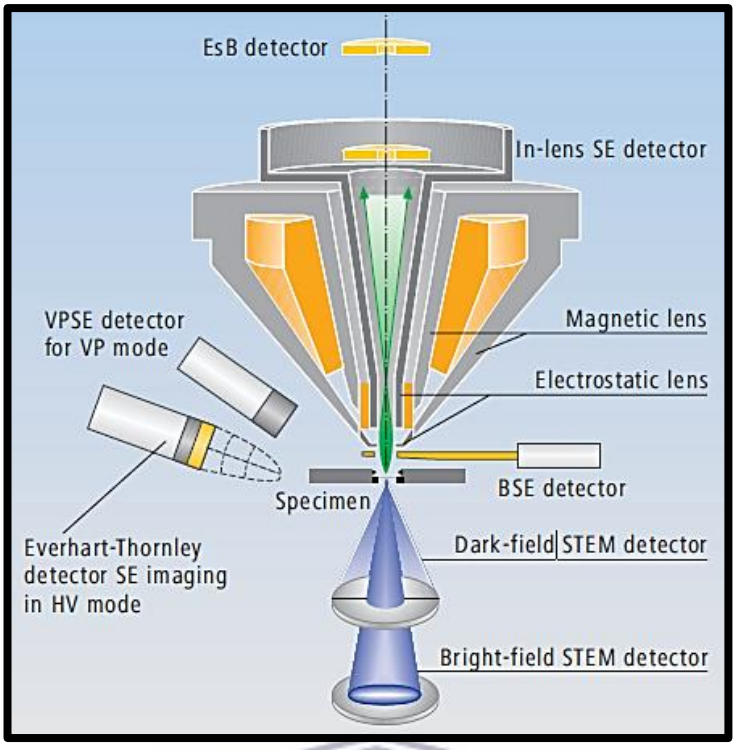

Figure 2.31: Gemini detectors.

Figure 2.32 shows the secondary electrons (SEs) (green) are project onto the lower In-lense detector and the backscatter electrons (BEs)(blue) are guided onto the upper EsB detector. Correct BSE detection is rather complicated and needs several detectors covering the whole solid angle depending on the primary energy of the initial electrons. A retractable quadrant diode detector installed beneath the objective lens collects BSE scattered under very low angle (almost parallel to the sample surface) and produces high quality material contrast images. Electrons passing the lower In-lens detector may be collected at the upper EsB detector. These are mainly called “high angle” backscattered electrons, including a small proportion of unwanted secondary electrons inside the phase space volume of the backscattered. The compositional information of the EsB detector is superimposed by an undesirable surface signal. To remove this contribution a negatively biased filtering grid is installed below the EsB detector to repel the secondary electrons.

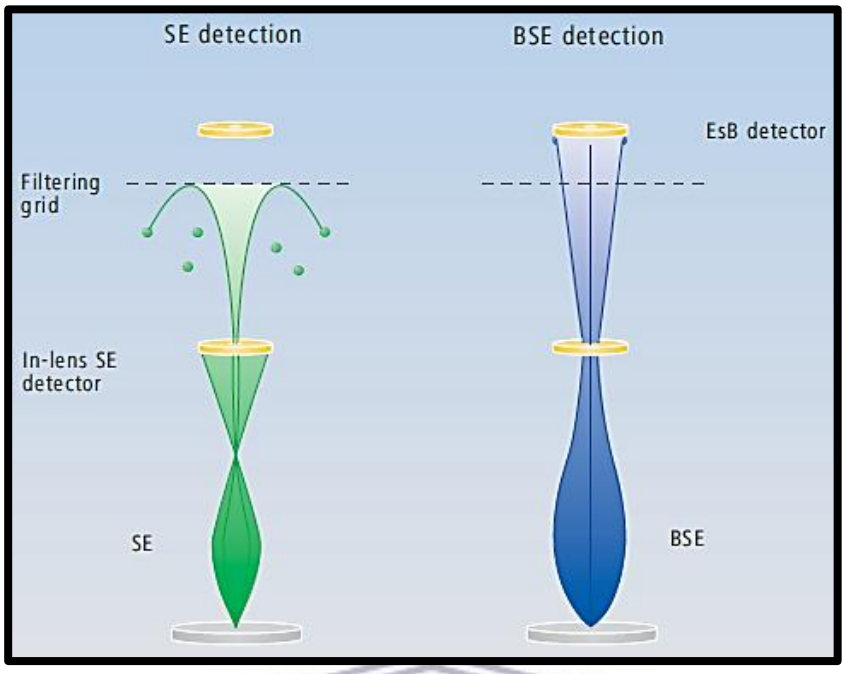

Figure 2.32: Diagram representing the SEs (green) projected onto the lower in-Lense detector and the BEs(blue)guided onto the upper EsB detector.

2.2.4 Focused ion beam (FIB)

Figure 2.33 shows a well detailed FIBSEM cross-sectional view. According to literature, the FIB instrument was first developed for specific sample preparations or machining of devices at a micrometre or sub-micrometre scale [2.14-2.20]. The focused ion beam (FIB) microscope has gained widespread use in fundamental materials studies and technological applications over the last several years because it offers both high-resolution imaging and flexible micromachining in a single platform. It finds broad applications in various scientific fields and is in materials science mainly used for deposition and ablation of materials. The FIB instrument is similar to a scanning electron microscope (SEM), except that the beam which is rastered over the sample is an ion beam rather than an electron beam. Secondary

electrons are generated by the interaction of the ion beam with the sample surface and can be used to obtain high-spatial-resolution images.

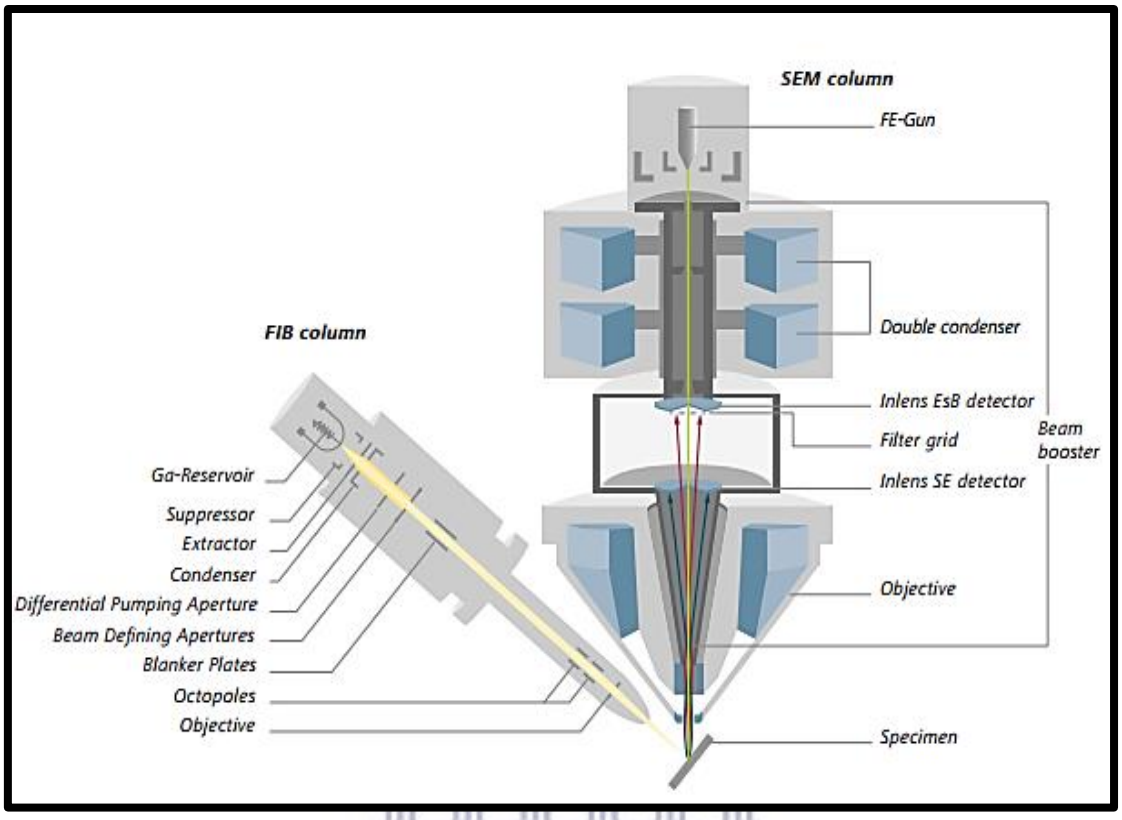

Figure 2.33: Detailed cross-section view of the FIBSEM.

Figure 2.34 shows the secondary electron image from the ion and e-beam. The FIB unit was enriched in the sense that the ionic gun has been coupled with a SEM column in what is called a dual-beam or double-column system. The ion beam and the electron beam complement each other in charge reduction, protective depositions, and imaging information in conjunction with the gas-injection capabilities on these systems.

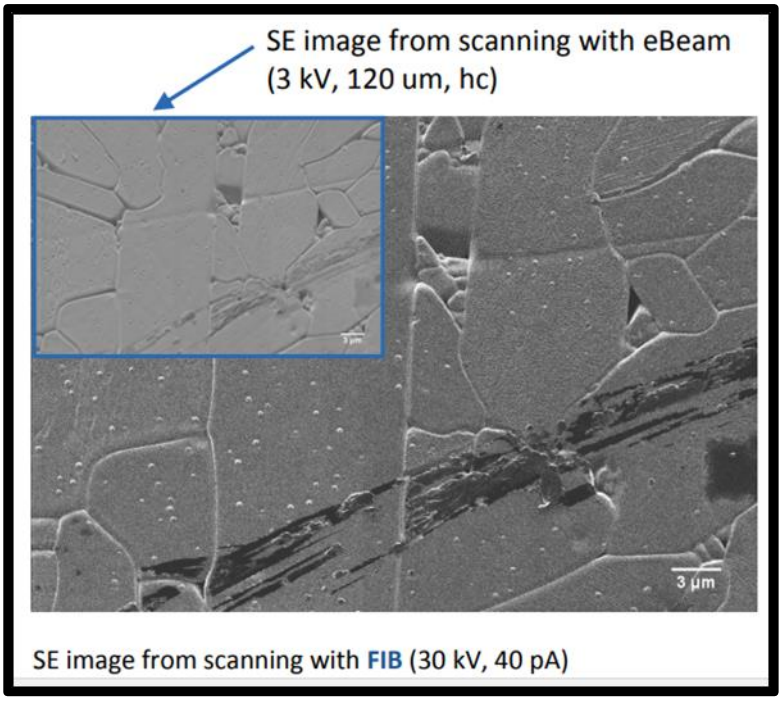

Figure 2.34: Secondary electron image from the ion and electron -beam.

2.2.4.1 Multiple gas injection system (M-GIS)

Figure 2.35 shows the multiple gas injection system in the FIBSEM. The GIS enable ion-beam-activated deposition and enhanced etching, a range of sample fabrication schemes are possible low ion beam currents are used for imaging and high beam currents are used for sputtering or milling the sample surface [2.21].

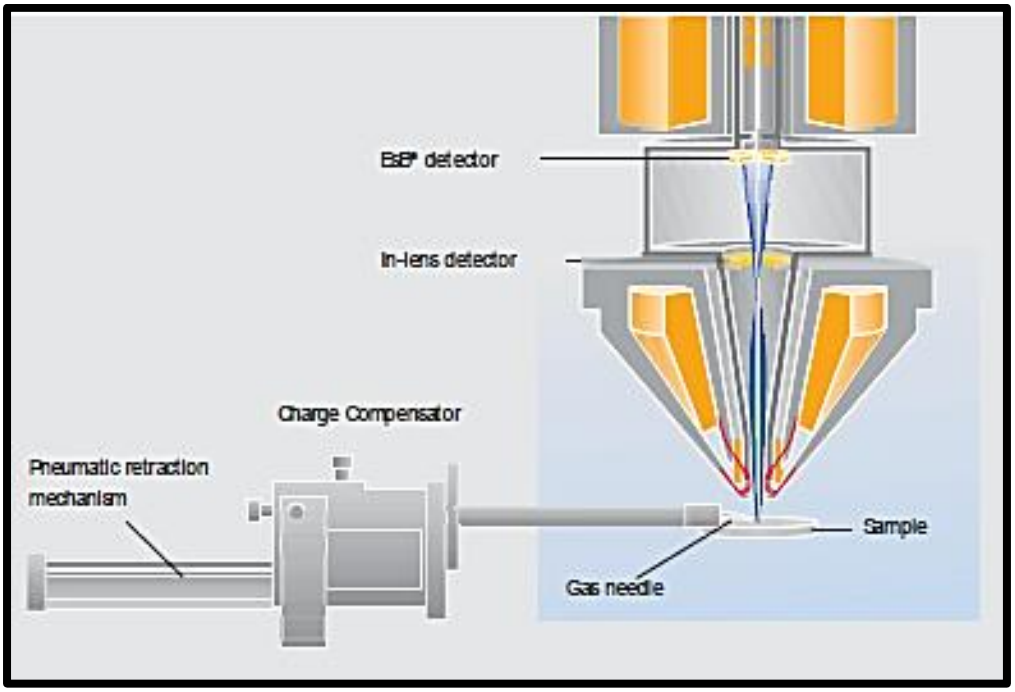

Figure 2.35: Gemini column with the multiple gas injection system.

Figure 2.36 shows the three modes of the FIB. Gas delivery systems are used in conjunction with the ion beam to produce site specific deposition of metals or insulators or to provide enhanced etching capabilities. The chemical precursors are obtained from a gas, liquid, or solid source that can be heated with the ion current of about the Area x 5 pA/μm^2 if required to produce the desired vapour pressure. Metals, such as W or Pt, are deposited by ion beam assisted chemical vapour deposition (CVD) of a precursor organometallic gas such as trimethyl-

methylcyclopentadienyl) platinum (IV) ($C_5H_4CH_3Pt(CH_3)3$) for platinum(Pt) deposition. The ion beam assisted CVD process consists of a fine balance between sputtering and deposition. If the primary beam current density is too high for the deposition region, milling will occur and damaging the region of interest on the sample. To avoid any damaging an e-beam for deposition of about 1 kV at a slow scanning speed can be done. The chemically enhanced sputtering is facilitated by the introduction of select species into the FIB chamber such as halogen-based species may enhance sputtering rates for specific substrate materials in the presence of the Ga+ ion beam. Water has been shown to provide enhanced etching for carbonaceous materials. The gas molecules are adsorbed on the surface near the gas inlet but decompose only where the ion beam strikes. Repeated adsorption and decomposition result in the build-up of material in the ion scanned region

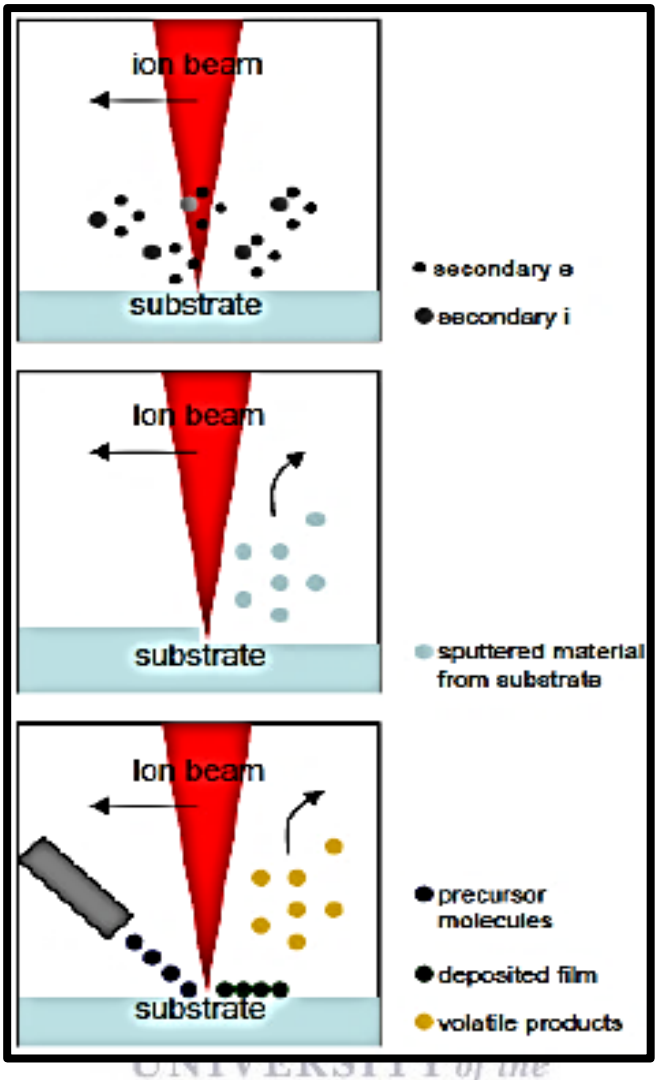

Figure 2.36: Schematic presentation of the three FIB modes.

2.2.4.2 FIB Capella for gallium ions (Ga+)

The image and schematic diagram of the Capella of gallium ion (Ga+) is illustrated in figure 2.37. The ion column typically has two lenses; the condenser lens (1, probe forming) and the objective lens (2, focus). A set of apertures define the probe size and provides a range of ion currents (10 pA – 30 nA). Typical accelerating voltage in FIB systems ranges from 1 to 30 keV. Cylindrical octopole lenses perform multiple functions such as beam deflection, alignment, and stigmation correction. Beam blankers are used to deflect the beam away from the centre of the column.

Different ion sources such as gold and iridium, but gallium (Ga+) is the most typically used in FIB instruments because of its low melting temperature (30 ºC), low volatility, low vapour pressure and their sputtering action enables precise machining of samples.

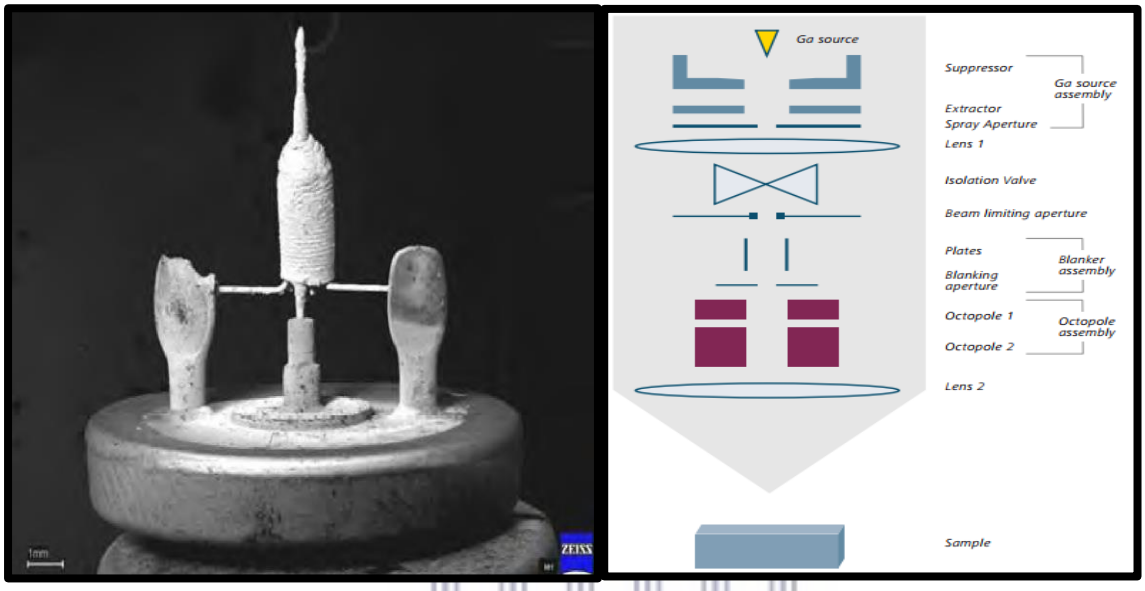

Figure 2.37: Image and schematic diagram of Capella Ga^{+}-FIB.

2.2.4.3 Nanofabrication/sample preparation

The angle between the FIB column and the SEM column is between 52 -55 ° as indicated in figure 2.38. The sample will be at the coincidence point to be analysed using both columns sequentially, the sample must be an angle ranging from 52° to 55°.

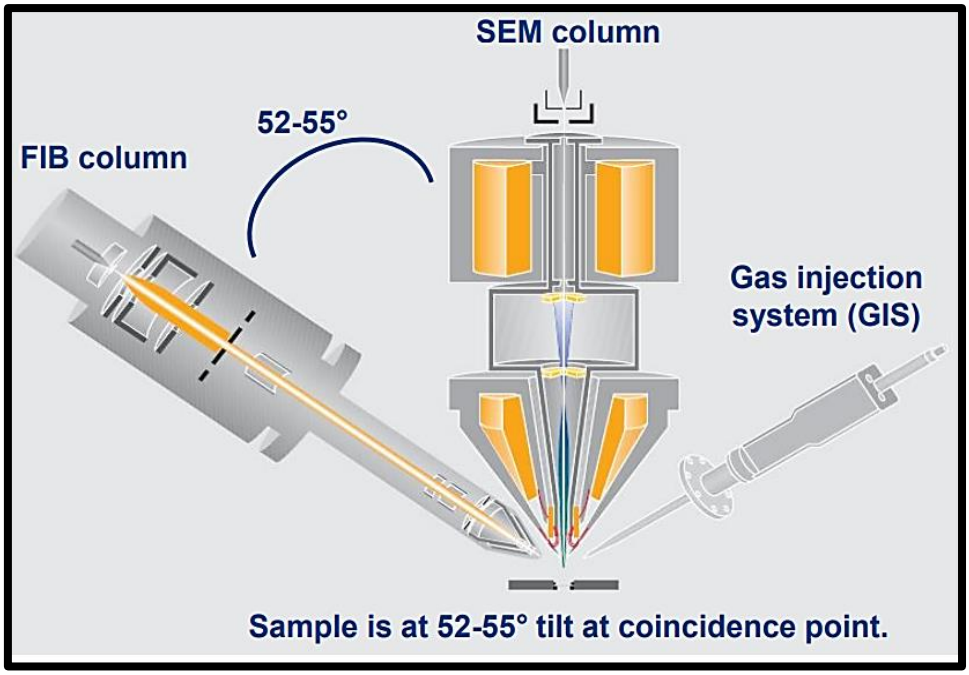

Figure 2.38: FIBSEM system showing the angle between FIB and SEM (52 - 55°).

Prior to the ion milling, a thin platinum layer with ~ 500 nm thickness can be deposited onto the sample surface as illustrated in figure 2.39. The e-beam Pt deposition will be a protective layer against the Ga+ ions.

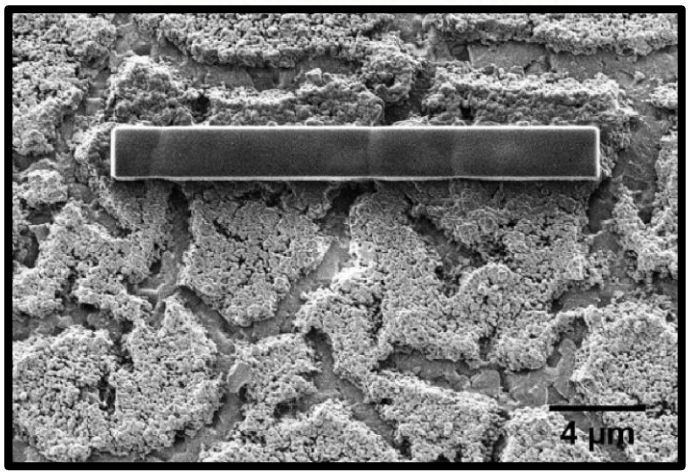

Figure 2.39: Platinum e-beam deposition on the substrate.

TEM Lamella formation

Figure 2.40 shows the ion interaction signals with the sample from the FIB column. The milling of the sample surface was performed by bombarding it with Ga+ ions to form a trench to observe the subsurface morphology of the sample in cross-section view. It uses series of decreasing currents. The sputter process has less damage at cutting surface for small currents, but high currents mill faster. A Ga+ ion source is used to remove material from the surface in the following order: coarse milling of about 10 nA, medium polishing of about 2 nA and final polishing of about 500 pA FIB current.

During milling, sample topography changes are based on the precise milling strategy. This change, in turn, affects the milling rate. Two milling styles are commonly distinguished line and frame milling. First, the ion dose is delivered line by line in a single pass. And the entire frame is milled multiple times until the total dose is delivered.

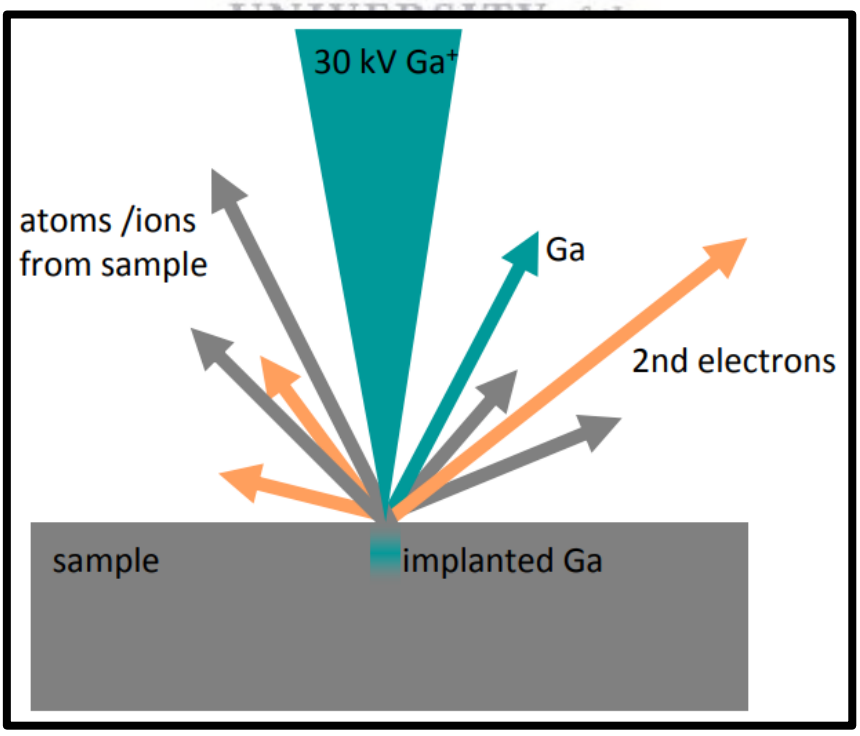

Figure 2.40: Ion-interaction signals with the sample in the FIB column.

The figure 2.41 below illustrates the milling steps. The first step to define the recipe or the shape and size of the trench to mill as indicated the two trapezoids on each side of the e-beam deposited layer. The “X” next to the desired recipe is the drift correction mark.

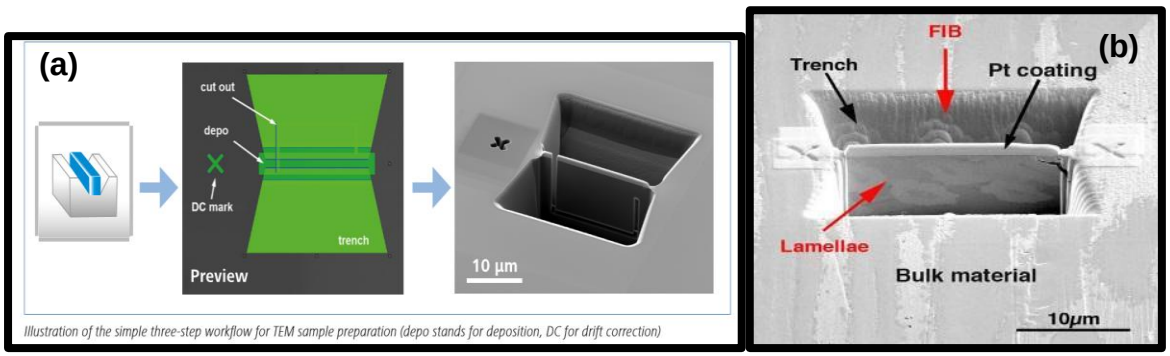

Figure 2.41: (a) illustration the sample three step workflow for TEM sample preparation ("depo" for deposition and DC for drift correction) [2.22]. (b) SEM image (secondary electrons) of a metal sample (Nb_3Sn/bronze) during FIB milling [2.23].

Figure 2.42 show the (a) nano-manipulator in SEM and FIB view (b) TEM lamella on the TEM grid (c) TEM lamella on the TEM grid. The nano-manipulator with a tip of about 200 nm in diameter is used to lift – off the TEM lamella on the sample to the grid for smoothing and polishing in preparation of further analysis. The lift – off done by drawing the nano-manipulator closer to the edge of the lamella and the Pt /W deposition to attach both the tip of the nano-manipulator with the lamella. The edged of the remaining part will be etched then the lamella will be transferred to the grid by the manipulator.

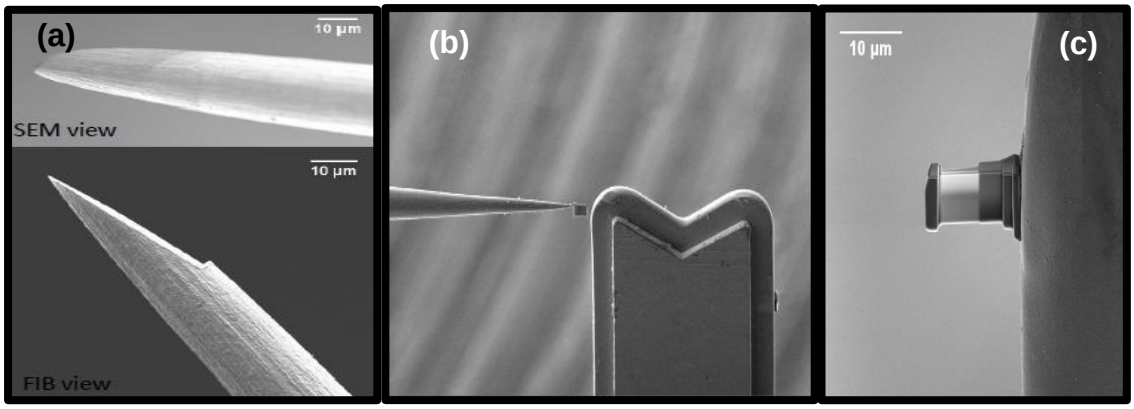

Figure 2.42: (a) SEM and FIB vies on the nanomanipulator tip transfer of the TEM lamella using the nanomanipulator to the TEM grid view (b) TEM lamella on the TEM grid (c) TEM lamella on the TEM grid.

Lamella thinning

Figure 2.43 illustrate the conventional lamella thinning. The conventional method of preparing a thin, electron-transparent window with the FIB consists of symmetrical milling from the upper sample edge down (Figure 2.41a). This is done step-wise with decreasing beam currents. When the window is thinned below a certain threshold, warping is caused because of intrinsic or milling induced strain.

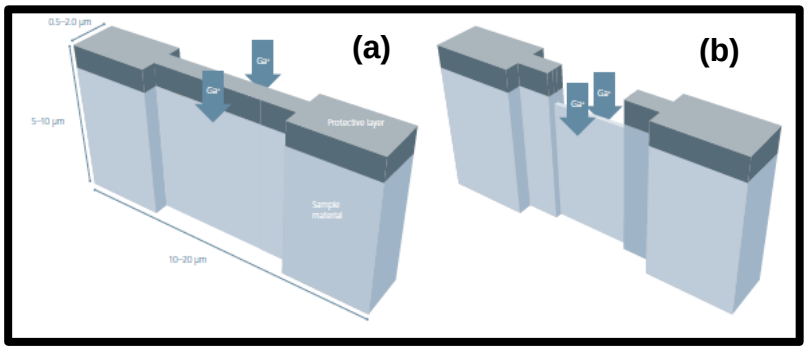

Figure 2.43: Principle of conventional lamella thinning.

Figure 2.44 displays the conventional FIB lamella preparation, bottom mount where the SEM micrographs recorded with SE2 and in-Lense detectors. The lamella is reduced from an initial 1 µm to approximately 300 nm using 240 pA FIB current at 30 kV and second step by using 20 pA current at 30 kV to produce an approximately 8 µm wide electron - transparent window.

The unintentional removal of the protection layer deposited on the sample surface before the lamella preparation is a further problem during thinning to the final thickness (Figure 2.44 b). When reducing the window thickness by only a few ten nanometres, the beam tails of the FIB beam can eat into the upper edge of the window by several micrometres (Figure 2.44b). This can be avoided by depositing very thick sacrificial protective layers, however it is a time consuming and expensive process. Further thinning will lead to uneven thickness and eventually to destruction of the lamella (Figure 2.44c).

The thickness of the lamella is very important in the TEM analysis as the detector within the FIBSEM system is located low the sample holder.

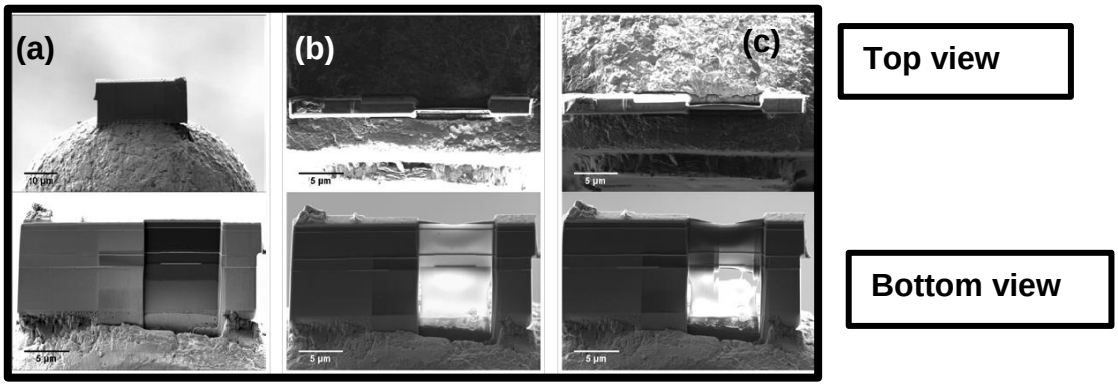

Figure 2.44: Conventional FIB lamella preparation, bottom mount. SEM micrographs recorded with SE2 and in-Lense detectors.

2.2.5 Transmission electron microscopy (TEM) system

The transmission electron microscope (TEM) is a technique that gives information on the crystals, polycrystalline materials, biological specimens, nanostructures and others, by using the transmitted electron beam through the sample. Furthermore, it can be applied to obtain images at atomic resolution. To get satisfactory results from TEM, a sample must be thin enough to be usable in the TEM to provide electron transparency. The resulting thickness of the specimen should be less than 90 - 100 nm. Cross-sectional TEM allows a better understanding on the internal structure of the material such as strain, interfacial diffusion and changes in chemical composition throughout the sample.

2.2.5.1 STEM detection

Figure 2.45 indicating the aSTEM detector situated below the STEM grid. STEM located in the FIBSEM system provides the simultaneous acquisition of multiple different image and spectroscopy signals while scanning the electron probe across the specimen. The signals from the sample can give information regarding the sample's different defect structures, such as, point defects, grain boundaries, or hetero-phase interfaces. The STEM can be used to examine internal structure and composition of thin or sectioned specimens. The enhanced imaging resolution, complementary contrasts and the insensitivity to the interaction volume inside the sample of the STEM makes it more favourable as compared to the conventional SEM.

The GEMINI Multi-Mode STEM detector was used in this study which consists of an electron detector underneath a thin specimen with the ability of simultaneous imaging and real-time mixing of bright-field and dark-field signals. The micrographs obtained with the STEM unit usually taken with primary beam energies of around 30

kV to enable electron transmission, are similar to images obtained by a TEM with a scanning attachment. The Transmission Electron Microscopy (TEM) specimens are mounted on a carrousel type TEM grid holder, which can hold up to 6 specimens.

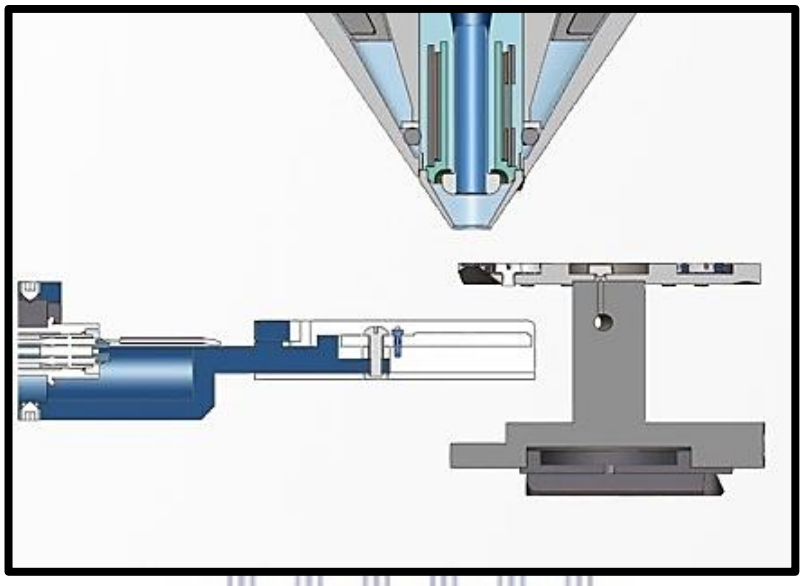

Figure 2.45: aSTEM detector below the STEM lamella sample holder/grid.

Figure 2.46 indicated the dark field and bright field STEM detectors and the corresponding imaging outputs of Au nanoparticles on silicon. The detectors detect transmitted electrons which means the sample need to be ultra-thin (<100 nm) to allow the electron beam to be transmitted. The increased detector area allows larger acceptance angles. The Gemini multi-mode STEM detection system comprises two parallel long-life diode-detector surfaces. The top detector (DF) has been divided into specific areas to allow orientated DF imaging and forms the aperture for the BF signals which are detector by the lower BF detector. Bright field (BF) and dark field (DF) signals can be clearly separated.

STEM detector with a large inner radius, a HAADF detector, electrons are collected which are not Bragg scattered. As such HAADF images show little or no diffraction effects, and their intensity is approximately proportional to Z^2. This imaging technique proves ideal for tomographic reconstruction as it generates sharp contrast that has a fully monotonic relationship with thickness. An annular dark field image formed only by very high angle, incoherently scattered electrons - as opposed to Bragg scattered electrons is highly sensitive to variations in the atomic number of atoms in the sample (Z-contrast images).

Furthermore, investigations at high primary energies cause low aberrations, resulting in highest resolution images. By collecting only Rutherford scattered electrons, the HAADF detector produces an image which (ideally) gives intensity: $I \propto tZ^2$, where t is thickness of the sample and Z is the average atomic number.

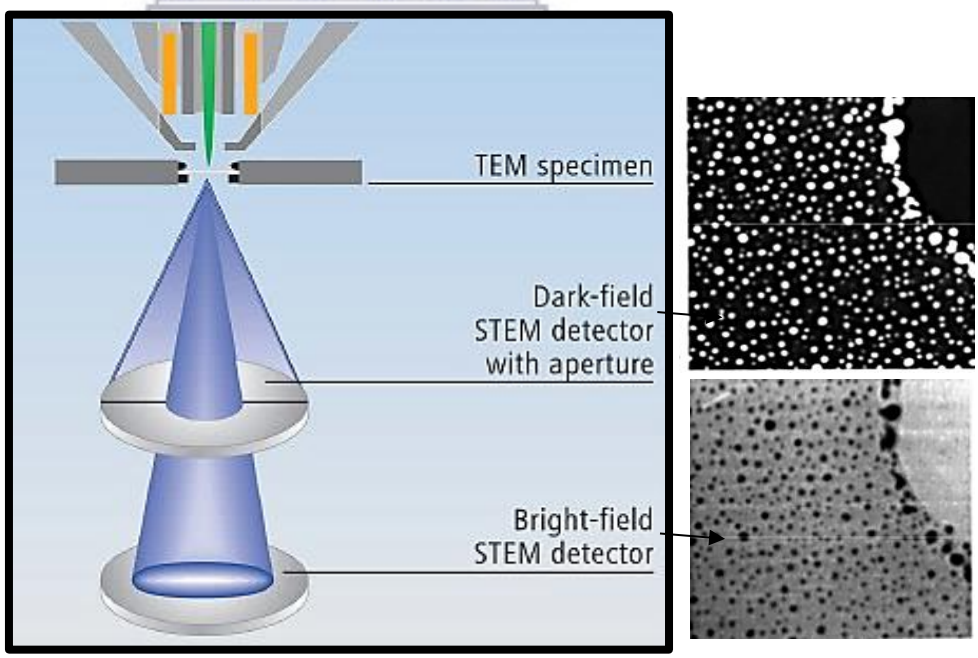

Figure 2.46: Dark-field and bright field STEM detectors and the corresponding imaging outputs of Au nanoparticles on silicon.

2.2.6 High-resolution transmitted electron microscopy (HRTEM) system

High-resolution (HR) TEM has the same principle as the TEM but with the improved imaging resolution. The sample information detection imaging requires very thin sample as in TEM, which depends on their properties, which can weakly modify the phase of the electron wave, while the amplitude remains constant. The unique part of the HRTEM is the crystallographic analysis, to determine the orientation of crystals or phases and analysis of interfaces, twinning and certain crystalline defects using the diffraction patterns. The HRTEM used for this experiment it was the FEI TECNAI F20.

2.2.6.1 HRTEM imaging

Figure 2.47 illustrates a schematic diagram of the conventional TEM and the beam interaction signals with the sample. The TEM column consists of a condenser system, objective lenses, projection system and detectors. The condenser system consists mainly of two or more electromagnetic lenses and an aperture. These lenses are used to control beam spot size and convergence to form an electron beam of the desired intensity, size and convergence angle at the specimen. By inserting a condenser aperture, only the electrons of a path close to the optic axes can pass through the aperture disc (around 40−160 mm radius). The sample is placed in a dedicated TEM holder that can be inserted in the TEM vacuum chamber allowing the beam to interact with the specimen [2.24]. The achievable image contrast mainly depends on the structure, thickness and elemental composition of the specimen as well as the chosen imaging parameters.

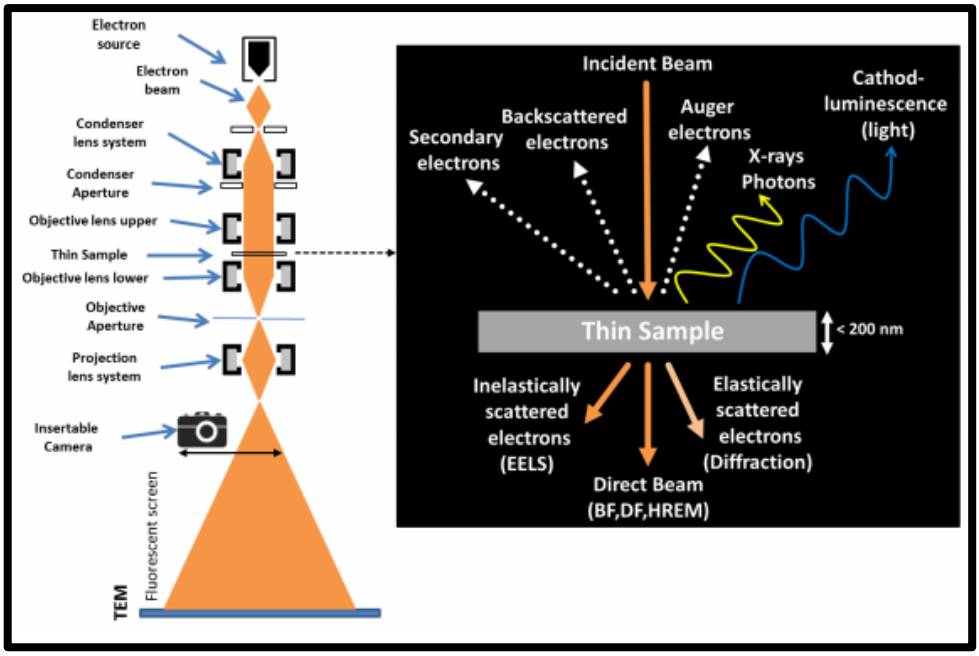

Figure 2.47: Schematic diagram of the TEM with the beam interaction signals from the sample.

Figure 2.48 shows the comparison of the bright field TEM, dark field TEM and HAADF – STEM. Conventional TEM imaging can be categorized as either amplitude contrast or phase contrast, depending on the size of the objective aperture, and amplitude contrast can be further categorized as due to mass-thickness contrast or diffraction contrast. Amplitude contrast is prevalent in bright-field (BF) or dark-field (DF) imaging, where electrons in the transmitted beam or a Bragg diffracted beam are collected using a small objective aperture. Mass-thickness contrast originates from the incoherent elastic scattering (Rutherford scattering), and the scattering cross-section is related to the average atomic number Z and the thickness of the specimen. The transmission electron microscopes (TEMs) can investigate the crystal structure on the atomic level (advancing into the sub-Ångström (Å) resolution regime) [2.25].

The principle of TEM is when an electron-transparent specimen is illuminated by a plane electron wave, whose phase and amplitude is altered upon propagation through the object, where the lens aberrations of the imaging lens system play a key role. The lenses provide a wide range of different imaging modes with the ability to provide information on elemental composition and electronic structure that of a single atom. The convergent beam electron diffraction provides information on crystal structure and crystallography. The interaction between the electron beam and the sample includes elastic and inelastic scattering.

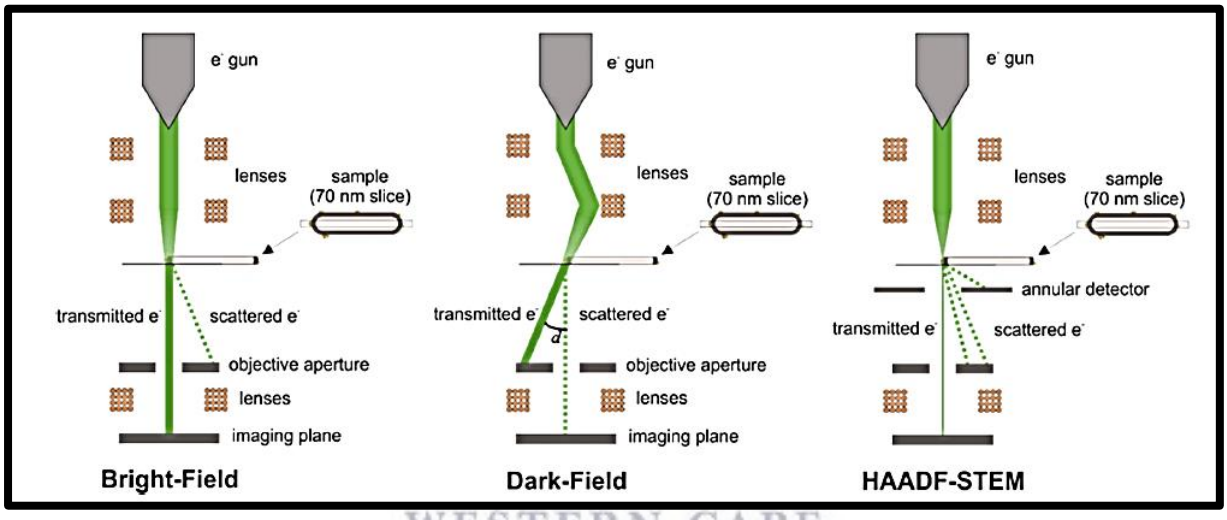

Figure 2.48: Comparison of the bright field TEM, dark field TEM and HAADF-STEM.

2.2.6.2 Elastic scattering

The elastically scattered electrons, only the directions are changed, providing information of images, diffraction patterns. This scattering is elastic, as the scattered electron conserves, almost all its kinetic energy. The elastic scattering process is called Rutherford scattering and is employed in STEM (Z number contrast imaging). The mass thickness contrast, regions in the sample with heavy atoms appear with darker contrast in the projected image than such with light atoms (mass/thickness

contrast). This is due to the stronger interaction between electrons and heavy atoms (with high charge Q2) compared to light atoms.

2.2.6.3 Inelastic scattering

The electrons of the high energy incident beam can transfer a significant amount of energy to an inner shell electron of an atom (ionization), causing the ejection of this electron and filling up the empty place by an electron with higher energy from an outer shell. The inelastically scattered electrons, both the direction and energy are changed, scattered electrons contribute to the EELS and EDS This process also causes the emission of characteristic Auger electrons or X - rays. The incident electron is scattered inelastically and loses a certain amount of energy (ionization energy).

2.2.6.4 Energy-dispersive x-ray spectroscopy (EDXS)

Figure 2.49 shows the Bohr's atomic model representation and electronic transitions generating the x-ray radiation where the electron from the beam is ejected (green wave). X-ray spectroscopy is a technique for qualitative and quantitative element analysis in mapping out elemental spatial distributions. Each element has characteristic peak positions corresponding to the possible transitions in its electron shell.

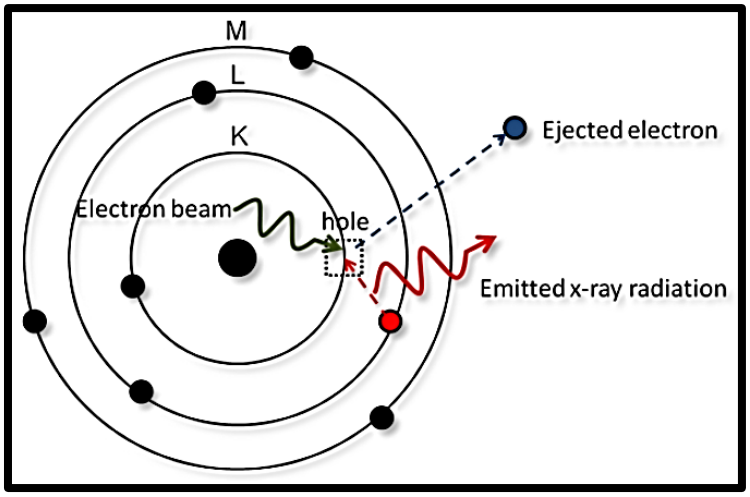

Figure 2.49: Representation of the Bohr's atomic model and electronic transitions generating the x-ray radiation.

Figure 2.50 shows the a) TEM and (d) EDS analysis of the CuO/Cu 2 O-GPC electrode material in the area [(e) HAADF, (f) C, (g) Cu, and (h) O] elemental mapping images of the CuO/Cu 2 O-GPC electrode material [2.26]. In energy-dispersive X-ray spectroscopy (EDX), the electron beam is scanned across the sample and the X-rays that are generated in the process are analysed with an energy spectrometer. The X-ray count from a specific element can then be plotted out and a line distribution for that element is generated. For example, the presence of copper, can be indicated by two K peaks at about 8.0 and 8.9 keV and a L peak at 0.85 eV. In heavy elements like tungsten, a lot of different transitions are possible, and many peaks are therefore present. TEMs are almost exclusively equipped with energy-dispersive spectrometers (energy-dispersive X-ray spectroscopy EDXS). EDS measures the energy and intensity distribution of X-rays generated by the impact of the electron beam on the surface of the sample. Despite the poor resolution, the technique is nonetheless very useful in identifying trends and correlating those to the other imaging techniques.

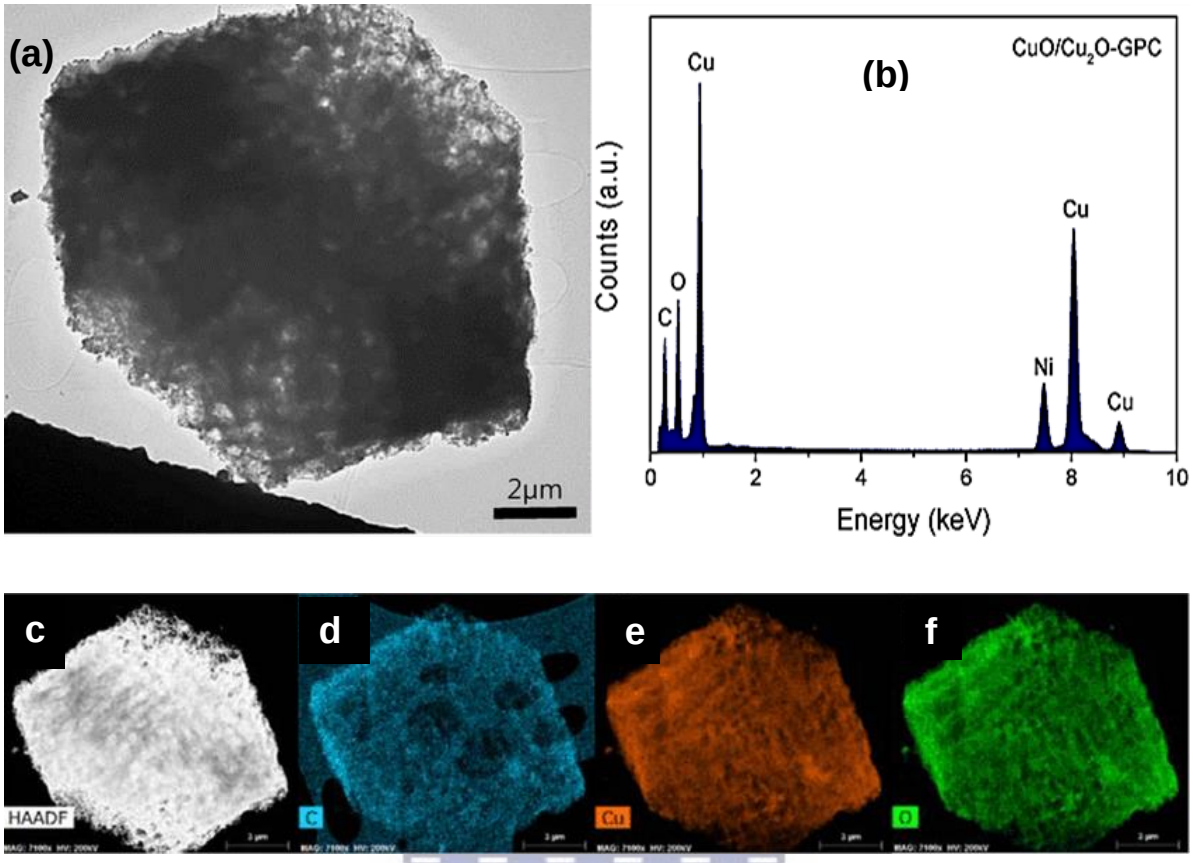

Figure 2.50: (a) TEM and (b) EDS analysis of the CuO/Cu 2 O-GPC electrode material in the area [(c) HAADF,(d) C,(e) O] elemental mapping images of the CuO/Cu 2 2 O-GPC electrode material [2.26]

2.2.6.5 Diffraction analysis

Figure 2.51 indicates the comparison of the lens conditions between TEM diffraction and TEM imaging modes.

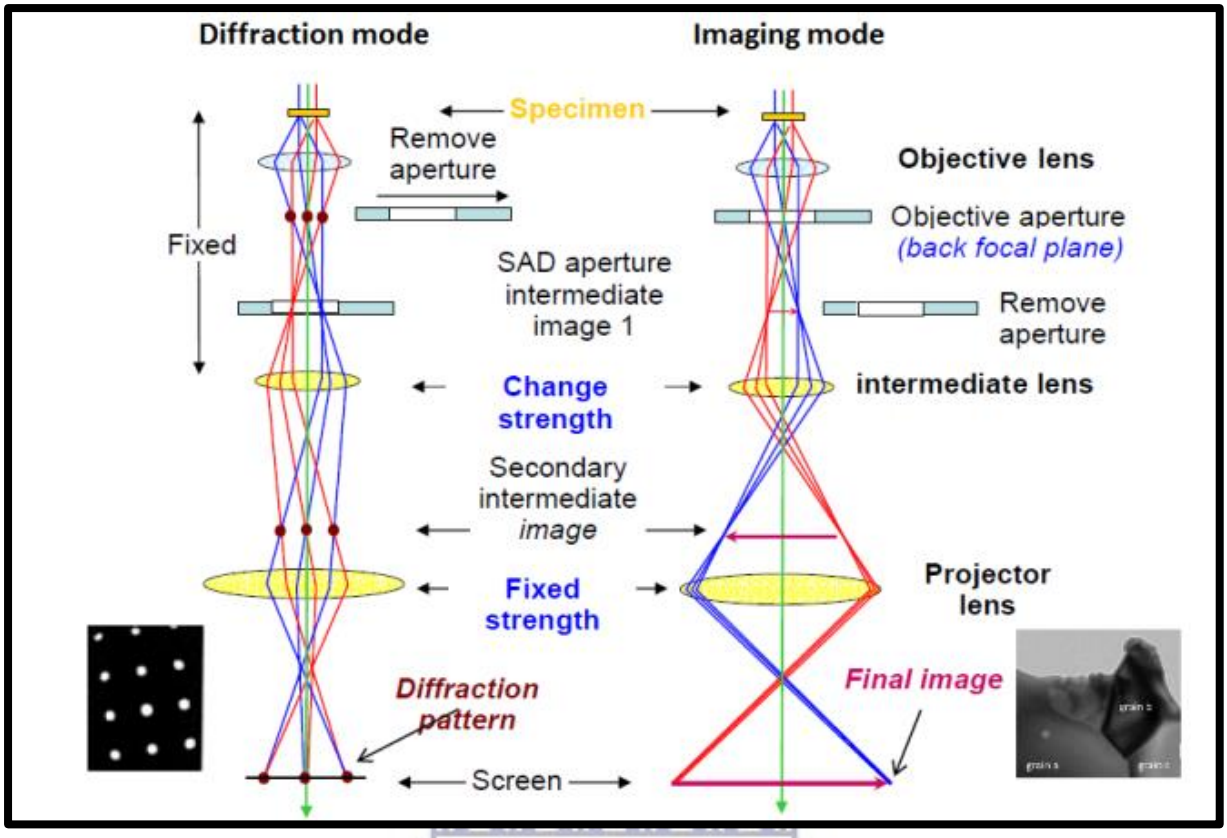

Figure 2.51: Comparison of the lens conditions between TEM diffraction and TEM imaging modes [2.27.]

2.2.6.6 Bragg scattering

As the electrons are transmitted through the sample, each atom in a regular crystal lattice acts as a scattering point. The scattered electron waves may interact with each other either forming constructive or destructive interference, which gives rise to a diffraction pattern (Bragg diffractions). This is formed by phase difference caused by scattering at atomic planes with inter-planar spacing d and can be explained using Bragg's Law:

$$n\lambda = 2d\sin\theta \qquad (2.3)$$

where λ is the wavelength of the incident electron beam, n is an integer, angles of incidence. The path difference (2d sin θ) is equal to an integer multiple n of the wavelength, then rays will be scattered and arrive at point in the same phase (i.e. constructive interference). This will result in a diffraction patterns in the back focal plane of the objective lens. Figure 2.52 shows a schematic picture of the Bragg diffraction. Two monochromatic beams approach a crystalline solid and are scattered off two different atoms. The path difference between the incident and the reflected rays is 2d sin θ [2.29].

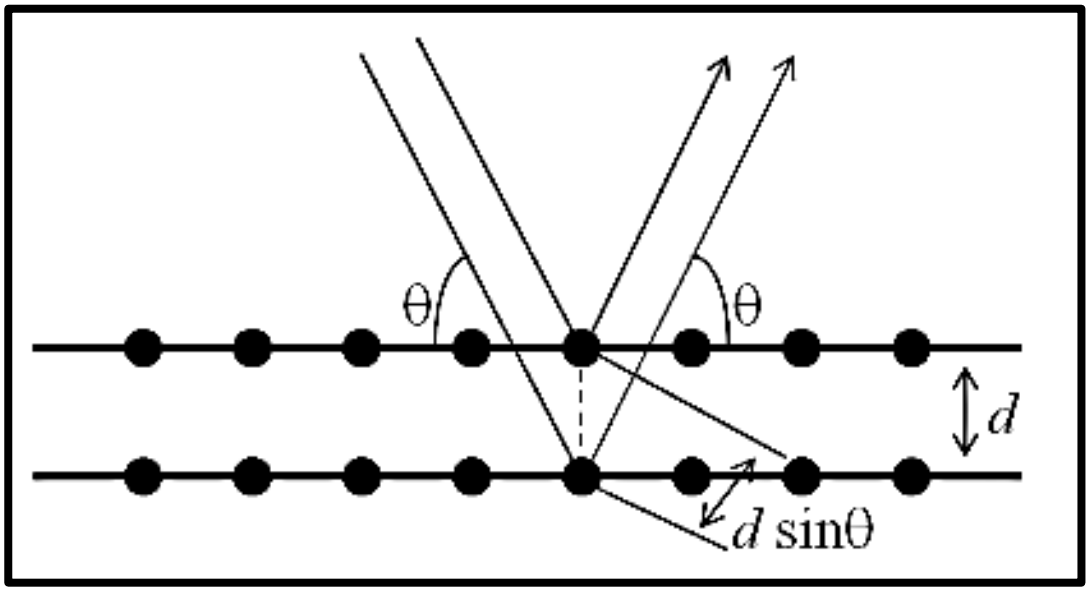

Figure 2.52: Schematic presentation of the Bragg diffraction. Two monochromatic beams approach a crystalline solid and scattered off two different atoms. The path difference between the incident and the reflected rays is 2dsin θ [2.29].

If the attention is focused on the lattice, the diffraction condition can be described by Bragg's law. Bragg's law is defined as the relation between an integer n, the wavelength of the X-ray, λ, the angle of incidence of the X-ray, θ, and the spacing between atomic layers, d(hkl). At certain angles, Bragg's law conditions (equation

2.2) are satisfied and constructive interferences increase the intensity of the signal collected by the detector. In transmission electron microscopy, because the wavelength of electrons is very small (~2×10^{-3} nm) and the Bragg angles are quite small (≈10^{-3} mrad). The Bragg's law can be approximated by the HRTEM imaging configuration, the atomic planes are oriented parallel to the incident electron beam in the microscope. This orientation produces a strong transmitted beam and a multitude of diffracted beams from the different sets of atomic planes that are parallel to the incident beam.

In electron microscopy, the high electron energy results in a very short wavelength of the electrons, the diffraction results even from atomic planes that are not oriented at a Bragg angle to the incident beam.

Figure 2.53 indicates the TEM and HRTEM images of the CuO/Cu 2 O-GPC electrode material in the area. This allows reconstructions of the crystal lattice to be obtained almost instantaneously and from a single sample orientation. The multitude of beams diffracted from the planes parallel to the incident beam are collected with a large objective aperture (OA) in the microscope and it is the interference of these beams that generates an image which is essentially a reconstruction of the crystal lattice. The resulting diffractogram is created by plotting the intensity of the diffraction peak against the value of 2θ. X-ray powder diffraction was used to characterize synthesized compounds and to obtain structural information from the heterostructures. The peaks on a diffractogram are indexed by comparing no similar structure. Lattice parameters are determined using Bragg’s law to calculate d(hkl) and the Miller indices corresponding to each peak for a given space group.

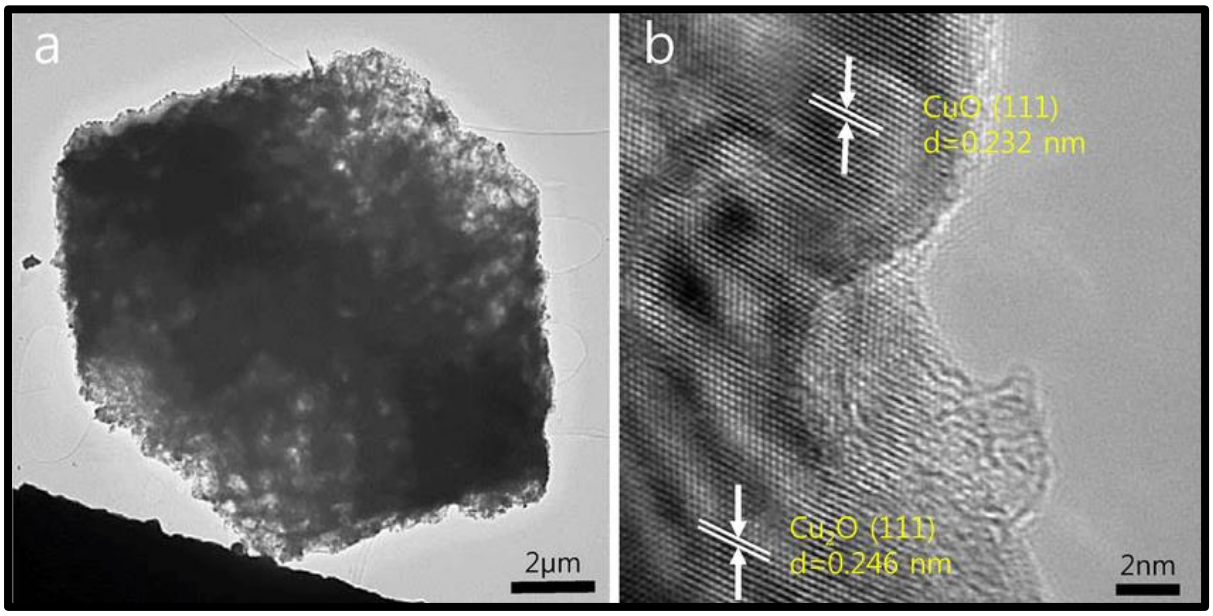

Figure 2.53: (a) TEM and (b) HRTEM images of the CuO/Cu 2 O-GPC electrode material in the arear [2.26].

2.2.7 Selected Area Electron Diffraction (SAED)

Figure 2.54 indicates the corresponding SAED pattern analysis of the CuO/Cu 2 O-GPC electrode material in the area. SAED focuses on extracting diffraction patterns from regions of the specimen of about 10 nm or less in diameter. where it views and record the electron diffraction pattern from a selected area of the specimen.

SAED pattern is obtained by illuminating which is partially blocked by a strip of metal with a hole; letting through only a fraction of the beam that interact with the sample the oriented specimen with a nearly parallel beam, and coherent elastic Bragg diffraction by the sample resulting in formation of a pattern of sharply focused spots; the diameter of the spots is determined by the incident beam divergence. The primary purpose of electron diffraction techniques is to identify the unit cell, or the crystal structure, of the materials under investigation, or to orient the crystal in each zone. At higher scattering angles, higher order Laue circles can be observed. In the

thicker regions of the specimen, Kikuchi lines will be well defined. These diffraction details reveal additional three-dimensional crystallographic and symmetry information about materials.

As the electron beam is directed to the sample in the TEM. According to Bragg's law, part of the electrons will be scattered to specific angles, dictated by the crystal structure of the sample. The scattered electrons form an image on the charge coupled device (CCD) detector. If the sample is crystalline, a series of spots will appear. If the beam goes through a layer of randomly oriented crystals, the multiple spots are combined on the image and appear as well-defined rings. In the case of an amorphous material, the rings appear very diffuse. Unlike powder X-ray diffraction, SAED allows measurement of areas smaller than a micron, whereas XRD typically collects diffraction patterns from areas of several square centimetres.

The obtained diffractogram is an image of the diffraction peaks or rings with the transmitted beam spot at its centre. To interpret the data, Bragg's law is applied in a very comparable manner to X-ray diffraction. The identification of the diffraction spots or rings, their positions from the centre will give the value of d.

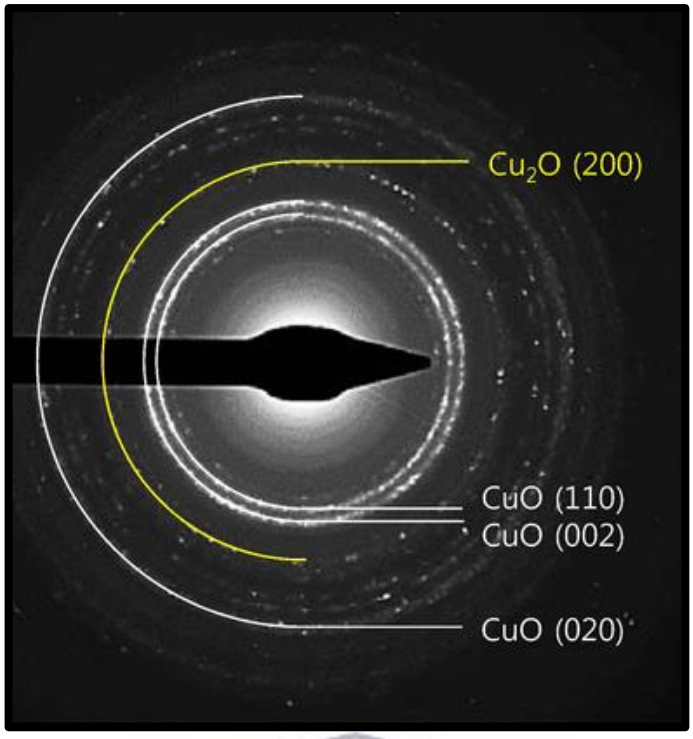

Figure 2.54: Corresponding SAED pattern analysis of the CuO/Cu 2 O-GPC electrode material in the area [2.26].

2.3 Surface analysis

Surface analysis is the term used to investigate of the surface phenomenon to understand the properties and reactivity of the surface of a material. The choice of a surface analysis technique depends on the nature of required information, the type of surface, and the resolution. Most of the surface analysis techniques are carried out in vacuum because particles are scattered by the molecules in the ambient gas and thus interfere with the analysis. Even photon-based techniques require vacuum since gas-phase absorption of photons can occur with the ambient molecules.

Micro analytical techniques require a high efficiency to conclude physical and chemical properties from a small sample volume. The elemental composition is ideally derived by identifying all atoms of a sample and counting them. Mass spectrometry follows this concept by disintegrating sample material into ionized atoms and separating them according to their mass (and charge).

The surface analysis technique used in this project was X-ray Photoelectron Spectroscopy (XPS) also known as Electron Spectroscopy for Chemical Analysis (ESCA). Basic XPS provides qualitative and quantitative information on almost all elements present.

2.3.1 Photoelectron Spectroscopy (PES)

Photoelectron spectroscopy (PES) is a method where the molecule is ionized by irradiating it with such photons that an electron is released. The weakly bound valence electrons can be released when using moderate photon energies. The harder rays in the X-ray region will also release electrons from the innermost core orbitals. When UV light is used the method is called UV photoelectron spectroscopy (UPS) and when X-rays are used it is called X-ray photoelectron spectroscopy XPS or ESCA (Electron Spectroscopy for Chemical Analysis).

2.3.2 Auger Spectroscopy

Ionization in one of the innermost core molecular orbitals results in a very highly excited ion. In the Auger process the hole in the core orbital is filled by dropping down a valence electron. This creates a new hole in the valence shell. At the same time, a large amount of energy is released because the energy of the core orbital is much lower than that of the donating valence orbital. This energy is used to release another valence electron [2.28].

2.4 X-ray photoelectron spectroscopy (XPS) system

X-ray photoelectron spectroscopy (XPS) is surface sensitive method which is widely used as a quantitative spectroscopic technique to determine elemental compositions, chemical and electronic states of the elements the surface of a solid sample [2.29]. XPS can estimate the chemical composition and chemical state of elements together with depth profile; it becomes an important method for microelectronics, metallurgy, heterogeneous catalysis, polymer technology and corrosion science [2.30].

2.4.1 XPS principles

Figure 2.55 illustrates a schematic drawing of a typical XPS setup with photon source (X-rays, UV-light, laser or Synchrotron radiation), a sample manipulation with different linear and rotational degrees of freedom, electron optics, an energy dispersive analyser and a detector. XP spectra (intensity vs. binding energy) are shown for four different metals with their element specific distribution of core level photoemission. The x-ray interaction with the sample can be observed through the binding and kinetic energy of the sample atoms. Binding energy is the energy with

which an orbital electron is bound to the nucleus of the atom. The closer the electron is to the nucleus, the more tightly the electron is bound to the nucleus. Binding energy varies with the type of atom as well as the number of other atoms bound to that atom. Since different isotopes of an element have the same nuclear charge, the isotopes do not affect the binding energy. Any variations of the binding energy are associated with the covalent or ionic bonds between atoms. [2.33]

XPS-technique understands that the binding energy of a photoelectron is sensitive to the chemical surrounding of the atom, i.e. there is a chemical shift in the binding energy. These shifts are crucial because they provide a tool to identify individual chemical states of an element [2.34]. The excitation process is known as the photoelectric effect.

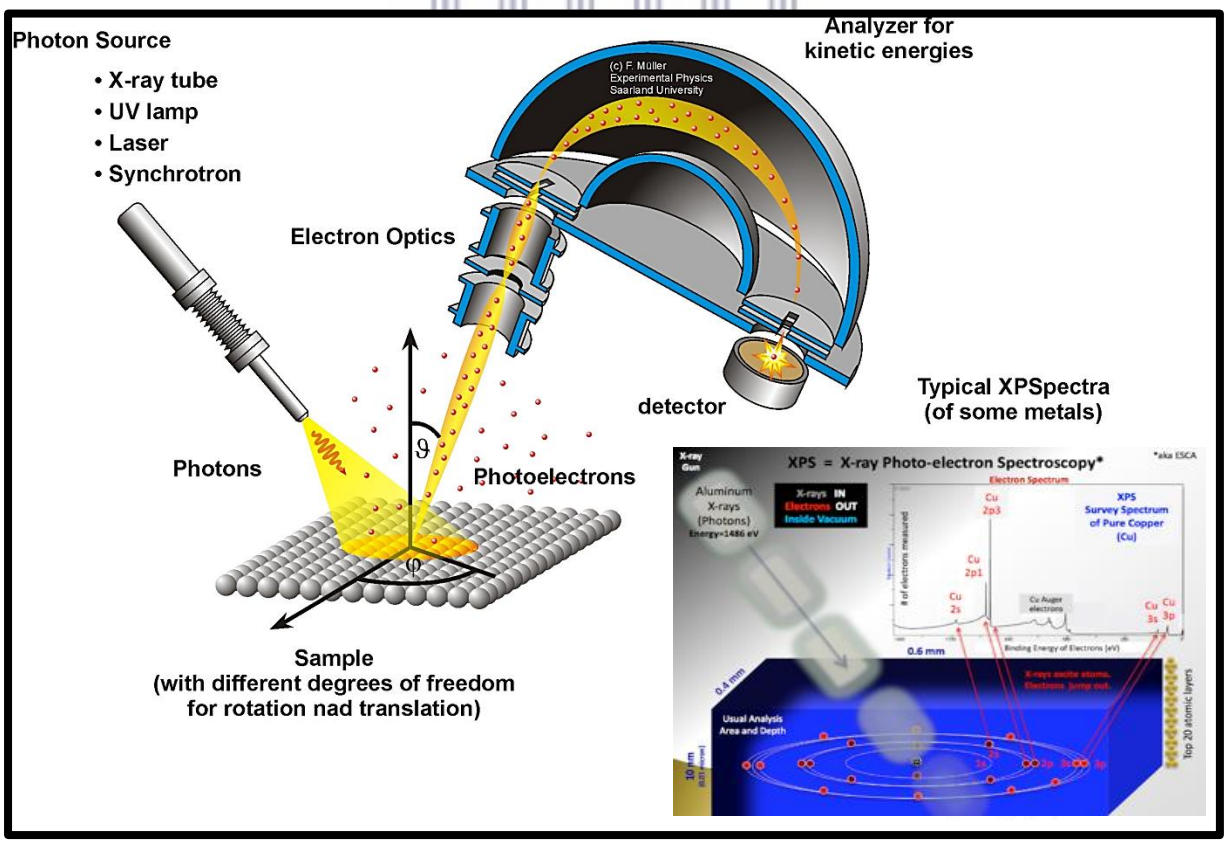

Figure 2.55: Schematic presentation of a typical XPS setup with photon source (X-rays, UV-light, laser or synchrotron radiation), a sample manipulation with different linear and rotational degrees of freedom, electron optics, an energy dispersive analyser and a detector. XP spectra (intensity versus binding energy) are shown for four different metals with their element's specific distribution of core photoemission [2.31, 2.33]

Figure 2.56 illustrated schematic presentation x-ray beam and electrons penetration depth. In principle, XPS spectra are obtained by irradiating a sample surface at with mono-energetic x-rays, and usually Mg Ka (1253.6 eV) or Al Ka (1486.6 eV) x-rays. The x-ray beam can penetrate up to 2-10 nm, but the electrons can be excited at the depth of ~1 µm and emitted at an area of ~1 × 1 µm (as illustrated in figure 2.57). The X-ray photon transfers its energy to a core-level electron. If this energy is larger than the energy which binds the electron to the atom, the electron will leave the atom. If the incident photon is of sufficiently high frequency υ, electrons are emitted from the atom with a specific kinetic energy [2.35]. According to the law of energy conservation, the emitted electrons have a certain kinetic energy which can be determined via the following equation:

$$KE = hv - BE - \Phi_s \qquad (2.4)$$

where hυ represents the energy of the absorbed photon and ϕ_s, where, s spectrometer is the work function of the spectrometer. The differences in chemical elements within the near surface region are identified based on their binding energy (BE), which is measured relative to the fermi level (EFermi) of the individual atoms. The KE and BE of the photoelectron are related via equation 2.3.

The energy of the photons and the spectrometer work function are known quantities, the measurement the electron binding energies can be obtained by measuring the kinetic energies of the photoelectrons. The emission of x-ray photons is low in the energy range used in XPS; photo ionisation normally leads to two emitted electrons: a photoelectron and an Auger electron [2.37]. In general, X-rays having energies in the 1-2 keV range will penetrate several hundred nm into a surface ionizing atom to that depth. For the resultant photoelectrons to be detected they first must escape from the surface without interacting with overlaying atoms; which may lead to loss of KE (inelastic scattering). The inelastic mean free path, λi is proportional to inelastic mean free path of an electron of intensity, I_o emitted at a depth, d below. According to the Beer-Lambert law the intensity, I_d of the same electron as it reaches the surface is sampling depth as indicated in equation 2.4. The sampling depth is from which 95 % of all photoelectrons are scattered.

$$I_D = I_O - e^{\frac{-d}{\lambda}} \qquad (2.4)$$

The XPS results are typically presented on a graph on which the electron counts measured are plotted as a function of binding energy. Thus, the XPS spectrum of a material consists of peaks which are associated with various elements. XPS analyses are typically performed by first taking a wide-spectrum scan covering more than 1000 eV, then performing a high-resolution scan over smaller ranges of around 20eV at the peaks in the wide-spectrum scan. The area under these peaks is related to the amount of each element present.

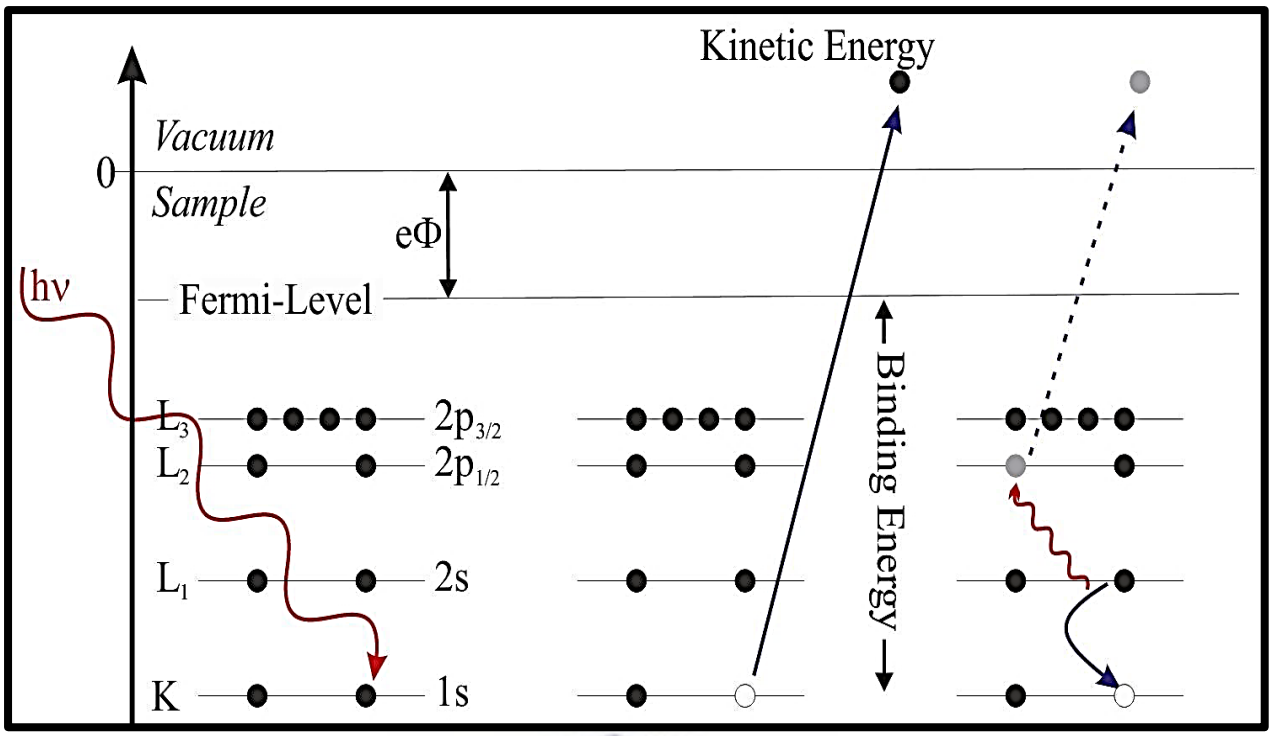

Figure 2.56: Schematic presentation of the photoelectric effect [2.35].

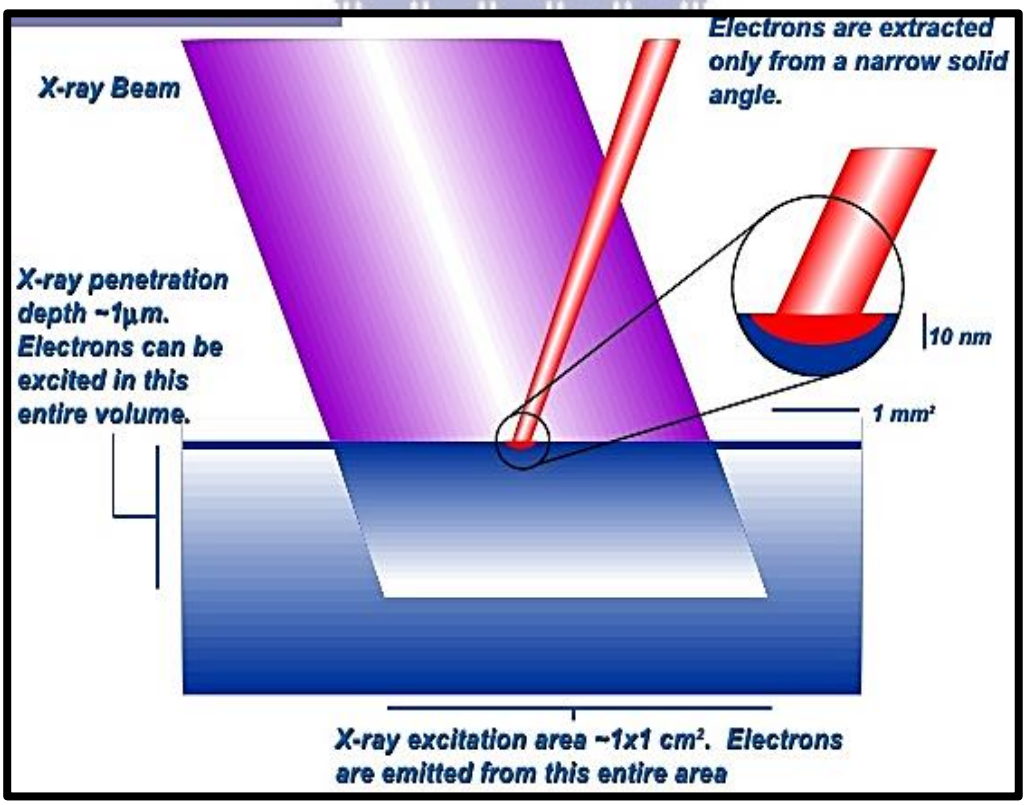

Figure 2.57: Schematic presentation of x-ray beam and electron penetration depth.

2.4.2 Depth of analysis

The depth analysis is widely used technique to determine the sequence and thickness of the multi layered structure such as a substrate coated with different metal, organic or inorganic material thin films. The XPS can also determine the depth distributions of elements and chemical compounds. The XPS has two ways to determine the depth profile of a sample. The XPS depth profile can be done destructively or non-destructive way.

a) Destructive depth profile

Figure 2.40 shows the sputtering view in a vacuum chamber and schematic principle of the Ar+ ion interaction with the sample. Depth profiling with Argon Ion Etching, e.g. a destructive XPS ion-sputter depth profiling technique, uses an ion beam of an inert gas such as argon to ablate the sample surface, and then chemical composition of the exposed sub-surface layer is determined by XPS analysis.

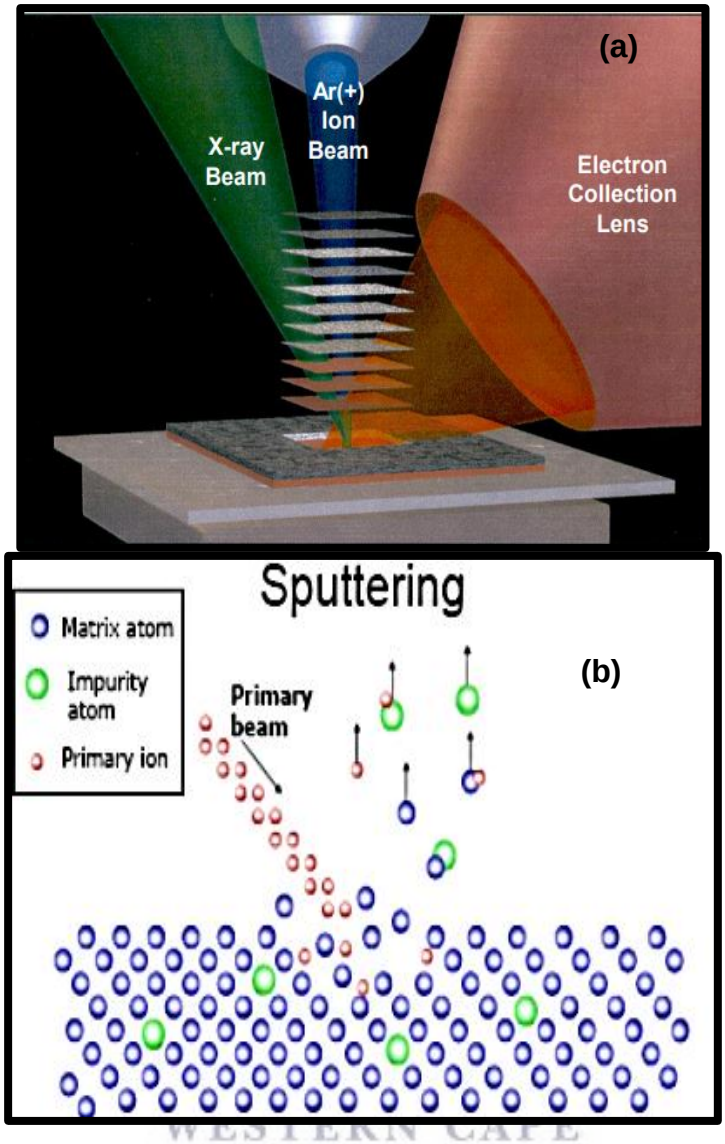

Figure 2.58: Sputtering view in a vacuum chamber and principle of the Ar+ ion interaction with the sample.

Figure 2.59 illustrate the steps for acquiring the sputter profile with the high-resolution spectra.

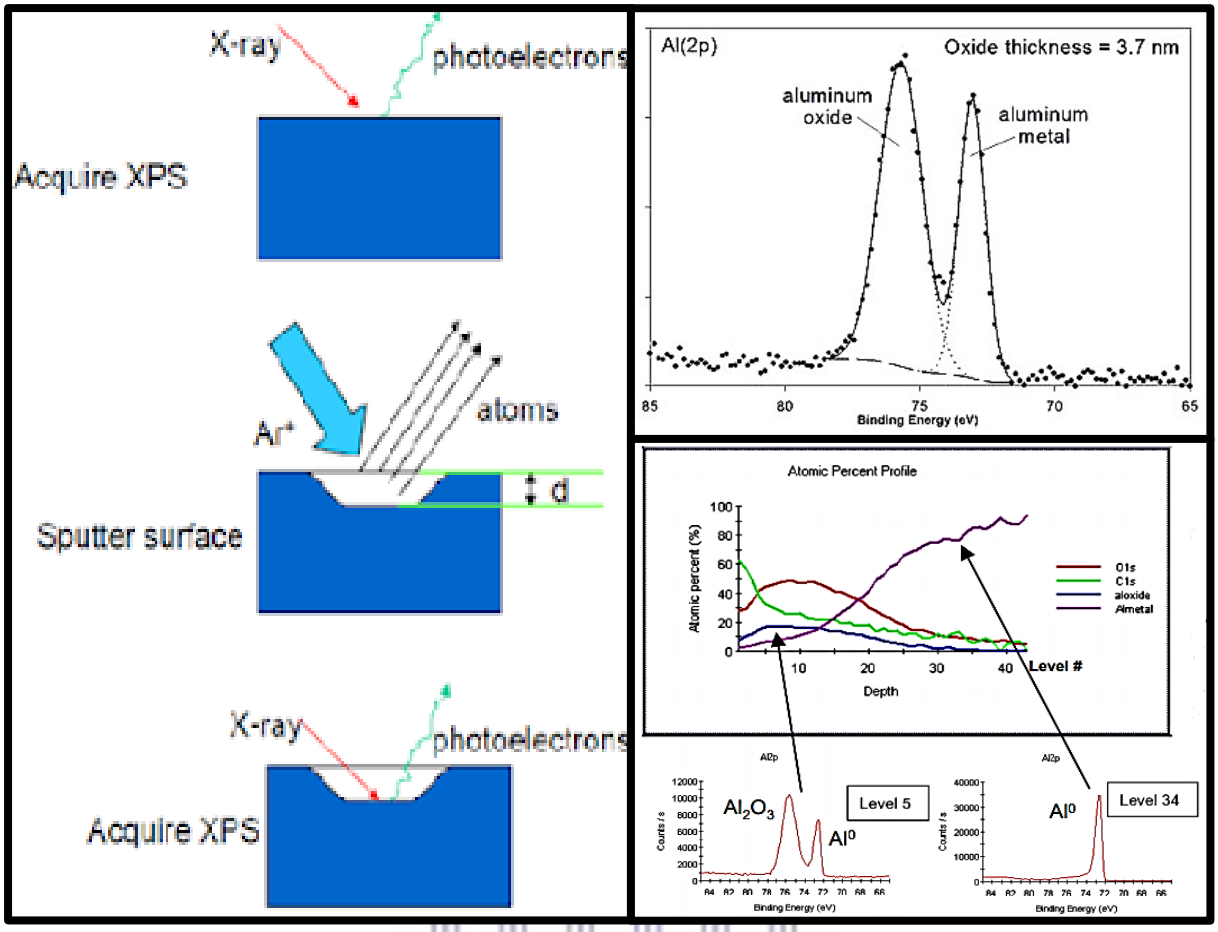

Figure 2.59: Steps for acquiring the sputter profile with the high-resolution spectra.

b) Non-destructive

Figure 2.60 shows an illustration of the analysis of a thin metal oxide on a metal. The diagrammatic spectra show the effect of the collection angle on the elemental and oxide peaks of the metal. Angle-resolved (or angle-dependent) XPS (ARXPS) is a variation of the ordinary XPS method developed to enhance its surface sensitivity. This method is non-destructive and often used to investigate compositional variations of the outermost layers of the solid and to assume a possible model of depth profile. By tilting the specimen away or towards the analyser, the signal can be made sensitive to the outermost layers.

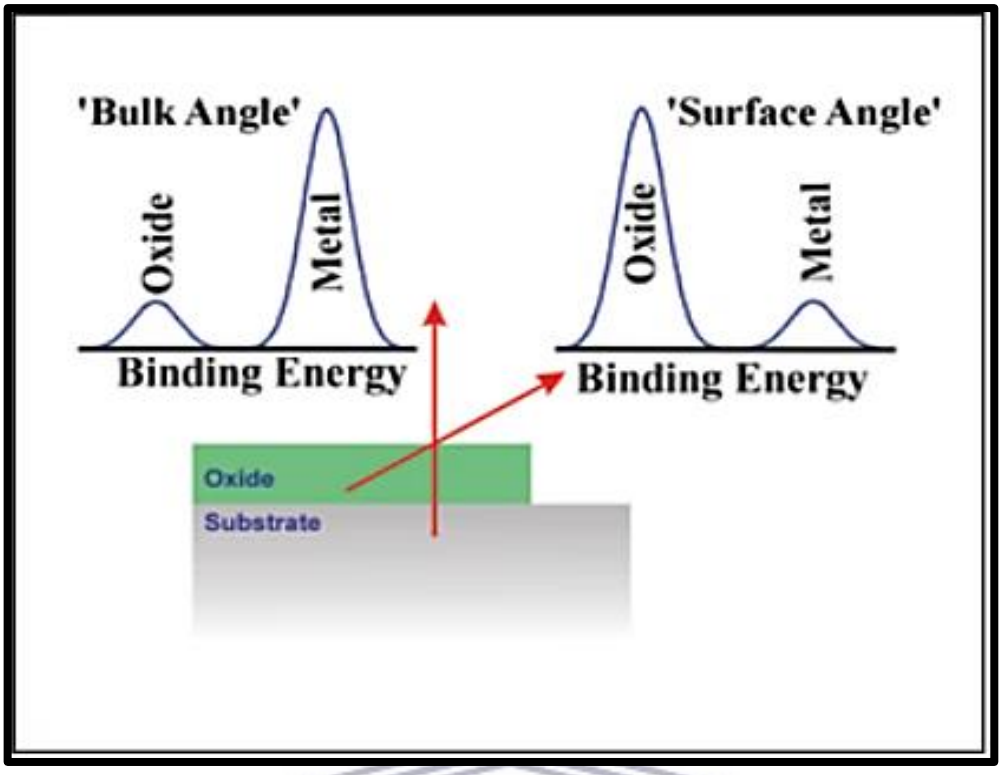

Figure 2.60: An illustration of the analysis of a thin metal oxide on a metal.

Figure 2.61 shows the surface sensitivity enhanced by variation of the electron take-off angle. According to theoretical basis of experimental techniques, by changing of the angle θ between the analysers and the surface is called an emission angle of the photoelectrons and the angle α between the analyser and the sample surface, this angle is called the take-off angle of the photoelectrons. To decrease the depth of analysis the take-off angle α should be decreased (θ in this case increases) (Figure. 2.4) as the averaged sampling depth depends on the sine of α (cosine of θ) (equation 2.4).

$$d_{\mathrm{av}} = d\sin\alpha = d\cos\theta \qquad (2.5)$$

The averaged sampling depth d_{av} is given by (equation 2.4) and is a maximum $d_{av}=d$ in the vertical direction when take-off angle α equals 90° (θ is correspondingly equal

to zero). Surface sensitivity is enhanced by variation of the electron take-off angle. In most commercial spectrometers (as well as in one used in this work) the angle between the incident X-rays and the direction of detection δ is fixed. This means that the asymmetry term L(δ) (cf. (E.)) which describes the anisotropy of photoemission takes on a constant value while the sample is tilted [2.38]

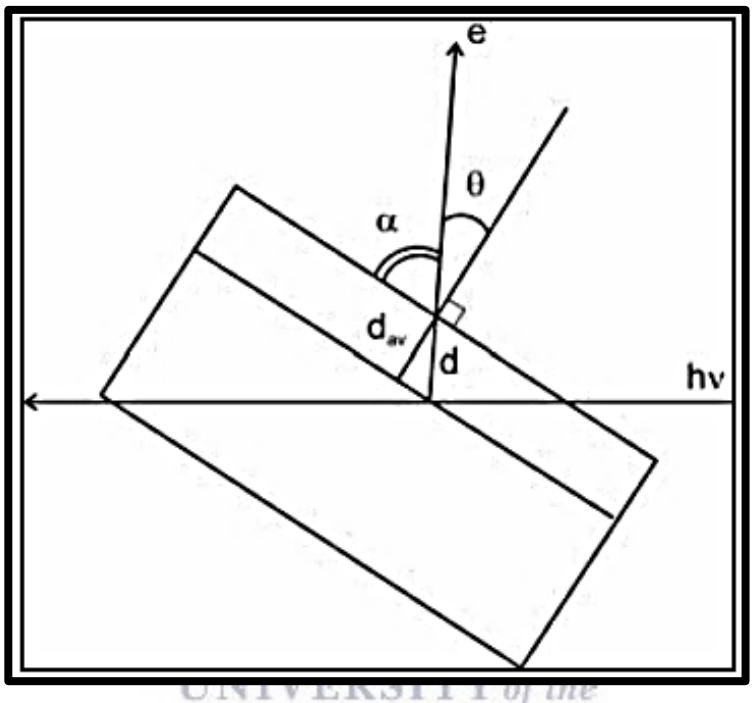

Figure 2.61: Surface sensitivity enhanced by variation of the electron take-off angle.

2.4.3 Instrumentation

This section will review the primary features and capabilities of the Thermo Scientific ESCALAB 250Xi XPS instrument as shown in figure 2.44. The ESCALB 250XI system contains the EX05 ion gun which can produce the sample current of more than 3 µA and for the depth profiling is of 1 µA. the energy of the ion beam which controls the momentum of the argon ions (Ar+) as they hit the sample (direct proportionality), a beam of 4 kV can damage the sample and 1kv is for gentle etching mostly when analysing thin samples.

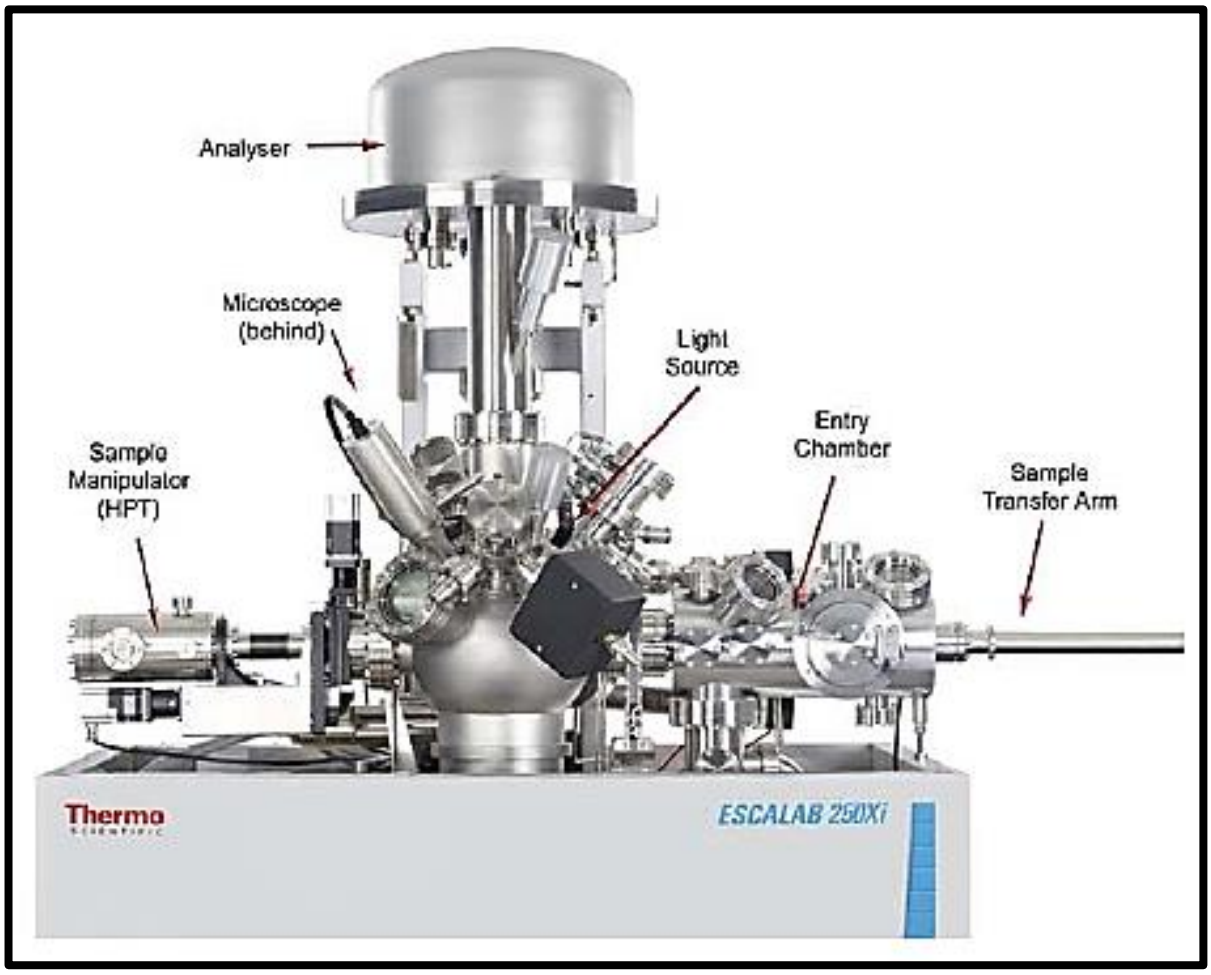

Figure 2.62: Thermo scientific ESCALAB 250Xi XPS instruments.

a) Vacuum system

Figure 2.63 presents the vacuum chamber of the XPS. X-ray photoelectron spectroscopy is a highly surface sensitive technique which allows the operator to analyse precisely the top-most atomic layer of the sample. The ultra-high vacuum (UHV) system is used to ensure that the surface of the sample is clean and is not contaminated during the analysis process. The importance of the UHV can be further be observed when the ejected photoelectron interacts with the gas molecules as it is transferred through the column. The UHV system should be of a pressure of 10^{-6} mbar, to accommodate the transfer of the photoelectron and reduce the contamination level on the sample surface during long periods of analysis.

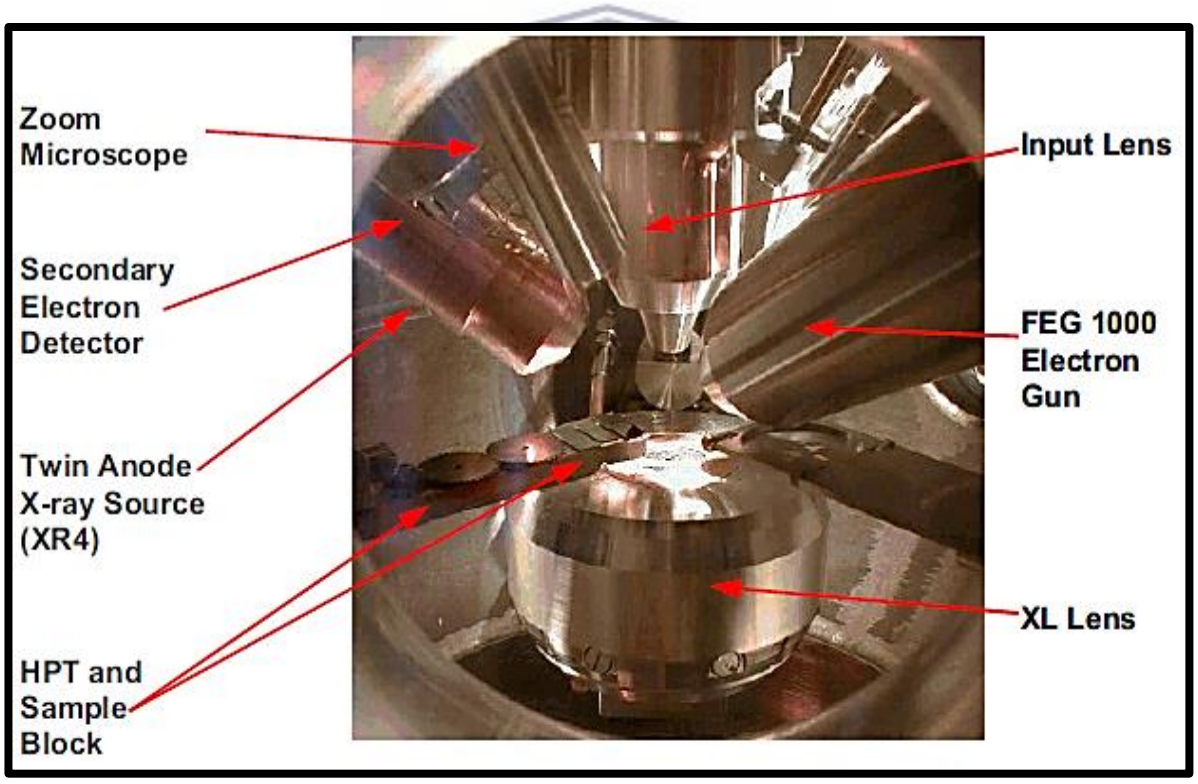

Figure 2.63: Vacuum chamber.

b) Photon source

Figure 2.46 shows a major mechanical component of the monochromator system. The ideal choice of the x-ray source depends on the (1) line width to not limit the energy resolution required and (2) the characteristics x-rays must be high enough that a sufficient range of core electrons can be photo ejected for an unambiguous analysis. The XPS chemical information is extracted by detailed analysis of individual elemental spectra, including resolution of contributions from the various chemical states present. The best energy resolution should be compatible with the signal-to-noise ratio in the specific spectrum. The materials used to get best resolution by the line width used for the analysis should be in general analytical works of the order of 1.0 eV.

The ESCALB 250Xi uses the XR6 gun as a source of monochromator x-ray beam for production of Al Kα x-rays. It consists of an electron-bombarding heated emitter (cathode), a control electrode, an electro static lens and water-cooled aluminium anode. The XR6 operates over a power range of <50 W to 300 W corresponding to a spot size on the anode in the range of ~ 200 µm to ~ 1 µm.

In principle, the x-rays are produced with a well-defined energy resolution and are focused onto the sample to give a spatially defined area of analysis. The XR6 electron gun provides a high-power source of focused electrons at energies of up to 15 kV. The electrons impact the anode, where a thin film coating of aluminium in water – cooled base to produce x-rays at energy of around 1486.6 eV.

The x-rays are then diffracted by pair of quartz crystals which are arranged such that the angles between the crystal lattice and the x-rays are of the Bragg angle. The diffracted x-rays are thus monochromated to give a pure Al Kα beam (of lower

energy spread). The crystals are also shaped and positioned so that the x-rays are focused into a well-defined spot on the sample surface at the analysis position.

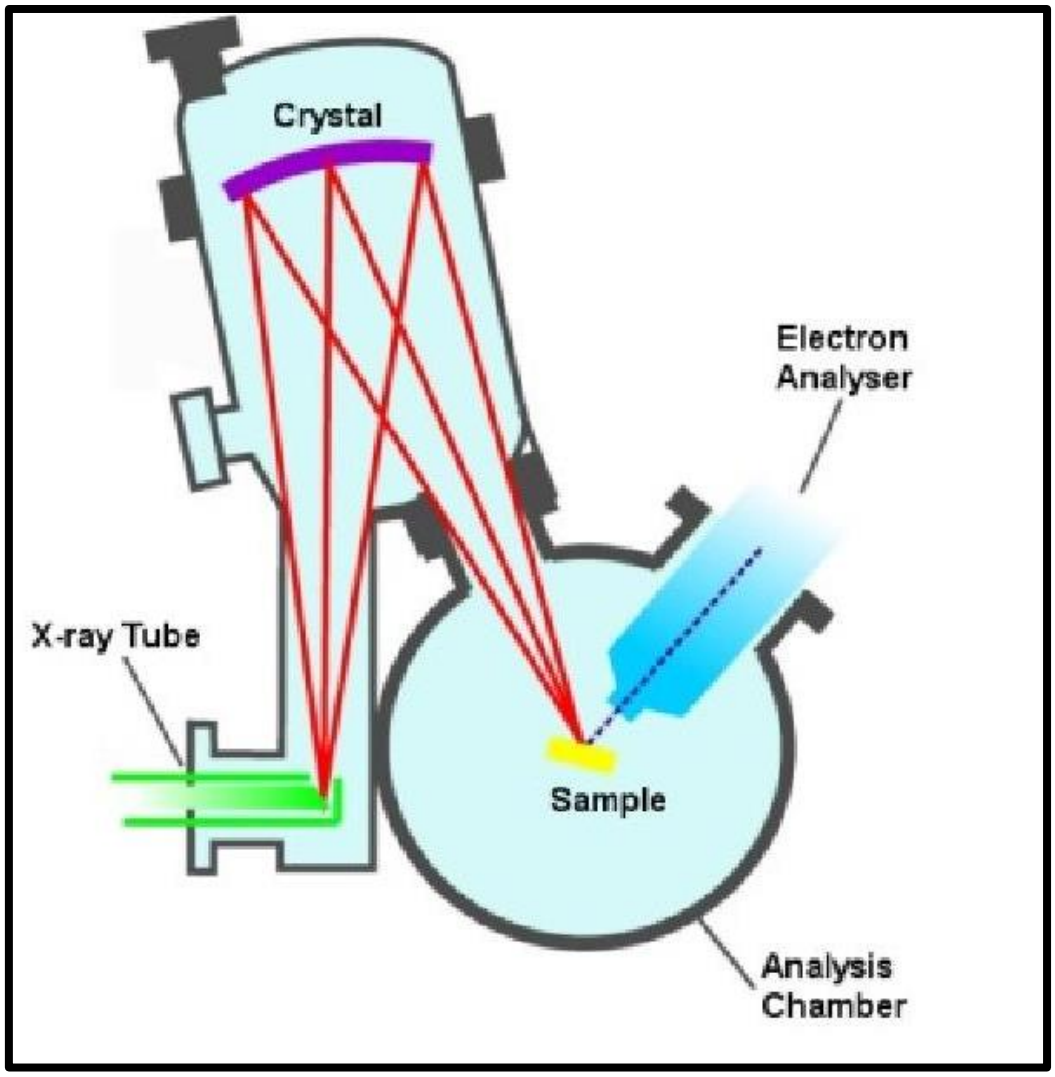

Figure 2.64: Major mechanical component of the monochromator system.

c) Column

Figure 2.47 schematic diagram Cross Section of the ESCALAB 250Xi Spectrometer

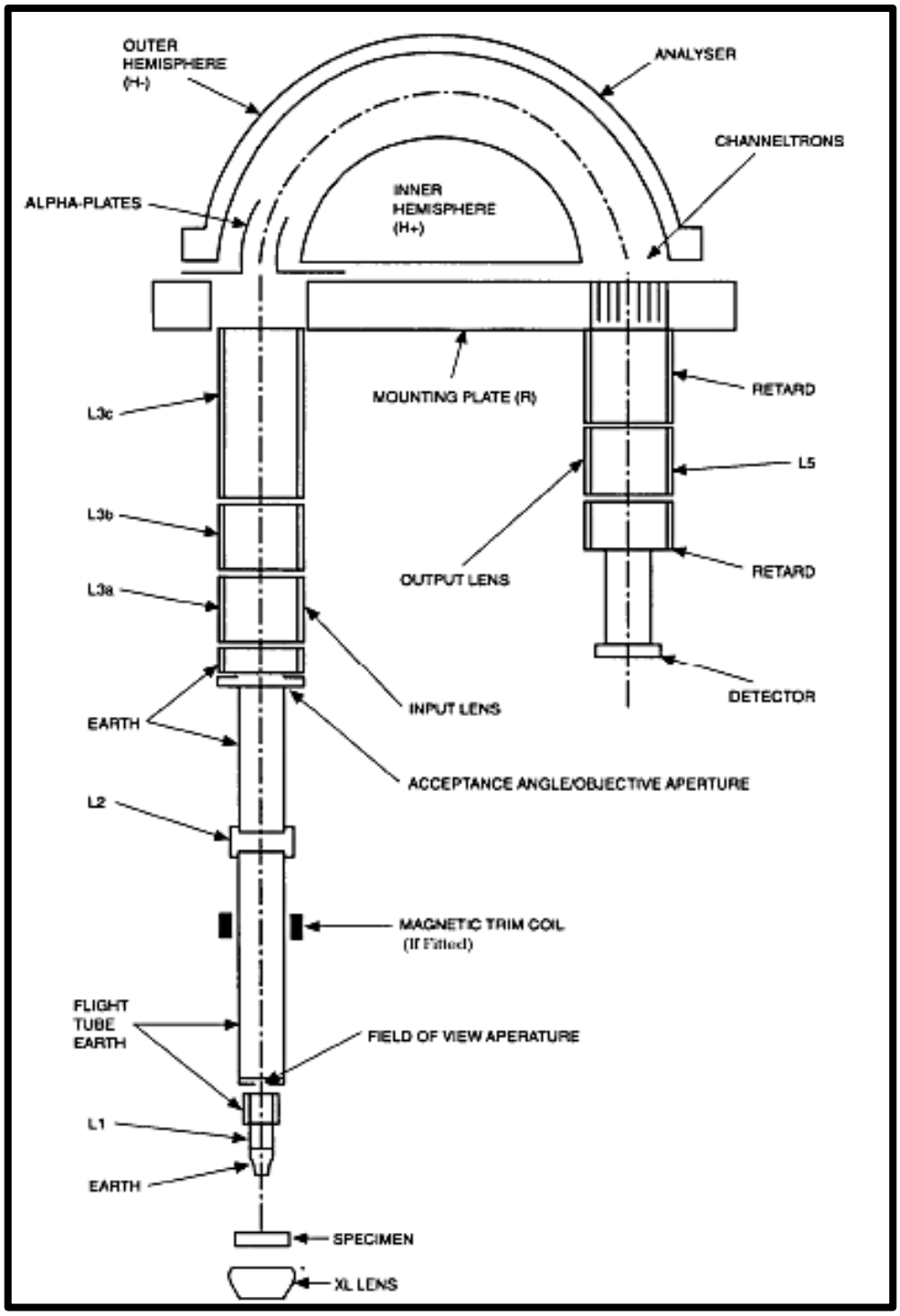

Figure 2.65: Schematic diagram of the cross-section of the ESCALAB 250Xi spectrometer.

d) Input lense system

The input lense captures the maximum possible number of emitted photoelectrons from the sample and transfer them to the analyser with a minimum loss of energy. The control and transfer are done by the electrostatic lenses (L1, L2 and the combination L3). For high sensitivity, the technique uses a magnetic immersed lense (or XL lense, which is located below the sample. The XL lense focuses electrons emitted from the sample over a cone up to ± 45°, into the main lense column.

e) Hemispherical energy analyser

The analyser filters the electrons (ions) emitted from the sample according to their energy. A photoelectron entering a region of varying potential is deflected by an amount that depends on its kinetic energy, its trajectory and the characteristics of the potential acting on it. different geometries for the electrostatic field are possible for achieving energy dispersion of photoelectrons. The ESCALAB 250Xi contains the spherical sector analyser.

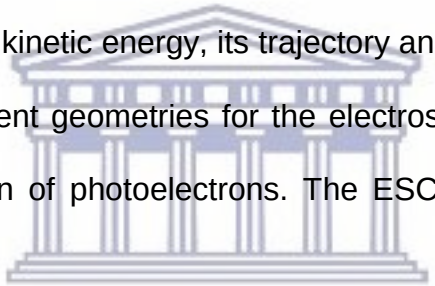

The hemispherical analyser consists of two concentric hemispheres of different radii. It is a band-pass spectrometer with a standard operation, where the slit is biased at ground potential same as the sample. A voltage is applied between the inner and outer (negative) hemisphere and swept to obtain energy spectrum. The electrons must possess a specific kinetic energy; which is the pass energy to be transmitted through the analyser.

f) Channeltron detector

The channeltron act as highly sensitive amplifier whose gain depends on the voltage applied across the detector. when the photoelectron hits the resistive coating at the input of a channeltron secondary electrons are detected. Each channeltron detects the presence of electrons in a specific energy window. The secondary electrons are in turn accelerating to hit a deeper channeltron wall and produce a further avalanche of electrons. The data sums the channeltron signals after applying a correction factor for the energy shift between channels. The gain of the channeltron depends on voltage which is from 2500 V to 4000 V. the ageing of the channeltron may leads to an increase in the voltage due to hey decreasing channeltron efficiency.

2.4.4 Data Acquisition

a) Calibration

The peak calibration is a the most important part of the data analysis as it determines any peak shift due to the sample charging or the instrumental errors. The valence spectra give information about the density, occupancy of electronic states in the valence band of the material and the chemical shift of the spectra.

The chemical state information in XPS comes directly from the energy position of the photoelectron core level peaks. Although the core levels are not directly involved in the chemical bonding process, their binding energy depends on the chemical environment. This effect is called the “chemical shift” originates from the change in electrostatic potential inside the orbitals of the valence electrons (i.e. at the location of the core electrons).

Large variations in chemical shifts are thus expected for different oxidation states but can also arise from difference in lattice site and molecular environment. In a more accurate model, the electron orbitals cannot be assumed to remain frozen during

photoemission and the electron density around the atom relaxes in response to the creation of the positively charged core hole. This reduces the kinetic energy of the outgoing photoelectron and increases the derived electron binding energy. Figure 2.66 shows the valence-band spectra at the ZnO surfaces (a) without and (b) with (NH4)2Sx treatment, illustrating the peak shift.

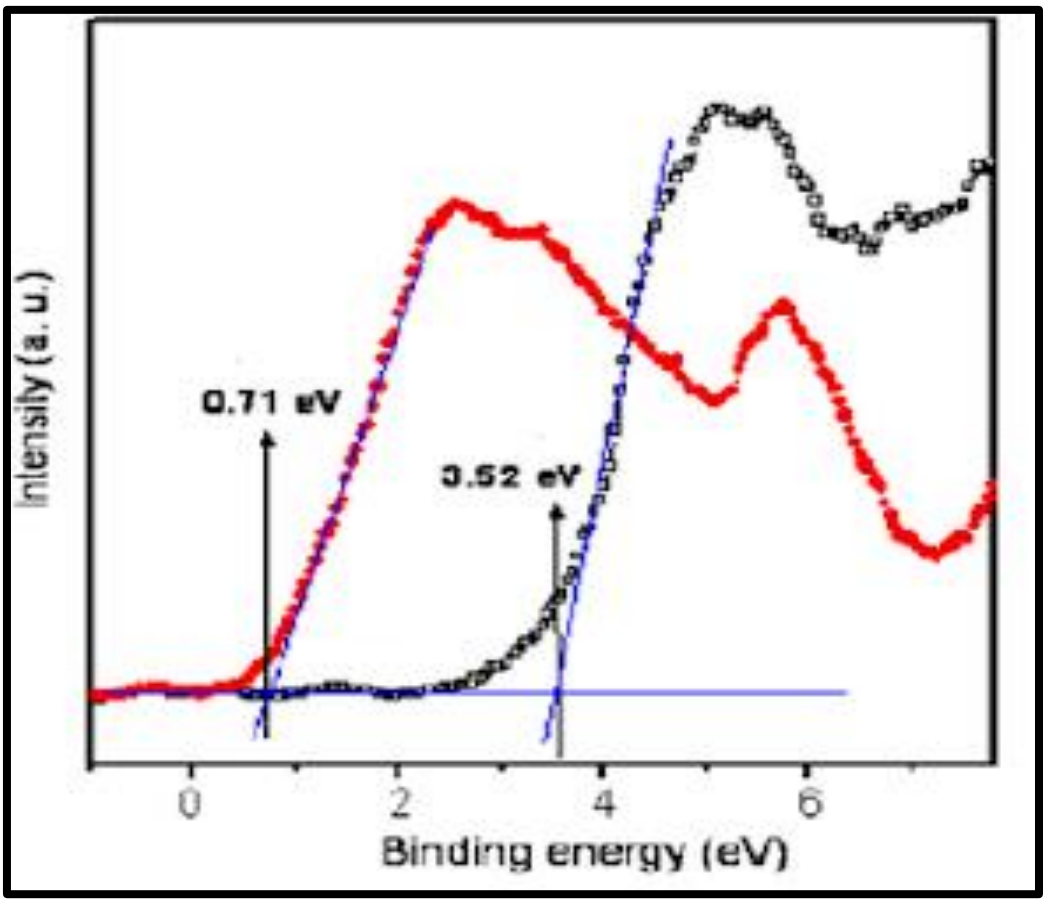

Figure 2.66: Valence -band spectra at the ZnO surfaces (a) without and (b) with (NH4)2Sx treatment [2.29].

b) Background subtraction

Mostly the background contributes in the photoelectron spectrum for exciting the Auger transitions from core level deep to the ionised. The electrostatic screening of the core hole created in the photo-excitation process the peak is asymmetric with features on the low energy side corresponding to the excitation of intrinsic plasmons. The electrons are part of the primary excitation spectrum. The photoelectrons may experience inelastic scattering events when ejected out of the solid, and as a result end up with a lower energy in the spectrum. The continuous background is called the Bremsstrahlung extending up to the incident electron energy on which the characteristic lines are located.

In acquiring the background subtraction, the peak range is determined by the markers on the spectrum. Peak range values should be constant to reduce systematic errors when comparing similar types of samples. For all background types, the intensity at each end of the range is calculated as an average intensity of several points close to that energy. This helps to reduce the effects of a single high or low intensity point especially on data with a higher noise level. The background average at start and end control defines the range of data used to define the start and end intensities of the background. Applying a range at the start and end of peak definition will enable the user to improve the accuracy of the peak area measurement. This is particularly important when using multilevel data (depth profiles, line scans, angular information etc.) where the peak definition maybe defined on a single level, but other levels in the data space may have a higher noise level and cause the background to be calculated from a single noise spike. The typical recommended value is 0.5 to 1 eV. On a survey spectrum with a typical step size of 1 eV, this will effectively have no averaging but on a typical region spectrum

with a typical step size of 0.1eV, this will give averaging over 10 points. Figure 2.67 indicates the effect of the background averaging ranges (0 eV,0.5 eV and 1 eV).

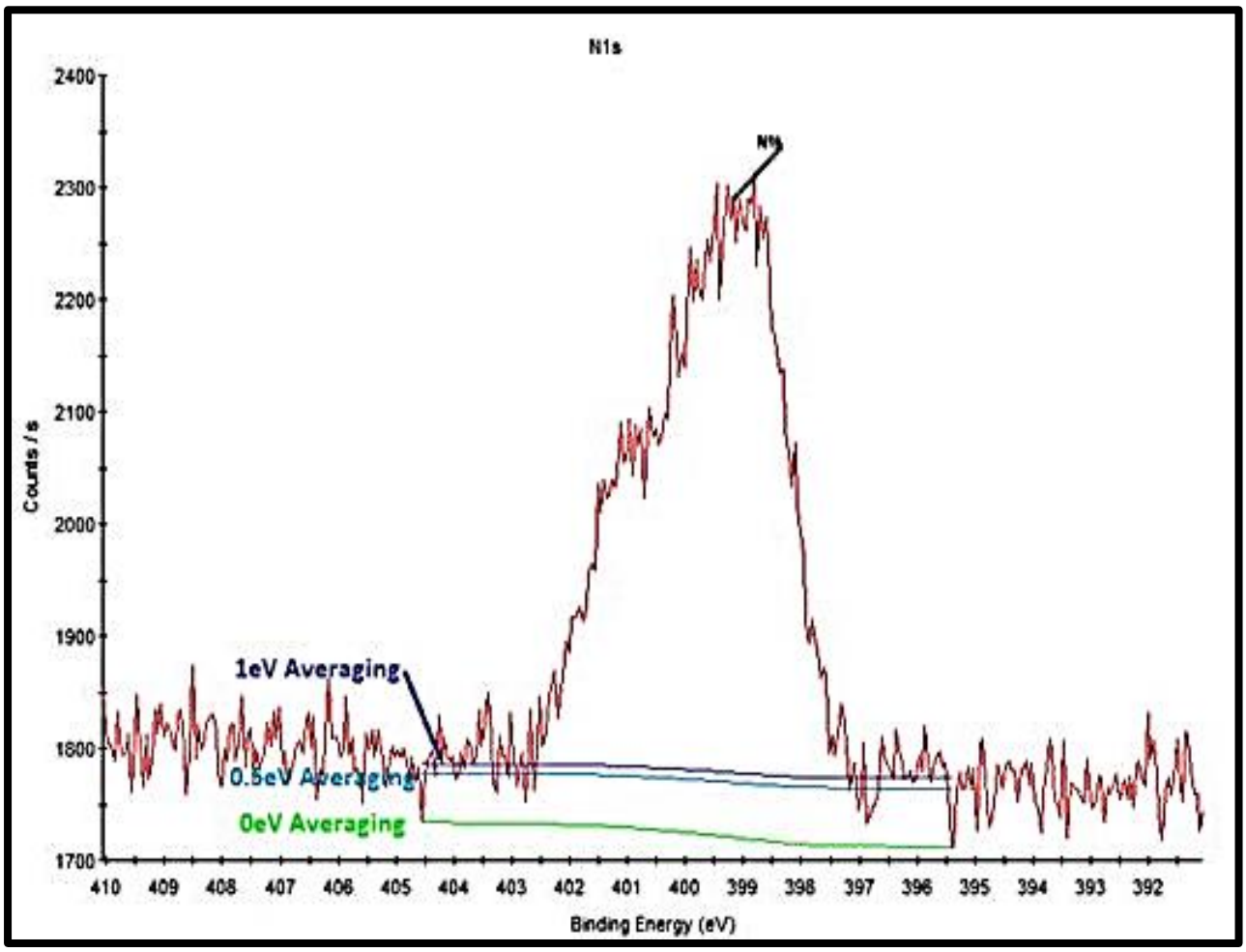

Figure 2.67: Effect of the background averaging ranges (0 eV, 0.5 eV and 1 eV).

Background subtraction methods are, in general, computed to ensure the background meets the data at the limits of the energy interval defining a set of peaks.

Background subtraction methods

Background is removed by applying different methods such as Shierly and Smart background. The Shirley background was widely used on the effect of the inelastic scattering of electrons, especially in its iterated form. Shirley is currently one of the most frequently used mathematical methods in the XPS of solids. To work correctly it requires the lower kinetic energy point to have a higher count value than the upper kinetic energy point. Convergence Limit is used to select the smallest allowable change in area under the peak between iterations of the algorithm.

Smart background

The Smart background method is based on the Shirley background with the additional constraint that the background should not be of a greater intensity than the actual data at any point in the region. The smart background can resolve the case of multilevel data, where the effect of changes in chemistry and shifts in peaks positions can make selection of a fixed background difficult. The background calculation attempts to maximize the peak area whilst for each calculation of the background, the constraint is checked to ensure the background is below the data. If the background is greater than the data, the background is set to follow the data and the effective start point of the Shirley-type background is moved further inside the defined region. This makes the calculated background much less sensitive to the selection of the background start and end positions.

In the case of depth profile or other multilevel data, the effect of changes in chemistry and shifts in peaks positions and overlapping peaks can make selection of a fixed background position difficult. This problem is avoided when using the Smart background. Figure 2.68 shows the comparison of the Shirley and Smart background subtraction on barium spectra.

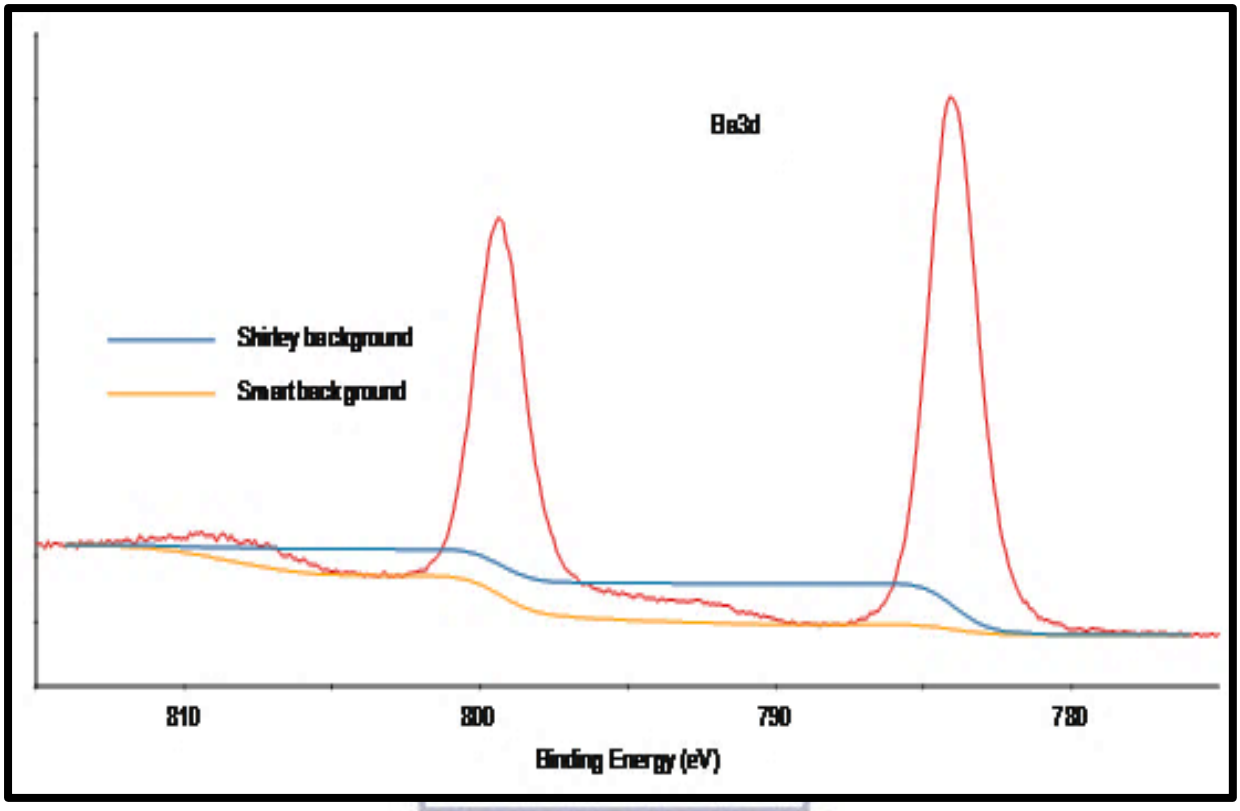

Figure 2.68: Comparison of the shirley (blue) and smart (orange) background subtraction on the barium spectra.

c) Qualitative analysis

The XPS analysis data can focus only on the identification of elements, changing x-ray sources, charging, interpretation of chemical shift, relaxation effects, Auger parameter, peak widths, line shapes, which is the qualitative part of the data. The survey spectra are usually measured first for the system to detect all the elements that are in the sample. The survey scan ranges from 1350-0 eV binding energy to identify all the detectable elements because most of the elements have the major photoelectron peaks below 1350 eV. The binding energy has a step size of 1 eV. The survey spectra will contain all the detectable elements with the elemental composition (atomic %).

The background step to low kinetic energy of the photoelectron peak is due to inelastic photoemission by Bremsstrahlung radiation. Bremsstrahlung radiation gives which rise to a general background which is dominant in the low binding energy of the spectrum. Secondary electron resulting from inelastic photoemission increasingly dominates the background at lower kinetic energy. The peaks can be grouped into three basic types due to photoemission from the core level electrons are defined as the inner quantum shell electrons which have the binding energy sensitive to the chemical environment of the element. The variation of the binding energy results in the shift of the corresponding XPS peak, ranging from 0.1 eV to 10 eV. The binding energy change of the core electrons of an element due to a change in the chemical bonding of that element, valence levels electrons with the binding energy (0-20 eV) which are involved in the delocalised or bonding orbitals and peaks due to Auger emission. Auger electrons are emitted because of relaxation of the excited ions remaining after photoemission. This Auger electron emission at the x-ray excited Auger emission between occurs roughly seconds after the photoelectric event from 1100 eV to 1200 eV.

d) Quantitative analysis

The survey spectra were regarded as for only the qualitative analysis since the background subtraction is not precise. The high-resolution spectra were used for the quantitative analysis. The high-resolution spectra are obtained at the pass energy between 100 eV and 20 eV. The quantitative data can be obtained from peak areas and identification of chemical states often can be made from exact measurements of peaks position and separation, as well as from certain spectral features. To determine the peak position and separate the convoluted peaks, the peak fitting is done. The peak fit will assist in fixing and linking the peak parameters of the doublet

peaks which enables the fitting parameters to be constrained to provide chemically physically valid solutions.

Peak fitting enables the position and intensity of overlapping peaks to be determined and hence a more accurate quantification can be obtained. This is usually used to separate chemical shifts and to separate overlapping core level peaks.

The mathematical process used it is defined by model peak shapes (Gaussian-Lorentzian (G/L) product function). The shape parameters for the peak (height, width, G/L function etc.) are varied until the best fit is achieved. The reason is that the profile of the measured XPS data is not only originating from the atomic level considered, but also from the instrument and its resolution. Thus, it might be that XPS profiles are often best described by a mixed function. Further effects may arise if you have a metallic species. In this case, the ejected photoelectrons may interact with the conduction electrons, loosing very small portions of energy. This may be accounted for by using an additional tail function (i.e. the peaks are asymmetric). The application of the synthetic peaks using a mixture of Gaussian and Lorentzian shapes will try to fit as close as possible the data obtained from an XPS experiment. The XPS peak can be described as a convolution (or mixture) of Gaussian and Lorentzian functions. The Gaussian describes the measurement process (instrumental and source) while the Lorentzian models the natural or intrinsic broadening. Peak fitting can be applied to a single spectrum or to a multilevel set of data, such as a depth profile.

Figure 2.69 shows the XPS fitting peaks of model compound of an O1s of Nphenyl-N!-("-triethoxysilane)-propyl thiourea (STU)/SiO_2. The original data is displayed along with the individual fitted peaks, the overall fitted spectrum and even the residual spectrum as indicated in figure 2.40. Peak fitting may also be applied to multilevel data including propagation of fitting constraints. The chemical state identification it is primarily depends on the accurate determination of the lines energy. Quantification of XPS data is a complex subject and to calculate the composition in more detail typically requires many assumptions to be made about the sample; effectively to have enough information about the sample before quantifying and this is where standards have an important function

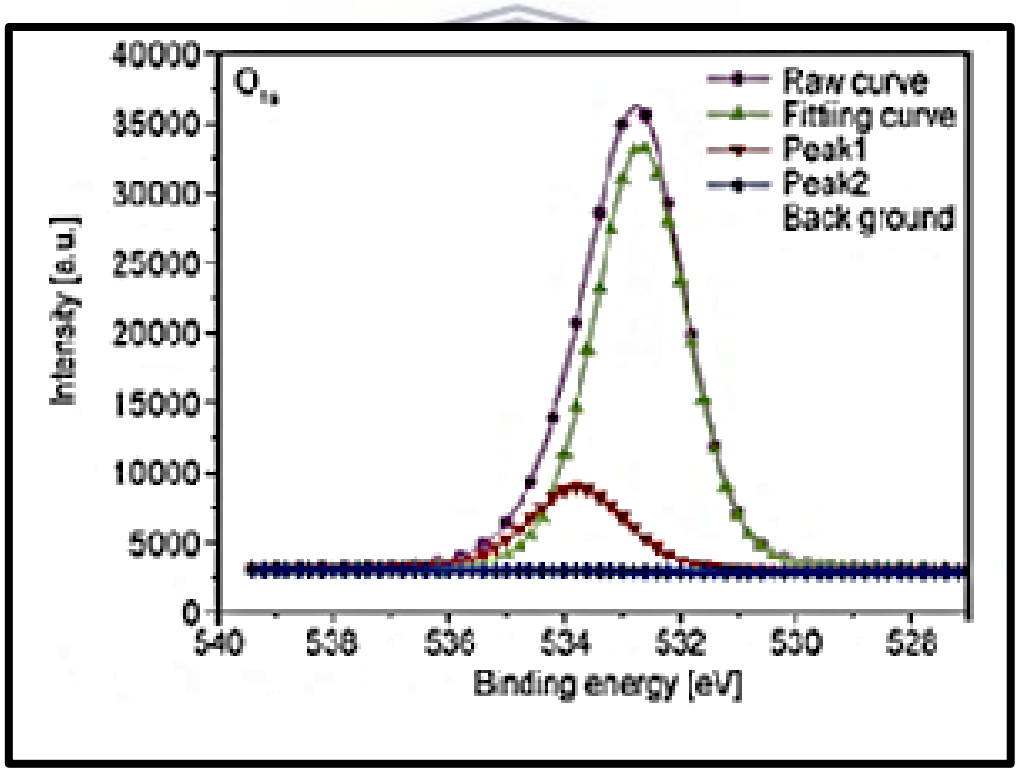

Figure 2.69: the XPS fitting peaks model compound of a O1s of Nphenyl-N!-("triethoxysilane)-propyl thiourea (STU)/SiO_2

Sensitivity factor

When quantifying XPS spectra, Relative Sensitivity Factors (RSF) are used to scale the measured peak areas so that variations in the peak areas are representative of the amount of material in the sample surface. An element library typically contains lists of RSFs for XPS transitions

They are derived from sensitivity factors generated by Wagner and Scofield. The Scofield sensitivity factors are theoretically derived from the photo-ionisation probabilities; the Wagner values were determined empirically from many compounds. The actual libraries have been optimised for the appropriate X-ray anode. The Wagner factors have assumed an instrument transmission function of KE^{-1}. The inelastic mean free path (IMFP) term is effectively included within the sensitivity factor. The Scofield factors assume that the IMFP term is $KE^{0.6}$. The standard quantification library data provide a good first approximation quantification but in some cases more accurate results may be obtained with the use of standards, relevant to the analysis being performed.

The intensity of a peak is related in some way to the number of atoms that generate that peak e.g. I_A α N_A, where I_A is the intensity of a peak and N_A is the number of atoms of element A. Each transition (e g C1s Al2p Si2s) has it's' own probability' of occurring of occurring - referred to a 'sensitivity factor' and are obtained from libraries. These are generally referred to the Scofield or Wagner libraries These are generally referred to the Scofield or Wagner libraries e.g. $I_A = NF.N_A$ ($N_A = I_A /NF$), where NF is normalisation factor, which includes terms for the efficiency (transmission) of the analyser at different kinetic energies, electron mean free path (λ) and the 'Sensitivity.

Wagner listed atomic sensitive factors for x-ray source at 90° and 54.7°. the values are used when the energy analyser used has the transmission characteristics of the spherical capacitor type analyser equipped with an Omni focus III lens supplied by physical electronics.

Table 2.1: Atomic sensitivity factors of selected elements.

		Atomic sensitive factors(ASF) X-ray source at an angle	
Elements	**Line**	**90°**	**54.7°**
Gold (Au)	4f	5.240	6.250
Aluminium (Al)	2p	0.193	0.234
Silicon (Si)	2p	0.283	0.339
Iron (Fe)	2p	2.686	2.957
Tin (Sn)	3d5/2	4.095	4.725
Oxygen (O)	1s	0.711	0.711
Carbon (C)	1s	0.296	0.296

Chemical states

XPS analysis can determine the chemical state of elements found on the surface. Chemical states determination using the XPS has become routine for most of the elements in the periodic table. The binding energy database such as the NIST database or the Phi handbook generally provides sufficient data for the determination of the chemical state for uncomplicated (single peak) spectra. The

objective of this database is to facilitate quantitative interpretation of Auger-electron and X-ray photoelectron spectra (AES/XPS) for surface analysis and to improve the accuracy of quantification in routine analysis. For this purpose, the database contains physical data required to perform quantitative interpretation of an electron spectrum for a specimen with a given composition [2.42].

The NIST X-ray Photoelectron Spectroscopy Database XPS contains over 33,000 data records that can be used for the identification of unknown lines, retrieval of data for selected elements (binding energy, Auger kinetic energy, chemical shift, and surface or interface core-level shift), retrieval of data for selected compounds (according to chemical name, selected groups of elements, or chemical classes), display of Wagner plots, and retrieval of data by scientific citation [2.43].

Table 2.2: Common Si2p binding energy values [2.44]

Sample	Binding Energy(eV)	Std.Dev.
Si	99.4	0.3
SiO2	103.5	0.3
SiC	100.3	0.3
SiN	101.7	0.5
Silicone/Siloxane	102.4	0.9
Silicates	Range from 101.6- 103.8 *	

Table 2.3: Common $Sn3d^{5/2}$ binding energy values [2.44].

Sample	Binding Energy(eV)	Std.Dev.
Sn	485.0	0.5
SnO	486.0	0.6
SnO_2	486.7	0.3
SnF_2	487.2	0.2
SnF_4	488.1	0.2
$SnCl_2$	486.6	0.1
Na_2SnO_3	486.7	0.4

2.5 Time of flight secondary ion mass spectroscopy (TOFSIMS) system

Figure 2.70 illustrate the TOFSIMS principle. Time of flight secondary ion mass spectroscopy (ToF-SIMS) is a technique for chemical characterisation using the, fundamentals of secondary ion generation. The secondary ions generated by primary ion impact on a surface are mainly based on sputtering and ionisation interactions [2.35, 2.36].

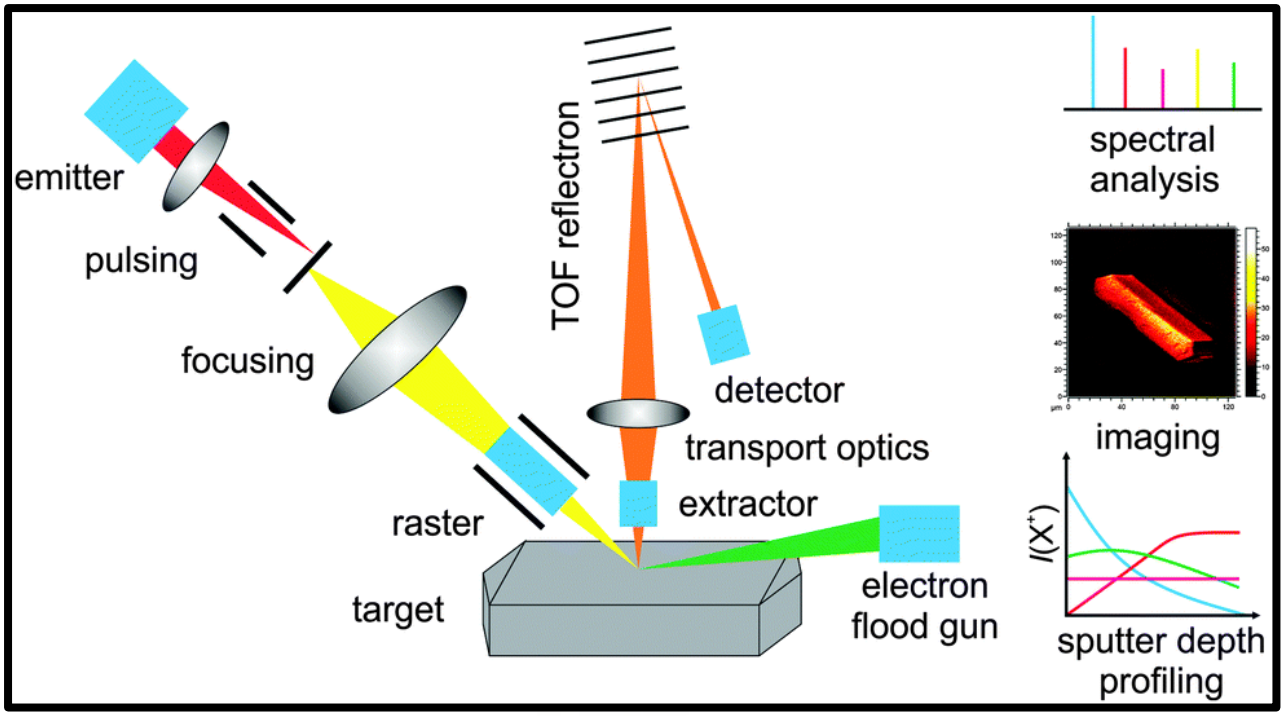

Figure 2.70: Schematic presentation of the TOFSIMS principle [2.37].

Figure 2.71 illustrate a linear collision cascade. The path of collided ions is indicated by black lines. The main principle behind the SIMS technique is the use of a focused ion beam of primary ions, generated by a liquid metal ion gun (LMIG) e.g. bismuth, which impinge upon the surface. ToF-SIMS is extremely surface sensitive, with information only coming from the top nanometres (2-10 nm) of the sample. The principle of the TOFSIMS is to probe the solid sample in the ultra-high vacuum chamber. The sample will be bombarded by a short –pulsed beam of primary ions, which are generated by a liquid metal ion gun (LMIG) such as bismuth. The primary ions on the sample surface result in a collision cascade at the outermost monolayer of the sample, transferring the kinetic energy on the surface. The kinetic energy transfer leads to the emission of neutral particles and positively and negatively charged secondary ions. Some of these collisions return to the surface, the result is

an emission of atoms, molecules or their clusters, some of which are ionised as they leave the surface. The ionised particles known as the “secondary ions” are analysed and detected by the mass spectrometry.

A quadrupole or a double focusing (DF) sector field spectrometer separates the ions according to their mass to charge ratio. Time-of-flight secondary ion mass spectrometry (TOF-SIMS) takes advantage of the differing drift times of secondary ions that were accelerated in the same electric field. They are produced by a short primary ion pulse and then pass an electrostatic extraction field that accelerates them. All equally charged ions gain the same kinetic energy. Ions having the same ionization state, but different masses will therefore obtain distinctive drift velocities after acceleration. Consequently, the drift times required to reach the detector are related with the mass to charge ratio of the ions [2.49]

There are two modes of operation depending on the ion dose, the first is static SIMS, which allows the identification of molecular information by using a low primary ion flux which makes it not destructive mode where <1% of the top monolayer is bombarded., and the second dynamic SIMS, which uses a high primary ion dose which promotes the sample damage to detect elements and small fragments. The modes lead to sputtering the sample from the outer most atoms to a macro or more into the sample.

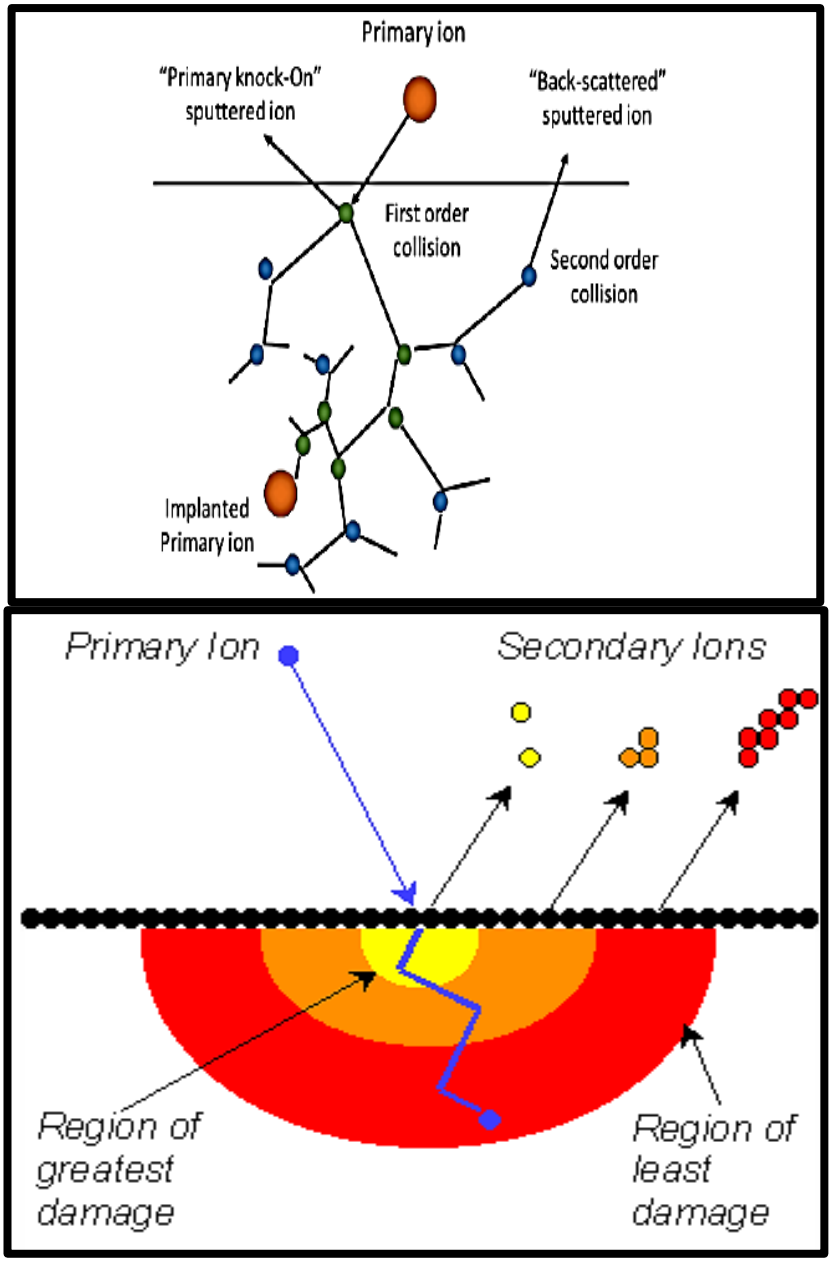

Figure 2.71: Schematic diagram of a linear collision cascade and the SIMS process [2.38].

a) Dynamic mode/Depth profiling for bulk analysis

SIMS traditionally employs atomic primary ions such as Ga^+, Ar^+, Cs^+, and Au^+, with the impact energy range of around 0.5 – 30 keV. The linear cascade theory assumes a low density of moving atoms in the target and each recoil collides only with target atoms at rest. From this theory, the sputtering yield (the number of sputtered atoms per incident ion) can be calculated using the total energy deposited near the surface. The sputter and analysis beams results in a series of spectra acquired at different depth points. Mass peaks are selected, and their intensity is plotted as a function of sputter time forming the in-depth profile [2.47]. Figure 2.54 shows the schematic diagram of the secondary ion mission process initiated by the impact of a primary ion and (b) the sputtering profile [2.49-2.50].

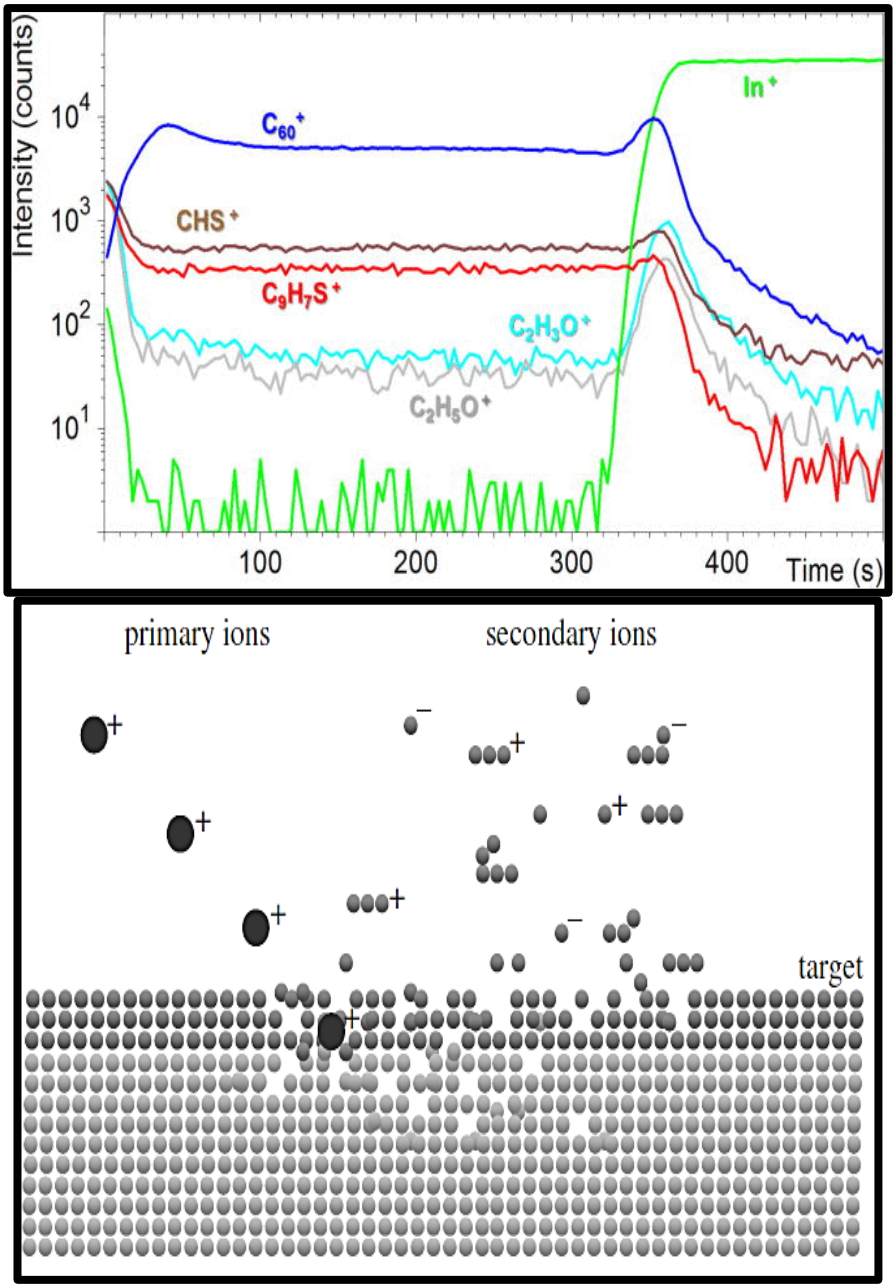

Figure 2.72: (a) Schematic diagram of the secondary ion emission process initiated by the impact of a primary ion and (b) the sputter profile [2.49-2.50]

References

2.1 Robinson, Ross. "removing contaminants from silicon wafers to facilitate euv optical characterization." PhD diss., Brigham Young University, 2003

2.2 Kern, Werner. "Handbook of semiconductor wafer cleaning technology." New Jersey: Noyes Publication (1993): 111-196. Kern, Werner. "The evolution of silicon wafer cleaning technology. *"Journal of the Electrochemical Society* 137, no. 6 (1990): 1887-1892

2.3 ZHOU, W., & YANG, H.. Flame retarding mechanism of polycarbonate containing methylphenyl-silicone. Thermochimica acta,2007, 452(1), 43-48.R.N.

2.4 Watt, "The principles and Practice of Electron Microscopy", 2nd Edition, Cambridge University Press, Great Britain (1997). https://cmrf.research.uiowa.edu/sites/cmrf.research.uiowa.edu/files/styles/large/public/sem1.gif?itok=uzYuMy9J 3.1]][

2.5 P. Goodhew, J. Humphreys and R. Beanland, "Electron Microscopy and Analysis", 3rd Edition, Taylor & Francis, London (2001).

2.6 I. Watt, "The principles and Practice of Electron Microscopy", 2nd Edition, Cambridge University Press, Great Britain (1997).

2.7 (1. JOHNSON, P. B., & CHRISTY, R. W. Optical constants of the noble metals. Physical Review B, 1972,6(12), 4370.

2.8 Zhang, Jin Zhong.*Optical properties and spectroscopy of nanomaterials*. 2009..

2.9 Egerton, Ray F. *Physical principles of electron microscopy*. New York: Springer, 2005.

2.10 P. J. Goodhew and F. J. Humphreys, Electron Microscopy and Analysis, 2nd Edition, Taylor & Francis, London (1988)

2.11 Miculescu, F., I. Jepu, C. Porosnicu, C. P. Lungu, M. Miculescu, and B. Burhala. "A study on the influence of the primary electronbeam on nanodimensional layers analysis." *Digest Journal of Nanomaterials and Biostructures* 6, no. 1 (2011): 307-317.

2.12 http://www.ammrf.org.au/myscope/sem/practice/principles/imagegeneration.php

2.13 Hafner, Bob. "Scanning electron microscopy primer. *"Characterization Facility, University of Minnesota-Twin Cities* (2007): 1-29.

2.14 http://www.nanoscience.com/technology/sem-technology/sample-electron-interaction/

2.15 Menard L.D., and Ramsey J.M. Fabrication of Sub-5 nm Nanochannels in Insulating Substrates Using Focused Ion Beam Milling. Nano Lett. (2011), vol.11, pp: 512–517.

2.16 Talbot C.G. A new application-specific FIB system architecture. Microelectronic Engineering (1996), vol.30, pp: 597–602.

2.17 Rubanov S., and Munroe P. The application of FIB milling for specimen preparation from crystalline germanium. Micron (2004), vol.35, pp: 549–556.

2.18 Giannuzzi L.A., and Stevie F.A. A review of focused ion beam milling techniques for TEM specimen preparation. Micron (1999), vol.30, pp: 197–204.

2.19 Gamo K. Nanofabrication by FIB. Microelectronic Engineering (1996), vol.32, pp: 159– 171

2.20 Li J., Malis T., and Dionne S. Recent advances in FIB–TEM specimen preparation techniques. Materials Characterization (2006), vol.57, pp: 64–70.

2.21 Zeiss, Instruction manual Zeiss multi GIS, Carl Zeiss NTS GmbH, Oberkochen, Germany, 2009.

2.22 Liao, Y. (2007) Practical Electron Microscopy and Database - An Online Book.http://www.globalsino.com/EM/. http://www.globalsino.com/EM/page3891.html

2.23 http://www.orsayphysics.com/upload/big_1467288479.jpg

2.24 Williams, David B., and C. Barry Carter. "High Energy-Loss Spectra and Images."*Transmission Electron Microscopy* (2009): 715-739.

2.25 O'keefe, M. A., C. J. D. Hetherington, Y. C. Wang, E. C. Nelson, J. H. Turner, C. Kisielowski, J-O. Malm et al. "Sub-Ångstrom high-resolution transmission electron microscopy at 300keV."*Ultramicroscopy* 89, no. 4 (2001): 215-241.

2.26 Kim, A-Young, Min Kyu Kim, Keumnam Cho, Jae-Young Woo, Yongho Lee, Sung-Hwan Han, Dongjin Byun, Wonchang Choi, and Joong Kee Lee. "One-Step Catalytic Synthesis of CuO/Cu2O in a Graphitized Porous C Matrix Derived from the Cu-Based Metal–Organic Framework for Li-and Na-Ion Batteries." ACS applied materials & interfaces 8, no. 30 (2016): 19514-19523.

2.27 http://www.globalsino.com/EM/page3891.html

2.28 Dogan, M., M. Ulu, G. G. Gennarakis, and T. J. M. Zouros. "Experimental energy resolution of a paracentric hemispherical deflector analyzer for different entry positions and bias."*Review of Scientific Instruments* 84, no. 4 (2013): 043105.

2.29 Turner, Noel H., and John A. Schreifels. "Surface analysis: X-ray photoelectron spectroscopy and auger electron spectroscopy." *Analytical chemistry* 72, no. 12 (2000): 99-110.

2.30 Kleimenov, Evgueni. "High-pressure X-ray photoelectron spectroscopy applied to vanadium phosphorus oxide catalysts under reaction conditions." (2005).

2.31 http://jacobs.physik.uni-saarland.de/instrumentation/uhvl.htm

2.32 Rough schematic of XPS physics – “Photoelectric Effect” http://www.nanolabtechnologies.com/instrument-xps-esca

2.33 Karkhanis, Nikhil. "Fabrication, electrical characterization, and annealing of aluminum, copper, and gold/4H-silicon carbide Schottky diodes." PhD diss., Clemson University, 2007.

2.34 Bexell, Ulf. "Surface characterisation using ToF-SIMS, AES and XPS of silane films and organic coatings deposited on metal substrates." PhD diss., Acta Universitatis Upsaliensis, 2003.

2.35 http://www.eagle-regpot.eu/EAgLE-Equipment_XPS.html

2.36 Merzlikin, Sergiy. "Depth Profiling by X-ray Photoelectron Spectroscopy."Fakultät für Chemie (2007).

2.37 Lin, Yow-Jon, Shih-Sheng Chang, Hsing-Cheng Chang, and Yang-Chun Liu. "High-barrier rectifying contacts on undoped ZnO films with (NH4) 2Sx treatment owing to Fermi-level pinning."*Journal of Physics D: Applied Physics* 42, no. 7 (2009): 075308.

2.38 Handbook of surface and interface analysis methods for problem-solving. Responsibility: edited by John C. Rivière, Sverre Myhra. Edition: 2nd ed.

2.39 Johnson, Sherena G. "NIST STandard Reference Database 100." (2010).

2.40 https://catalog.data.gov/dataset/nist-x-ray-photoelectron-spectroscopy-database-xps-version-4-1-srd-20

2.41 C.D. Wagner, A.V. Naumkin, A. Kraut-Vass, J.W. Allison, C.J. Powell, J.R.Jr. Rumble, NIST Standard Reference Database 20, Version 3.4 (web version) (http:/srdata.nist.gov/xps/) 2003. For Si 2p3/2 valueshttp://www.xpsfitting.com/2012/01/silicon.html

2.42 Belu, Anna M., Daniel J. Graham, and David G. Castner. "Time-of-flight secondary ion mass spectrometry: techniques and applications for the characterization of biomaterial surfaces. "*Biomaterials* 24, no. 21 (2003): 3635-3653.

2.43 Vickerman, John C. "Molecular imaging and depth profiling by mass spectrometry—SIMS, MALDI or DESI?."*Analyst* 136, no. 11 (2011): 2199-2217.

2.44 Hofmann, Jan P., Marcus Rohnke, and Bert M. Weckhuysen. "Recent advances in secondary ion mass spectrometry of solid acid catalysts: large zeolite crystals under bombardment." Physical Chemistry Chemical Physics16, no. 12 (2014): 5465-5474.

2.45 http://kompozite.com/wordpress/wpcontent/uploads/2014/03/clip_image001.gif

2.46 Parsnnm, G. E. O. F. D. B. S. C. H. U. N. G. S. Z. E. N. T. B. U. M. "Scientific Technical Report. "*Astron. Nachr* 316, no. 5 (1995): 311-318.

2.47 Scarazzini, Riccardo. "ToF-SIMS characterisation of fragile materials used in microelectronic and microsystem devices: validation and enhancement of the chemical information." PhD diss., Université Grenoble Alpes, 2016.

2.48 Smentkowski, Vincent S., Gilad Zorn, Amanda Misner, Gautam Parthasarathy, Aaron Couture, Elke Tallarek, and Birgit Hagenhoff. "ToF-SIMS depth profiling of organic solar cell layers using an Ar cluster ion source." Journal of Vacuum Science & Technology A: Vacuum, Surfaces, and Films 31, no. 3 (2013): 030601.Rost, Detlef. "TOF-SIMS-Analysen Interplanetarer Staubteilchen." PhD diss., 2000.

2.49 Richter, Katrin. *Application of imaging ToF-SIMS in cell and tissue research*. Inst of Biomedicine. Dept of Medical Biochemistry and Cell Biology, 2007.

2.50 Smentkowski, Vincent S., Gilad Zorn, Amanda Misner, Gautam Parthasarathy, Aaron Couture, Elke Tallarek, and Birgit Hagenhoff. "ToF-SIMS depth profiling of organic solar cell layers using an Ar cluster ion source."*Journal of Vacuum Science & Technology A: Vacuum, Surfaces, and Films* 31, no. 3 (2013): 030601.

CHAPTER 3

Chemical evolution of tin catalyst annealed in vacuum within an x-ray photoelectron spectroscopy system

Abstract

The properties of SiNWs are influenced by their diameter, which in turn are regulated by the diameter of the nano sized metal catalyst. Understanding the relationship between the metal catalyst and the SiNW properties will contribute to the controlled synthesis of SiNWs with tailored optoelectronic properties for solar cell applications. Surface analysis of the metal catalyst at elevated temperatures will provide valuable insights into the state of the catalyst's surface prior to SiNW growth. This chapter reports on the surface analysis of a 3 nm Sn thin film annealed during x-ray photoelectron spectroscopy (XPS). The XPS analysis indicated that the surface consisted of Sn- and Si-oxides covered by an adventitious carbon film. Increasing the temperature to 232 °C led to the removal of the adventitious carbon accompanied by increasing Sn and Si concentrations. The formation Sn nano-islands are tentatively ascribed to form at temperatures above 232 °C which corresponds to the occurrence of a higher Si concentration compared to Sn. Depth profile analysis revealed the presence of an underlying Sn metal core encapsulated by SnO and Sn_2O.

Introduction

The metal catalyst is one of the principal factors which control the size and the orientation of the nanowire. The diameter of the SiNWs is confined by the size of the metal catalyst and coupled with their 3D vertical structure, leads to an improved light trapping ability for solar cell devices. According to thermodynamics [3.1, 3.2], the control of the metal catalyst nanoparticles via heating the thin film is found to be difficult to manipulate when downsizing a metal nanoparticles or droplets because nanoparticles have strong van der Waals attractive forces and thus agglomerate into larger particles. The metal catalyst is found to be one of the factors that affect the SiNWs' stability and commercially available in the solar cell application, which implies that even the choice of the metal catalyst used should also be taken into consideration.

The metal catalyst is used to grow SiNWs via the VLS mechanism. Gold (Au) is a well-known metal catalyst as it has been used for SiNW growth [3.3]. Au is a desirable choice for the synthesis because according to the Au-Si binary phase system it has the eutectic point of 363 °C at which the composition of the liquid alloy is 18.6 at.% Si [3.4]. The relatively high Si solubility and surface tension of the Au-Si alloy make Au very favourable for wire growth [3.3]. However, Au has its drawback as it forms deep level metal impurity in Si leading to centres for charge - carrier recombination and ultimately a reduction of the minority charge - carrier lifetime [3.5, 3.6].

Tin (Sn) is one of the alternative metal catalysts proposed to overcome some of the limitations suffered from Au catalysts. According to the phase diagram of the Sn-Si binary system also shows a single dominant eutectic point at 232 °C which allow the synthesis of SiNWs at low temperature (240 °C). Sn is isoelectronic with Si and

hence a neutral impurity, so it is expected to introduce low and shallower energy levels in the silicon band gap than Au [3.7]. Theoretically, Nebol'sin *et al*. [2005] proved that Sn is an unstable metal to grow SiNWs [3.8]. However, there have been experimental results which show successful SiNW growth. The studies continued to manipulate the Sn by trying to control the diameter of the SiNWs through the thickness of the Sn film and growing temperature.

Recently, the effects of Sn thin film thickness on the growing SiNWs using different techniques have been receiving scientific attention. The use of a 1 nm Sn thin film for SiNW growth was reported where the Sn nanoparticles were around 20 nm after annealing at 400 °C [3.9]. The behaviour of the Sn thin film on the substrate under elevated temperatures leads to formation of nanoparticles.

The behaviour of the Sn thin film on the substrate under elevated temperature influences the Sn nanoparticle size. The Sn thin film (20 nm) coated substrate was subjected to temperatures ranging from 250 to 400 °C and Sn nanoparticles had an average of 30 - 50 nm [3.9]. The heat on the thin film leads to Ostwald ripening process which converts the thin film to nanoparticles due to the surface tension. The nanoparticles tend to form large particles (energetically favourable) due to their strong van der Waal attractive forces as the temperature increases [3.2]. Mullane *et al* [2013], showed the abrupt termination of crystalline fringes due to the amorphous region at the Sn-Si interface [3.10]. Prior the growth of the nanowires, the chemical behaviour such as oxidation of the metal catalyst should be well understood in order to reduce any nanowire growth distraction.

X-ray photoelectron spectroscopy (XPS) is a widely used surface sensitive analytical technique to determine the chemical bonding (information/energy) of materials.

Typically, the materials can be organic or inorganic, powders or thin films. According to the physics principle governing XPS, the escape depth of the photoelectron with characteristic binding energies is about 2 – 10 nm, which allows for quantitative thin film analysis. The additions of heating stages on modern XPS systems give information regarding the chemical behaviour of materials under non-ambient conditions, which provides further insights into the thermal effects on the material properties [3.12-3.19].

Investigations of the materials employed within actively researched fields on microelectronic applications such as gas sensors and organic/inorganic solar cells benefits from the quantitative surface analysis capabilities of XPS. Kwoka *et al*. [3.16] reported on the XPS analysis of SnO_2 which is a widely used materials for gas sensors because it response to oxidising and reducing gases. XPS results confirm that after air exposure the nanolayers still consisted of a mixture of SnO and SnO_2, but with a strong domination of the latter. The amount of elemental tin did not change significantly. The variation of the different tin oxidation states takes place mainly between Sn^{2+} and Sn^{4+}, which was confirmed by analysis of O 1s region where O-Sn^{4+} signal was increasing after exposure. The contamination-related signal was slightly emerging. XPS results showed an increase of relative [O]/ [Sn] concentration from 1.62 to 1.80 after air exposure. The application of the XPS analysis will give an understanding on the chemical and electronic behaviour by extracting information regarding the sensitivity and selectivity of the metal oxide thin film-based gas sensors under different conditions such ambient and temperature or doping the materials [3.17]. Thøgersen *et al.* [3.19] also reported on the use of the XPS to investigate the silicon thin film for surface coating. The XPS results indicated that during oxidation of the porous silicon (PS) elements such as pure Si (Si^0), Si_2O (Si^+),

SiO (Si^{2+}), Si_2O_3 (Si^{3+}), and SiO_2 (Si^{4+}) were detected. In addition, both hydrogen and carbon were introduced to the PS in the form of Si_3SiH and CO. Also, when sputtering the PS with argon (Ar) for depth profiling, aSi is created in the structure. Oxidation states such as Si_3SiH, Si_2SiH_2 or Si_3SiC may also occur due to HF etching and C contamination at the surface. Si_3SiH can be due to elemental silicon bonded to one hydrogen atom, and has higher binding energy than for elemental silicon, while the compound Si_2SiH_2 has a higher binding energy.

This chapter investigates the chemical evolution of a 3 nm Sn thin film thermally evaporated on a Si (100) wafer and subsequently heated within an x-ray photoelectron spectroscopy (XPS) vacuum at different temperatures. The goal is to determine the optimum temperature at which the Sn nanoparticles are formed and probing the corresponding chemical composition.

3.1 Experimental

The sample preparation was done by cutting a (100) Si wafer into several 1 cm × 1 cm sample. The Si (100) wafers were first cleaned sequentially with ultrasonic agitation for 5 minutes in a bath containing acetone then ethanol and then deionized water. Afterwards, the Si wafers were dipped in a 5 % Hydrofluoric acid for 1 minute then allowed to air dry. The Sn thin film was deposited on the cleaned Si (100) wafers using an EDWARDS Auto 306 vacuum thermal evaporator. The 99 % pure Sn powder was placed in a crucible and evaporated via a resistively heated filament set to a current about 4 A. The gradual flow in current gave a well dispersed Sn vapour evaporated on the Si substrate at a vacuum pressure of 8×10^{-6} Pa. The crystal monitor on the thermal evaporator was used to estimate the 3 nm thin film thickness. The thickness of the Sn thin film was confirmed using the layer probe

software which will be briefly explained in chapter 4. Five Sn coated Si (100) wafer samples of the same area were prepared prior the XPS analysis.

3.2 XPS calibration and characterisation

XPS analysis was conducted using a Thermo Scientific ESCALAB 250Xi with a monochromatic Al Kα (1487 eV) x-ray beam. The depth profile analysis was done using the Argon (Ar+) ions. The binding energy have been obtained from Avantage software using a 30% Gaussian/Lorentzian mix function.

The x-ray power was fixed at 300 W with a beam diameter of 900 µm. The pass energies for the survey and narrow scan modes were 100 eV and 20 eV, respectively. The temperatures 180, 232, 350 and 450 °C for the XPS analysis were selected based on typical HWCVD synthesis conditions and the Sn-Si phase diagram. The 450 °C was selected as the highest temperature in the experiment because of the XPS techniques' limitations not being able to be set at the highest temperature above 600K [3.20] and due to the thickness (3 nm) of the Sn film, to avoid losing the film through evaporation in to the vacuum at elevated temperature.

All the reported binding energy data were calibrated using the valence spectra shown in figure 3.1.

Figure 3.1 illustrate the valence band spectra of the as deposited (25 °C), 180, 232, 350 and 450 °C. The valence band peaks for the temperatures 25, 180 and 232 °C have the same behaviour as the SnO valence band [3.21]. The valence band peaks for the 350 °C and 450 °C ends at -0.9 eV, of which was corrected on all the measurements conducted under these annealing temperatures. The cut off-point of the secondary electron (sharp fall at high binding energy) is due to the loss of electrons with high kinetic energy to overcome the work function of the surface.

The electrons at high binding energy cut-off in the spectrum have zero kinetic energy [3.22]. The well-known XPS calibration is done by using carbon, which also form part of the results. The carbon peak position will be investigated at the end of this section and compared to the valence band spectra. The XPS data was reflected first as the survey spectra indicating all the detected elements with their atomic percentages (at %).

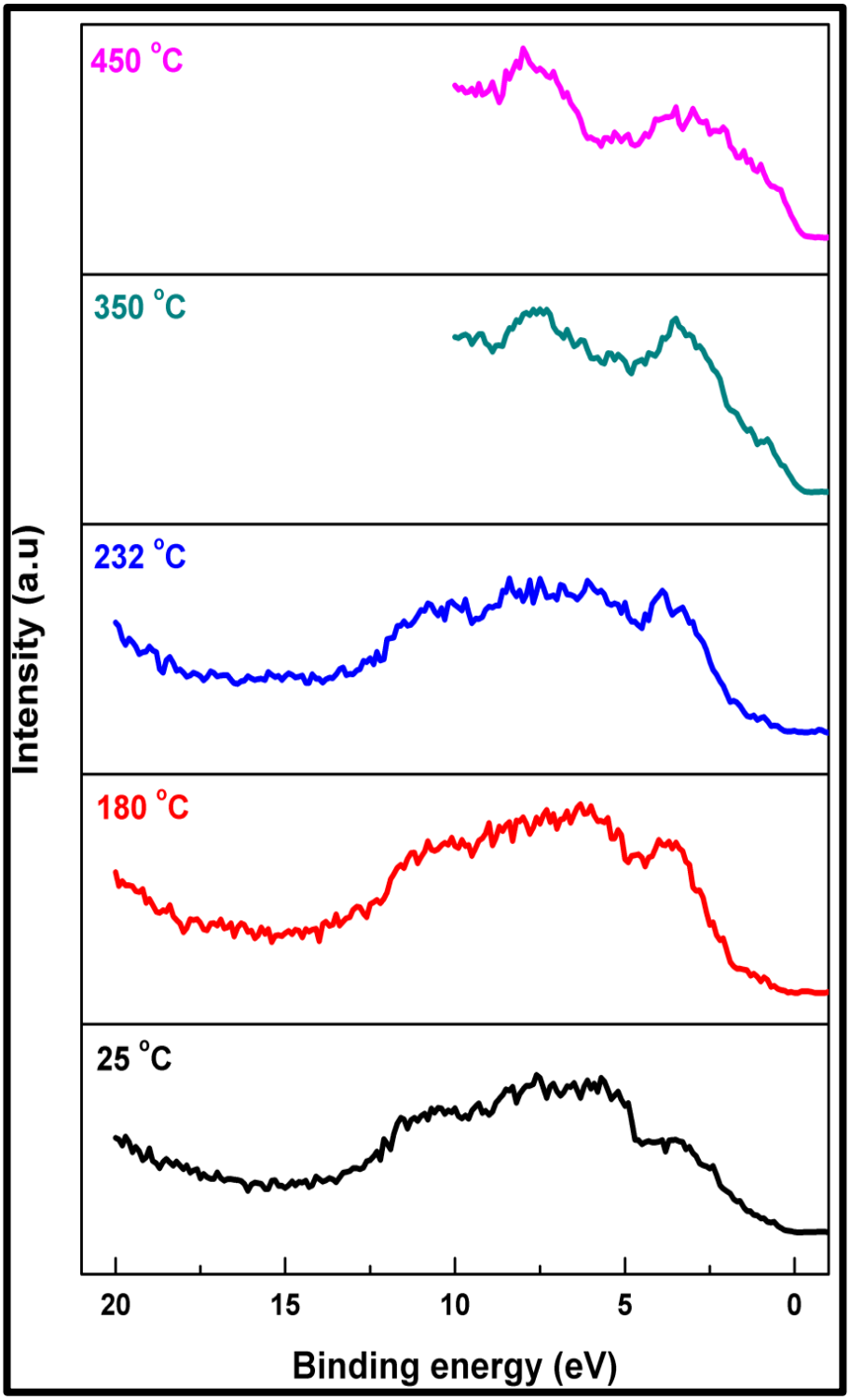

Figure 3.73: Valence spectra at as deposited (25 °C) 180, 232, 350 and 450 °C

3.3 XPS survey results

Figure 3.2 shows XPS survey spectra of the Sn thin film at as-deposited (25 °C) , 180, 232, 350 and 450 °C. The spectra were recorded over a wide energy range. The spectra contain two basic types of the peaks corresponding to the photoemission from the core and valence levels of Sn and Si electrons. The Sn3d peak has $Sn3d^{5/2}$ and $Sn3d^{3/2}$ doublets are separated by a binding energy of approximately 8.5 eV. The $Sn3d^{5/2}$ and $Sn3d^{3/2}$ peaks are accompanied by O1s and C1s peaks, indicating surface oxidation and/or contaminations of the thin film. The $Sn3d^{5/2}$ peaks however reduce in intensity as the temperature increase which can be due to Sn evaporation, or Sn infusion, or the formation Sn nanoparticles. In contrast, the Si2p peak increases in intensity as the temperature increases.

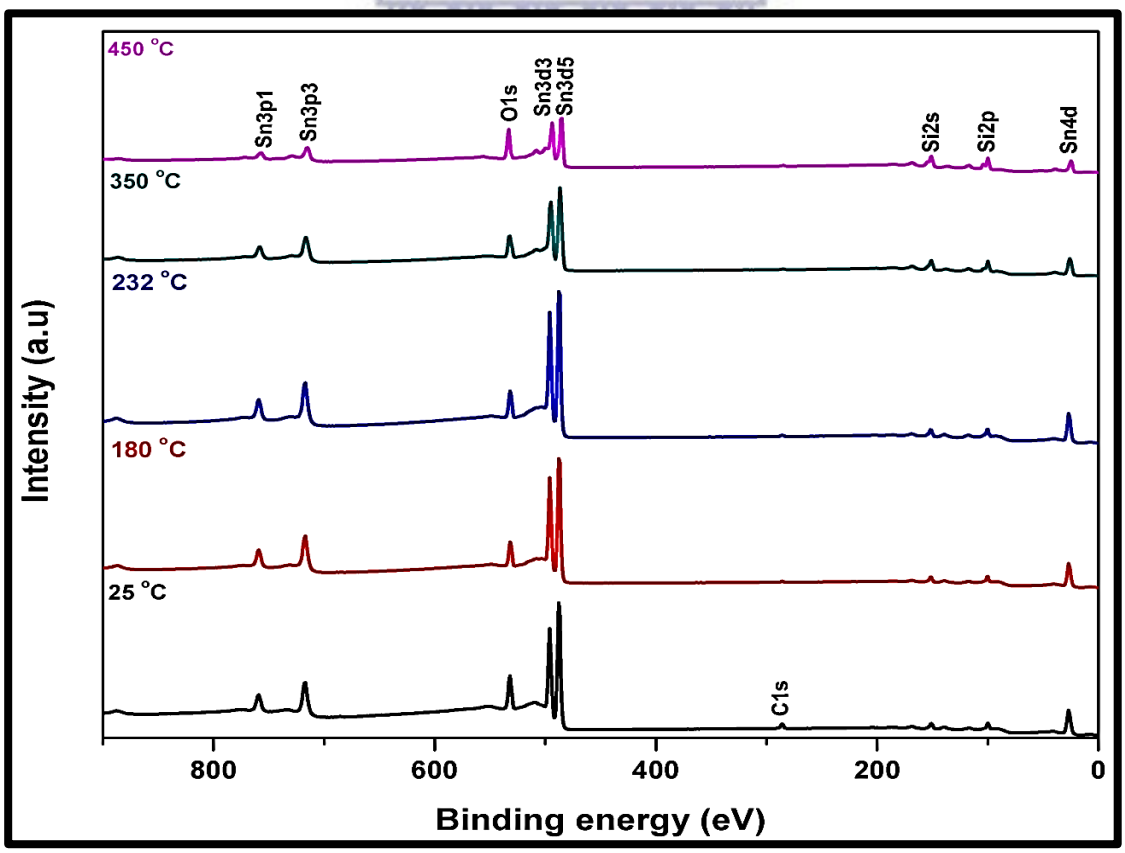

Figure 3.74: XPS survey spectrum of the as-deposited (25 °C), 180, 232, 350 and 450 °C Sn thin film.

Figure 3.75 shows the summary of the amount (at.%) of each element acquired at the different XPS stage temperatures. The graphical summary of the survey results indicates the behaviour of all the detected elements as the temperature increases. The amount of adventitious carbon was observed to decrease as the temperature increases. The carbon content is not completely removed as the peak can be observed on samples with no carbon. The C can still be detected because of the high sensitivity of XPS analysis. The carbon remaining at temperatures ≥ 180 °C in this experiment was about 0.4 at. %.

The surface oxygen (O) content decreases with an increase in temperature until 350 °C, which can be attributed to the exposure of the oxidised Si substrate. This is further supported by a rapid drop of the Sn and enhancing Si content at 279 °C, eventually leading to O and Si with a similar atomic content of 43.6 % at 450 °C. In these results is not clear where the O is originated since the survey spectra give information on the elements present in the sample and the amount in percentages. The formation of the Sn nanoparticles is tentatively expected to occur at 279 °C, which is above the Si-Sn eutectic temperature (232 °C). The increase in the heating temperature can lead to Ostwald ripening where the small particles agglomerate to form bigger particles due to strong van der Wall attractive forces between the nanoparticles. The larger particles are formed as they are energetically favourable side because of the surface tension.

The surface tension is caused by the thermal-expansion difference between the substrates and interconnection materials leads to high mechanical stresses in thin-film structures.

The XPS results does not show any change in the film surface at the temperatures below 232 °C. The ideal annealing temperature can be ranging between 279 and 350 °C for Sn nanoparticle formation. From the survey spectra, the high-resolution spectra for each element in the sample can then be extracted to observe the changes of the elemental composition and bonding with temperature.

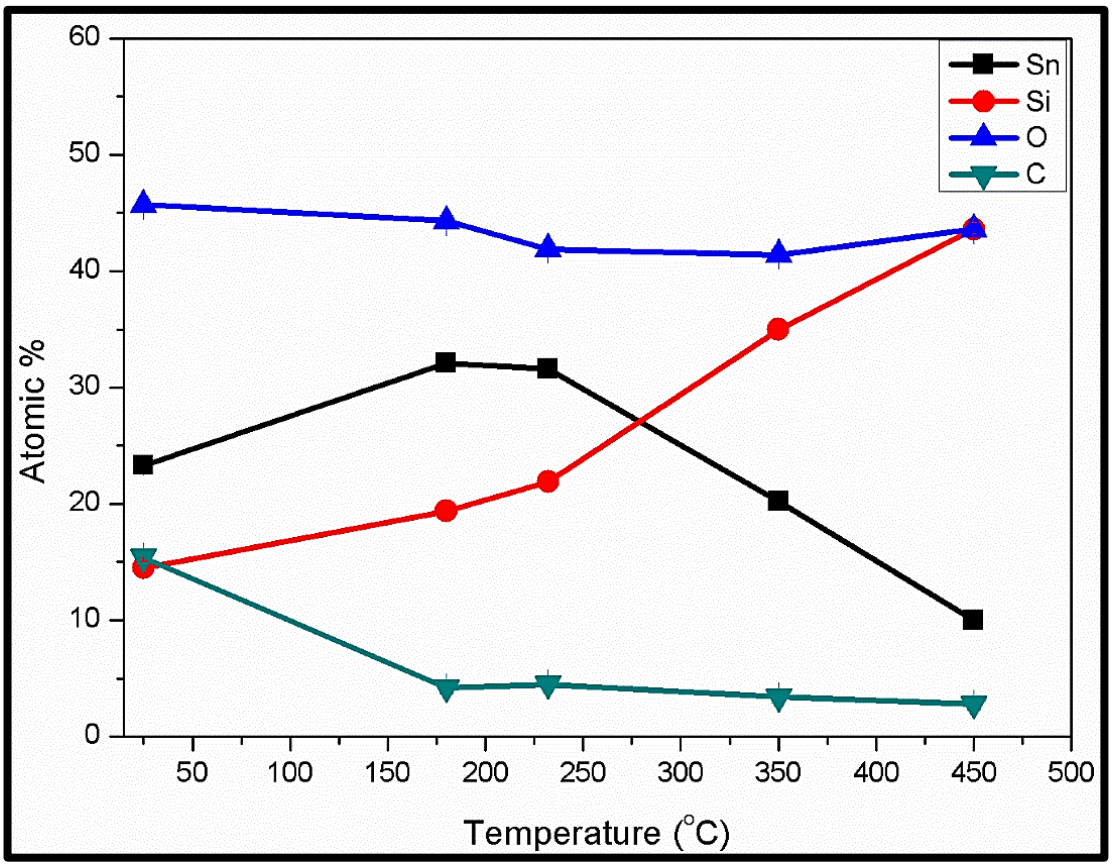

Figure 3.75: Atomic percentages of Sn, Si, O and C at various temperatures.

3.5 High resolution XPS analysis

Figure 3.76 displays high-resolution spectra of the Sn at as deposited temperature of 25 °C, 180, 232, 350 and 450 °C. The quantitative results will be from the $Sn3d^{5/2}$ because it possesses high intense order over $Sn3d^{3/2}$. The XPS results clearly show that the Sn is oxidised due to the presence of SnO / SnO_2. XPS has shown a peak at 485.7 eV and it is assigned to Sn and its oxide. Above the 232 °C, the SnO/Sn peak increases in intensity while the SnO_2 decreases in intensity. This observation can be due to decomposition of SnO_2 into Sn and O. The $Sn3d^{5/2}$ is observed to be shifting to lower binding energy which can be due to decrease of O content on the surface due to absorption of oxygen into the XPS vacuum. The Sn/SnO peak increases in intensity when reaching 350 °C which can be due to an increase in the O content possessed by Si substrate. The 450 °C sample indicates a single Sn/SnO peak, shifted from 485.7 eV to higher binding energy of 486.2 eV. The O content increases at a temperature of 450 °C, which can be attributed to the exposure of the Si substrate during the expected formation of the Sn nanoparticles.

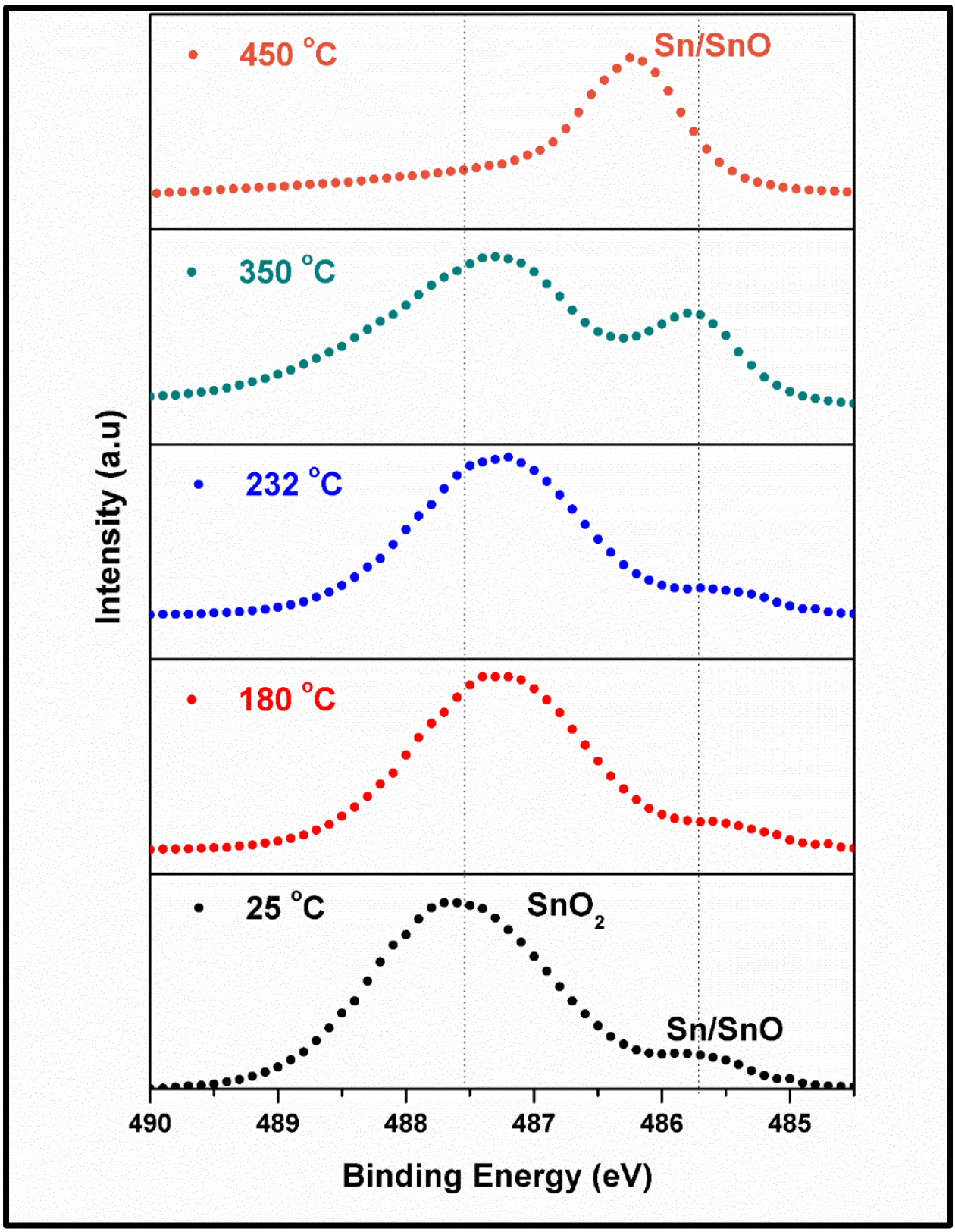

Figure 3.76: High resolution spectra of the Sn at as deposited (25 °C), 180, 232, 350 and 450 °C.

Figure 3.77 reveals the fitted high-resolution spectra of the as-deposited Sn film at as deposited (25 °C) and 450 °C. The high-resolution spectra of the Sn peak were deconvoluted using a mix Gaussian/Lorentzian area with peaks centred at 485.3 eV and 486.7 eV which correspond to pure Sn and SnO_2, respectively. At temperatures < 232 °C, the SnO_2 become a stable oxidation state of Sn, indicative of oxidation during the transferal of the sample from the thermal evaporator to the XPS system. As the temperature increases from 232 to 350 °C, the SnO_2 is converted to SnO while the intensity of the pure Sn peak. This is attributed to the Sn-oxides removed by the excessive heat exposing the pure underlying Sn. For the temperature 450 °C, it was observed that the pure Sn oxidises to SnO which can be due to the exposure of O residing at the Sn and Si interface. The main parameters used in the applied fitting procedure as well as the fitting parameters are summarised in table 3.2.

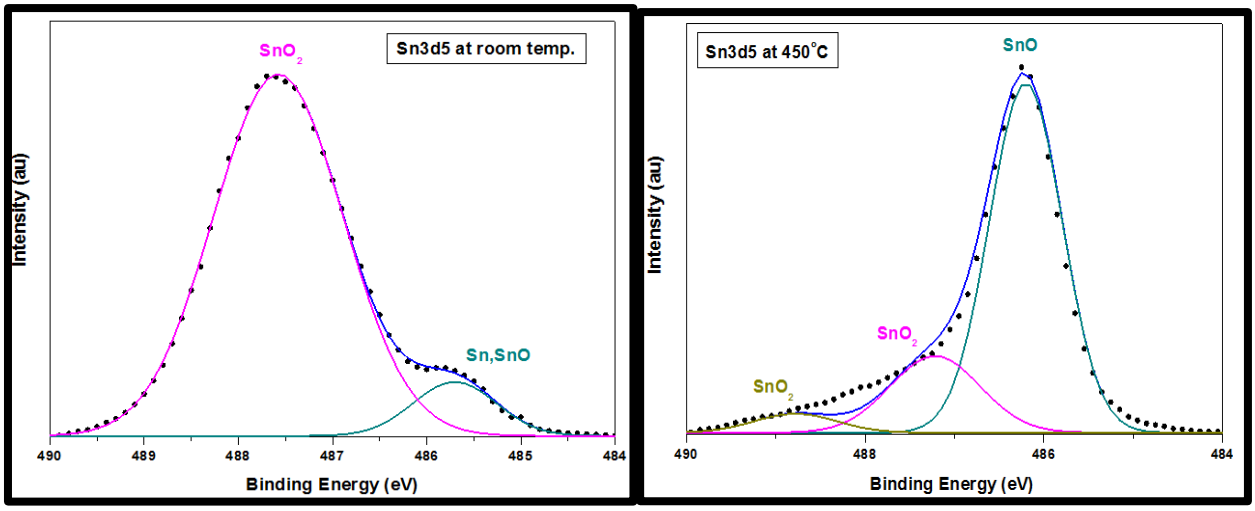

Figure 3.77: Fitted high-resolution spectra of the Sn at as deposited (25 °C) and 450 °C

Table 3.2: The atomic percentage, percentage area, binding energy, FWHM and probable bond(s)/compound of the XPS $Sn3d^{5/2}$ peak at as-deposited,180, 232, 350 and 450°C [3.26].

Temperature (°C)	Atomic %	Area (%)	Peak Position (eV)	*FWHM (eV)	Probable bond(s)/compound(s)
25	10	8.3	485.7	0.9	Sn; SnO
	90	91.7	487.6	1.6	SnO_2
180	9	9.8	485.7	1.6	Sn; SnO
	91	90.2	487.3	1.6	SnO ;SnO_2
232	9	9.8	485.6	1.5	Sn; SnO
	91	90.3	487.3	1.6	SnO_2
350	22	15.9	485.7	0.8	Sn; SnO
	78	84.1	487.4	2.0	SnO_2
450	86	73.7	486.2	0.9	SnO
	9	14.5	487.2	1.1	SnO_2
	5	11.8	488.3	1.7	SnO_2

*FWHM-Full Width Half Maximum

The 3 nm Sn thin film under XPS vacuum shows the surface oxidation with the high-resolution binding energy of 485.7 and 487.6 eV. According to NIST database the binding energy of pure Sn is at 485.0 eV. The temperature increase from 25 °C to 232 °C (Si-Sn eutectic temperature) [3.1] leads to elemental decomposition of SnO (10 %) and SnO_2 (90 %). There is no clear change on the Sn oxide which confirms the Sn-Si phase diagram that indicates that the change in the film surface can be observed above the Sn-Si alloy eutectic temperature (232 °C). The 350 °C indicates changes as the SnO_2 being reduced to 78 % and Sn/SnO to 22 % with the FWHM of 2.0 and 0.8 eV respectively. The increase in temperature does show the $Sn3d^{5/2}$ peak shift, at an average of about 0.6 eV to higher binding energy.

At the highest temperature of the experiment (450 °C), there is a third peak observed with high atomic content at the binding energy of 486.2 eV which is the SnO. The decrease in the O content can be observed as the SnO_2 with a difference of 5 % compared to Sn/SnO which is 9 %. The reduction of the SnO_2 to SnO occurs as the temperature increases where the SnO peak become narrower with the FWHM of 0.9 and SnO_2 become broader from a FWHM of 1.6 to 1.7 eV.

The Sn film surface shows a high amount of O, which can limit the growth of the Sn catalysed silicon nanowires. The relative concentration of pure Sn was calculated to determine the amount of the Sn in SnO_2 as the temperature increases. Table 3.3 shows the relative concentration of pure Sn in SnO_2.

Table 3.3: Relative concentrations of Sn in SnO_2 from room temperature, 180, 232, 350 and 450 °C.

Temperature (°C)	[Sn]/[SnO_2]
As deposited	9.22 ± 0.05
180	13.75 ± 0.05
232	13.64 ± 0.05
350	34.08 ± 0.05
450	3.33 ± 0.05

The relative concentration is calculated using the relative sensitive factors ($Sn3d^{5/2}$:22.00) of each element and the scaled peak area. The results show that at 25 °C only 9.22 % of [Sn]/ [SnO_2] remained on the surface and it increases to 34.08 % as the temperature increases to 350 °C. The sample heating leads to thermal decomposition, this observation can be due to the O being released form the sample and absorbed in the XPS vacuum. At the highest temperature (450 °C) the Sn concentration decreases to 3.3 %. The decrease in the Sn concentration relative to the SnO_2 can be due to the Sn-oxides at the Sn and Si interface as observed in the XPS high-resolution spectra as illustrated in figure 3.78.

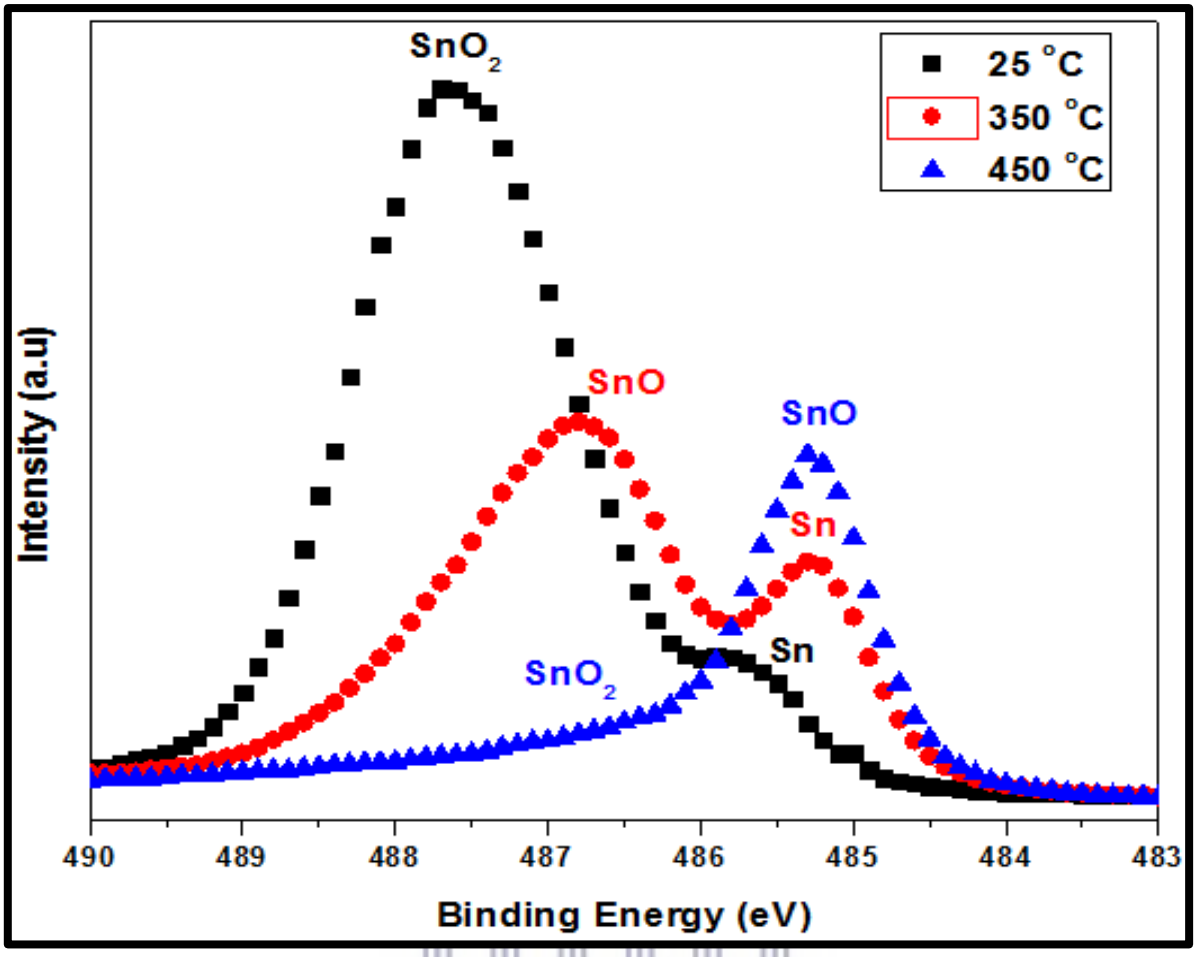

Figure 3.78: High resolution spectra of the Sn at as deposited (25 °C), 350 and 450 °C.

Figure 3.79 shows the high-resolution spectra of the Si at room, 180,232, 350 and 450 °C. The Si spectrum at < 232 °C is consistent to the typical Si2p XPS spectrum [3.28]. The broad Si2p peak does show a double peak formation at higher binding energy (eV). The Si2p peak shift from 99.9 eV to 100.9 eV and the SiO_2 peak increases in intensity as the temperature increases which is due to the thickness of the oxygen layer.

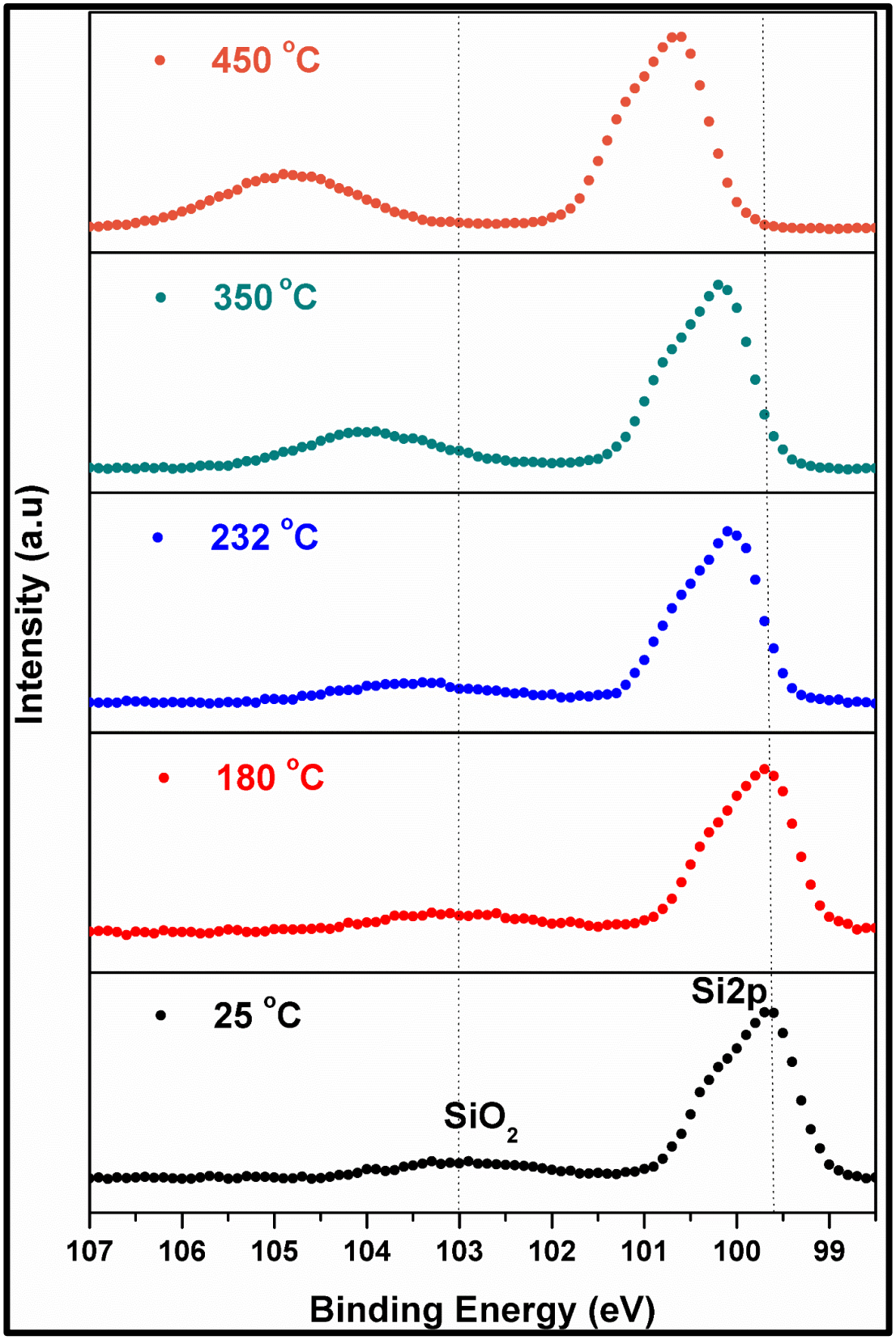

Figure 3. 79: High-resolution spectra of the Si at room temperature, 180, 232, 350 and 450 °C.

Figure 3.80 shows the fitted high-resolution spectra of the Si at room, 180 and 450 °C. The high-resolution Si spectra indicate the pure Si2p deconvoluted into $Si2p^{1/2}$ and $Si2p^{3/2}$ double spin-orbital, which are separated by 0.6 eV with the intensity ratio of 0.5. The asymmetric Si peak is observed at the temperatures < 232 °C. There is a Si oxide peak with low intensity with at binding energy of 102.2 eV. The SiO_2 from the Si substrate becomes prominent at temperatures at 350 to 450 °C which can be the O at the Si and Sn interface. The intense Si peaks become more defined at 450 °C. The main parameters used in the applied fitting procedure as well as the fitting parameters are summarised in table 3.3.

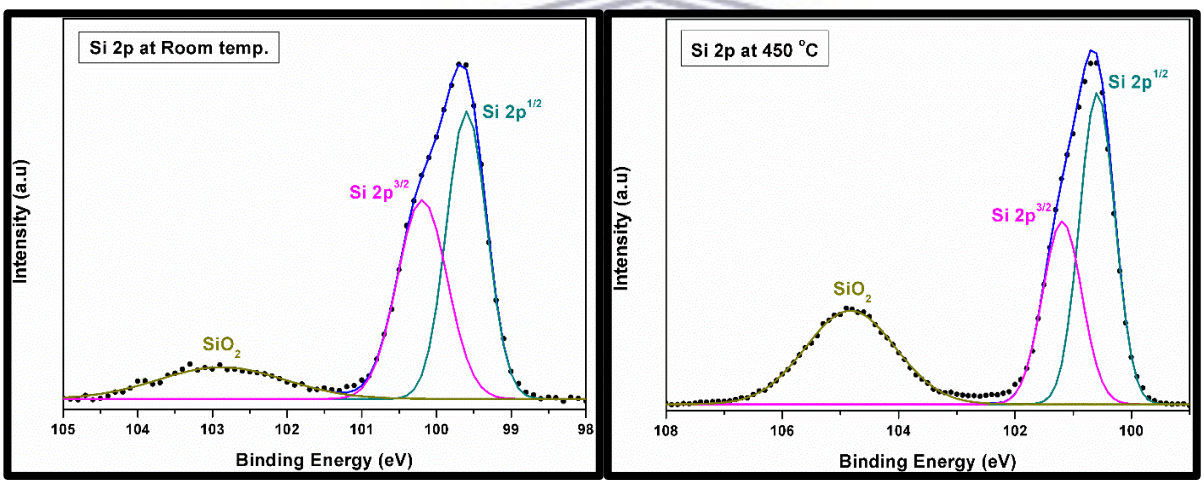

Figure 3.80: Fitted high- resolution spectra of the Si as deposited and 450 °C.

Table 3.3: The atomic %, % area, binding energy, FWHM and probable bond(s)/compound of the XPS Si2p peak of temperatures, as-deposited, 180, 232, 350 and 450 °C [3.26].

Temperature (°C)	Atomic %	Area (%)	Peak Position (eV)	*FWHM (eV)	Probable bond(s)/compound(s)
25	48	45.4	99.6	0.6	Si $2p^{1/2}$
	39	38.9	100.2	0.8	Si $2p^{3/2}$
	13	15.7	102.9	1.9	SiO_2
180	51	48.0	99.6	0.7	Si $2p^{1/2}$
	34	31.6	100.3	0.8	Si $2p^{3/2}$
	15	20.3	102.9	2.4	SiO_2
232	51	40.4	99.9	0.6	Si $2p^{1/2}$
	34	40.9	100.5	0.8	Si $2p^{3/2}$
	15	18.6	103.4	2.1	SiO_2
350	69	46.6	100.1	0.68	Si $2p^{1/2}$
	16	27.1	100.8	0.70	Si $2p^{3/2}$
	15	26.3	103.9	1.9	SiO_2
450	44	37.7	100.6	0.7	Si $2p^{1/2}$
	27	29.0	101.2	0.8	Si $2p^{3/2}$
	29	33.3	104.8	1.9	SiO_2

*FWHM-Full Width Half Maximum

The Si2p peak FWHM broadens with an increasing temperature up to 232 °C, which can be due to the Si oxidation. The FWHM of the broad SiO_2 peak makes the Si2p peak to shift to a higher binding energy with an average of about 1.7 eV. The 350 °C indicates the at.% of the deconvoluted Si2p peaks ($Si2p^{1/2}$ and $Si2p^{3/2}$) shows the

increases from 48 % to 69 % for the $Si2p^{1/2}$ and decrease for the $Si2p^{3/2}$ from 39 % to 16 % as temperature increases. Ley *et al.* [3.27] studied amorphous Si and found that the broadening in the XPS Si-2p peaks was due to a distribution of chemically shifted Si-2p lines. This shift occurred because of random charge fluctuations as the result of bond length variations in the SiO_2 amorphous network. The highest temperature (450 °C) of the experiment shows the $Si2p^{1/2}$ decrease in the at. % to 44 % while the $Si2p^{3/2}$ becomes 27 % and the SiO_2 increases further from 13 to 29 %.

Based on the discussions of the XPS technique in chapter 2, the photoelectron escape depth is about 2-10 nm, which means that XPS can detect the contaminations such as oxygen (O) and carbon (C) on the surface (observed from the survey spectra). The Sn film oxidation was observed as the XPS results indicated the presence of SnO_x peaks.

Figure 3.81 displays the high-resolution spectra of the O bonds at room (as-deposited), 180, 232, 350 and 450 °C. The metal oxide peak at room temperature was detected which indicates the surface oxidation. The metal oxide can be assigned to the oxidised Sn thin film as it was also observed on the Sn spectra. The broad metal oxide shows that there can be double peak present. At 180 °C a peak is formed with the binding energy of 532.8 eV which corresponds with SiO_2, O-(C-H) bond/compound.

At a temperature of 350 °C, the SiO_2 peak becomes broader and more intense as compared to the metal oxide peak, which can be due to oxygen situated between Si and Sn film. The SiO_2 originate from the Si substrate. At 450 °C only the SiO_2 peak at 534.2 eV was detected, which can be the exposure of the Si substrate due to the formation Sn nanoparticles. According to Floro *et al.* [3.28], the presence of the SiO_2 peak can also indicate the Volmer-Weber thin film growth, where the direct nucleation of small clusters to the substrate surface, resulting in coalescence into a continuous film. Even though the Si wafer was dipped into hydrofluoric acid (HF) to remove the oxide, the Si can be easily oxidised due to atmospheric air if it is not completely covered with the thin film.

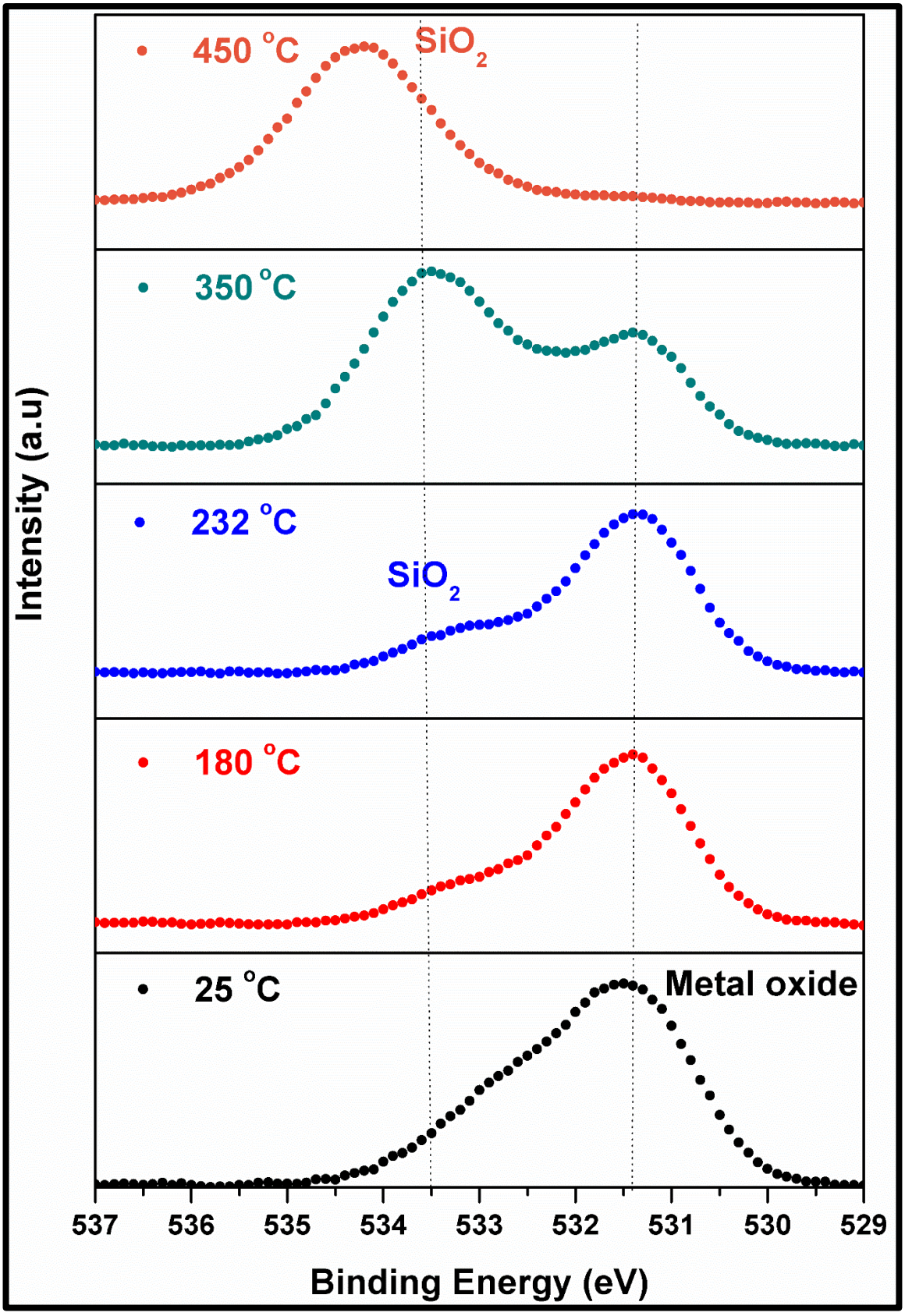

Figure 3.81: High-resolution spectra of O at as deposited,180, 232, 350, and 450 °C

Figure 3.82 shows the fitted high-resolution spectra of the O at room (as-deposited), 180 and 450 °C. From the quantitative observations, the O1s peak displayed a peak formation, after the deconvolution, SiO_2 is observed with the binding energy of 532.5 eV while the metal oxide peak is at 531.3 eV. The SiO_2 is broad with low intensity as compared to the metal oxide peak. At the highest temperature of the analysis (450 °C), the metal oxide is no longer visible and only the SiO_2 remains which can be the Si substrate which indicates the film agglomeration. The main parameters used in the applied fitting procedure as well as the fitting parameters are summarised in table 3.4.

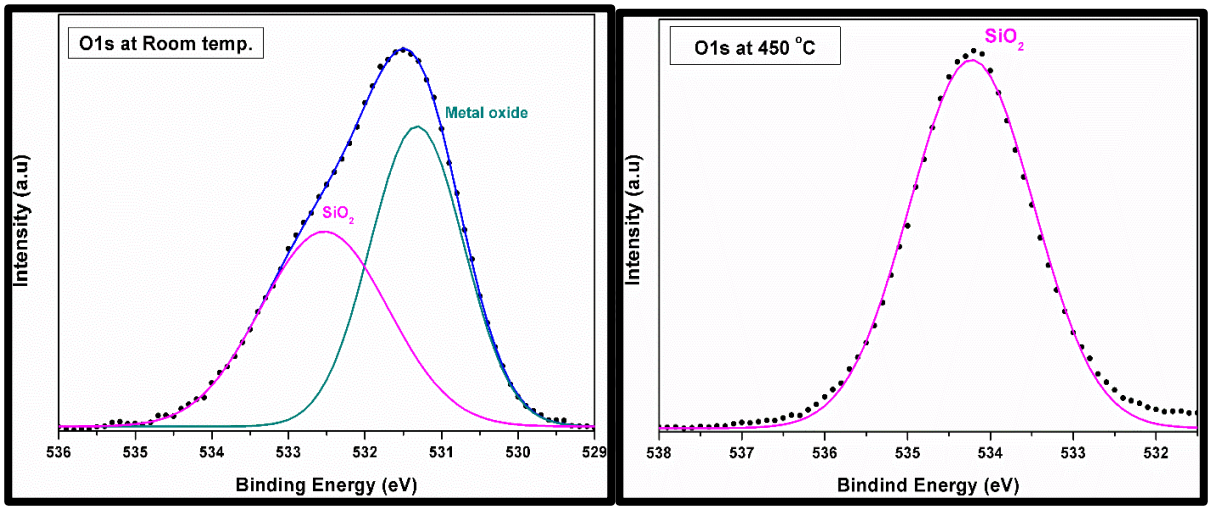

Figure3.82: Fitted high-resolution spectra of the O at as deposited and 450 °C

Table 3.4: The atomic %, % area, binding energy, FWHM and probable bond(s)/compound of the XPS O1s peak of temperatures, as-deposited,180, 232, 350 and 450 °C [3.26]. The metal oxide is observed on the as-deposited O1s spectra with the at. % of 54 % and SiO_2, O-(C, H) with 46 %. The increase in metal oxide at 180 °C and a sudden drop at > 180°C was detected, which indicates the removal of O film with the increase in temperature.

Temperature (°C)	Atomic %	Area (%)	Peak Position (eV)	*FWHM (eV)	Probable bond(s)/compound(s)
25	54	53.1	531.3	1.4	Metal oxide
	46	46.9	532.5	1.9	SiO_2; O- (C, H)
180	80	74.1	531.4	1.4	Metal oxide
	20	25.9	532.9	1.8	SiO_2; O- (C, H)
232	78	74.9	531.4	1.4	Metal oxide
	22	25.1	532.9	1.6	SiO_2; O- (C, H)
350	22	21.3	531.2	1.2	Metal oxide
	29	22.6	532.2	1.6	SiO_2
	49	56.1	533.5	1.5	C-O (ether) as SiO_2
450	100	100	534.2	1.8	SiO_2

*FWHM-Full Width Half Maximum

Figure 3.83 illustrates high-resolution spectra of C at as deposited,180, 232, 350 and 450 °C. The adventitious carbon peaks were observed which can be due to the surface contamination because the intensity of the carbon peaks decreases with the increase in temperature. The C1s peak at as deposited is relatively broader, asymmetrical feature that occurs at the binding energy of 285.6 eV [3.26]. The quantitative analysis was conducted by fitting of the peaks at room temperature (25°) and 450 °C.

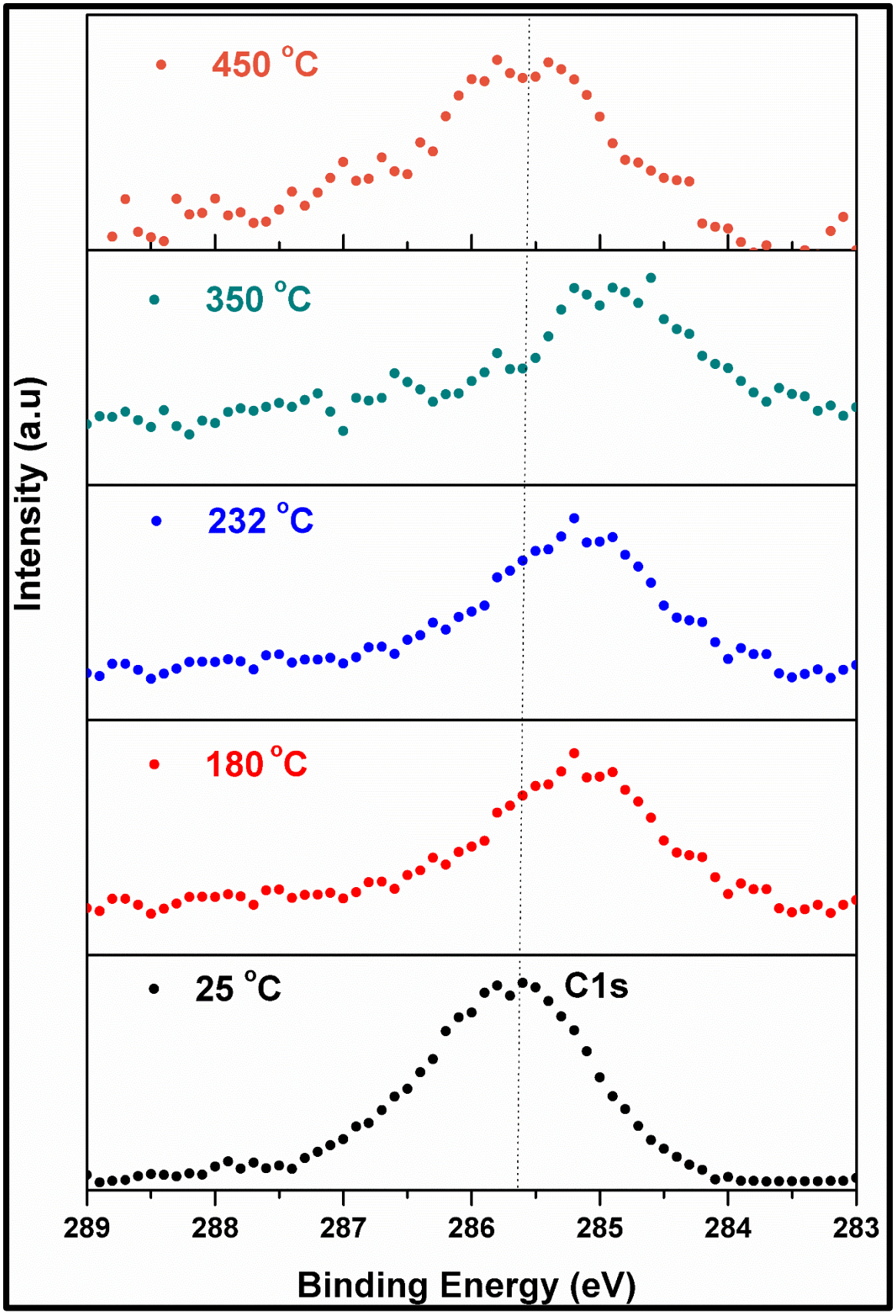

Figure 3.83: High-resolution spectra of C at as deposited, 180, 232, 350 and 450 °C

Figure 3.84 displays the fitted high-resolution spectra of the carbon at room temperature (as-deposited), 180 and 450 °C. The increase in temperature reduces the intensity of the carbon peak. At 450 °C, the C peak is found to have shifted by 0.1 eV towards high energies, which can be due to conductive sample. The C peak at 450 °C has lower intensity as compared to the room temperature. The C1s peak shift to lower binding energy of around 285 eV which is the peak value used for XPS calibration [3.13].

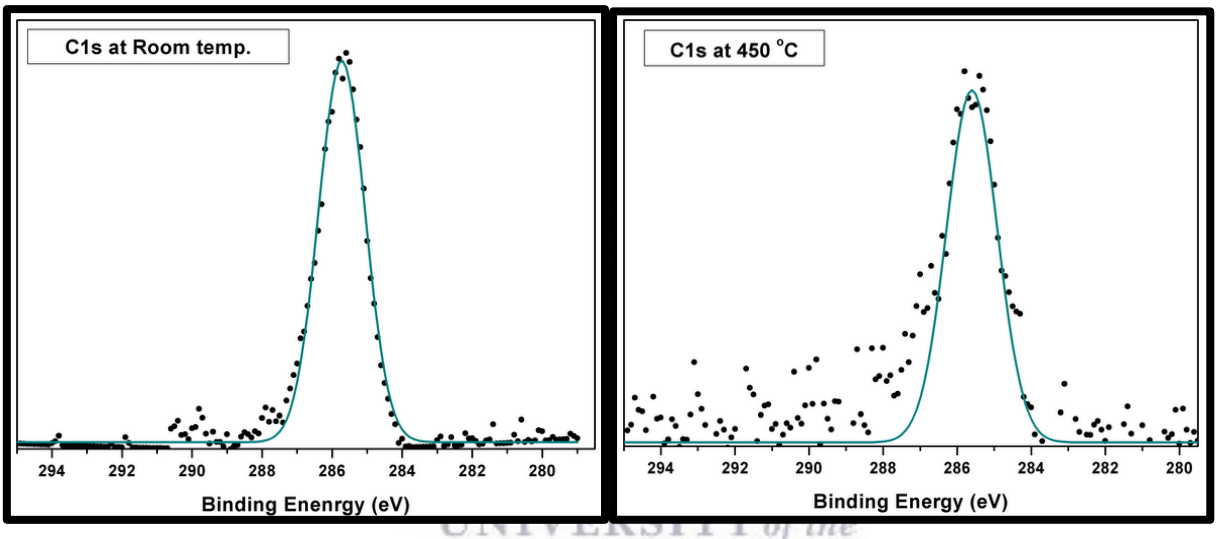

Figure 3.84: Fitted high-resolution spectra of C at as deposited and 450 °C

Table 3.5: The atomic %, binding energy, FWHM and probable bond(s)/compound of the XPS C1s peak of temperatures, as-deposited, 180, 232, 350 and 450 °C [3.26].

Temperature (°C)	Atomic %	Peak Position (eV)	*FWHM (eV)	Probable bond(s)/compound(s)
25	15.4	285.7	1.6	C- (C, H, O)
180	4.2	285.4	1.6	C- (C, H, O)
232	4.5	285.2	1.6	C- (C, H, O)
350	3.4	284.9	1.9	C- (C, H, O)
450	2.8	285.7	2.1	C- (C, H, O)

*FWHM-Full Width Half Maximum

The C1s peak indicates a decrease in atomic content as the temperature increases. The FWHM shows the direct proportionality with temperature. The peak position is observed to be a non-linear in respect to temperature increase and the peak shift has a difference of about 0.7 eV.

3.4 Oxidation states of Sn

Figure 3.85 displays the fitted high-resolution spectra of $Sn3d^{5/2}$ and O1s at room temperature. The surface oxidation was further analysed to determine the behaviour of oxidised Sn and Si using the high-resolution XPS results. The chemical compositions (atomic ratio) and oxidation states of Sn (Sn^{0+}, Sn^{2+}, and Sn^{4+}) in the SnOx thin-films could be examined quantitatively by deconvolution the $Sn3d^{5/2}$ spectra superimposed by the Sn^{0+}, Sn^{2+}, and Sn^{4+} components. The oxidation is confirmed by the shape analysis of the corresponding XPS $Sn3d^{5/2}$ and O1s peaks at 180 °C. The $Sn3d^{5/2}$ spectrum shows a broad as compared to the normal Sn peak and asymmetric peak which contains Sn oxidation states such as Sn^{2+} (485.7 eV) and Sn^{4+} (487.6 eV) [3.29]. The two components corresponding to Sn^{2+} and Sn^{4+} ions are separated by binding energy of 1.7 eV. The Sn thin film shows that it contains a mixture of tin oxide (SnO) and tin dioxide (SnO_2).

The O1s peaks also show that it is a wide and asymmetric that exhibits an evident shoulder at the high binding energy side of the spectrum. It is evident that it should contain the components corresponding to O atoms (ions) in bonding with various Sn atoms (ions) at the oxidising steps. The two components corresponding to the O-Sn^{4+}(531.3 eV) [3.30] and O-Si^{2+}(532.5 eV) [3.31,3.32] separated by binding energy of 1.5 eV. The O-Si^{2+} oxidation step was considered because of the thickness (3 nm) of the Sn thin film as well as the photoelectron escapes depth (2-10 nm) of the XPS technique. The change in the peak shape is also observed at 350°C.

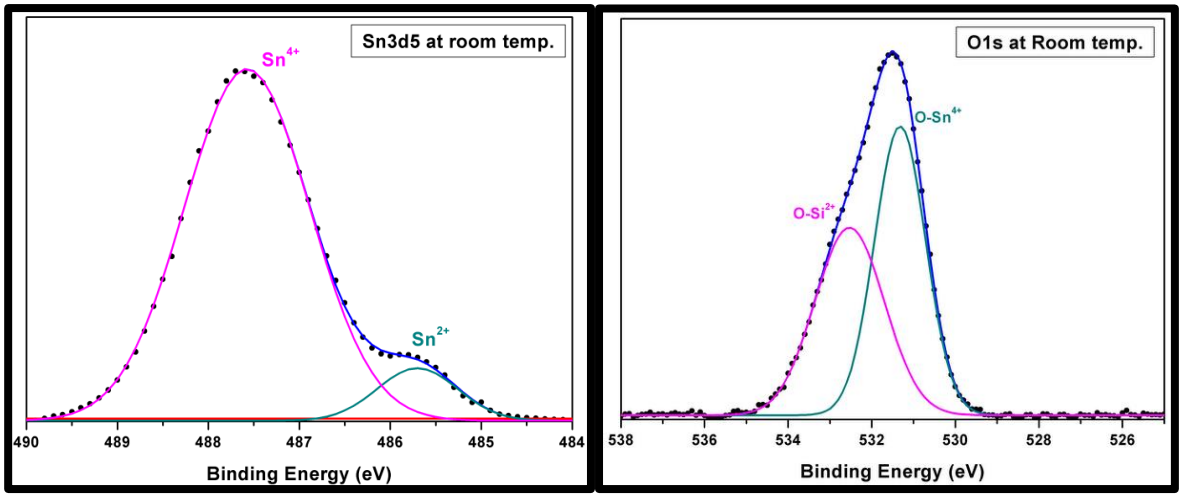

Figure 3.85: Fitted high-resolution spectra of sn3d$^{5/2}$ and O1s at room temperature.

Figure 3.86 displays the fitted high-resolution spectra of $Sn3d^{5/2}$ and O1s at 350 °C. The $Sn3d^{5/2}$ peaks are wide as compared to the pure Sn peak and asymmetrical with the oxidation states of Sn^{2+} and Sn^{4+} at higher binding energies of 485.7 eV and 487.4 eV, respectively. The Sn^{4+} peak which corresponds to SnO_2 has lower atomic content (at %) of 78%. The Sn^{2+} ion which corresponds to the SnO has higher at% of 22% as compared to the as deposited peaks. The reduced oxidation can be due to the increase in temperature leading to the O being absorbed in the vacuum.

The O1s peak is broad as compared the pure O peak and asymmetrical. The peak shape has taken the $Sn3d^{5/2}$ peak which is superimposed by the, $O\text{-}Sn^{2+}$, $O\text{-}Si^{2+}$ and $O\text{-}Si^{4+}$ components. The $O\text{-}Sn^{2+}$ peak at 531.2 eV with atomic content of 21.3 %. During air exposure, more of the O is absorbed on the film while some amounts of O are transferred towards deeper regions of the film. The Si spectra displays oxidation states that corresponds to the $O\text{-}Si^{2+}$ (532.2 eV) and (C-O (ether) as SiO_2) $O\text{-}Si^{4+}$ (533.5 eV) ions having the at% of 29% and 49%, respectively. The increase in the O content on the Si and Sn interface can be due to the Si oxidation.

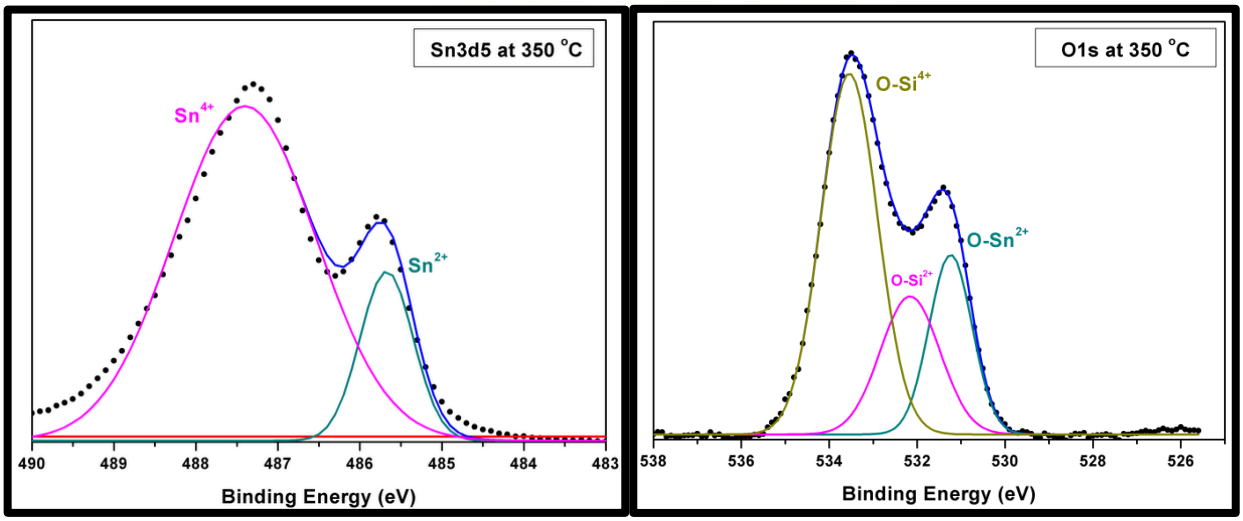

Figure 3.86: Fitted high-resolution spectra of $Sn3d^{5/2}$ and O1s at 350 °C.

A summary of the oxidation states of Sn and Si is shown in Tables 3.6 and 3.7, respectively.

Table 3.6: Oxidation states of Sn at room temperature, 180,232,350, and 450 °C.

Temperature (°C)	O1s ($Sn3d^{5/2}$) at. %		$Sn3d^{5/2}$ at.%	
	$O – Sn^{2+}$	**$O – Sn^{4+}$**	**Sn^{2+}**	**Sn^{4+}**
As deposited	54	46	10	90
180	80	20	9	91
232	78	22	9	91
350	22	-	22	78
450	-	-	86	14

Table 3.7: Oxidation states of Si at room temperature, 180,232,350, and 450 °C.

Temperature (°C)	O1s (Si2p) at. %		Si2p at. %				
	$O-Si^{2+}$	**$O-Si^{4+}$**	**Si^{0+}**	**Si^{1+}**	**Si^{2+}**	**Si^{3+}**	**Si^{4+}**
As deposited	-	-	48	39	-	13	-
180	-	-	51	34	-	-	15
232	-	-	51	34	-	-	15
350	29	49	69	16	-	-	15
450	-	100	-	44	27	-	29

3.5 Depth profile

The presence of oxygen (O) in silicon can form a deep level impurity, blocking carrier charge within the solar cell. Oxygen can also influence the growth of the Sn catalyst silicon nanowires via the VLS mechanism, as it forms a hard cover shell over the metal catalyst nanoparticles preventing the gaseous Si atom to diffuse in the catalyst to form a nanowire. The O at the Sn/Si interface (as observed in section 3.6) can limit the growth of the nanowires by creating the amorphous layer at the interface, preventing the gaseous Si to be saturated at the Sn/Si interface.

Probing the thin film surface with an ion sputter gun to determine the internal layer diffusion of O was found to be the ideal method to understand the amount and location of O in the Sn and Si interface.

The XPS depth profile analysis was done using a beam of argon clusters. The thickness of the film, most of the Sn might not be detected due to rapid material removal. Moreover, Ar sputtering may lead to the creation of amorphous Si (aSi) [4.33, 4.34] but the Ar cluster sputtering overcomes the limitations of Ar ion sputtering by employing a cluster of Ar impinging on the film surface. The larger Ar clusters ensures that the beam impinge with less energy on the film surface which results in a reduced rate of material removal suitable for photoelectron detection from thin films < 10 nm.

The sputter analysis was done up to the Si substrate to determine the film composition as it was observed to have oxides. The as deposited, 350 and 450 °C annealed samples were analysed as they have shown changes in the surface analysis. Figure 3.87 presents the full overview of the sputter profiles of the as deposited sample and subsequently annealed at 350 °C and 450 °C.

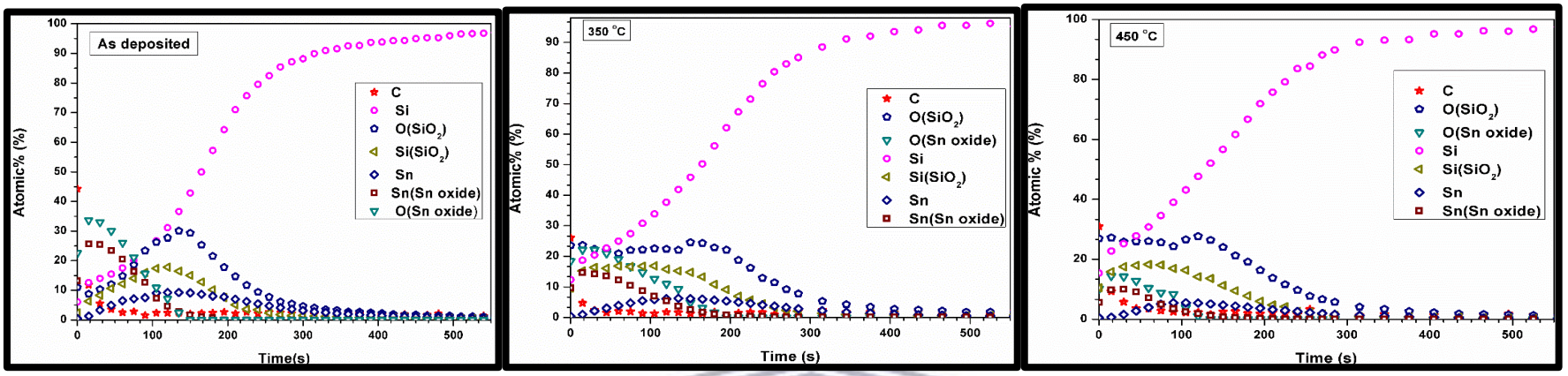

Figure 3.87: Overview of the sputter profile of the as deposited, 350 °C and 450 °C.

The as deposited ,350 and 450 °C sputter profiles shows a clear behaviour of the oxidised metal oxide as the temperature increases. The carbon contamination is limited to the sample surface. The Si profile does show that it is the bulk material as it forms broader slope within the time range (600 s) .The profiles were separated to understand the behaviour of each element with an increasing temperature.

Figure 3.88 illustrates the comparison of pure Sn and Si elements with their respective oxides at the temperatures: as-deposited, 350 and 450 °C. The oxides are the SnO_2 detected in the $Sn_3d^{5/2}$, metal oxide detected on the O1s, SiO_2 detected on the Si2p and SiO_2 detected on the O1s high resolution spectra.

The temperature increases lead to a decrease in the atomic % (at. %) and sputter time. The agglomeration process (forming larger Sn particles) as the temperature increases was detected as the sputter profile shows the decrease in the spread of Sn nanoparticles on the Si surface. Moreover, the amount of pure Sn can be reduced through oxidation of which some of the O can be absorbed in the XPS vacuum when annealed. This is observed when the SnO_2 from the $Sn3d^{5/2}$ spectra decrease in at. % while the sputter time is reduced from 145 s (as deposited) to 120 s for the sample annealed at 450 °C. The SnO_2 from $Sn3d^{5/2}$ spectra shows no linearity in the sputter time since the 350 °C has sputtered to completion for 180 s which is longer as compared to as deposited (145 s) and 450 °C (120 s). The same observations were found on the metal oxide detected in O1s spectra, where the sputter time is 224 s to completion for 350 °C and 450 °C (188 s). The longer etching time can be due to O on the Si substrate; this can be explained on the Si2p spectra.

The SiO_2 detected on the Si2p spectra shows that as the temperature increases the SiO_2 content decreases but the 350 °C sample indicated an increase in O content which can be located on the Si substrate. The as-deposited sample took longer to etch to completion (800 s) as compared to 350 °C and 450 °C (720 s). The results are consistent with the SiO_2 detected on the O1s spectra (see Figure 3.80).

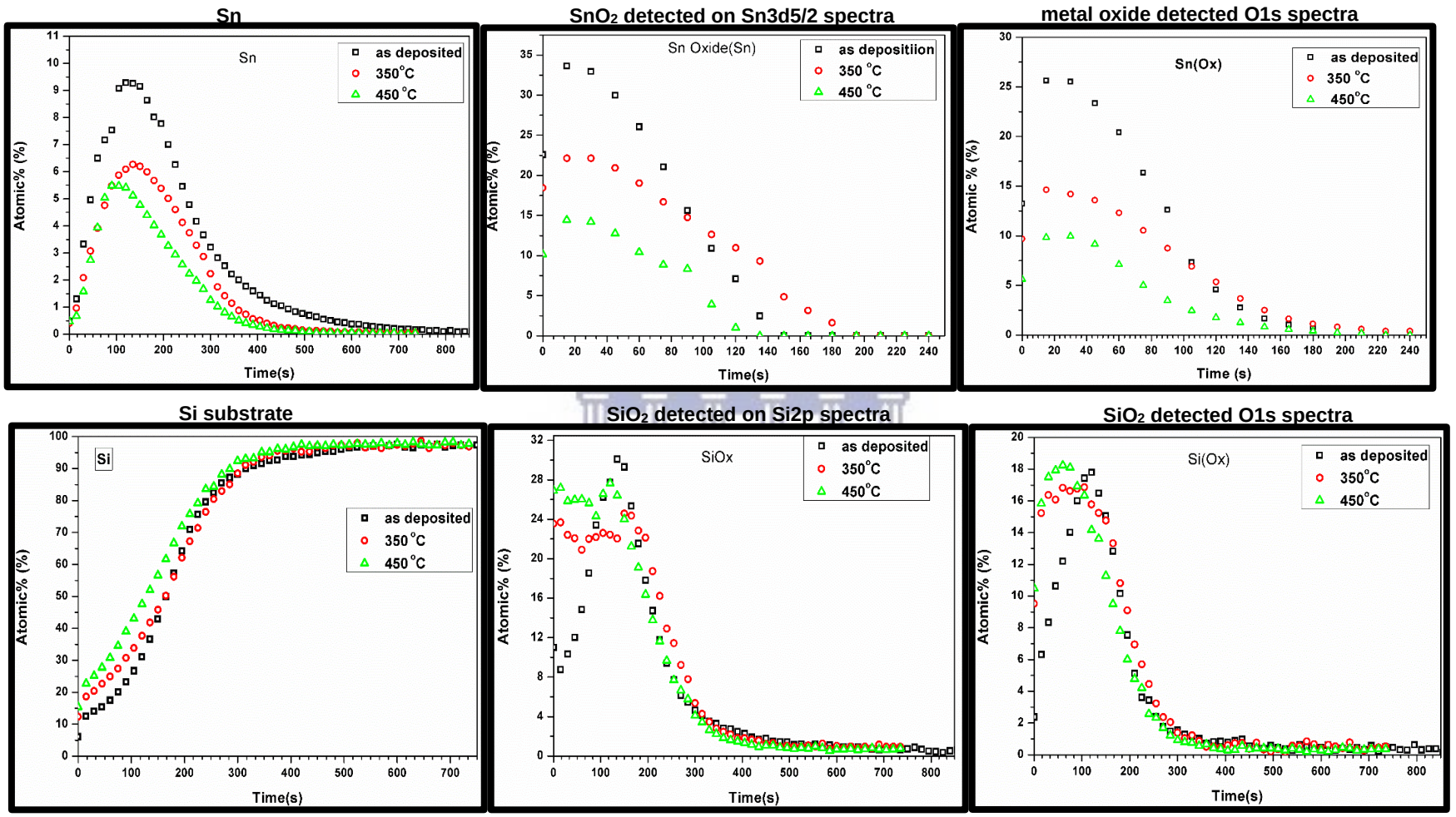

Figure 3.88: Comparison of pure Sn and Si elements with their oxides at the temperatures, as deposited, 350 and 450°C.

Figure 3.89 presents the high-resolution analysis for oxygen, tin and silicon during the sample sputtering period. The high-resolution (HR) spectra reveals information regarding the surface, Sn/O interface and the Sn/Si interface regions during the sputtering process. The surface of the thin film consists of a metal oxide (SnO_x) which was identified as Sn dioxide (SnO_2) according to the NIST database, (see the as deposited Sn HR spectra in Figure 3.76). The Sn/O interface shows SnO_2 reduced to SnO while the SiO_2 from the Si substrate is detected on the O1s spectra. The reduction of the SnO_2 is also observed in Sn spectra and the SiO_2 in the Si spectra at 350 °C. The O1s spectra at 350 °C displayed the SnO_x signal at the Sn/Si interface. Pure Sn is detected on the Sn/O and Sn/Si interface at the Sn spectra at the temperatures displayed. This clearly indicates that Sn is not completely oxidised, which is beneficial for SiNW synthesis.

The SiO_2 diminishes and only Si is detected at the silicon (Sn/Si interface) spectra at temperatures > 232 °C. The increase in temperature to 350 °C shows a decrease in the Sn intensity and at 450 °C the pure Sn has higher intensity at Sn/O but low at the Sn/Si interface. This can be explained by the removal of the oxides and contaminations with an increase in temperature exposing the pure Sn.

The depth profile and XPS results, does show the presences of the pure Sn which leads to the possibility of SiNW synthesis with the assistance of the hydrogen plasma treatment to remove the access O on the Sn surface and the Sn/Si interface.

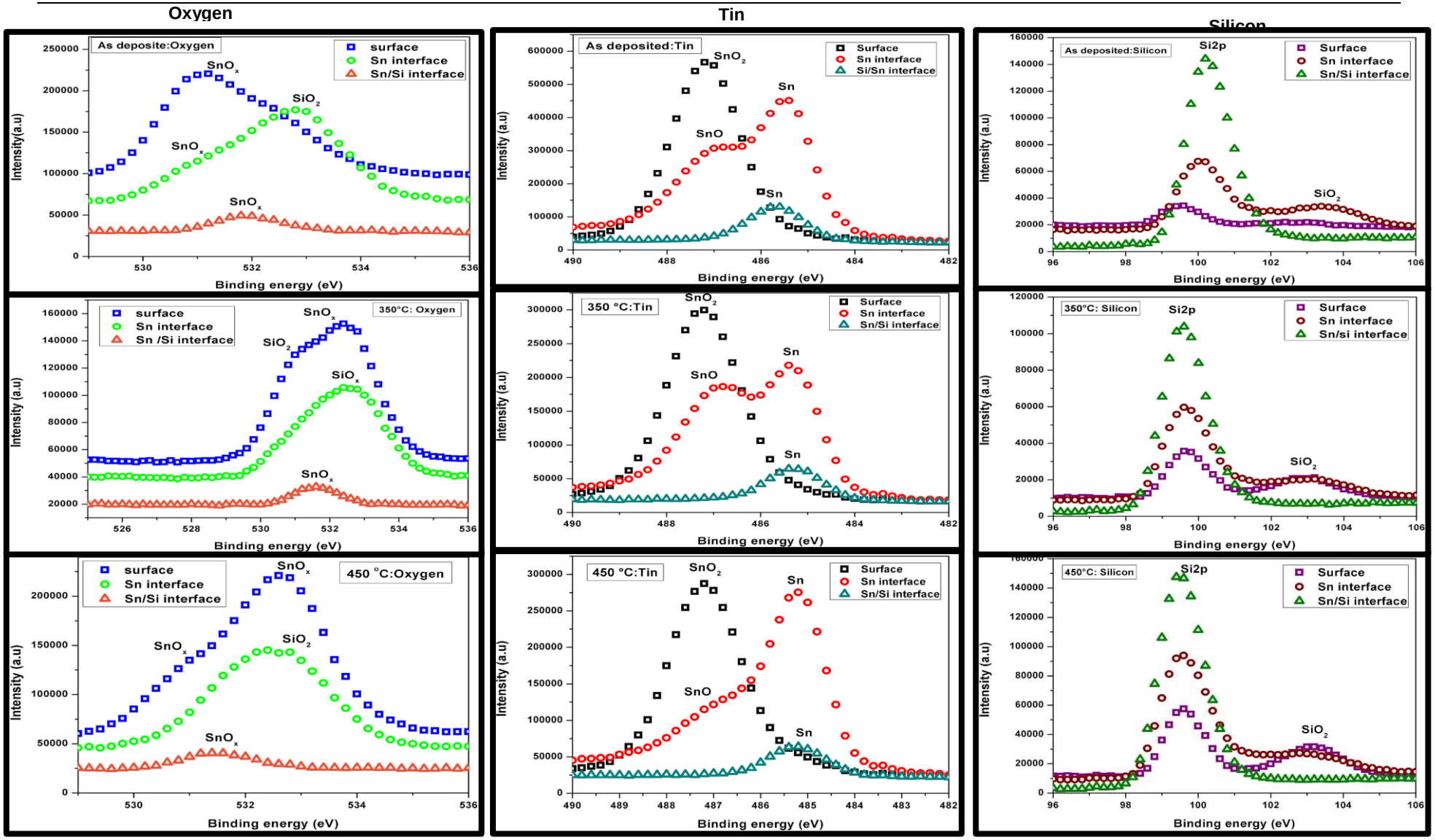

Figure 3.89: High resolution analysis for oxygen, tin and silicon.

3.6 CONCLUSION

A 3 nm Sn thin film evaporated onto a Si (100) wafer was subjected to different annealing temperatures within an XPS high vacuum system. The chemical behaviour of Sn, O and Si elements in the sample were observed when monitoring the change in the corresponding binding energies at a varying XPS stage temperature. The sample was contaminated since adventitious carbon was observed in as deposited sample and decreased as the temperature increased. The atomic content of Sn increases till 232 °C and then decreased at the 350 °C, which could probably indicate the formation of isolated Sn nanoparticles. This observation was consistent with the exposure of the Si substrate atomic content increase with temperature. The Sn and Si oxides were observed which could be due to the exposure to atmospheric air. The depth profile analysis indicated the oxides reside on the Sn film surface and at the Sn/Si interface. The pure Sn is not completely oxidised which bodes well for SiNW synthesis.

References

3.1 Al-Taay, H. F., M. A. Mahdi, D. Parlevliet, and P. Jennings. "Controlling the diameter of silicon nanowires grown using a tin catalyst."Materials Science in Semiconductor Processing 16, no. 1 (2013): 15-22.

3.2 Choi, Heon-Jin. "Vapor–liquid–solid growth of semiconductor nanowires." In Semiconductor Nanostructures for Optoelectronic Devices, pp. 1-36. Springer Berlin Heidelberg, 2012.

3.3 Wagner, R. S., and W. C. Ellis. "Vapor-liquid-solid mechanism of single crystal growth."Applied physics letters 4, no. 5 (1964): 89-90.

3.4 K. A. Dick, “A review of nanowire growth promoted by alloys and non-alloying elements with emphasis on Au – assisted iii-v nanowires,” Prog. Cryst. Growth Charact. Mater. 54(3-4), 138–173 (2008).

3.5 V. Schmidt, J. V. Wittemann, and U. Gösele, “Growth, thermodynamics, and electrical properties of silicon nanowires,” Chem. Rev. 110(1), 361–388 (2010).

3.6 Schmidt, Volker, Joerg V. Wittemann, Stephan Senz, and Ulrich Gösele. "Silicon nanowires: a review on aspects of their growth and their electrical properties." Advanced Materials 21, no. 25-26 (2009): 2681-2702.

3.7 D.A. Fraser, The Physics of Semiconductor Devices, Clarendon press, Oxford University Press, New York, USA, 1986.

3.8 Misra, Sou, Linwei Yu, Martin Foldyna, and Pere Roca iCabarrocas. "High efficiency and stable hydrogenated amorphous silicon radial junction solar cells built on VLS-grown silicon nanowires.”Solar Energy Materials and Solar Cells 118 (2013): 90-95

3.9 Nebol'sin, V. A., A. A. Shchetinin, A. A. Dolgachev, and V. V. Korneeva. "Effect of the nature of the metal solvent on the vapor-liquid-solid growth rate of silicon whiskers." Inorganic materials 41, no. 12 (2005): 1256-1259

3.10 Kumar, R. Rakesh, K. Narasimha Rao, K. Rajanna, and A. R. Phani. "Growth of tin catalysed silicon nanowires by electron beam evaporation." Adv Mater Lett 4 (2013): 836-840.

3.11 Mullane, Emma, Tadhg Kennedy, Hugh Geaney, Calum Dickinson, and Kevin M. Ryan. "Synthesis of tin catalysed silicon and germanium nanowires in a solvent–vapor system and optimization of the seed/nanowire interface for dual lithium cycling." Chemistry of Materials 25, no. 9 (2013): 1816-1822.

3.12 Fondell, Mattis, Mihaela Gorgoi, Mats Boman, and Andreas Lindblad. "An HAXPES study of Sn, SnS, SnO and SnO 2."Journal of Electron Spectroscopy and Related Phenomena 195 (2014): 195-199.

3.13 Kwoka, Monika, Luca Ottaviano, Piotr Koscielniak, and Jacek Szuber. "XPS, TDS, and AFM studies of surface chemistry and morphology of Ag-covered L-CVD SnO2 nanolayers."Nanoscale research letters 9, no. 1 (2014): 260.

3.14 Wang, Ying-Hui, Matiar R. Howlader, Kenji Nishida, Takashi Kimura, and Tadatomo Suga. "Study on Sn–Ag oxidation and feasibility of room temperature bonding of Sn–Ag–Cu solder."Materials transactions” 46, no. 11 (2005): 2431-2436.

3.15 Rabis, Annett. "The Impact of Metal Oxides on the Electrocatalytic Activity of Platinum Catalysts." PhD diss., 2015.

3.16 Kwoka, Monika, and Maciej Krzywiecki. "Impact of air exposure and annealing on the chemical and electronic properties of the surface of SnO2 nanolayers

deposited by rheotaxial growth and vacuum oxidation."Beilstein journal of nanotechnology (2017): 514.

3.17 Abad, J., C. Gonzalez, P. L. de Andres, and E. Roman. "Characterization of thin silicon overlayers on rutile TiO_2 $(110)-(1\times 1)$."Physical Review B 82, no. 16 (2010): 165420.

3.18 Crist, B. Vincent. "A review of XPS data-banks."XPS Reports 1, no. 1 (2007).

3.19 Thøgersen, Annett, Josefine H. Selj, and Erik S. Marstein. "Oxidation effects on graded porous silicon anti-reflection coatings." Journal of The Electrochemical Society 159, no. 5 (2012): D276-D281.

3.20 Handbook of surface and interface analysis methods for problem-solving. Responsibility: edited by John C. Rivière, Sverre Myhra. Edition: 2nd ed.

3.21 https://xpssimplified.com/elements/tin.php

3.22 Stelzner, Th, M. Pietsch, G. Andrä, F. Falk, E. Ose, and S. Christiansen. "Silicon nanowire-based solar cells." Nanotechnology 19, no. 29 (2008): 295203.

3.23 Nix, William D. Mechanical properties of materials with nanometer scale microstructures. Stanford University, 2004.

3.24 Vinci, R. P., E. M. Zielinski, and J. C. Bravman. "Thermal strain and stress in copper thin films." Thin solid films 262, no. 1-2 (1995): 142-153.

3.25 Smith, Ulf, Nils Kristensen, Fredric Ericson, and Jan-Åke Schweitz. "Local stress relaxation phenomena in thin aluminum films." Journal of Vacuum Science & Technology A: Vacuum, Surfaces, and Films 9, no. 4 (1991): 2527-2535

3.26 Lu, Wei, and Charles M. Lieber. "Semiconductor nanowires." Journal of Physics D: Applied Physics 39, no. 21 (2006): R387.

3.27 Ley, L., J. Reichardt, and R. L. Johnson. "Static charge fluctuations in amorphous silicon." Physical Review Letters 49, no. 22 (1982): 1664.

3.28 Floro, Jerrold A., Eric Chason, Robert C. Cammarata, and David J. Srolovitz. "Physical origins of intrinsic stresses in Volmer–Weber thin films." MRS bulletin 27, no. 1 (2002): 19-25.

3.29 Pasquier A D, Mastrogiovanni D D T, Klein L A, Wang T and Garfunkel E 2007 Applied Physics Letters 91 183501-3

3.30 Kelzenberg, Michael D., Daniel B. Turner-Evans, Brendan M. Kayes, Michael A. Filler, Morgan C. Putnam, Nathan S. Lewis, and Harry A. Atwater. "Photovoltaic measurements in single-nanowire silicon solar cells." Nano letters 8, no. 2 (2008): 710-714.

3.31 Tian, Bozhi, Xiaolin Zheng, Thomas J. Kempa, Ying Fang, Nanfang Yu, Guihua Yu, Jinlin Huang, and Charles M. Lieber. "Coaxial silicon nanowires as solar cells and nanoelectronic power sources." Nature 449, no. 7164 (2007): 885-889.

3.32 https://static.thermoscientific.com/images/D16100~.pdf

3.33 Westsson, Emma, and Ger JM Koper. "How to determine the core-shell nature in bimetallic catalyst particles." Catalysts 4, no. 4 (2014): 375-396.

CHAPTER 4

Structural Characterisation of an annealed Sn thin film

Abstract

The chemical and structural properties of the nano-sized metal catalyst influence the properties of the SiNW emanating from the nano-sized catalyst. The previous chapter provided valuable insights into the chemical bonding of the Sn film at elevated temperatures. This chapter will report on the corresponding structural characterisation of the annealed Sn thin films on a Si wafer was performed to investigate the external and internal structural changes of the film prior to and after annealing at different temperatures using electron beam based microanalysis techniques. The formation of separated Sn nanoparticles occurs at 350 °C and is accompanied by oxygen (O) and carbon (C) according to the x-ray analysis within the electron microscope. HRTEM results revealed the presence of an SnO_2 amorphous layer on the surface and Sn/Si interface. The crystalline Sn core was confirmed which augurs well for SiNW synthesis. The corroboration with the x-ray photoelectron spectroscopy analysis and the implications for silicon nanowire synthesis are discussed.

Introduction

The field of nanotechnology focuses on the science, engineering, and technology of materials in the range of less than one hundred nanometres [4.1]. The nano research had great attention which brought new discoveries and inventions of unique nano-characterization techniques to bring a different approach of investigating and controlling the morphology, size and dimensions of the materials at nanoscale [4.2]. In the case of silicon nanowires (SiNWs) the ideal diameter for solar cell applications are found to be at < 10 nm, which is suitable for light trapping properties [4.3]

The length and diameter of the SiNWs improves the absorption properties of the solar cell. SiNW's unique aspects of their physical, chemical and mechanical properties are comparable to visible light in wavelength from 400 to 650 nm. The optical properties of the SiNWs depends on their diameter, since the band gap of semiconductor silicon which determines the wavelength of luminescence of the semiconductor nanowires is normalised by the SiNW's diameter [4.4]. The band gap will become wider as the diameter approaches the sub-10 nm scale (Bohr exciton radius), changing the semiconductor characteristics of Si [4.5] from an indirect to a direct band gap [4.6, 4.7].

The reflectance of an SiNW array is dependent on the length of SiNWs; the reflection becomes lower with higher length [4.8]. The large surface area to volume ratio of the SiNWs ensured efficient collection of photo-generated carriers. The spacing between the nanowires should be smaller than the wavelength of incident light to achieve optimal omni-directional antireflection [4.9, 4.10].

The diameter and length of the SiNWs are crucial in the solar cell application and can be controlled by the metal catalyst nanoparticles size using the vapour liquid solid (VLS) mechanism (refer to chapter 1). The ideal metal catalyst should be well

understood prior SiNW synthesis. Tin (Sn) is one of the alternative metal catalysts for SiNWs growth for the solar cell application instead of the generally used gold catalysts [4.11, 4.12, 4.13]. According to Ekstrøm [2011], Au is not an ideal metal catalyst to grow SiNWs for solar cell application because it forms deep level defects in Si band gap which can affect the charge-carrier lifetime by acting as centres for charge-carrier recombination [4.14].

To reach the ideal < 10 nm diameter of SiNWs, the diameter of the Sn nanoparticles should be at with diameters in the sub-one hundred nanometer scale [4.15] by controlling the thickness of the film and annealing temperature. The archived diameters reported where 1 nm Sn thin film thermally evaporated on ZnO: Al substrate then annealed under vacuum at the temperatures 200 and 400 °C (H_2 plasma treated) and the Sn nanoparticles had a diameter ranging from 1-13 nm which lead to SiNW of the diameter of around 40 nm [4.16.]

The other factor that contributes to SiNW growth is the Sn catalyst composition [4.12, 4.18]. The oxidised metal catalyst has effect on the silicon nanowire growth as it can prevent the absorption of the Si precursor gas through the metal catalyst [4.16]. The oxygen at the metal catalyst and the Si/catalyst interface retract super saturation of the Si precursor gas to form nanowire. Mullane *et al,* [2013], showed the abrupt termination of crystalline fringes due to the amorphous region at the Sn-Si interface [4.19].

The unique nano-characterisation techniques which unveil the metal catalyst's internal and external structural changes are used mainly in research studies. Techniques such as scanning electron microscopy (SEM) which is a non-destructive high-resolution imaging technique that can give the morphology and elemental

composition of a sample using an accelerated electron beam and specialised detectors (Refer to chapter 2). SEM is a widely used technique which can analyse the sample at the nano scale, where one can identify the SiNWs grown using any method (VLS, Lithography, Chemical vapour deposition (CVD), etc.). The report on the growth of tin catalysed silicon nanowires by electron beam evaporation observed the SEM micrograph of the tin nanoparticles on a p-type Si (100) wafer with the size measurements of some of the nanoparticles [4.20]. The thin film was annealed for 15 min at the temperatures 300 – 480 °C, lead spherical Sn nanoparticles with a diameter in the range of 30 – 100 nm. The SEM displayed the occurrence of the VLS mechanism which was observed by the Sn nanoparticles at the top of the SiNW synthesised.

The internal structure such as the crystallinity of the nanowires can be characterised using the scanning transmission electron microscopy (STEM) which is found in the HRTEM and FIBSEM system. HRTEM can identify the elemental composition using the Energy-dispersive x-ray spectroscopy (EDX) detector (refer to chapter 2). Márquez *et al.* [2011] applied HRTEM on silicon nanowires grown with gold (Au) and platinum (Pt) as catalysts to find an alternative route for the synthesis of silicon nanowires via anodic alumina mask. HRTEM revealed the amorphous nature of the Si NWs, possibly due to low growth temperature used during the synthesis. EDX and XPS, confirmed the observation where they have shown that they are composed of Si^0 and silicon oxides (SiO_2-SiO_x) possibly forming a Si^0 core surrounded by a silicon oxide shell [4.21].

Moreover, Yiying Wu and Peidong Yang also conducted the TEM analysis on their working on direct observation of growth of 1D Ge structures by vapour solid liquid mechanism using Au as a catalyst [4.22]. An *in situ* high-temperature transmission

electron microscope (TEM) study revealed a direct observation of nanowire growth unambiguously confirms the validity of vapor-liquid-solid crystal growth mechanism at the nanometer scale [4.22].

The XPS results reported in Chapter Three disclosed that the Sn thin film is oxidised (SnO_2 and SnO) with a pure Sn core and dewett at temperatures of 350 and 450 °C. This chapter will report on the electron beam based analysis of the 3 nm Sn film coated Si (100) wafer after it was annealed in the XPS vacuum. The morphology, crystallinity and elemental composition of the annealed thin films will be discussed with emphasis on comparisons with the XPS results and implications for SiNW growth using Sn as a catalyst.

4.1 Sample preparation

The Sn thin film (thickness of ~ 3 nm) was coated on a silicon (100) wafer using a thermal evaporation thin film deposition system equipped with a crystal monitor for film thickness. The Sn thin film was cut into approximately 1x1 cm pieces and were subsequently heated to temperatures of 25 °C, 180 °C, 232 °C, 350 °C and 450 °C within an EXCALAB XPS system. The scanning electron microscope (SEM) was used to confirm the XPS observations. The SEM and energy-dispersive X-ray spectroscopy (EDS) analysis was conducted using the Zeiss Crossbeam 540 and LEO 1525 FEGSEM respectively. The analysis was conducted using the inLense signal with a probe current of 100 pA, EHT voltage of 5kV at a working distance of 1.2 mm and taken at the magnification of 100.00kx. The EDS system is equipped with the Layer Probe software which estimates the Sn thin film thickness through a theoretical model based on the mass density and SEM operating conditions.

In addition, the windowless Oxford X-Max Extreme silicon drift detector was used to investigate the elements composition of the thin film at low acceleration voltages.

The EDS spectra were acquired at 5 and 1.5 kV for 35 seconds, which is suitable for probing the surface of thin films within an SEM. The thickness estimation and surface chemical mapping are the latest technological abilities of the new generation EDS detectors and software.

The cross-sections (lamella) of the as-deposited and 350°C samples were prepared on a Zeiss Cross Beam 540 FIBSEM. Initially, a Pt layer was grown via electron beam assisted deposition using trimethyl- methylcyclopentadienyl platinum (IV) ($C_5H_4CH_3Pt(CH_3)_3$) as a precursor gas to protect the Sn film against the more aggressive Gallium (Ga+) ion Pt-deposition during the TEM lamella milling. The lamella was formed by using a Ga+ ion beam set to series of decreasing currents of35 nA to 1 pA. The TEM lamella was then viewed on the FIBSEM using an angular scanning transmission electron microscopy (aSTEM) detector operated at an at an EHT of 30 kV and acquiring images in high annular angular dark field (HAADF) and bright field (BF) modes. HRTEM analysis was performed the prepared lamellae on a FEI TECNAI HRTEM housed at University of Western Cape (UWC). The HRTEM was operated at an acceleration voltage of 120 kV to determine the crystallinity and elemental properties of the Sn thin films after the annealing in the XPS vacuum.

4.2 Thickness analysis

Prior the XPS analysis, the thickness of the as-deposited Sn thin film was confirmed using the Layer Probe softer which uses the EDS spectra to evaluate the Sn/Si model. Figure 4.1 displays the EDS spectra from the Layer probe be simulated to determine the thickness of the Sn film.

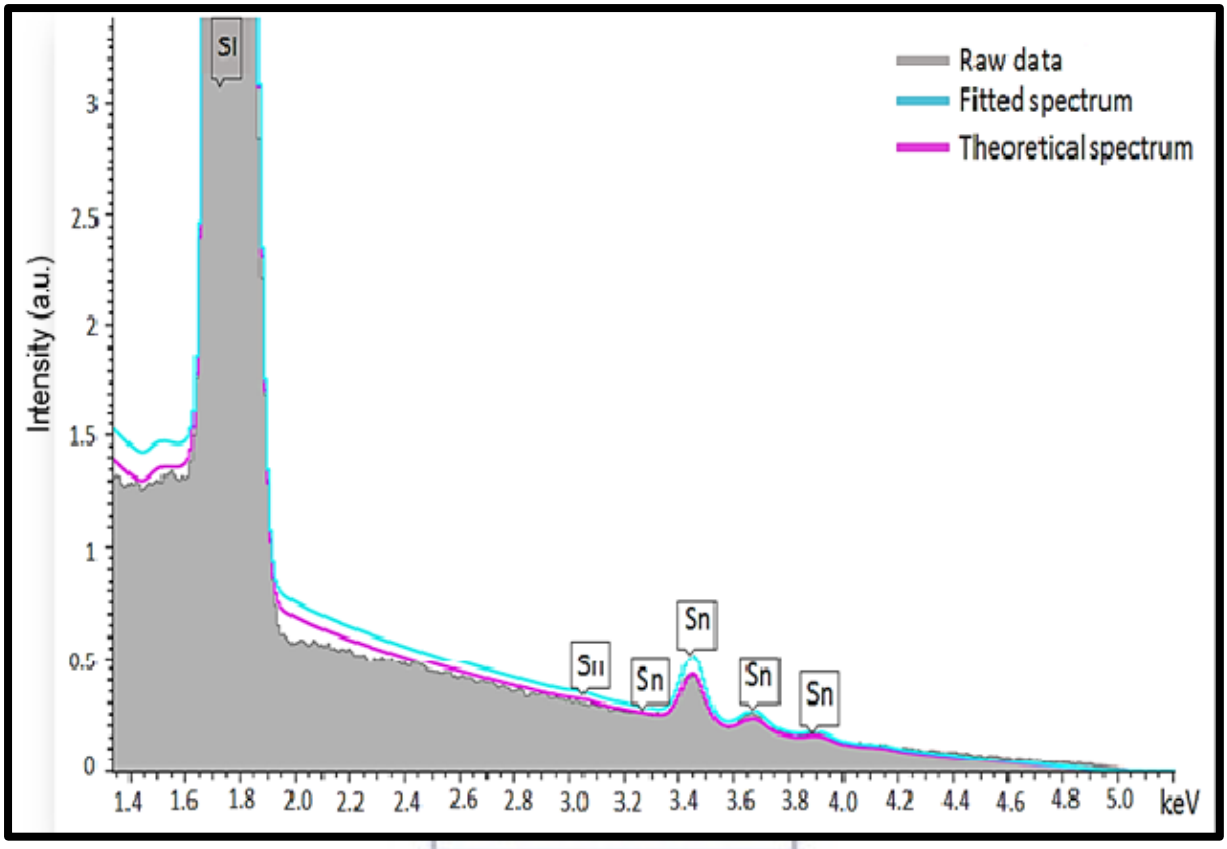

Figure 4.89: EDS spectrum overlaid with simulations to estimate the Sn thin film thickness.

There are two lines overlaid on the measured data which are used to determine the thickness of the film theoretically and experimentally. The pink line indicates the theoretical spectrum calculates a full x-ray spectrum from the composition defined for the current model. The fitted spectrum (cyan) is based on the elements defined for the composition of the model [4.23]. Measurements were performed at four different areas of the Sn film surface, they are tabulated.

Table 4.7 illustrate the calculation of the repeated thickness measurements of the film as calculated from the theoretical & fitted spectrum results.

Table 4.7: Layer probe results

Spectrum label	Layer thickness (nm)
1	3.22
2	3.30
3	3.75
4	3.79
Maximum	3.79
Minimum	3.22
Average	3.51
Standard deviation	0.30

The thickness of the Sn thin film is found to be: 3.51 ± 0.30 nm which is acceptable value for the Sn thin film compared to the crystal monitor. The results indicated are when the pure Sn has no defects; however, there can be some surface changes such as porosity of the Sn due to thickness, oxidation or contaminations. According to Hernández-Nava *et.al*. [3.24], the density of the metal can be changed by the porosity as the thickness of the film reaches a nanometer scale. In this simulation, the model depends on the mass-thickness of the material, however if there can be any chemical changes such as oxidation in the material then the density will change. In this case the focus was the thickness of the Sn film deposited is 3 nm.

4.3 Surface morphology

Figure 4.2 shows an SEM micrograph for the as-deposited Sn thin film. The SEM micrograph was acquired using the secondary electron detector, where the film can be distinguished to the bulk substrate by the contrast difference as there is a small component of backscatter electrons detected by the secondary detector. The Sn film appears brighter compared to the Si substrate since the atomic number is larger (Z = 50) than Si (Z = 14).

The Sn thin film is composed of clusters with different diameters and shape. The formation of the clusters can be due to the thickness of the Sn thin film of approximately 3 nm. Thin film of metal deposited over foreign substrates naturally tend to reconfigure into drops. This occurs because atoms at the surface of a solid or liquid, being bound by fewer neighbouring atoms than they would be in the bulk of the material, are in unstable structural states. The physical characteristics of a thin film can be determined by surface diffusion and nucleation during deposition. Basic modes of thin film growth such as island in the Volmer-Weber mode, layer by layer in the two -dimensional Frank van der Merwe mode, and layer plus island in the Stranski-Krastanov mode. The film growth observed in this study is Volmer-Weber thin film growth whereby the adatoms nucleate at certain spots and pile up to form dots [4.25].

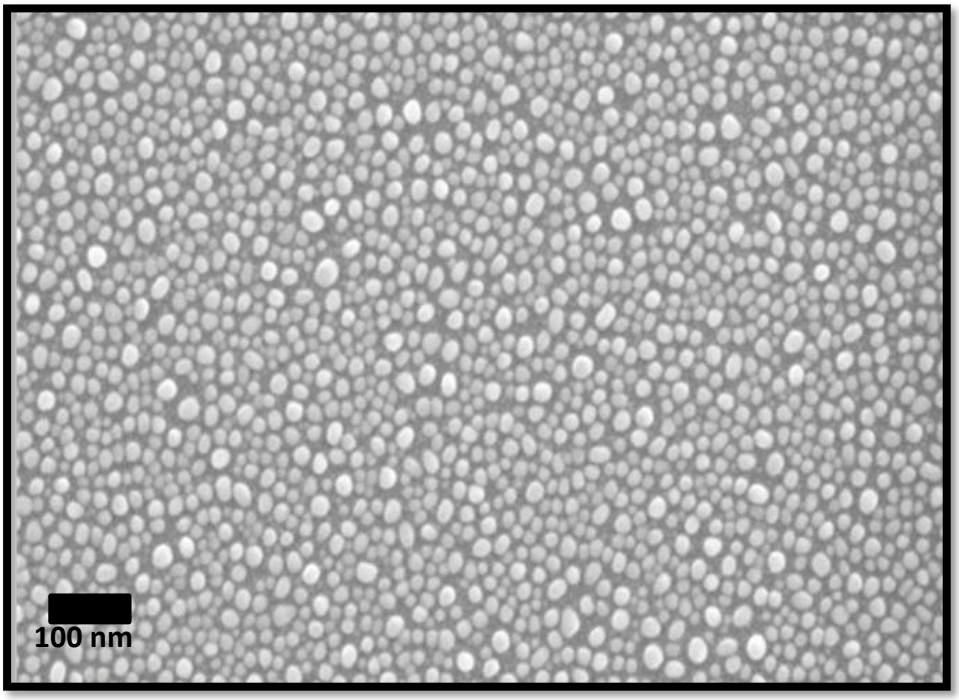

Figure 4.90: SEM micrographs for Sn thin film at temperature 25°C.

The surface morphology of the Sn sample heated at 180 and 232 °C shows the presence of Sn nanoparticles which is of the same diameter as the as-deposited sample. Moreover, the sudden drop in the Sn atomic percentage (at. %) and increase in the Si at 350 °C observed in the XPS results corresponds to the formation of larger Sn nanoparticles via agglomeration which exposes the underlying Si substrate (shown in 4.3 (c)). The 350 °C temperature indicates that the formation of the Sn nanoparticles may lead to ideal SiNW synthesis. At 450 °C the dispersion of the Sn nanoparticles and exposed Si substrate is more pronounced. The particle size measurements for the Sn film at as-deposited, 350 and 450 °C amounted to 14.9 ± 0.3 nm, 19.2 ± 0.3 nm and 18.2 ± 0.1 nm, respectively. The increase in temperature leads to an increase in the Sn nanoparticles diameter size due to the surface tension, which causes stronger van der Waals force created between the small diameter nanoparticles to agglomerate forming bigger particles. Further

analysis was conducted to confirm the observations on the SEM surface morphology using the EDS analysis.

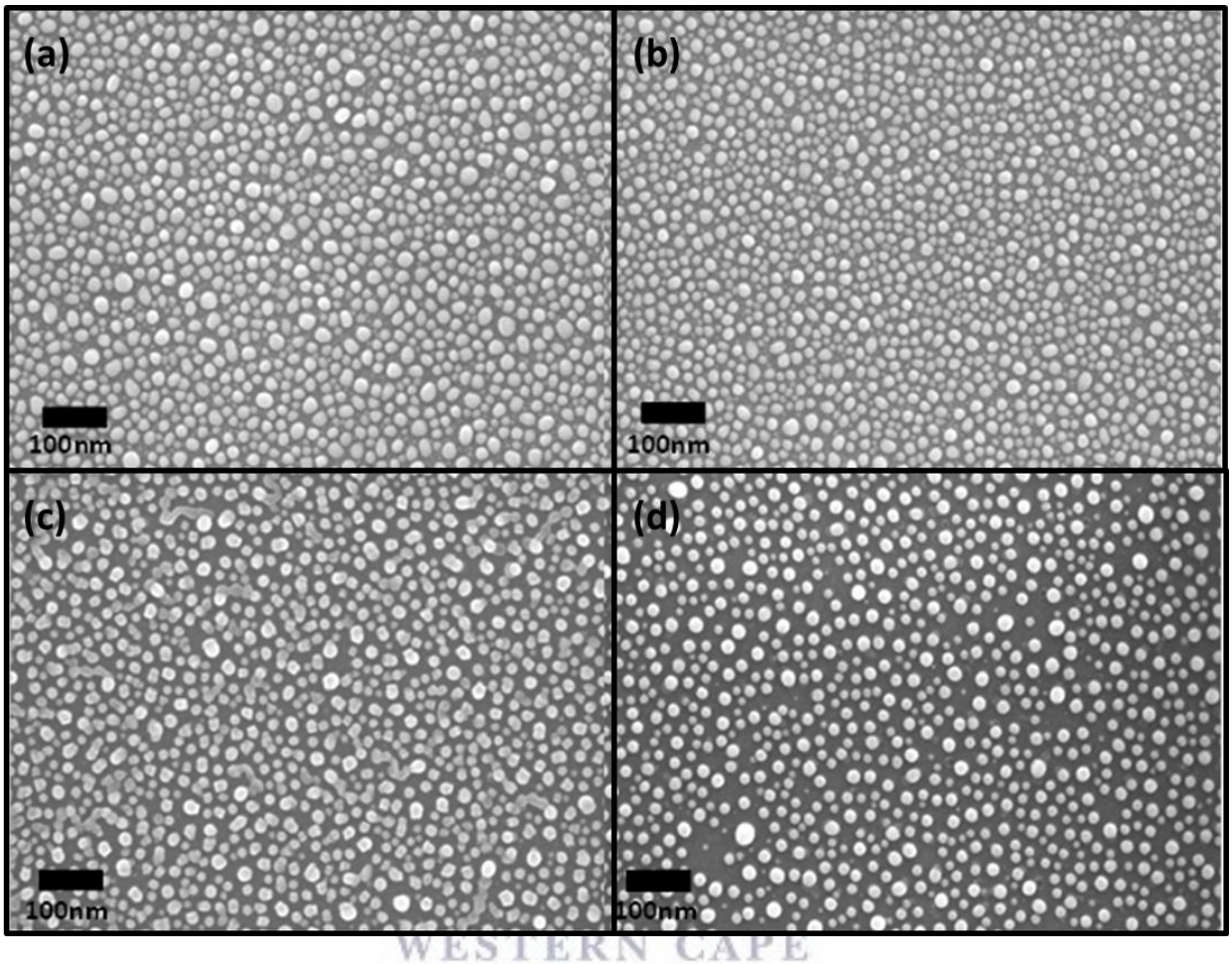

Figure 4.91: SEM images for 3nm Sn at temperature (a) 180, (b) 232, (c) 350 and 450°C.

4.4 EDS analysis

Figure 4.92 displays the EDS spectrum for the as-deposited Sn thin film. EDS analysis was done not only to ascertain the chemical composition of the surface morphology (see figure 4.3), but also as a comparison to the XPS findings discussed in chapter 3. The Sn content amounted to 2.33 at. % and the intense Si peak corresponds to 93.05 at. %. The C and O amounted to 1.65 at. % and 2.98 at. %, respectively which is indicative of surface contamination due to atmospheric air exposure of the Sn coated silicon wafer. The contamination is due to moving the

samples from one system to the other and is consistent with the XPS results presented in Chapter 3.

The fluorine is observed in the spectrum which, it is originating from the cleaning step, where the hydrofluoric acid was used to remove the native oxide prior to Sn film deposition. The EDS spectra and XPS results did not show any of the fluorine (F) content at the temperatures 180, 232, 350 and 450 °C, which can be due to exposing the F containing sample to elevated temperatures.

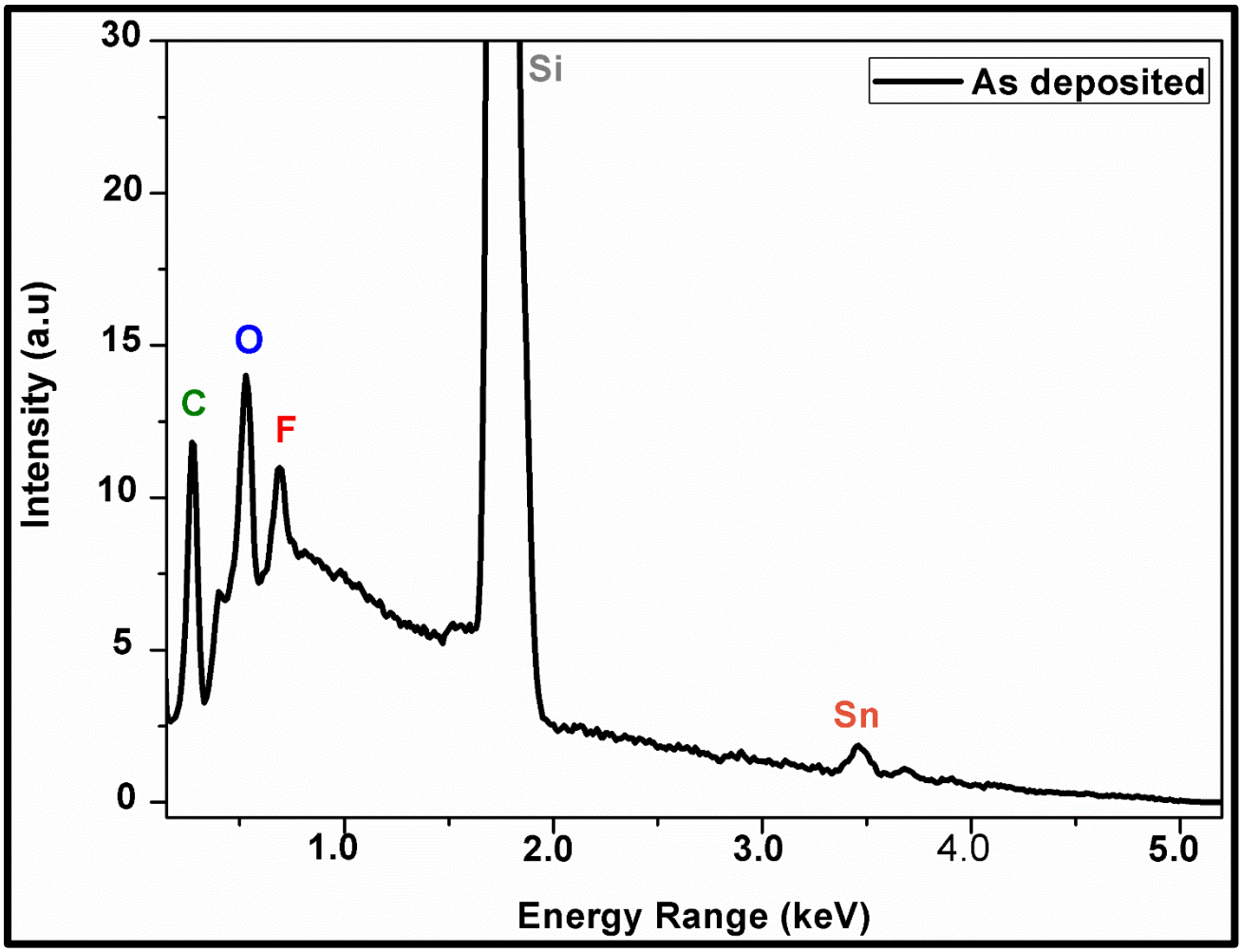

Figure 4.92: EDS spectrum for the as-deposited Sn thin film.

The variation of the at. % with temperature was not clearly observed when overlaying the 25 with the 180, 232, 350 and 450 °C. The atomic percentages of the

EDS spectra for all elements were not consistent to the XPS due to the difference in the escape depths of the photo-electron and x-ray generation within the sample surface. The XPS photo-electron escape depth ranges between 2-10 nm [4.26]. On the other hand, the EDS x-ray generation depth (Rx) amounts to 414.88 nm with the energy dispersion of 5 kV according to the Anderson and Hasler equation [4.6]:

$$\rho R = 0.064(E_o^{1.68} - E_c^{1.68}) \qquad (4.1)$$

, where the ρ is the mean specimen density in g/cm^3, R is the x-ray range in µm, E_o is the SEM accelerating voltage in keV and E_c is the critical excitation voltage for the elemental line under consideration. According to equation 4.1 an increase in acceleration voltage and a decrease in density of the sample leads to a deeper x-ray penetration depth and consequently an increasing substrate x-ray signal intensity. The above equation 4.1 was applied to pure elements however in our study it is Sn on Si substrate which is better explained by the Monte Carlo simulation. Figure 4.93 illustrate the Monte Carlo simulation calculated form the Casino software [4.27], showing the interaction volume generated for a theoretical model of 3 nm Sn on Si at voltages of 5, 3 and 1.5 kV. The blue line is the backscattered electrons and the red is the secondary electron escape depth.

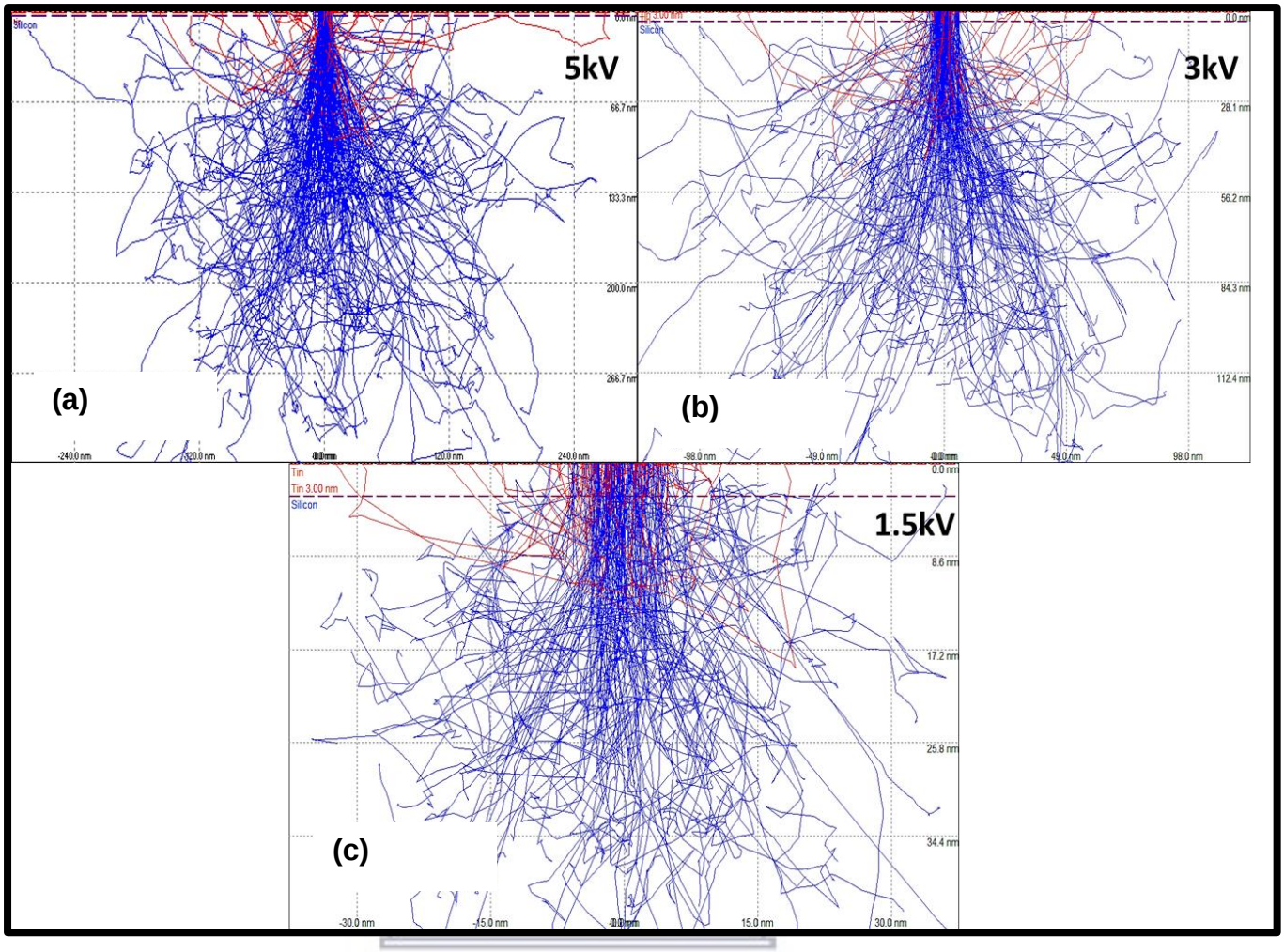

Figure 4.93: Monte Carlo simulations of the interaction volume of the Sn/Si model at the voltage of 5,3 and 1.5 kV. The blue line is the backscattered electrons and the red is the secondary electron depth.

An increase in the acceleration voltage leads to a high interaction volume of the signal to higher depth which can give signals from the bulk substrate (Si) other than the film. The signal's spot size on the surface is too small to detect surface signals (figure 4.5a, b).

When decreasing the acceleration voltage from 5 kV to 3 kV, the interaction volume or the electron escape depth is reduced from 266.7 nm to 112.4 nm respectively.

The lowest kV (acceleration voltage) which is 1.5 kV in this section, illustrates that the interaction volume becomes broader and close to the surface because of a bigger spot size spreading on the film surface. The signal depth is reduced on the bulk substrate to 34.4 nm. This observation can explain the amount of the electron high tension (EHT) needed for the sample under study, looking at the thickness of the film. The X-Max Extreme silicon drift detector benefits from the so-called windowless technology, i.e. no protective x-ray transparent film like conventional EDS detector thereby eliminating the absorption of low energy x-rays. In conjunction with a close proximity to the sample and low kVs, the interaction volume reduces significantly ultimately leading to an improved spatial resolution of the EDS map.

4.4.1 Windowless EDS analysis at 5 kV

Figure 4.94 presents the EDS spectrum of the as-deposited sample acquired at 5kV where spectrum 1 and 2 correspond to spot analysis performed on a Sn nanoparticle and Si substrate, respectively. The elemental characterisation of the as-deposited Sn thin film was acquired at 5 kV for 35 seconds. There is a clear difference between the silicon substrate (spectrum 2) and Sn nanoparticles (spectrum 1) which does indicate that the deposition growth is the Volmer-Weber growth [4.25]. The spectra indicate the high intense Si peak as it is the bulk material (substrate) and the relatively lower intensity Sn peaks are observed because of its thickness (3 nm). The surface oxidation is implied as the O1s peak is more intense on Sn nanoparticle (spectrum 1) as compared to Si substrate (spectrum 2). This observation can be that, at 5 kV the Si can still be “seen” from the Sn spot, according to the Monte Carlo simulations. This means that oxygen x-ray generated from the silicon-oxide region can also travel like the silicon x-ray through the Sn particle to the detector due to the

high escape depth (approximately 266.7 nm) at 5 kV. The Si substrate is also oxidised from spectrum 2, confirming the XPS findings.

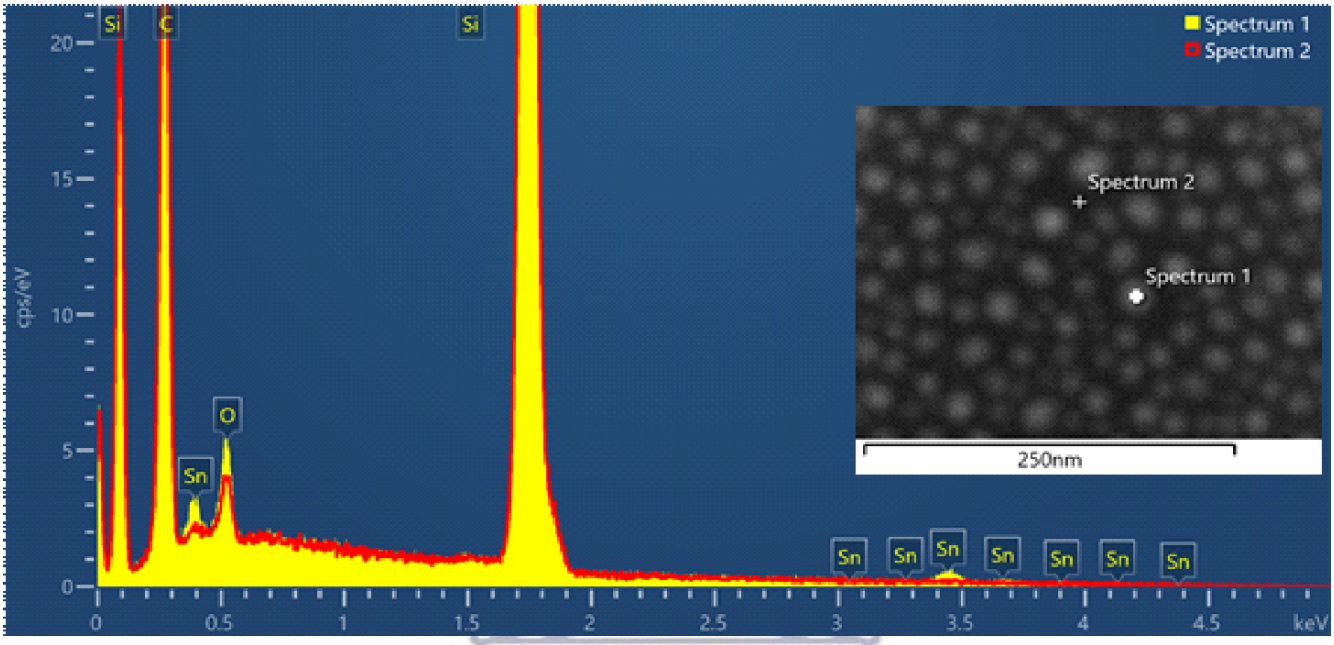

Figure 4.94: EDS spectra of the as-deposited sample acquired at 5 kV.

Figure 4.95 displays SEM micrographs highlighting the surface contamination build-up on the as-deposited and 350 °C thin films ascribed to the redeposition of carbon from the dissociation of volatile hydrocarbons present within the SEM chamber during imaging.

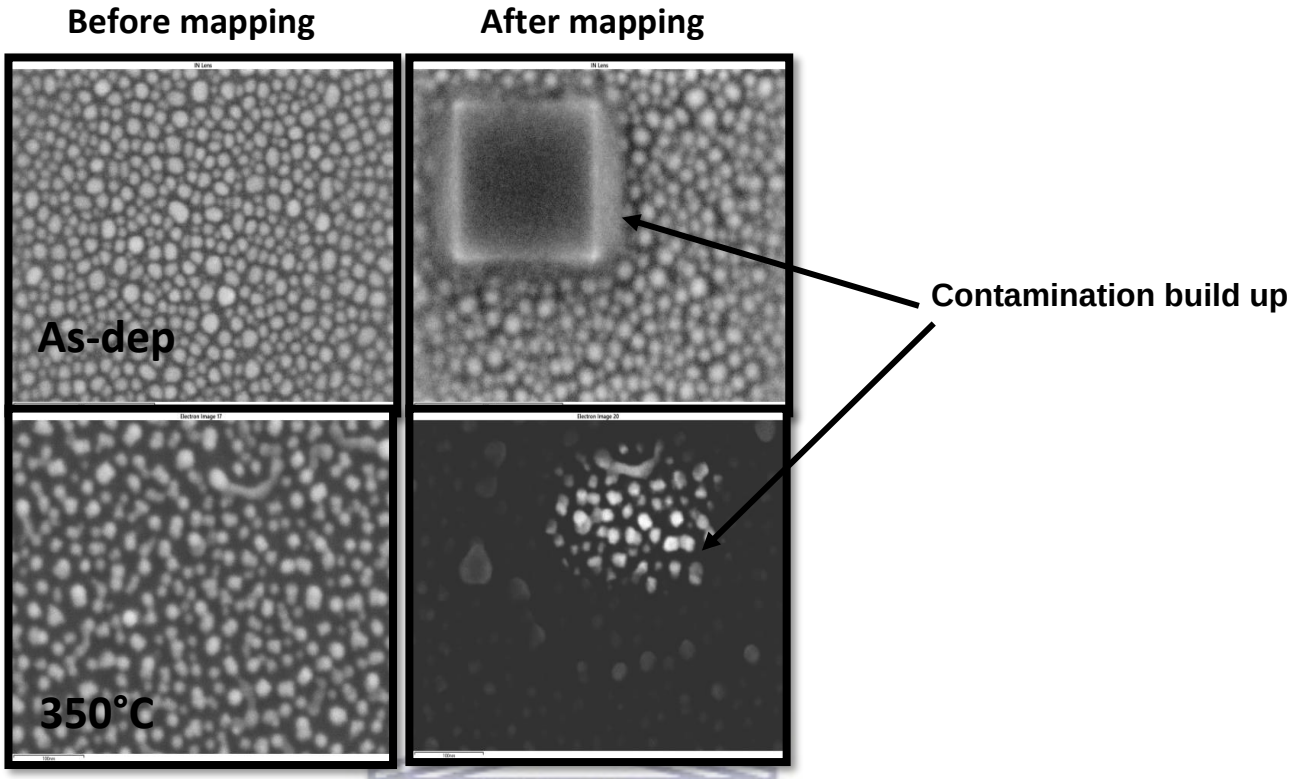

Figure 4.95: SEM micrograph showing the surface contamination builds- up on the as-deposited and 350 °C.

The carbon contamination on the sample was also detected, however the intensity is not high as compared to 5 kV spectrum, which can be re-deposition of volatile hydrocarbon in the SEM chamber. The electron beam “cracks” these hydrocarbons, releasing smaller gaseous molecules and building up non-volatile carbon deposits. If carbon is an element of interest in the analysis, then the additional carbon x-ray emission contributed by the carbon in the contamination layer will distort the results. To reduce the carbon detection, the migration of hydrocarbons across the specimen surface to the beam side can be minimised by intentionally irradiating the specimen over a large area with the electron beam as to lock down a thin carbon layer that is immobile [4.28]. According to the Monte Carlo simulation the low acceleration voltage will lead to a bigger spot size which then spread the beam on the sample surface (figure 4.93c).

Figure 4.96 displays the EDS spectrum of the 350 °C sample acquired at 1.5 kV where spectrum 5 is the Sn nanoparticle and spectrum 6 is the Si substrate. Spectrum 5, acquired on the Sn nanoparticle, only shows the Sn L x-ray peak at 0.39 keV because it was acquired at 1.5 kV. In addition to reducing the interaction volume, the EDS analysis at 1.5 kV have the added benefit of minimising contamination build-up on the sample surface.

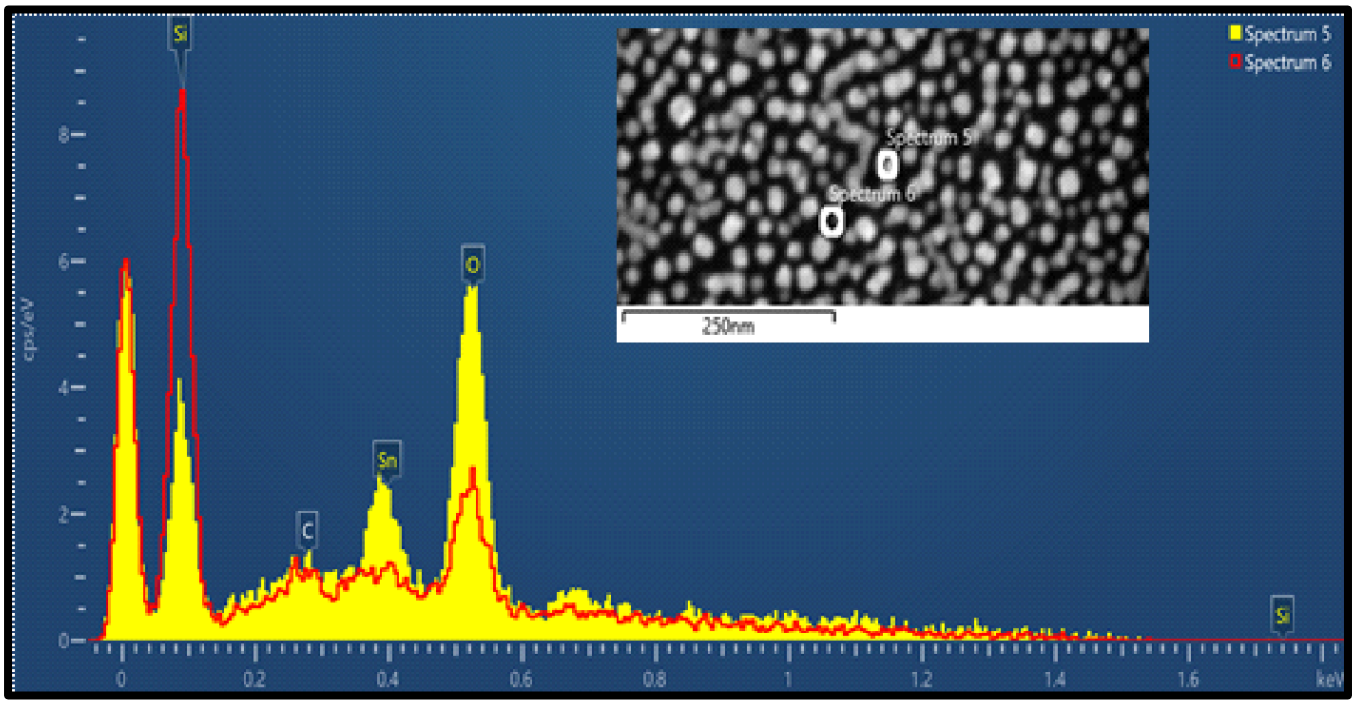

Figure 4.96: EDS spectra of the 350 °C sample acquired at 1.5 kV.

The Sn peak intensity relative to Si is enhanced at the low kV as compared to the as-deposited sample. There is oxygen (O) on the Sn nanoparticle which is at high intensity (spectrum 5) as compared to the O on Si substrate (spectrum 6). The carbon peak is less intense as compared to the as-deposited sample. The electron escape depth has shown less intense Si peak as compare to the 5 kV spectrum. This was due to the interaction volume decrease with the acceleration voltage, as explained by the Monte Carlo simulation. The O peaks are more intense as

compared to the 5 kV which shows that at 1.5 kV, the interaction volume it's small and more intense on the surface.

4.5 Surface elemental mapping at low kV EDS conditions

Figure 4.97 illustrates the elemental EDS mapping of the 350 °C sample's surface. The mapping of the as-deposited and 350 °C Sn thin film indicated that the surface was contaminated which can be also observed on the Gemini SEM (secondary detector) which was cleaned within the SEM using a nitrogen plasma. In this experimental set-up, the contamination was minimised by using a low magnification scan. The carbon is from the re-deposition of C from hydrocarbons present in the SEM chamber. The use of a plasma sample cleaning treatment was done but it did not have much effect. The acceleration voltage can be reduced which will lead to irradiation over a large surface area with the electron beam to slow down the carbon re - deposition.

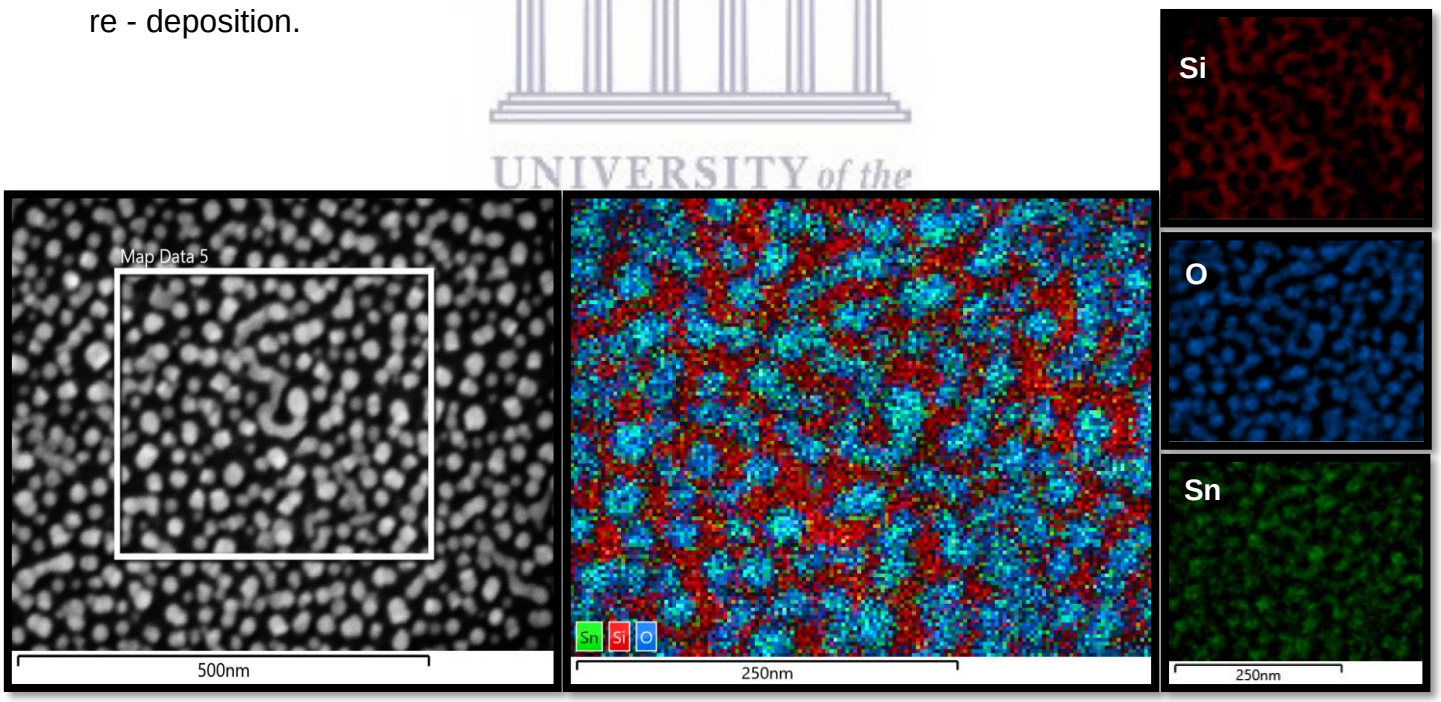

Figure 4.97: Elemental mapping on the 350 °C sample surface.

The elemental mapping was acquired on the 350 °C with the acceleration voltage of 1.5 kV. According to Monte Carlo simulation (figure 4.5c), the detectable x-rays will be closer to the film surface because of the short escape depth. The mapping of the 350 °C sample showed clearly the elements overlaid on the surface. The mapping indicated that there is O on the Sn and Si regions. The EDS spectra for 350 °C shows no Sn peaks within the Si regions, i.e. the Sn restructured as isolated nanoparticles. The presence of pure Sn does give an opportunity to determine the amount of oxides on the surface and at the Sn/Si interface.

4.6 FIBSEM-aSTEM analysis on TEM lamella

Figure 4.98 presents the FIBSEM-aSTEM images of the as-deposited sample in (a) HAADF and (b) BF mode. The amount of Sn present can be measured using the cross-sectional view of the sample. The STEM micrograph of the as-deposited sample displays the platinum (Pt) ion deposition which is formed during the milling and the Pt electron deposition serve as the protective layer over the Sn nanoparticles. The high angular annular dark field (HAADF) mode is atomic number dependent, thus the Sn nanoparticles are brighter as compared to the Si substrate. The dark line at the Pt/Sn nanoparticle interface can be the oxide region as shown by the XPS analysis. The bright field imaging mode it is a mass - thickness contrast dependent, which means that as the thickness of the specimen increase, the contrast also increases.

The bright field mode indicates the bright interface at the Sn/Si interface which can be due to the oxygen layer as detected on the windowless EDS spectra and it shows Volmer-Weber film growth which is consistent to the SEM surface morphology (insert figure 4.10a). The as-deposited Sn nanoparticles had a width of 20.2 ± 1.5 nm and height of 12.9 ± 1.4 nm.

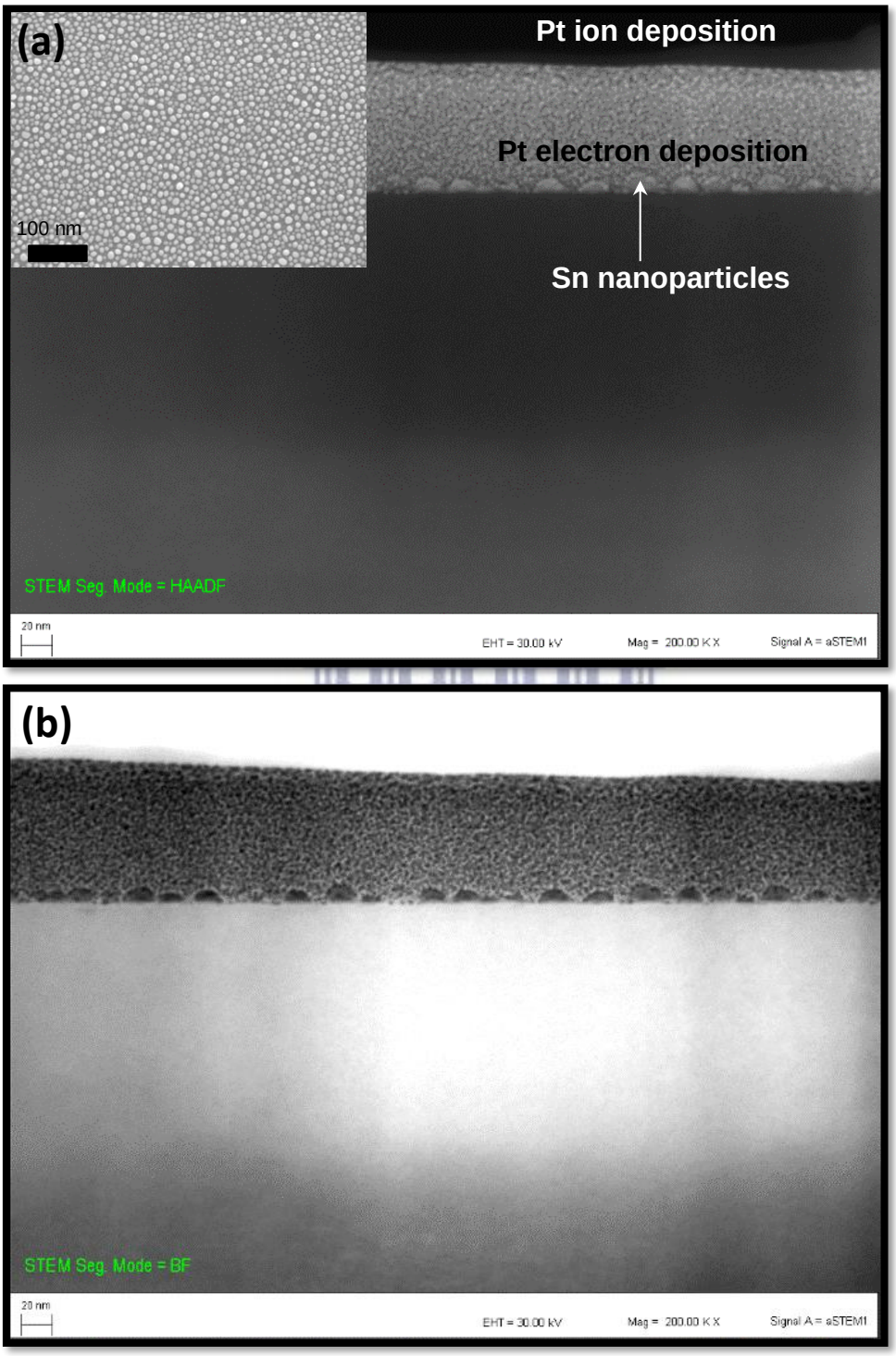

Figure 4.98: FIBSEM-aSTEM images of the as-deposited sample in (a) HAADF and (b) BF mode.

Figure 4.99 displays the FIBSEM-aSTEM images of the 350 °C sample in HAADF (insert: top view of the surface) and (b) BF mode. The HAADF mode clearly indicates

the Pt e-beam protective layer covered by the Pt-ion deposition layer. The Ga^+ ion deposited Pt is observed to be etching into the e-beam deposited Pt protective layer, which indicates how aggressive the Pt deposited by ions are and the minimal influence on Sn nanoparticles' structure (observed in figure 4.99).

The HAADF mode shows that the Sn nanoparticles are brighter due to its higher atomic number (Z = 50). The Sn nanoparticle/Si substrate interface indicates the presence of an oxygen layer. The bright field mode in Figure 4.11b shows the Sn nanoparticles as darker because Sn is high mass - thickness as compared to Si. The bright line at the Sn nanoparticle/Si substrate interface can be oxygen which is less heavy as compared to Si and Sn. The size of the nanoparticles was estimated on the STEM micrographs and for the as-deposited Sn film amounted to a width of 19.2 ± 1.5 nm and height of 11.5 ± 1.5 nm. The Sn particles increase in diameter with increase in temperature due to Ostwald ripening, where the particles coalescence to form larger particle size.

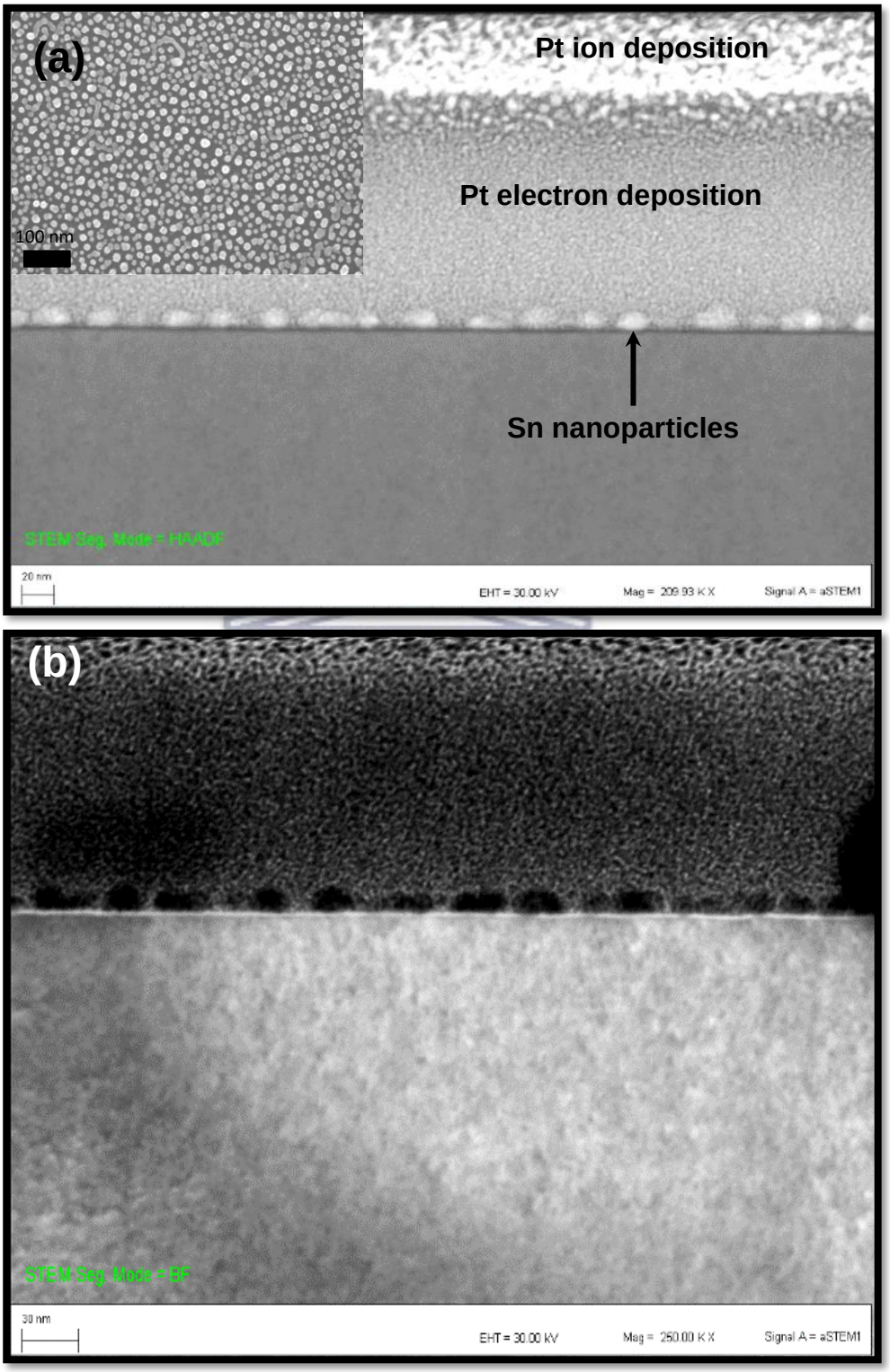

Figure 4.99: FIBSEM-aSTEM images of the 350°C sample in HAADF (insert :top view of the surface) and (b) BF mode.

4.7 HRTEM image analysis

Figure 4.100 shows the HRTEM-STEM (a) BF image showing an overview of the as-deposited sample (a) BF mode (b) HAADF with an insert images a high magnification. The as-deposited clearly show the film deposition and how the Sn clusters are arranged on the Si substrate in a cross-sectional view. The similarity between the HRTEM-STEM results and the aSTEM images illustrate the good performance of the aSTEM detector within the FIBSEM. However, HRTEM have the capability to show the particles at higher resolutions and the diffraction planes can be observed on the crystalline sample.

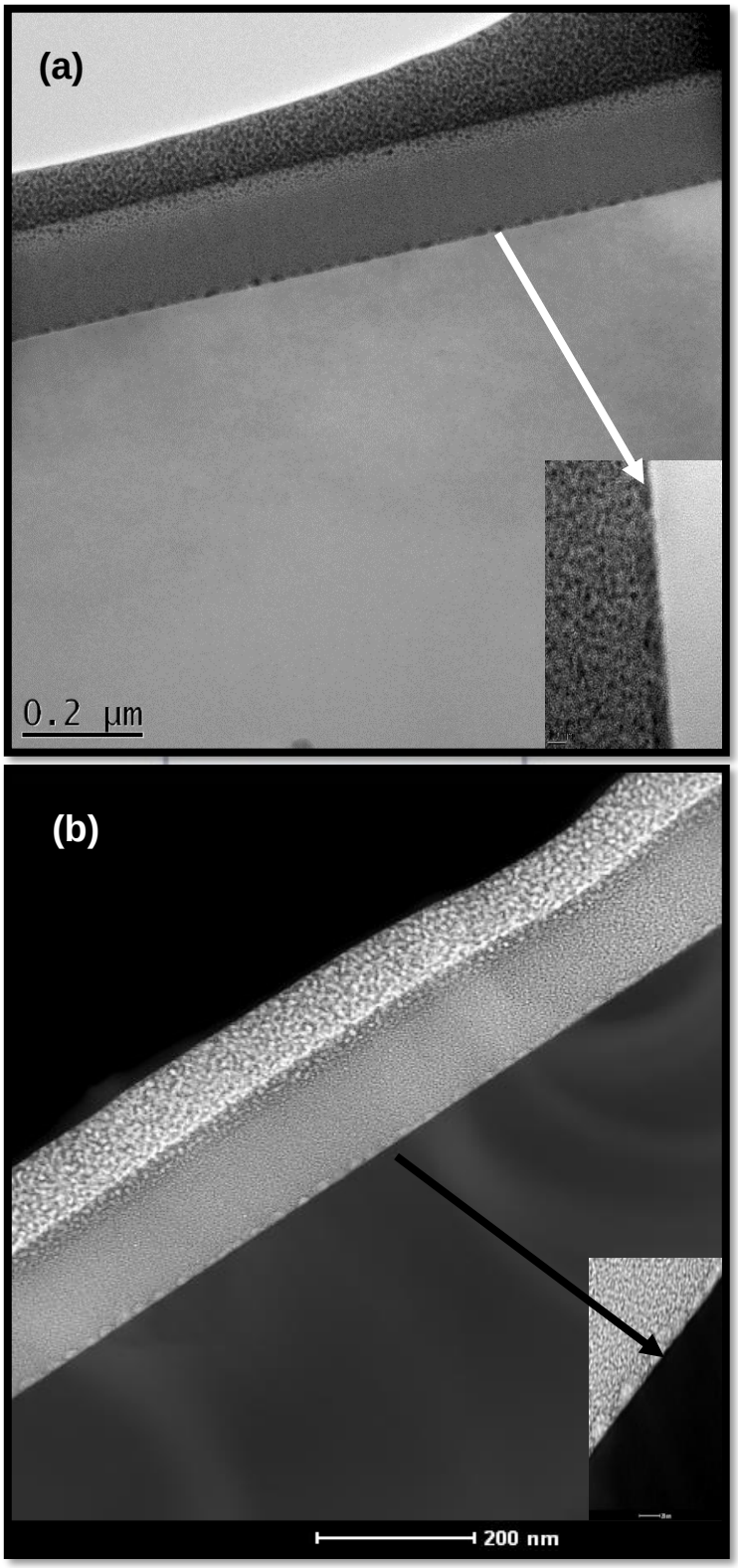

Figure 4.100: HRTEM-STEM (a) BF image showing an overview of the as-deposited sample (a) BF mode (b) HAADF with an insert images a high magnification.

Figure 4.101 displays HRTEM-STEM images of the Sn film annealed at 350 °C revealing the dewetting behaviour of the Sn nanoparticles. The Sn nanoparticles on the substrate as observed on the top view (refer to section 4.7). The XPS results discussed in Chapter 3 showed that the Sn film is oxidised because of the Volmer-Weber film growth which exposes the easily oxidised Si substrate. The Si oxidation is due to the Sn film not completely covering the substrate because the thickness was 3 nm hence the Volmer-weber growth deposition. The HRTEM and SEM-EDS analysis corroborates the XPS findings on the presence of O, Sn and Si as well as the oxidised Si and Sn regions. However, the STEM-EDS mapping was conducted on the samples using bright filed mode.

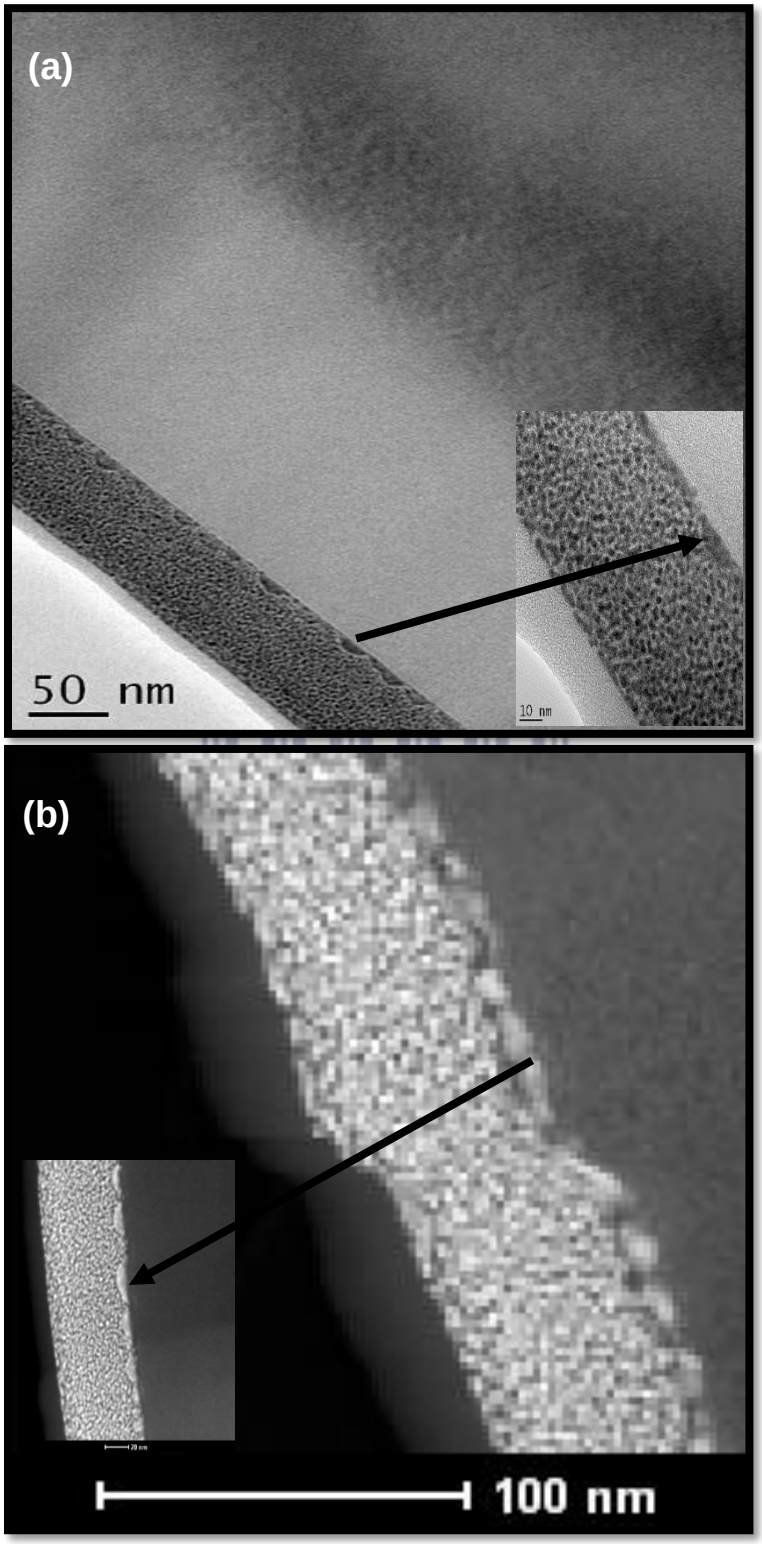

Figure 4.101: HRTEM-STEM (a) BF image showing an overview of the 350°C sample (a) BF mode (b) HAADF with an insert images a high magnification.

4.8 EDX elemental mapping

Figure 4.102 reveals a STEM-EDS map of the as-deposited sample containing elements such as carbon (C), oxygen (O), platinum (Pt), tin (Sn) and silicon (Si). STEM-EDS map indicates carbon to be concentrated on the Pt protective layer grown via electron beam deposition from the precursor gas. The O has the same trend as the Sn nanoparticles, which indicates the oxidation of Sn and Si, confirming the EDS and XPS results.

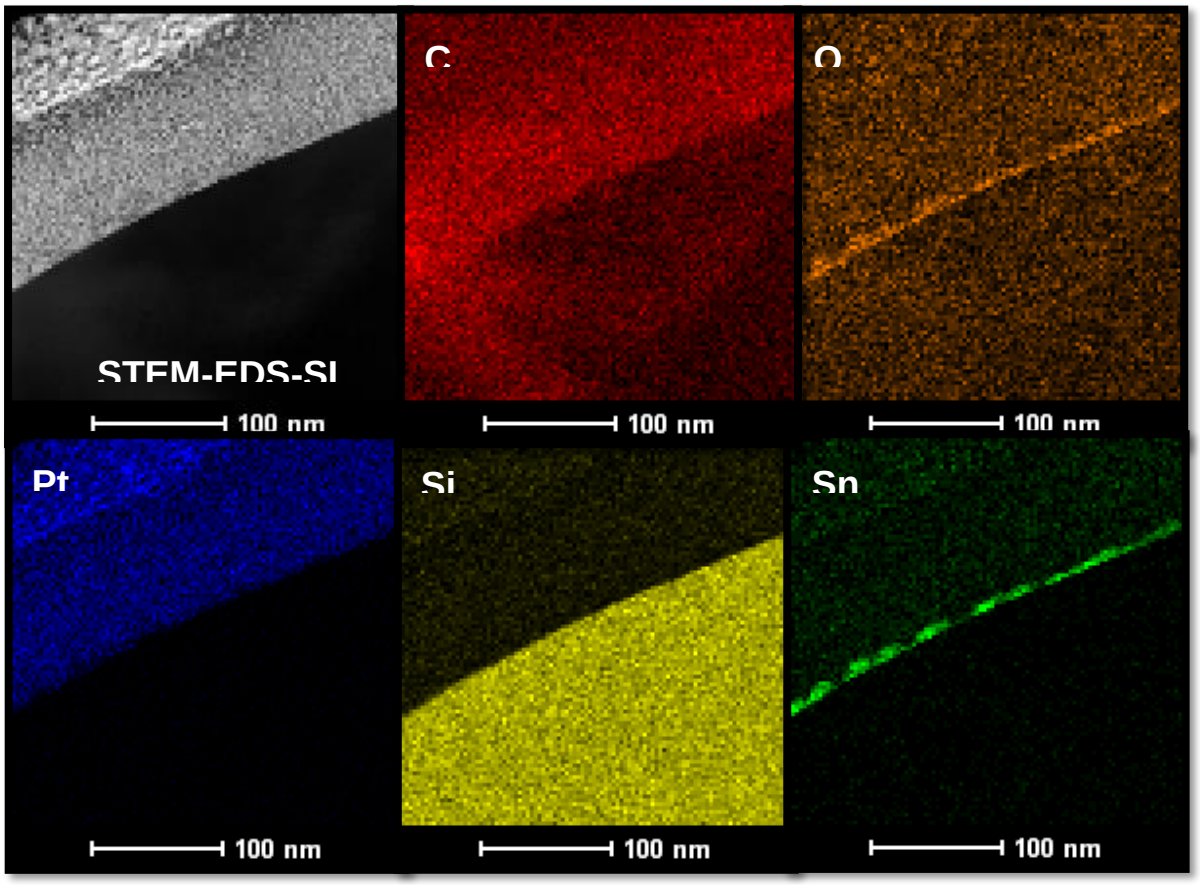

Figure 4.102: STEM-EDS elemental maps of the as-deposited sample's cross section revealing the distribution of C, O, Pt, Sn and Si.

Figure 4.103 displays STEM-EDS elemental maps of carbon (C), oxygen (O), platinum (Pt), tin (Sn) and silicon (Si) on the 350 °C sample.

STEM-EDS elemental map reveal that C and Pt are correlated because the Pt layer is covered with carbon. The carbon is observed to have covered the sample. The sample contamination prior annealing in the XPS vacuum chamber can be due to moving the sample from thermal coating system to the XPS. The other contamination can be due to the TEM lamella formation in the FIBSEM where Platinum is used in the FIB chamber which is deposited using the Trimethyl (methylcyclopentadienyl) platinum (IV) which can cause the hydrocarbon contamination on the sample. The surface of the particulate Sn regions is oxidised and encapsulates a relatively higher intensity Sn region which indicates that the Sn particles are not fully oxidised, which compliments the XPS results. This is promising for SiNW deposition as there are core Sn regions with low amounts of O. The morphology and elemental composition will be further investigated by determining the crystallinity of Sn on the as-deposited and 350 °C samples. In addition to the chemical properties and particle size, establishing the crystallinity of the Sn catalyst is vital for understanding the relationship between the catalyst structure and the properties of the SiNW growing from it.

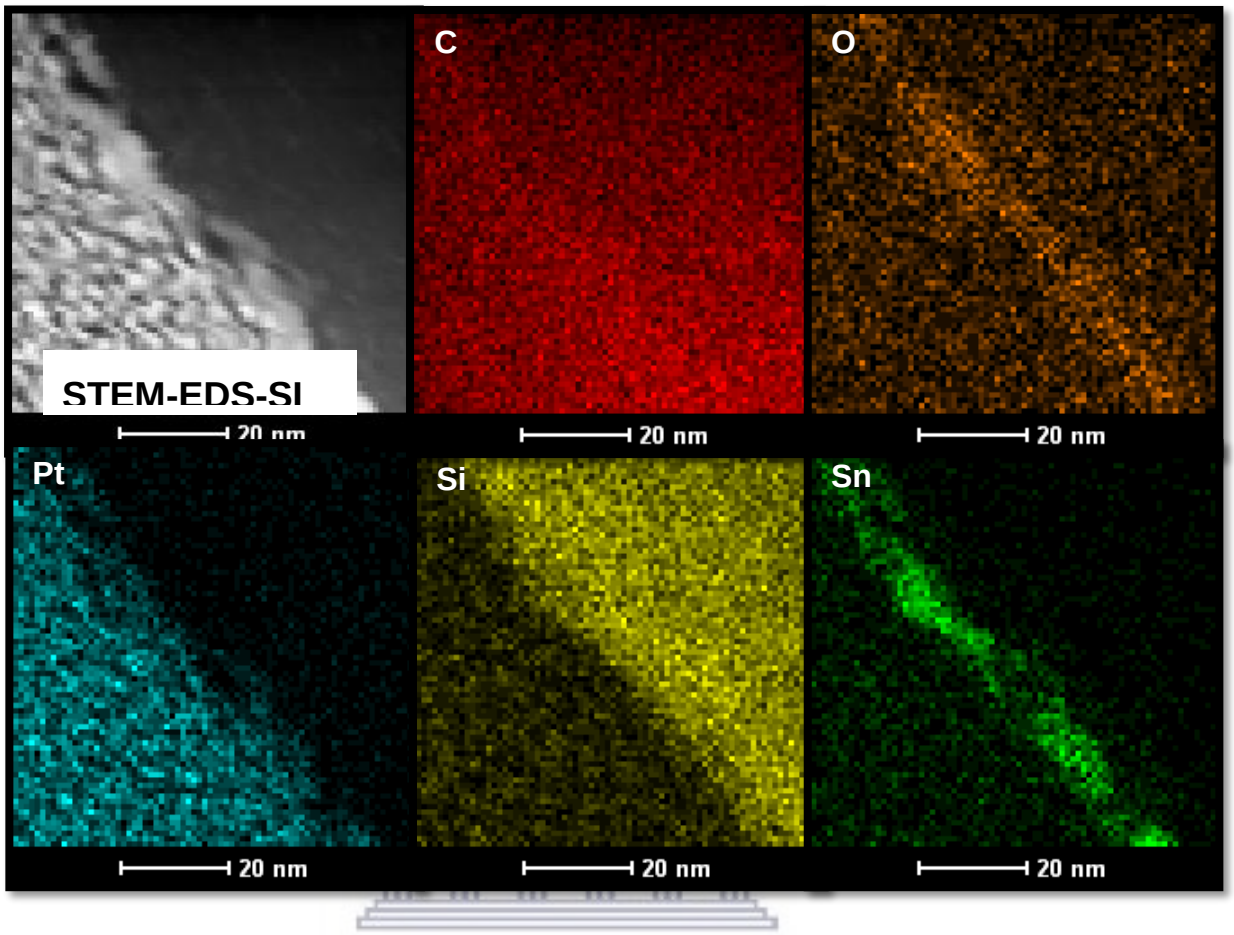

Figure 4.103: STEM-EDS elemental map of the 350 °C sample of C, O, Pt, Sn and Si.

4.9 Crystallinity analysis

Figure 4.104 presents the HRTEM micrographs at high magnification of the as-deposited and 350 °C. Lines are drawn as a guide for the eye.

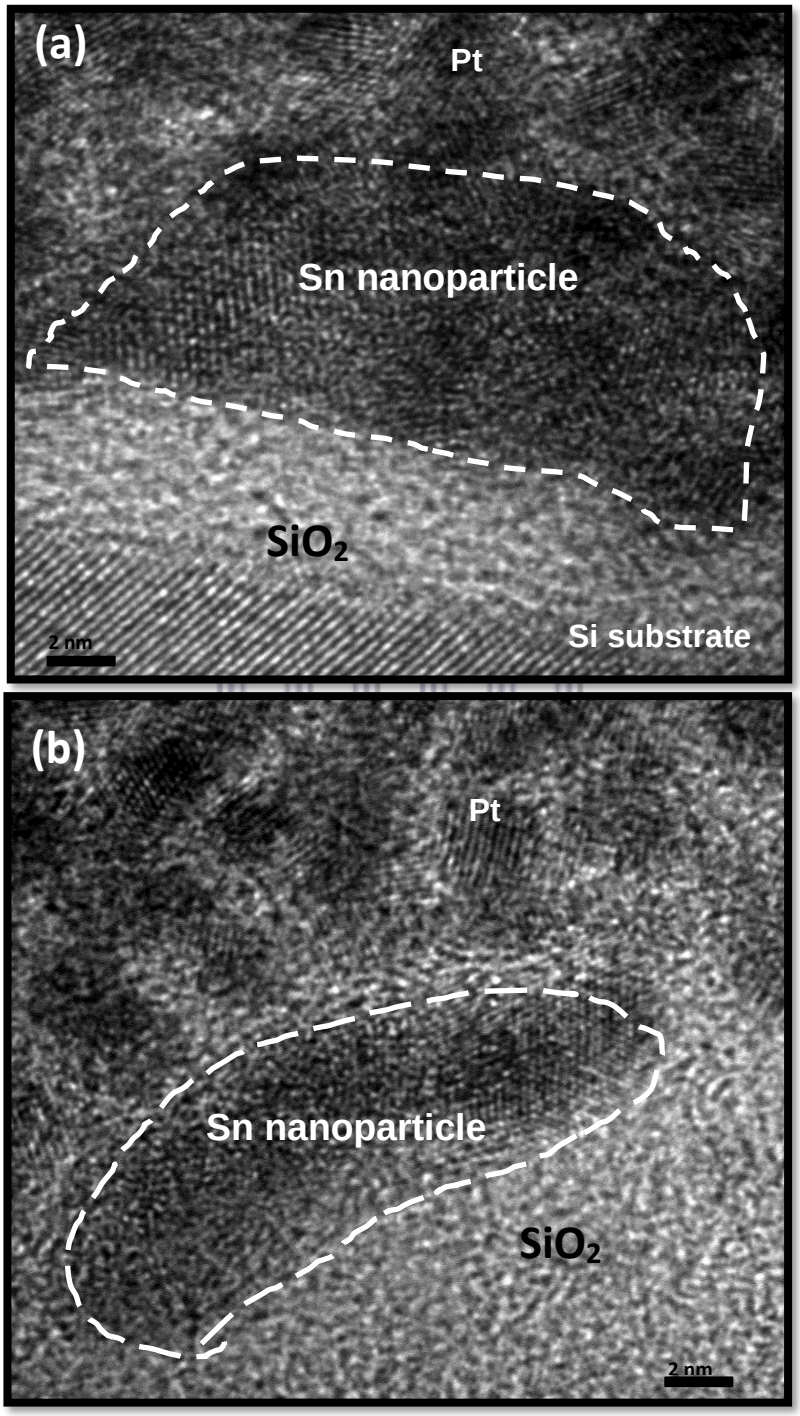

Figure 4.104: HRTEM micrographs at high magnification of the Sn film at (a) as-deposited and (b) after annealing at 350 °C.

The as-deposited Sn film consists of crystalline nanoparticles. The as-deposited

displays the Sn nanoparticles which illustrate the film growth is Volmer-Weber thin film growth. The Volmer-Weber (VW) growth for metal films deposited single crystal surfaces it exhibits three-dimensional island growth [3.25]. The direct nucleation of small clusters to the substrate surface, resulting in coalescence into a continuous film. The thickness of the Sn film deposited has leads to Volmer-Weber growth as it was limited to cover the whole Si surface, these observations were found on the SEM and STEM micrographs on the surface and cross-sectional morphology of the as-deposited sample.

The Sn nanoparticles however have regions of contrast suggesting possible Pt grains (dark spots) etched within the Sn nanoparticle or oxidised Sn regions. The particles comprise both crystalline and amorphous areas. The oxygen interface (amorphous) and the Si substrate (crystalline) are observed. However, the 350 °C samples shows the Sn nanoparticles at a small angle relative to the substrate as compared to the as-deposited particle. The Sn thin film dewetting is where Sn nanoparticles agglomerates to form larger Sn particles at 450 °C due to surface tension as the as-deposited sample is exposed to elevated temperatures. The Sn nanoparticle shows no full diffraction planes which can be due to the amorphous parts of the particle. The diffraction plane can indicate Sn and Si oxidation states and their probable orientation with increase in temperature.

The SAED pattern analysis was done to determine the d-spacing of the fringes on the Sn nanoparticle.

Figure 4.105 presents the SAED patterns for the Si substrate and the Sn nanoparticle. The SAED patterns clearly shows significant difference, as the Si substrate has clear rims with bright dots showing that silicon is a monocrystalline

material. The SAED acquired from a region containing the Sn and Pt films has blurred rings, indicative of Pt planes. The blurred rings are due to the small size of the crystallites, which is referred to polycrystalline oxides. The spots can be due to the Si or Pt since the spot size is 30 µm which is too big for a single Sn nanoparticle analysis. The diffraction micrographs were used to indicate the d-spacing of the clear crystalline fringes, using ImageJ and High score software to confirm the indices and intensity.

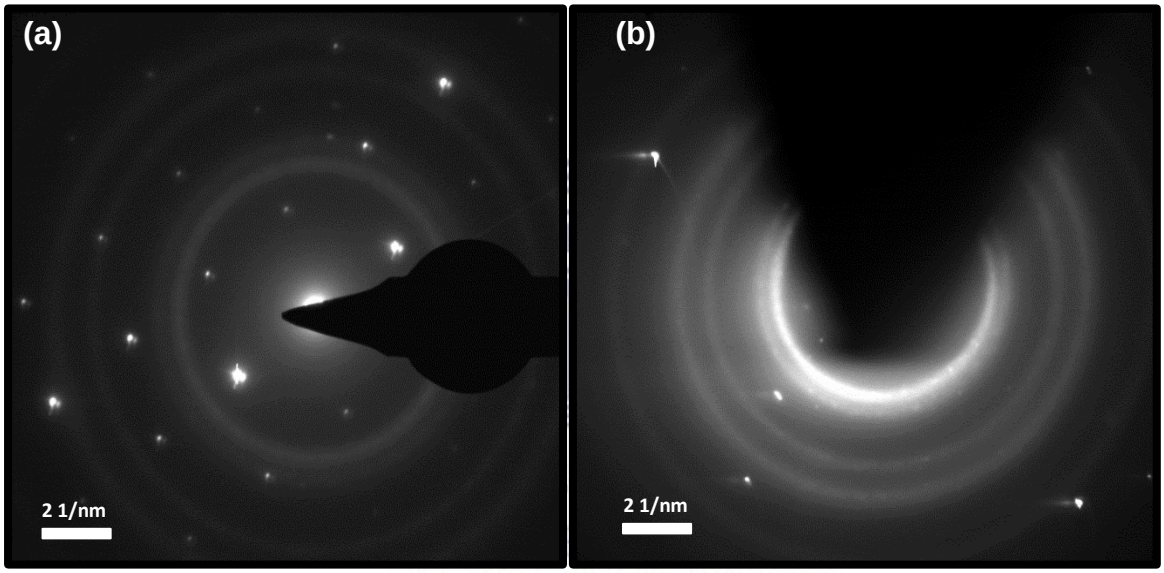

Figure 4.105: SAED patterns for the (a) Si substrate and (b) Sn nanoparticle.

Figure 4.106 presents the HRTEM diffraction images for the as-deposited samples at a low and high magnification. Lines are drawn as a guide for the eyes. The crystallinity of the sample is observed in Figure 4.106b which shows the oxidised Si substrate (SiO_2) at the diffraction plane of Si (100) and Sn at (200). At higher magnification, the Sn nanoparticle shows the diffraction planes (200) corresponding to metallic Sn. The Volmer-Weber thin film growth deposition was observed to expose the Si substrate. According to Wright *et al.* [4.29] the Si is easily oxidised, and its stable oxidation state is SiO_2. The oxygen on the substrate can also oxidise

the Sn thin film leading to SnO_x on the surface. The slow exposure to atmospheric air will lead to stannic oxide (SnO_2) [4.30]. This statement was confirmed as the SnO and SnO_2 with diffraction planes of (101) and (200) respectively are situated next to the amorphous SiO_2 region.

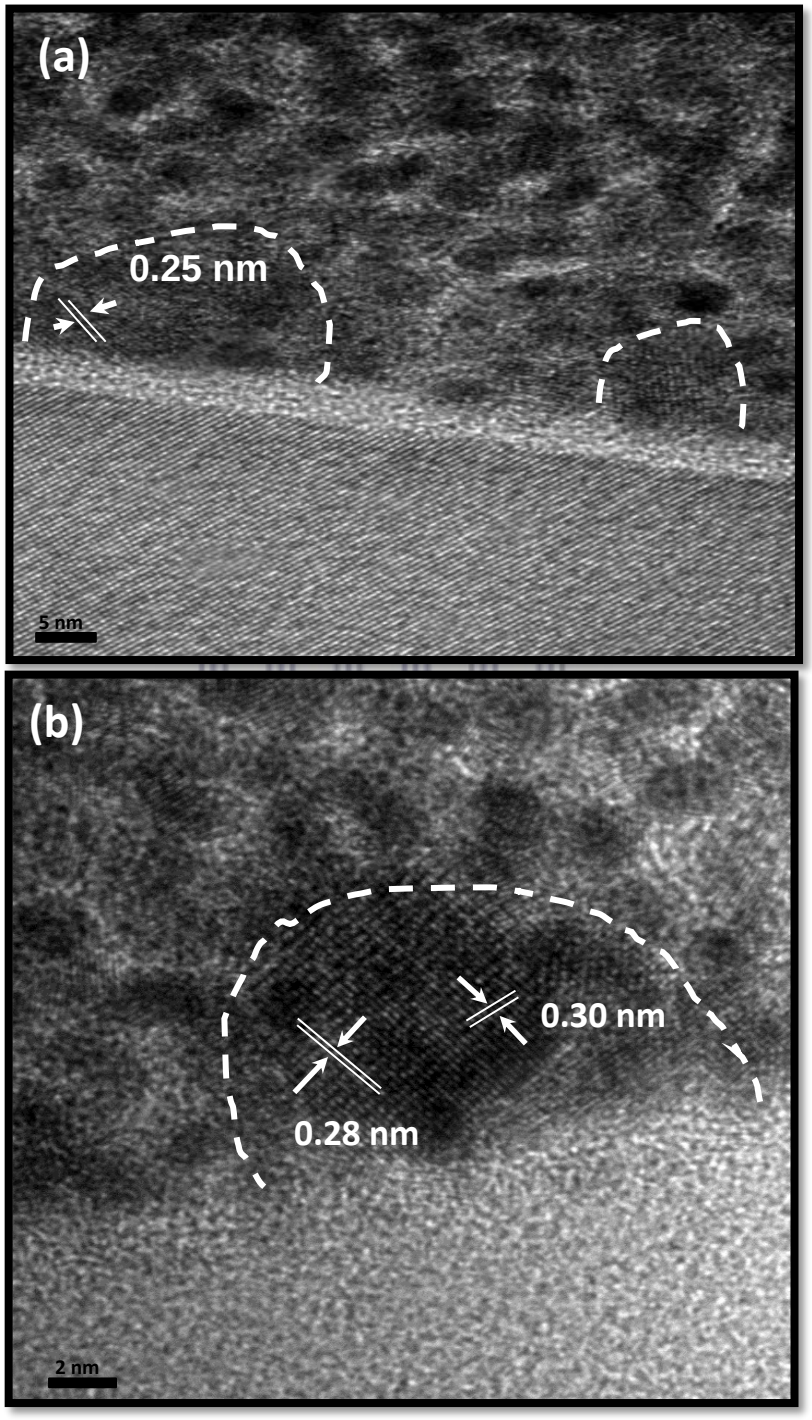

Figure 4.106: HRTEM diffraction images for the as-deposited samples (a) 5 nm scale and (b) 2 nm scale. Lines are drawn as a guide for the eyes.

Figure 4.107 displays the HRTEM diffraction micrographs for the 350 °C sample at random areas. In this limited area of the sample, an observation is made that there is an increasing intensity of the (200) lattice compared to that of (101) plane from the as-deposited sample. The intensity corresponds to the d-spacing value of each plane. The planes become more defined as compared to the as-deposited sample (less amorphous).

The purity of the metal catalyst it is important for the growth of the crystalline SiNW it is important as it reduces any defects that can limit the SiNW application. The crystallinity of the metal catalyst allows the incorporation of the Si precursor gas in the Si-Sn alloy to grow the crystalline SiNW. The crystallinity of the SiNWs does improves the light trapping ability and the charge carrier pathway. HRTEM showed that the pure Sn core it was crystalline which means the SiNW growth it is possible. The TEM lamella under HRTEM analysis showed that the oxide layer is not only on the surface but also the Sn/Si interface which will require to hydrogen plasma cleaning to remove the oxide layers for a successful SiNW synthesis.

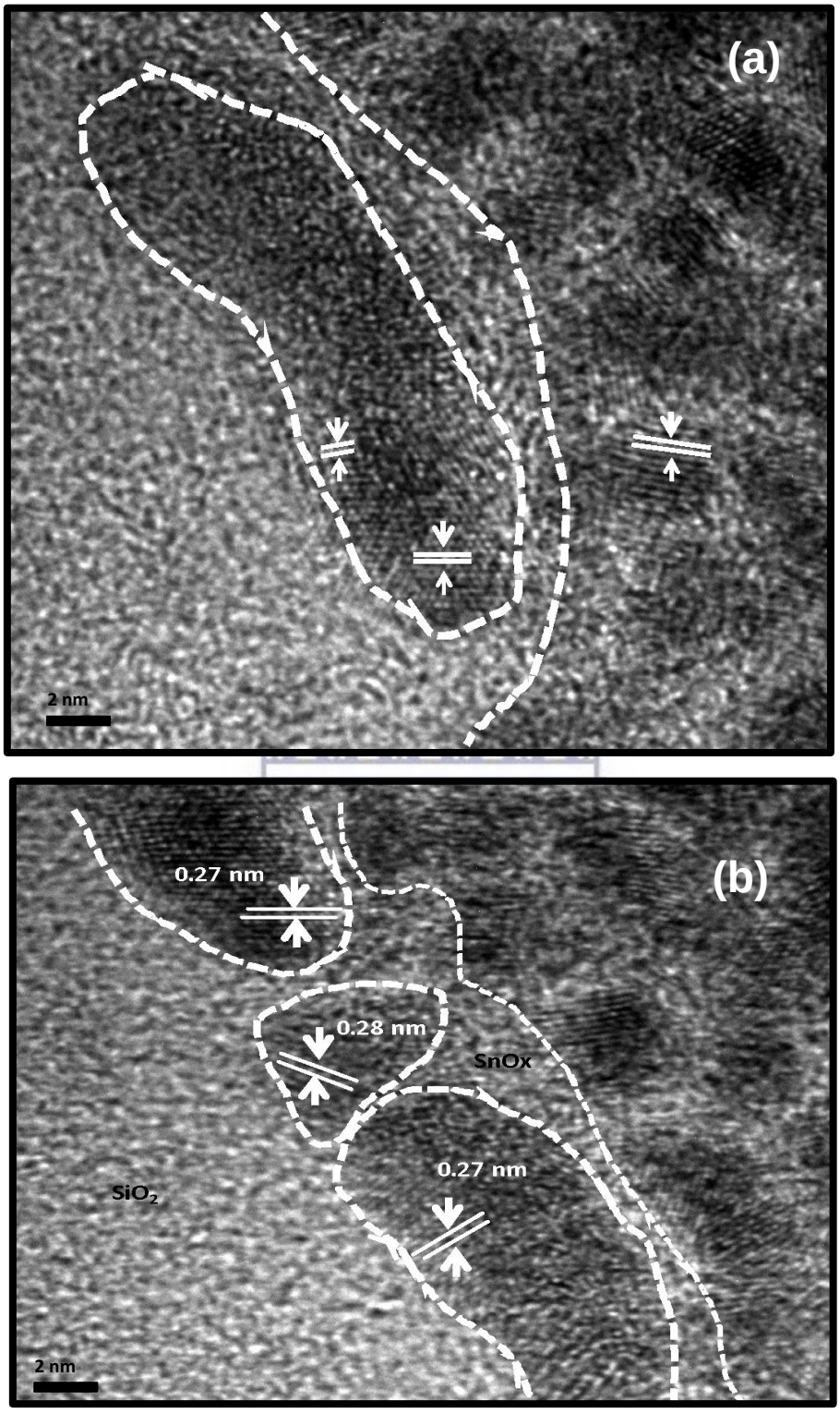

Figure 4.107: HRTEM diffraction images for the 350 °C sample at random areas.

Lines are down as guide for the eye.

4.10 Conclusion

The structural properties of Sn nanoparticles which influence the SiNW properties were investigated. The surface and interior structure of the annealed sample showed the elements (carbon, oxygen, tin and silicon) detected by XPS were present. The particle size increase with temperature was confirmed with the surface and cross-sectional FIBSEM/STEM analysis. The effect of oxygen on the crystallinity of the Sn nanoparticle was found to have significant impact, the nanoparticles were surrounded by amorphous layer. The HRTEM results showed that there was pure Sn (polycrystalline) which indicates the possibility of growing SiNWs. The surface treatment can be conducted to avoid termination of the SiNW growth due to amorphous layer.

References

4.1 K.D. Sattler, Handbook of Nanophysics, Principles and Methods (CRC, New York, 2010)

4.2 Joshi, M., A. Bhattacharyya, and S. Wazed Ali. "Characterisation techniques for nanotechnology applications in textiles." (2008).].

4.3 Garnett, Erik, and Peidong Yang. "Light trapping in silicon nanowire solar cells." Nano letters 10, no. 3 (2010): 1082-1087

4.4 Harris, Clive, and E. P. O'Reilly. "Nature of the band gap of silicon and germanium nanowires." *Physica E: Low-dimensional Systems and Nanostructures* 32, no. 1-2 (2006): 341-345

4.5 Delley, B., and E. F. Steigmeier. "Size dependence of band gaps in silicon nanostructures." *Applied physics letters* 67, no. 16 (1995): 2370-2372

4.6 Kumar, Challa SSR, ed. *UV-VIS and photoluminescence spectroscopy for nanomaterials characterisation*. Berlin, Heidelberg: Springer, 20134

4.7 Choi, Heon-Jin. "Vapor–liquid–solid growth of semiconductor nanowires." In Semiconductor Nanostructures for Optoelectronic Devices, pp. 1-36. Springer, Berlin, Heidelberg, 2012..

4.8 Dutta, Mrinal, Hung Thang Bui, and Naoki Fukata. "Effect of nanowire length on the performance of silicon nanowires based solar cell." *Advances in Natural Sciences: Nanoscience and Nanotechnology* 5, no. 4 (2014): 045014

4.9 Thiyagu, Subramani, B. Parvathy Devi, and Zingway Pei. "Fabrication of large area high density, ultra-low reflection silicon nanowire arrays for efficient solar cell applications." *Nano Research* 4, no. 11 (2011): 1136-1143.

4.10 Heine, Claus, and Rudolf H. Morf. "Submicrometer gratings for solar energy applications." Applied Optics 34, no. 14 (1995): 2476-2482

4.11 Rathi, Somilkumar J., Bhavin N. Jariwala, Joseph D. Beach, Paul Stradins, P. Craig Taylor, Xiaojun Weng, Yue Ke, Joan M. Redwing, Sumit Agarwal, and Reuben T. Collins. "Tin-catalysed plasma-assisted growth of silicon nanowires." *The Journal of Physical Chemistry C* 115, no. 10 (2011): 3833-38394

4.12 Mullane, Emma, Tadhg Kennedy, Hugh Geaney, Calum Dickinson, and Kevin M. Ryan. "Synthesis of tin catalysed silicon and germanium nanowires in a solvent–vapor system and optimization of the seed/nanowire interface for dual lithium cycling." *Chemistry of Materials* 25, no. 9 (2013): 1816-1822

4.13 Tang, Jian, Jean-Luc Maurice, Wanghua Chen, Soumyadeep Misra, Martin Foldyna, Erik V. Johnson, and Pere Roca i Cabarrocas. "Plasma-assisted growth of silicon nanowires by Sn catalyst: step-by-step observation." *Nanoscale research letters* 11, no. 1 (2016): 455

4.14 Ekstrøm, Kai Erik. "Growth and Characterization of Silicon Nanowires for Solar Cell Applications." (2011).

4.15 Choi, Heon-Jin. "Vapor–liquid–solid growth of semiconductor nanowires." In Semiconductor Nanostructures for Optoelectronic Devices, pp. 1-36. Springer, Berlin, Heidelberg, 2012

4.16 Tang, Jian, Jean-Luc Maurice, Wanghua Chen, Soumyadeep Misra, Martin Foldyna, Erik V. Johnson, and Pere Roca i Cabarrocas. "Plasma-assisted growth of silicon nanowires by Sn catalyst: step-by-step observation." *Nanoscale research letters* 11, no. 1 (2016): 455

4.17 Choi, Heon-Jin. "Vapor–liquid–solid growth of semiconductor nanowires." In Semiconductor Nanostructures for Optoelectronic Devices, pp. 1-36. Springer Berlin Heidelberg, 2012.

4.18 Liu, Ruiyuan, Fute Zhang, Celal Con, Bo Cui, and Baoquan Sun. "Lithography-free fabrication of silicon nanowire and nanohole arrays by metal-assisted chemical etching." Nanoscale research letters 8, no. 1 (2013): 1-8.

4.19 Jeong, Sangmoo, Matthew T. McDowell, and Yi Cui. "Low-temperature self-catalytic growth of tin oxide nanocones over large areas."*ACS nano*5, no. 7 (2011): 5800-5807

4.20 Kumar, R. Rakesh, K. Narasimha Rao, K. Rajanna, and A. R. Phani. "Growth of tin catalysed silicon nanowires by electron beam evaporation."Adv. Mater. Lett 4, no. 11 (2013): 836-840.

4.21 Márquez, Francisco, Carmen Morant, Vicente López, Félix Zamora, Teresa Campo, and Eduardo Elizalde. "An alternative route for the synthesis of silicon nanowires via porous anodic alumina masks." Nanoscale research letters 6, no. 1 (2011): 495.

4.22 Wu, Yiying, and Peidong Yang. "Direct observation of vapor – liquid – solid nanowire growth." Journal of the American Chemical Society 123, no. 13 (2001): 3165-3166.

4.23 Yin, Qixun, and Leng Chen. "The correlation of electrical conductivity with the microstructure of $Ge_2Sb_2Te_5$ thin films alloyed with Sn." Materials Research Express 4, no. 1 (2017): 016407.

4.24 Hernández-Nava, E., C. J. Smith, F. Derguti, S. Tammas-Williams, Fabien Léonard, P. J. Withers, I. Todd, and R. Goodall. "The effect of density and feature size on mechanical properties of isostructural metallic foams produced by additive manufacturing." Acta Materialia 85 (2015): 387-395.

4.25 Leifeld, O., A. Beyer, E. Müller, D. Grützmacher, and K. Kern. "Nucleation of Ge quantum dots on the C-alloyed Si (001) surface." Thin Solid Films 380, no. 1 (2000): 176-179.

4.26 Korin, Efrat, Natalya Froumin, and Smadar Cohen. "Surface Analysis of Nanocomplexes by X-ray Photoelectron Spectroscopy (XPS)." ACS Biomaterials Science & Engineering (2017).

4.27 http://www.gel.usherbrooke.ca/casino/

4.28 Williams, Thomas J. "Scanning electron microscopy and x-ray microanalysis, By Joseph Goldstein, Dale Newbury, David Joy, Charles Lyman, Patrick Echlin, Eric Lifshin, Linda Sawyer, Joseph Michael Kluwer Academic Publishers, New York (2003) ISBN 0306472929; hardback; 688." Scanning 27, no. 4 (2005): 215-216..

4.29 Wright, Jason T., Daniel J. Carbaugh, Morgan E. Haggerty, Andrea L. Richard, David C. Ingram, Savas Kaya, Wojciech M. Jadwisienczak, and Faiz Rahman. "Thermal oxidation of silicon in a residual oxygen atmosphere—the RESOX process—for self-limiting growth of thin silicon dioxide films." *Semiconductor Science and Technology* 31, no. 10 (2016): 105007.],

4.30 Alam, Syed Nasimul, and Manas Kumar Mishra. "SEM and EDX study of intermetallics in a copper-tin system and the oxidation behavior of tin."*Microsyst. Technol* 27 (2013): 7-11.

SUMMARY

This study was focused on the control of the SiNW diameter, length and composition by a metal catalyst. The diameter of nanowires improves the light trapping ability of the solar cell. It is also ideal for photovoltaic cells due to the large junction area that extends along the entire length of the nanowire with carrier separation in the radial direction, which promises high efficiency. The structural and chemical behaviour of the Sn catalyst behaviour with temperature increase was investigated.

The Sn coated Si wafer was subjected to various temperature (180, 232, 350 and 450 °C) while observing the chemical composition of the Sn film. The x-ray photoelectron spectroscopy results obtained contained the adventitious carbon as well as the Sn oxides (SnO and SnO_2). The results indicate surface contamination and Sn film oxidation. The exposure of the Si substrate was also detected. According to the high resolution XPS results there is an increase in the Si content while the amount of Sn decreases at the temperature of 279 °C and it was assumed to be the Sn nanoparticle formation since the temperature it's above the Si-Sn eutectic (232 °C)

The surface morphology analysis was done using the scanning electron microscope. The SEM results indicated the Sn clusters with Si substrate exposed on the as-deposited sample, which indicates the Volmer-Weber thin film growth because of the 3 nm thickness of the film. The 350 °C clearly indicates the Sn nanoparticles coalescence due to elevated temperatures, which will lead to Sn nanoparticle agglomeration in to bigger diameter size due to surface tension. The well dispersed

bigger Sn nanoparticles were observed at 450 °C.

The elemental composition the windowless EDS analysis was conducted which indicated the presence of the carbon, Sn and oxygen on the Si surface. According to the EDS mapping the oxygen has spread over the surface leading to SnOx and SiO_2. The carbon was found to be due to surface contamination which was observed on the SEM micrograph and XPS results.

The further investigation was done to determine if the Sn was completely oxidised. The EDX elemental mapping on the TEM lamella of the as-deposited and the 350 °C samples indicated the presence of pure Sn which is covered by its oxides and the oxides were also at the Sn/Si interface. HRTEM showed that the pure Sn core it was crystalline at 350 °C. These observations indicate the possibility of crystalline SiNW synthesis.

For future work, the hydrogen plasma can be used to remove the oxygen on the surface as well as the Sn/Si interface. The removal of the oxygen can lead to a successful SiNW synthesis.